Springer Series in Materials Science 312

Yuan Cheng
Tian Wang
Gang Zhang *Editors*

Artificial Intelligence for Materials Science

Springer

Springer Series in Materials Science

Volume 312

The Springer Series in Materials Science covers the complete spectrum of materials research and technology, including fundamental principles, physical properties, materials theory and design. Recognizing the increasing importance of materials science in future device technologies, the book titles in this series reflect the state-of-the-art in understanding and controlling the structure and properties of all important classes of materials.

More information about this series at http://www.springer.com/series/856

Yuan Cheng • Tian Wang • Gang Zhang
Editors

Artificial Intelligence for Materials Science

Springer

Editors
Yuan Cheng
Monash Suzhou Research Institute
Suzhou, P.R. China

Gang Zhang
Institute of High Performance Computing
Singapore, Singapore

Tian Wang
Institute of Artificial Intelligence
Beihang University
Beijing, China

ISSN 0933-033X ISSN 2196-2812 (electronic)
Springer Series in Materials Science
ISBN 978-3-030-68309-2 ISBN 978-3-030-68310-8 (eBook)
https://doi.org/10.1007/978-3-030-68310-8

This Springer imprint is published by the registered company Springer Nature Switzerland AG
The registered company address is: Gewerbestrasse 11, 6330 Cham, Switzerland

Preface

Developing algorithmic approaches for the design and discovery of new functional materials can have huge technological and social impact. Usually, such rational design requires a holistic perspective over the full multistage design process. With big data generated by theory and experiments, machine learning approaches have been extensively employed in materials genome initiatives and materials informatics, which can potentially solve some of our challenges on the way to rational materials design. Over the last few decades, materials research has shifted toward more rational design. There are now many examples, such as the accelerated discovery of thermoelectric materials, high-entropy alloys, and thermal functional materials.

Machine learning methods have lowered the cost of exploring new structures of unknown compounds. Furthermore, machine learning methods can be used to predict reasonable expectations, and then the output of the machine learning models can be validated by experimental results. In recent years, new insight has been revealed, and several elaborative tools have been developed for materials science and engineering. Moreover, searchable and interactive databases could promote research regarding emerging materials. Recently, the databases containing a large number of high-quality material properties for new advanced materials discovery have been developed. The development of machine learning will allow us to pursue our aim of understanding and designing of materials in a new way. Moreover, it looks set to make a significant impact on human life and, with numerous commercial developments emerging, will become a major academic topic over the coming years.

This book sets the subject into context by first of all describing the chief advancements of these artificial intelligence methods and their applications in materials design. The aim of this book is to provide an introduction both to existing scientific community in this field and for new people who wish to enter it. The book should also be useful for graduate-level students who want to explore this new field of research. With content relevant to both academic and commercial viewpoints, the book will interest researchers and postgraduates as well as consultants and industrial engineers.

The single chapters have been written by internationally recognized experts in computer science and material science and provide in-depth introductions to the directions of their research. Moreover, one chapter outlines the basic information about the AI principles and algorithm, followed by chapters addressing most important and commonly adopted computational and analysis methods in computational material science, and application of these functional materials in various fields, including electronics, optoelectronics, thermoelectric energy conversion, high-entropy alloys, and robotics. We are sure that this book will be a useful reference not only for scientists and engineers exploring material science but also for graduate and postgraduate students specializing in computer, physics, and material science.

We are most grateful to Springer Nature publisher for the invitation to edit this book, and for kind and efficient assistance in editing this book. We are also grateful to all book chapter authors for sharing their expertise in this multi-author monograph. Their strong efforts and enthusiasm for this project were indispensable for bringing it to success.

Suzhou, P.R. China — Yuan Cheng

Beijing, China — Tian Wang

Singapore, Singapore — Gang Zhang

Contents

Brief Introduction of the Machine Learning Method

Tian Wang

1 Introduction

In [1], machine learning is defined as:

Definition: A computer program is said to learn from experience E with respect to some class of tasks T and performance measure P, if its performance at tasks in T, as measured by P, improves with experience E.

With big data generated by theory and experiments, machine learning approaches have been extensively employed in materials genome initiatives and materials informatics. In addition to the data calculated based on first principles theory, the experimental data from imaging, spectroscopy, inelastic neutron scattering techniques, etc. have also been adopted to accelerate the process of materials design and discovery. The quality and rate of theoretical predictions for the design of functional materials have been improved with data from technical advances. Machine learning methods have lowered the cost of exploring new structures of unknown compounds. Furthermore, machine learning methods can be used to predict reasonable expectations, and then the output of the machine learning models can be validated by experimental results. Both qualitative and quantitative methods, which are based on high-throughput computations and autonomous workflows, were employed to facilitate thermoelectric research with respect to novel material discovery, design, synthesis, and optimization [2].

To satisfy target functionality, an inverse design method was introduced. As shown in Fig. 1 from [3], a cycle procedure consisting of prediction, synthesis, and characterization was adopted to discover new materials with the desired functionalities [3]. The bottom part of the figure consists of possible compounds

T. Wang (✉)
Institute of Artificial Intelligence, Beihang University, Beijing, China
e-mail: wangtian@buaa.edu.cn

Y. Cheng et al. (eds.), *Artificial Intelligence for Materials Science*, Springer Series in Materials Science 312, https://doi.org/10.1007/978-3-030-68310-8_1

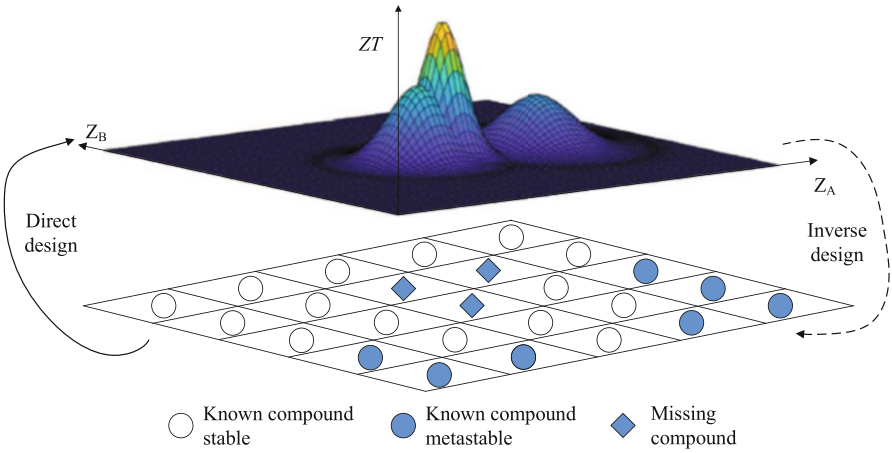

Fig. 1 Direct and inverse approaches for the design of materials. The bottom part of the figure is composed of compounds of known structure and unreported compounds. The contour in the upper part of the figure delineates the variation of the target property or functionality. In the direct design approach, all possible compounds are investigated first. Then, a calculation of target functionality is carried out for each compound. Conversely, in the inverse design approach, the compounds with desirable functionality are investigated

of the material. The blue and white circles are the existing compounds of known composition and structure. The blue diamonds represent chemically plausible but unreported compounds. The upper part of the figure is a contour of the considered property. In direct design approaches, all possible compounds are investigated, and their properties are calculated to predict a new material. Alternately, in the inverse design approaches, the functionality is declared and calculated first, and then only the compounds with desirable properties are investigated. For the design of materials, machine learning has been applied to the synthesis step to accelerate the process of strategy searching.

Direct design approach

- Task T: calculation of target functionality; all compounds are investigated firstly.
- Performance measure P: part of the materials with the accurately predicted properties.
- Training experience E: a database of the materials with given properties; the properties are the supervised labels.

Inverse design approach

- Task T: search the appropriate materials; the functionality is declared and calculated first.
- The P and E are as the same as direct design approach.

2 Notation

In computer systems, "experience" (E) usually exists in the form of "data." With the computational methods, machine learning studies the strategies to improve performance. With the learning algorithm and the experience data, the appropriate model can provide a corresponding judgment for the new situation.

For the materials research, the set of records establish a *data set*. Each record is the description of the *instance* or the *sample*. The components that reflect the performance or characteristics of an object in a certain aspect are called *attributes* or *features*. The values of the attributes or features are called *attribute values*. The space formed by attributes is called *attribute space* or *sample space*.

The procedure that obtains the model from the data is *learning* or *training*, which is achieved by the learning algorithms. The data employed in the training procedure is called *training data*. Each sample is a *training sample*. The training samples construct the *training set*. (x_i, y_i) is the i-th sample. $y_i \in Y$ is the label of x_i. Y is the *label space*, which is the set of the labels. For most practical applications, the original input data are typically *pre-processed* to transform them into some new space of variables, where the pattern recognition problem will be easier to solve. This pre-processing stage is sometimes also called *feature extraction*. Note that new test data must be pre-processed using the same steps as the training data.

Take $D = \{x_1, x_2, \ldots, x_m\}$ as a data set consists of m instances. Each instance is described with d attributes. Each instance $x_i = (x_{i1}; x_{i1}; \ldots; x_{id}), x_i \in X$ is a *feature vector* in the sample space X with the d dimensionality. x_{ij} is the j-th value of the x_i.

The learning task can be generally divided into two categories: *supervised learning* and *unsupervised learning*. Applications in which the training data comprises examples of the input vectors along with their corresponding target vectors are known as *supervised learning* problems. *Classification* and *regression* are the supervised learning method. The aim of the classification problems is to assign each input to a finite number of discrete categories. If the desired output consists of one or more continuous variables, then the task is called *regression*. In the supervised learning method, the goal is to learn the function from the input x to the targets t. For a labeled set $\{(x_i, t_i)\}_{i=1}^{N}$, which is the training set, the number of the training samples is N.

In *unsupervised learning* problems, the training data consists of a set of input vectors x without any corresponding target values. *Clustering, density estimation*, and *visualization* are the unsupervised learning method. The goal of *clustering* is to discover groups of similar examples within the data. *Density estimation* is to determine the distribution of data within the input space. The purpose of the *visualization* is to project the data from a high-dimensional space down to two or three dimensions.

3 Support Vector Machine

SVM can be adopted in the materials classification problem. The two-class classification problem using linear models is:

$$y(x) = w^{\mathrm{T}}\phi(x) + b, \tag{1}$$

where $\phi(x)$ denotes a fixed feature-space transformation. b is a bias parameter. The training data set comprises N input vectors $x_1, \ldots, x_N$, with corresponding target values $t_1, \ldots, t_N$ where $t_n \in \{-1, 1\}$, and new data points x are classified according to the sign of $y(x)$. If the training data set is linearly separable in feature space, w and b satisfy $y(x_n) > 0$ for points having $t_n = +1$ and $y(x_n) < 0$ for points having $t_n = -1$, $t_n y(x_n) > 0$ for all training data points.

To classify the training data set, the solution should try to find the one that will give the smallest generalization error. The support vector machine approaches this problem through the concept of the margin, which is defined to be the smallest distance between the decision boundary and any of the samples, as illustrated in Fig. 2.

The perpendicular distance of a point x from a hyperplane defined by $y(x)$ where $y(x)$ takes the form Eq. 1 is given by $\frac{|y(x)|}{||w||}$. The distance of a point x_n to the decision surface is given by

$$\frac{t_n y(x_n)}{||w||} = \frac{t_n(w^T\phi(x_n) + b)}{||w||}. \tag{2}$$

The margin is given by the perpendicular distance to the closest point x_n from the data set. w and b are optimized to maximize this distance. Thus, the maximum margin solution is found by solving:

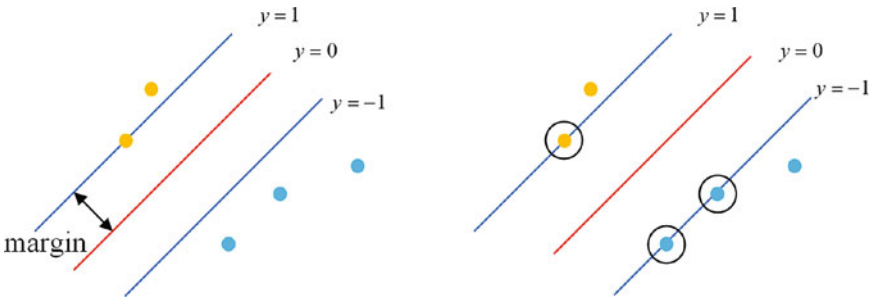

Fig. 2 As shown in the left figure, the margin is defined as the perpendicular distance between the decision boundary and the closest of the data points. As shown in the right figure, maximizing the margin leads to a particular choice of the decision boundary. The support vectors, which are indicated by the circles, determine the location of this boundary

$$\arg\max_{w,b}\{\frac{1}{||w||}\min_{n}[t_n(w^T\phi(x_n)+b)]\}. \tag{3}$$

where $\frac{1}{||w||}$ is outside the optimization over n because w does not depend on n. If $w \to kw$ and $b \to kb$ are rescaled, the distance $\frac{t_n y(x_n)}{||w||}$ is unchanged. For the point that is closest to the surface

$$t_n(w^T\phi(x_n)+b) = 1. \tag{4}$$

All data points will satisfy the constraints

$$t_n(w^T\phi(x_n)+b) \geq 1 \quad n = 1, \ldots, N. \tag{5}$$

This is known as the canonical representation of the decision hyperplane. The data points where the equality holds, the constraints are said to be active. The remainder is inactive. Maximizing $||w||^{-1}$ is equivalent to minimizing $||w||^2$:

$$\arg\min_{w,b}\frac{1}{2}||w||^2, \tag{6}$$

subject to the constraints given by Eq. 5. Lagrange multipliers $a_n \geq 0$ is introduced to solve the constrained optimization problem. The Lagrangian function is

$$L(w,b,a) = \frac{1}{2}||w||^2 - \sum_{n=1}^{N} a_n\{t_n(w^T\phi(x_n)+b) - 1\}, \tag{7}$$

where $a = (a_1, \ldots, a_N)^T$. Setting the derivatives of $L(w,b,a)$ with respect to w and b equal to zero

$$w = \sum_{n=1}^{N} a_n t_n \phi(x_n). \tag{8}$$

$$\sum_{n=1}^{N} a_n t_n = 0. \tag{9}$$

Eliminate w and b from $L(w,b,a)$. The dual representation of the maximum margin problem is

$$L(a) = \sum_{n=1}^{N} a_n - \frac{1}{2}\sum_{n=1}^{N}\sum_{m=1}^{N} a_n a_m t_n t_m k(x_n, x_m), \tag{10}$$

$$a_n \geq 0 \quad n = 1, \ldots, N, \tag{11}$$

$$\sum_{n=1}^{N} a_n t_n = 0. \tag{12}$$

The kernel function is defined by $k(x, x') = \phi(x)^T \phi(x')$. In order to classify new data points using the trained model, the sign of $y(x)$ is evaluated.

$$y(x) = \sum_{n=1}^{N} a_n t_n k(x, x_n) + b. \tag{13}$$

A constrained optimization of this form satisfies the Karush-Kuhn-Tucker (KKT) conditions, which in this case require that the following three properties hold

$$a_n \geq 0, \tag{14}$$

$$t_n y(x_n) - 1 \geq 0, \tag{15}$$

$$a_n \{t_n y(x_n) - 1\} = 0. \tag{16}$$

Thus for every data point, either $a_n = 0$ or $t_n y(x_n) = 1$. Any data point for which $a_n = 0$ will play no role in making predictions. The remaining data points are called support vectors. Once the model is trained, only the support vectors retained.

$$t_n \left(\sum_{m \in S} a_m t_m k(x_n, x_m) + b \right) = 1, \tag{17}$$

where S denotes the set of indices of the support vectors. b is given by

$$b = \frac{1}{N_S} \sum_{S} \left(t_n - \sum_{m \in S} a_m t_m k(x_n, x_m) \right), \tag{18}$$

where N_S is the total number of support vectors. The maximum margin hyperplane is defined by the support vectors.

4 Clustering

Cluster is adopted for the task of dividing data into meaningful groups based on the information of data. Clustering is an unsupervised machine learning method.

Typical models contain centroid models (e.g., k-means algorithm), connectivity models (e.g., hierarchical clustering), and density models (e.g., density-based spatial clustering of applications with noise (DBSCAN)). The similarity within a cluster and the difference between clusters indicate the structure or properties within the data. K-means clustering is introduced.

In terms of the most common clustering method k-means, given a set of d-dimensional Euclidean variables, i.e., observations, $(\mathbf{x_1}, \mathbf{x_2}, \ldots, \mathbf{x_n})$, k-means is aimed at dividing n observations into $k(k \leq n)$ sets $\mathbf{S} = \{S_1, S_2, \ldots, S_k\}$ satisfying the objective:

$$arg \min_{S} \sum_{i=1}^{k} \sum_{\mathbf{x} \in S_i} \|\mathbf{x} - \mu_{\mathbf{i}}\|^{\mathbf{2}} = arg \min_{\boldsymbol{S}} \sum_{i=1}^{k} |S_i| \text{ Var } S_i, \tag{19}$$

where $\boldsymbol{\mu_i}$ is the mean of the data in the set S_i and n observations are partitioned into k clusters where each observation belongs to a cluster with the nearest mean.

It is convenient at this point to define some notation to describe the assignment of data points to clusters. For each data point x_n, we introduce a corresponding set of binary indicator variables $r_{nk} \in \{0, 1\}$ where $k = 1, \ldots, K$ describing which of the K clusters the data point x_n is assigned to, so that if data point x_n is assigned to cluster k, then $r_{nk} = 1$ and $r_{nj} = 0$ for $j \neq k$. This is known as the 1-of-K coding scheme. We can then define an objective function, sometimes called a *distortion measure*, given by

$$J = \sum_{n=1}^{N} \sum_{k=1}^{K} r_{nk} \|x_n - \mu_k\|^2, \tag{20}$$

which represents the sum of the squares of the distance of each data point to its assigned vector μ_k. Our goal is to find values for the $\{r_{nk}\}$ and the $\{\mu_k\}$ to minimize J.

Consider first the determination of the r_{nk}. Because J is a linear function of r_{nk}, this optimization can be performed easily to give a closed form solution. The terms involving different n are independent, and we can optimize for each n separately by choosing r_{nk} to be 1 for whichever value of k gives the minimum value of $\|x_n - \mu_k\|^2$. In other words, we simply assign the n-th data point to the closest cluster center. More formally, this can be expressed as

$$r_{nk} = \begin{cases} 1 \text{ if } k = \arg\min_j \|x_n - \mu_j\|^2 \\ 0 \text{ otherwise.} \end{cases} \tag{21}$$

Now consider the optimization of the μ_k with the r_{nk} held fixed. The objective function J is a quadratic function of μ_k, and it can be minimized by setting its derivative with respect to μ_k to zero giving

$$2\sum_{n=1}^{N} r_{nk}(x_n - \mu_k) = 0. \tag{22}$$

which we can easily solve for μ_k to give

$$\mu_k = \frac{\sum_n r_{nk} x_n}{\sum_n r_{nk}}. \tag{23}$$

The denominator in this expression is equal to the number of points assigned to cluster k, and so this result has a simple interpretation, namely, set μ_k equal to the mean of all of the data points x_n assigned to cluster k. For this reason, the procedure is known as the *k-means* algorithm. Updating r_{nk} and updating μ_k correspond respectively to the E (expectation) and M (maximization) steps of the EM algorithm.

4.1 Expectation-Maximization Algorithm

In many practical learning settings, only a subset of the relevant instance features might be observable. Consider a problem in which the data D is a set of instances generated by a probability distribution that is a mixture of k distinct Normal distributions.

Applied to k-means problem, the EM algorithm searches for a maximum likelihood hypothesis by repeatedly re-estimating the expected values of the hidden variables z_{ij} given its current hypothesis $(\mu_i \ldots \mu_k)$ and then recalculating the maximum likelihood hypothesis using these expected values for the hidden variables. The EM algorithm first initializes the hypothesis to $h = (\mu_1, \mu_2)$, where μ_1 and μ_2 are arbitrary initial values. It then iteratively re-estimates h by repeating the following two steps until the procedure converges to a stationary value for h.

1 Calculate the expected value $E[z_{ij}]$ of each hidden variable z_{ij}, assuming the current hypothesis $h = (\mu_1, \mu_2)$ holds.
2 Calculate a new maximum likelihood hypothesis $h' = (\mu_i', \mu_2')$, assuming the value taken on by each hidden variable z_{ij} is its expected value $E[z_{ij}]$ calculated in Step 1. Then replace the hypothesis $h = (\mu_i, \mu_2)$ with the new hypothesis $h' = (\mu_i', \mu_2')$ and iterate.

Step 1 must calculate the expected value of each z_{ij}. This $E[z_{ij}]$ is just the probability that instance x_i was generated by the j-th Normal distribution.

$$\begin{aligned} E[z_{ij}] &= \frac{p(x = x_i | \mu = \mu_j)}{\sum_{n=1}^{2} p(x = x_i | \mu = \mu_n)} \\ &= \frac{e^{-\frac{1}{2\sigma^2}(x_i - \mu_j)^2}}{\sum_{n=1}^{2} e^{-\frac{1}{2\sigma^2}(x_i - \mu_n)^2}}. \end{aligned} \tag{24}$$

Thus the first step is implemented by substituting the current values (μ_l, μ_2) and the observed x_i into the above expression. In the second step, we use the $E[z_{ij}]$ calculated during Step 1 to derive a new maximum likelihood hypothesis $h' = (\mu_i', \mu_2')$. As we will discuss later, the maximum likelihood hypothesis in this case is given by

$$\mu_j \leftarrow \frac{\sum_{i=1}^{m} E[z_{ij}]x_i}{\sum_{i=1}^{m} E[z_{ij}]}. \tag{25}$$

The above algorithm for estimating the means of a mixture of k Normal distributions illustrates the essence of the EM approach: The current hypothesis is used to estimate the unobserved variables, and the expected values of these variables are then used to calculate an improved hypothesis. It can be proved that on each iteration through this loop, the EM algorithm increases the likelihood $P(D|h)$ unless it is at a local maximum. The algorithm thus converges to a local maximum likelihood hypothesis for (μ_l, μ_2).

4.2 EM Related to K-Means

The comparison of the k-means algorithm with the EM algorithm for Gaussian mixtures shows that there is a close similarity. Whereas the k-means algorithm performs a hard assignment of data points to clusters, in which each data point is associated uniquely with one cluster, the EM algorithm makes a soft assignment based on the posterior probabilities. In fact, we can derive the k-means algorithm as a particular limit of EM for Gaussian mixtures as follows. Consider a Gaussian mixture model in which the covariance matrices of the mixture components are given by εI, where ε is a variance parameter that is shared by all of the components, and I denotes the identity matrix, so that

$$p(x|\mu_k, \Sigma_k) = \frac{1}{(2\pi\varepsilon)^{1/2}} exp\left\{-\frac{1}{2\varepsilon}\|x - \mu_k\|^2\right\}. \tag{26}$$

Consider the EM algorithm for a mixture of K Gaussians of this form in which we treat ε as a fixed constant instead of a parameter to be re-estimated. The posterior probabilities, or responsibilities, for a particular data point x_n, are given by

$$\gamma(z_{nk}) = \frac{\pi_k exp\{-\|x_n - \mu_k\|^2/2\varepsilon\}}{\sum_j \pi_j exp\{-\|x_n - \mu_k\|^2/2\varepsilon\}} \tag{27}$$

Consider the limit $\varepsilon \to 0$, we see that in the denominator, the term for which $\|x_n - \mu_j\|^2$ is smallest will go to zero most slowly, and hence the responsibilities $\gamma(z_{nk})$ for the data point x_n all go to zero except for term j, for which the responsibility $\gamma(z_{nk})$ will go to unity. Note that this holds independence of the

values of the πk so long as none of the πk is zero. Thus, in this limit, we obtain a hard assignment of data points to cluster, just as in the K-means algorithm, so that $\gamma(z_{nk}) \to r_{nk}$. Each data point is thereby assigned to the cluster having the closest mean.

The EM re-estimation equation for the μ_k then reduces to the k-means result. Note that the re-estimation formula for the mixing coefficients simply re-sets the value of πk to be equal to the fraction of data points assigned to cluster k, although these parameters no longer play an active role in the algorithm. Finally, with the limit $\varepsilon \to 0$, the expected complete data log-likelihood becomes

$$\mathbb{E}_Z[\ln p(X, Z|\mu, \Sigma, \pi)] \to -\frac{1}{2}\sum_{n=1}^{N}\sum_{k=1}^{K} r_{nk}\|x_n - \mu_k\|^2 + \text{const.} \tag{28}$$

Maximizing the expected complete data log-likelihood is equivalent to minimizing the distortion measure J for the K-means algorithm. Note that the K-means algorithm does not estimate the covariances of the clusters but only the cluster means.

5 Regression

In the field of machine learning, regression analysis is a statistical analysis process for estimating the quantitative relationships among two or more variables. Most commonly, the regression function represents the relationship between a dependent variable and one or more independent variables. Many techniques for solving regression problems have been developed, such as linear regression, logistic regression, polynomial regression, ridge regression, and LASSO regression.

If there is a data set consists of N samples x_i, $i = 1, \ldots, N$, and a response t_i, e.g., the $x_i, t_i \in \mathbb{R}$, the task about regression is to predict the value of t of a new sample x. The direct way is to build a function $y(x)$ whose values for new inputs x are to predict the values t.

5.1 Linear Regression

Linear regression models a linear relationship between independent variables $\mathbf{x}$ and the response $\mathbf{y}$. In general, given a data set $\{\mathbf{y}_i, \mathbf{x}_{i1}, \mathbf{x}_{i2}, \ldots, \mathbf{x}_{ip}\}_{i=1}^{n}$ of n statistical units, the model takes the following form:

$$y_i = w + w_1\mathbf{x}_{i1} + w_2\mathbf{x}_{i2} + \ldots + w_p\mathbf{x}_{ip} + \varepsilon_i, i = 1, 2, \ldots, n, \tag{29}$$

where ε_i is an unobserved random error.

Often these n equations are arranged in matrix notation as

$$\mathbf{y} = X\mathbf{w} + \boldsymbol{\varepsilon}, \tag{30}$$

where

$$\mathbf{y} = \begin{pmatrix} y_1 \\ y_2 \\ \vdots \\ y_n \end{pmatrix}, X = \begin{pmatrix} \mathbf{x_1^T} \\ \mathbf{x_2^T} \\ \vdots \\ \mathbf{x_n^T} \end{pmatrix} = \begin{pmatrix} 1 & x_{11} & \cdots & x_{1p} \\ 1 & x_{21} & \cdots & x_{2p} \\ \vdots & \vdots & \ddots & \vdots \\ 1 & x_{n1} & \cdots & x_{np} \end{pmatrix}, \mathbf{w} = \begin{pmatrix} w_0 \\ w_1 \\ \vdots \\ w_p \end{pmatrix}, \varepsilon = \begin{pmatrix} \varepsilon_1 \\ \varepsilon_2 \\ \vdots \\ \varepsilon_n \end{pmatrix}. \tag{31}$$

The optimization of linear regression seeks to minimize the loss function, which evaluates the difference between predicted and true values. In most cases, quadratic loss function J are used as loss function for linear regression models.

$$J_{\mathbf{w}} = \min_{w} \{\|X\mathbf{w} - \mathbf{y}^2\|_2^2\}. \tag{32}$$

Linear regression models are usually used to fit a predictive model training set and predict new explanatory variables.

The linear combination of the input variables is

$$y(\mathbf{x}, \mathbf{w}) = w_0 + w_1 x_1 + \cdots + w_D x_D \tag{33}$$

where $\mathbf{x} = (x_1, \cdots, x_D)^{\mathrm{T}}$ and $\mathbf{w} = (w_0, w_1, \cdots, x_D)^{\mathrm{T}}$. If the input x is computed with the nonlinear function ϕ, which is called basis function, the model can be extended into:

$$y(\mathbf{x}, \mathbf{w}) = w_0 + \sum_{j=1}^{M-1} w_i \phi_j(\mathbf{x}). \tag{34}$$

The transformed function is:

$$y(\mathbf{x}, \mathbf{w}) = \sum_{j=0}^{M-1} w_i \phi_j(\mathbf{x}) = \mathbf{w}^{\mathrm{T}} \boldsymbol{\phi}(\mathbf{x}). \tag{35}$$

where $\mathbf{w} = (w_0, \cdots, w_{M-1})^{\mathrm{T}}$, $\boldsymbol{\phi} = (\phi_0, \cdots, \phi_{M-1})^{\mathrm{T}}$, and $\phi_0 = 1$.

The target t is given by a deterministic function y with the noise ε

$$t = y(\mathbf{x}, \mathbf{w}) + \varepsilon. \tag{36}$$

where ε is the residual error between the linear predictions and the true response. ε is assumed to have a Gaussian or normal distribution. $\varepsilon \sim \mathcal{N}(\mu, \sigma^2)$. μ and σ are the mean and the variance, respectively.

5.2 Polynomial Regression

Polynomial regression is a method used to model the nonlinear relationship between the independent variables and response. In general, y is modeled as an n-th degree polynomial:

$$\mathbf{y} = X\mathbf{w} + \boldsymbol{\varepsilon}, \tag{37}$$

$$\mathbf{y} = \begin{pmatrix} y_1 \\ y_2 \\ \vdots \\ y_n \end{pmatrix}, X = \begin{pmatrix} \mathbf{x_1^T} \\ \mathbf{x_2^T} \\ \vdots \\ \mathbf{x_n^T} \end{pmatrix} = \begin{pmatrix} 1 & x_1 & x_1^2 & \cdots & x_1^m \\ 1 & x_2 & \cdots & & x_2^m \\ \vdots & \vdots & \ddots & & \vdots \\ 1 & x_n & \cdots & & x_n^m \end{pmatrix}, \mathbf{w} = \begin{pmatrix} w_0 \\ w_1 \\ \vdots \\ w_m \end{pmatrix}, \varepsilon = \begin{pmatrix} \varepsilon_1 \\ \varepsilon_2 \\ \vdots \\ \varepsilon_n \end{pmatrix}, \tag{38}$$

where ε is a random unobserved error. Quadratic loss functions are usually used as the loss functions of polynomial regression models. A high-order equation increases the complexity of the model, but at the same time, a broader range of functions can be modeled. Moreover, the incorporation of the holder means (also called the power means) to construct descriptors can consider a large range of functions and include the different orders of means from harmonic to quadric means.

5.3 Ridge Regression and LASSO Regression

The results from linear and polynomial models are influenced by the noise in the training set. Therefore, including more adjustable parameters may fail to make reliable predictions. In principle, if the model exactly reproduces the training samples but cannot provide the correct prediction, then the phenomenon referred to as overfitting has ensued. Generally, overfitting occurs when there are too many adjustable parameters and the training set is not large enough. Ridge regression is a regression method that prevents overfitting by introducing the $L2$ regularization term $\alpha||w||^2$, so the loss function of ridge regression can be written as:

$$J(w) = \min_{\mathbf{w}} \{\|X\mathbf{w} - \mathbf{y}\|_2^2 + \alpha\|\mathbf{w}\|^2\}. \tag{39}$$

LASSO regression carries out $L1$ regularization in the form of $\alpha\|w\|_1$ to avoid overfitting. Its loss function can be written as:

$$J(w) = \min_{\mathbf{w}} \left\{ \frac{1}{2N} \|X\mathbf{w} - \mathbf{y}\|_2^2 + \alpha\|\mathbf{w}\|_1 \right\}. \tag{40}$$

When a ridge regression or a LASSO regression model is trained, $L2$ regularization enforces the coefficients of the irrelevant features to be lower, while the

$L1$ regularization method will set those coefficients to zero. In this way, a ridge regression model or a LASSO regression model limits its complexity. Therefore, this approach avoids overfitting and can identify essential descriptors.

6 Decision Tree and Ensemble Learning

Decision tree is a type of supervised machine learning method for approximating discrete-valued target functions. Each tree is composed of two entities, i.e., leaves and decision nodes. Decision nodes are the places that split the data, and the leaves provide the decisions or the final outcomes. Each branch descending from that node corresponds to one of the possible values for this attribute, and each node in the tree specifies a test of some attribute of the instance. Decision trees can handle both numeric and categorical data and are easy to interpret as a white model. Iterative dichotomizer 3 (ID3), C4.5, and classification and regression trees (CART) are the most famous algorithms used to generate a decision tree. Entropy is the basis of ID3 and C4.5. If the data set is S, then the set of classes in S is X and the proportion of the elements in class x to the number of elements in S is $p(x)$. Entropy H of S can be written as:

$$H(S) = \sum_{x \in X} -p(x) log_2 p(x). \tag{41}$$

In ID3, the information gain is used to split the data set S:

$$IG(S, A) = H(S) - \sum_{t \in T} p(t)H(t) = H(S) - H(S|A), \tag{42}$$

where A is an attribute that splits set S, T represents the subsets generated from splitting set S by attribute A so that $S = \cup_{t \in T} t$, and $p(t)$ is the proportion of the number of elements in t to the number of elements in set S.

C4.5 uses the gain ratio $Gain\_ratio$ instead.

$$Gain\_ratio(S, A) = IG(S, A)/IV(A), \tag{43}$$

where $IV(A) = -\sum_{t \in T} p(t) log_2 p(t)$, i.e., the intrinsic value of A.

As for CART, the Gini impurity I is a measure of the difference.

$$I_S = 1 - \sum_{x \in X} p(x)^2, \tag{44}$$

where I_S is the Gini impurity of set S.

Decision tree learning is generally best suited to problems with the following characteristics:

- Instances are represented by attribute-value pairs.
- The target function has discrete output values.
- Disjunctive descriptions may be required. Decision trees naturally represent disjunctive expressions.
- The training data may contain errors. Decision tree learning methods are robust to errors, both errors in classifications of the training examples and errors in the attribute values that describe these examples.
- The training data may contain missing attribute values.

The basic learning algorithm of ID3 learns decision trees by constructing them top-down. Each instance attribute is evaluated using a statistical test to determine how well it alone classifies the training examples. The best attribute is selected and used as the test at the root node of the tree. A descendant of the root node is then created for each possible value of this attribute, and the training examples are sorted to the appropriate descendant node. The entire process is then repeated using the training examples associated with each descendant node to select the best attribute to test at that point in the tree. This forms a greedy search for an acceptable decision tree. The information gain is adopted to select the most useful attribute. Entropy characterizes the (im)purity of an arbitrary collection of examples. For a collection S contains positive and negative examples of some target concept, the entropy of S relative to this Boolean classification is

$$Entropy(S) = -p_{\oplus} log_2 p_{\oplus} - p_{\ominus} log_2 p_{\ominus}, \tag{45}$$

where $p_{\oplus}$ is the proportion of positive examples in S and $p_{\ominus}$ is the proportion of negative examples in S. $0log0$ is 0.

Entropy specifies the minimum number of bits of information needed to encode the classification of an arbitrary member of S. For example, if $p_{\oplus}$ is 1, the receiver knows the drawn example will be positive, so no message need to be sent, and the entropy is zero. If $p_{\ominus}$ is 0.5, one bit is required to indicate whether the drawn example is positive or negative.

If the target attribute can take on c different values, then the entropy of S relative to this c-wise classification is defined as

$$Entropy(S) \equiv \sum_{i=1}^{c} -p_i log_2 p_i, \tag{46}$$

where p_i is the proportion of S belonging to class i. If the target attribute can take on c possible values, the entropy can be as large as $log_2 c$.

Based on the entropy, information gain is defined to measure the effectiveness of an attribute in classifying the training data. $Gain(S, A)$ of an attribute A, relative to a collection of examples S, is defined as

Algorithm 1 ID3: Examples are the training examples. TargetMttribute is the attribute whose value is to be predicted by the tree. Attributes is a list of other attributes that may be tested by the learned decision tree. Returns a decision tree that correctly classifies the given Examples

Require: $Examples, TargetMttribute, Attributes$
Ensure: A decision tree
Init Root node for the tree
if all $Examples$ are positive **then**
  return the single-node tree $Root$, with label $= +$
else if all $Examples$ are negative **then**
  return the single-node tree $Root$, with label $= -$
else if $Attributes$ is empty **then**
  return the single-node tree $Root$, with label = most common value of $TargetMttribute$ in $Examples$
end if
$A \leftarrow$ the attribute from $Attributes$ that $best^*$ classifies $Examples$.
The decision attribute for $Root \leftarrow A$
for each possible value, v_i, of A **do**
  Add a new tree branch below $Root$, corresponding to the test $A = v_i$
  Let $Examples\ v_i$ be the subset of $Examples$ that have value v_i for A
  if $Examples\ v_i$ is empty **then**
    below this new branch add a leaf node with label = most common value of $TargetMttribute$ in $Examples$.
  else
    below this new branch add the subtree $ID3(Examples\ v_i, TargetMttribute, Attributes\backslash A))$
  end if
end for
return $Root$

$$Gain(S, A) = Entropy(S) - \sum_{v \in Values(A)} \frac{|S_v|}{|S|} Entropy(S_v), \tag{47}$$

where $Values(A)$ is the set of all possible values for attribute A and S_v is the subset of S for which attribute A has value v (i.e., $S_v = \{s \in S | A(s) = v\}$). Note the first term is just the entropy of the original collection S and the second term is the expected value of the entropy after S is partitioned using attribute A. The expected entropy described by this second term is simply the sum of the entropies of each subset S_v, weighted by the fraction of examples $\frac{|S_v|}{|S|}$ that belong to S_v. $Gain(S, A)$ is therefore the expected reduction in entropy caused by knowing the value of attribute A. $Gain(S, A)$ is the information provided about the target function value, given the value of some other attribute A. The value of $Gain(S, A)$ is the number of bits saved when encoding the target value of an arbitrary member of S, by knowing the value of attribute A.

7 Neural Network

A neural network (NN) is a machine learning method inspired by biological neural networks; it tries to find mathematical representations of information processing in biological systems. Conventional computers use some algorithms to solve problems that we already know how to address, but NNs may find the solution to problems that humans do not precisely know how to solve. These NNs are capable of modeling any complex function and achieving high accuracies on the premise that large amounts of data are available.

The basic neural network model can be described as a series of functional transformations. First we construct M linear combinations of the input variables $x_1, \ldots, x_D$ in the form

$$a_j = \sum_{i=1}^{D} w_{ji}^{(1)} x_i + w_{j0}^{(1)}, \tag{48}$$

where $j = 1, \ldots, M$, and the superscript (1) indicates that the corresponding parameters are in the first "layer" of the network. $w_{ji}^{(1)}$ are weights. $w_{j0}^{(1)}$ are biases. a_j are activations. Each of them is then transformed using a differentiable, nonlinear activation function $h(\cdot)$

$$z_j = h(a_j). \tag{49}$$

These values are again linearly combined to give output unit activations

$$a_k = \sum_{j=1}^{M} w_{kj}^{(2)} z_j + w_{k0}^{(2)}, \tag{50}$$

where $k = 1, \ldots, K$, and K is the total number of outputs. This transformation corresponds to the second layer of the network. The $w_{k0}^{(2)}$ are bias parameters. The output unit activations are transformed using an appropriate activation function to give a set of network outputs y_k. The choice of the activation function is determined by the nature of the data and the assumed distribution of target variables.

The neural network model comprises two stages of processing, each of which resembles the perceptron model, and for this reason, the neural network is also known as the multilayer perceptron (MLP). A key difference compared to the perceptron, however, is that the neural network uses continuous sigmoidal nonlinearities in the hidden units, whereas the perceptron uses step-function nonlinearities. This means that the neural network function is differentiable with respect to the network parameters, and this property will play a central role in network training.

If the activation functions of all the hidden units in a network are taken to be linear, then for any such network, we can always find an equivalent network without hidden units. This follows from the fact that the composition of successive

linear transformations is itself a linear transformation. However, if the number of hidden units is smaller than either the number of input or output units, then the transformations that the network can generate are not the most general possible linear transformations from inputs to outputs because the information is lost in the dimensionality reduction at the hidden units. In general, however, there is little interest in multilayer networks of linear units.

x is the input, and **y** is the output. Given a training set comprising a set of input vectors $\{\mathbf{x}_n\}$, where $n = 1, \ldots, N$, together with a corresponding set of target vectors $\{\mathbf{t}_n\}$, the error function is

$$E(\mathbf{w}) = \frac{1}{2}\sum_{n=1}^{N} \|\mathbf{y}(\mathbf{x}_n, \mathbf{w}) - \mathbf{t}_n\|^2 .$$

The error backpropagation is adopted for evaluating the gradient of an error function $E(\mathbf{w})$ for a feedforward neural network. A local message-passing scheme is adopted in which information is sent alternately forwards and backwards through the network. Most training algorithms involve an iterative procedure for minimization of an error function, with adjustments to the weights being made in a sequence of steps. At each such step, we can distinguish between two distinct stages. In the first stage, the derivatives of the error function with respect to the weights must be evaluated. In the second stage, the derivatives are then used to compute the adjustments to be made to the weights.

Take the network with a single layer of sigmoidal hidden units together with a sum-of-squares error as an example. Many error functions of practical interest comprise a sum of terms, one for each data point in the training set

$$E(\mathbf{w}) = \sum_{n=1}^{N} E_n(\mathbf{w}).$$

Consider first a simple linear model in which the outputs y_k are linear combinations of the input variables s_i

$$y_k = \sum_i w_{ki} x_i ,$$

together with an error function that, for a particular input pattern n, the error function is

$y_{nk} = y_k(\mathbf{x}_n, \mathbf{w})$.

The gradient of this error function with respect to a weight w_{ji} is given by

$$\frac{\partial E_n}{\partial w_{ji}} = \left(y_{nj} - t_{nj}\right) x_{ni} ,$$

which can be interpreted as a "local" computation involving the product of an "error signal" $y_{nj} - t_{nj}$ associated with the output end of the link w_{ji} and the variable x_{ni} associated with the input end of the link. It is the basic component for the multilayer feedforward networks.

Regularization is adopted to control the complexity of a neural network model in order to avoid overfitting. One regularizer is quadratic, giving a regularized error of the form

$$\tilde{E}(\mathbf{w}) = E(\mathbf{w}) + \frac{\lambda}{2}\mathbf{w}^{\mathrm{T}}\mathbf{w}.$$

This regularizer is also known as weight decay. The effective model complexity is then determined by the choice of the regularization coefficient λ.

8 Data Set

The materials data and informative landscape are the most important sources of the machine learning method. Taking the TE materials as an example, the data resources related to TE materials are collected in Table 1 from [3]. Some specific databases in materials informatics could be used for transfer learning and providing research tools.

9 Conclusion

Considerable effort has been devoted to improving the performance of materials. The optimization of multiple interrelated characteristics is required to be analyzed. As the data analysis capability of the machine learning methods, they have been applied in research on materials. A brief introduction of the typical machine learning methods, i.e., SVM, clustering, regression, decision tree, and neural network, which can be employed in the material studies is provided. Furthermore, some data sets could be adopted in the properties analysis of the machine learning are introduced. The high-throughput computation and machine learning methods will play an indispensable role in the field of materials research. The data in the experimental results and the simulation output could be researched. With the development of the machine learning and the materials, the breakthroughs in the integration may arise.

Table 1 Material databases for machine learning

Name	URL	Category
TEDesignLab	www.tedesignlab.org	Thermoelectrics
UCSB-MRL thermoelectric database	www.mrl.ucsb.edu:8080/datamine/thermoelectric.jsp	Thermoelectrics
NIST-JANAF	janaf.nist.gov	Thermochemical
ASM phase diagrams	www.asminternational.org/AsmEnterprise/APD	Thermodynamics
CALPHAD databases	www.thermocalc.com/products-services/databases/thermodynamic	Thermodynamics
Thermophysical Properties of Matter Database	cindasdata.com/products/tpmd	Thermophysics
Cambridge Structural Database (CSD)	www.ccdc.cam.ac.uk/solutions/csd-system/components/csd	Crystallography
Crystallography Open Database	www.crystallography.net	Crystallography
CRYSTMET	www.semanticscholar.com	Crystallography
Inorganic Crystal Structure Database	cds.dl.ac.uk/cds/datasets/crys/icsd/llicsd.html	Crystallography
Pearson's Crystal Data	www.crystalimpact.com/pcd/Default.htm	Crystallography
Powder Diffraction File (PDF)	www.icdd.com/products/index.htm	Crystallography
The Cambridge Crystallographic Data Centre	www.ccdc.cam.ac.uk/pages/Home.aspx	Crystallography
AFLOWLIB	aflowlib.org	Computational
NIST Interatomic Potentials Repository	www.ctcms.nist.gov/potentials	Computational
NoMaD	nomad-repository.eu/cms	Computational
Open Knowledgebase of Interatomic Models (OpenKIM)	openkim.org	Computational
phononDB	phonondb.mtl.kyoto-u.ac.jp	Computational
The Open Quantum Materials Database	oqmd.org	Computational
nanoHUB	nanohub.org	Nanomaterials
Nanomaterial Registry	www.nanomaterialregistry.org	Nanomaterials
AIST Research Information Database	www.aist.go.jp/aist_e/list/database/riodb	General Materials Data

(continued)

Table 1 (continued)

Name	URL	Category
Citrination	citrination.com	General materials data
InfoChem	www.infochem.de	General materials data
Knovel	app.knovel.com/web/browse.v	General materials data
MatNavi (NIMS)	mits.nims.go.jp/index_en.html	General materials data
MatWeb	www.matweb.com	General materials data
NIMS Materials Database (MatNavi)	mits.nims.go.jp/index_en.html	General materials data
NIST Materials Data Repository (DSpace)	materialsdata.nist.gov/dspace/xmlui	General materials data
Pauling File	paulingfile.com	General materials data
Pearson's Crystal Data	www.crystalimpact.com/pcd/Default.htm	General materials data
The Open Quantum Materials Database	quantum-machine.org/datasets	General materials data
NRELMatDB	materials.nrel.gov	General materials data
SpringerMaterials	materials.springer.com	General materials data
The Computational Materials Repository	cmr.fysik.dtu.dk	General materials data
The Materials Project	materialsproject.org	General materials data
Total Materia	www.totalmateria.com	General materials data
ChemSpider	www.chemspider.com	Chemical data
PubChem	pubchem.ncbi.nlm.nih.gov	Chemical data
Reaxys	www.elsevier.com/solutions/reaxys	Chemical data

References

1. Mitchell, T. M. (1997). *Machine learning*. McGraw-Hill Science.
2. Bishop, C. M. (2006). *Pattern recognition and machine learning*. P101. Springer.
3. Wang, T., Zhang, C., Snoussi, H., & Zhang, G. (2020). Machine learning approaches for thermoelectric materials research. *Advanced Functional Materials, 30*(5), 1906041.

Machine Learning for High-Entropy Alloys

Shuai Chen, Yuan Cheng, and Huajian Gao

1 Overview of High-Entropy Alloys

In 2004, Yeh et al. [1] and Cantor et al. [2] independently proposed a novel category of multi-principal component alloys consisting of five or more constituent elements with atomic compositions between 5 and 35 atomic percent, which are today widely termed as HEAs. With multi-principal components, HEAs possess unique microstructures with fundamental core effects and exhibit many impressive properties for practical applications. In this section, we will give an overview of HEAs. Four fundamental core effects of HEAs are discussed in Sect. 1.1. Some popular preparation methods of HEAs are introduced in Sect. 1.2. The reported excellent properties of HEAs are summarized in Sect. 1.3.

S. Chen
Institute of High Performance Computing, A*STAR, Singapore, Singapore
e-mail: chens@ihpc.a-star.edu.sg

Y. Cheng (✉)
Monash Suzhou Research Institute, Suzhou, P.R. China
e-mail: Yuan.Cheng@monash.edu

H. Gao
Institute of High Performance Computing, A*STAR, Singapore, Singapore

School of Mechanical and Aerospace Engineering, College of Engineering, Nanyang Technological University, Singapore, Singapore
e-mail: huajian.gao@ntu.edu.sg

Y. Cheng et al. (eds.), *Artificial Intelligence for Materials Science*, Springer Series in Materials Science 312, https://doi.org/10.1007/978-3-030-68310-8_2

1.1 Fundamentals of High-Entropy Alloys

Due to the complex elemental compositions, the outstanding mechanical properties of HEAs are featured by four fundamental core effects, which are summarized as: (1) high-entropy effect for thermodynamics; (2) sluggish diffusion effect for kinetics; (3) severe lattice distortion effect for structures; and (4) cocktail effect for properties. High-entropy effect determines the thermodynamic equilibrium phase and associated microstructure. Sluggish diffusion effect influences the kinetics during phase transformation. Severe lattice distortion effect affects the deformation behaviour and the structure-property relation. Cocktail effect implies the unexpected behaviour appeared after alloying different elements. We will discuss these four fundamental core effects separately.

1.1.1 High-Entropy Effect

It was first proposed by Yeh et al. [1] that, in multi-principal component alloys consisting of five or more elements in near equimolar concentrations, intermetallic compounds could be suppressed and solid-solution phases stabilized by the high-entropy effect. Based on the second law of thermodynamics, at given pressure and temperature, an alloy system attains its thermodynamically equilibrium state if its Gibbs free energy is the lowest [3]. The Gibbs free energy of forming alloys from mixing elemental components is expressed as:

$$\Delta G_{\text{mix}} = \Delta H_{\text{mix}} - T\Delta S_{\text{mix}} \tag{1}$$

where ΔG_{mix} is the Gibbs free energy of mixing, ΔH_{mix} the enthalpy of mixing, T the absolute temperature, and ΔS_{mix} the entropy of mixing.

The entropy of mixing can be calculated from the following four contributions:

$$\Delta S_{\text{mix}} = \Delta S_{\text{mix}}^{\text{conf}} + \Delta S_{\text{mix}}^{\text{vib}} + \Delta S_{\text{mix}}^{\text{elec}} + \Delta S_{\text{mix}}^{\text{mag}} \tag{2}$$

where $\Delta S_{\text{mix}}^{\text{conf}}$ is the configurational entropy, $\Delta S_{\text{mix}}^{\text{vib}}$ the vibrational entropy, $\Delta S_{\text{mix}}^{\text{elec}}$ the electronic randomness entropy, and $\Delta S_{\text{mix}}^{\text{mag}}$ the magnetic dipole entropy. The configurational entropy is always dominant among all four types of entropies, and represents the mixing entropy in the alloys system [3]. For an alloy system of n elements in a random solid solution, the configurational entropy is [4]:

$$\Delta S_{\text{mix}}^{\text{conf}} = -R\sum_{i=1}^{n} c_i \ln c_i \tag{3}$$

where R is the gas constant, and c_i is the mole fraction of the i^{th} element. The enthalpy of mixing for the n-element alloy can be calculated as [5]:

$$\Delta H_{\text{mix}} = \sum_{i=1, i\neq j}^{n} 4\Delta H_{\text{AB}}^{\text{mix}} c_i c_j \tag{4}$$

where ΔH_{AB}^{mix} is the mixing enthalpy of binary equimolar AB alloys, and the values can be obtained from literature [5, 6].

Elemental phases with one principal element have slightly negative ΔH_{mix} and slightly positive ΔS_{mix}, intermetallic compounds possess highly negative ΔH_{mix} but slightly positive ΔS_{mix}, and solid-solution phases consisting of multiple elements feature moderately negative ΔH_{mix} but highly positive ΔS_{mix}, which enhances their stability. Therefore, high-entropy effect helps to stabilize the formation of solid-solution phases with superior properties.

1.1.2 Sluggish Diffusion Effect

The diffusion is sluggish in HEA, as compared with conventional alloys. Diffusion is difficult to measure experimentally, so early support of this effect relies on indirect evidence [4], such as secondary observations that include formations of nanocrystals and amorphous phases upon solidification and on qualitative interpretations of microstructural stability upon cooling. Direct diffusion experiments were performed by Tsai et al. [7] in 2013 with a near-ideal solution system of CoCrFeMnNi in stable single face-centre-cubic (FCC) solid solution. The experimental measurements showed that the diffusion coefficients in the CoCrFeMnNi HEA are lower than those in the FCC FeCrNi alloys and FCC pure metals. Correspondingly, the activation energies in the HEA are higher than those in the FeCrNi alloys and pure metals. Among the five elements in the CoCrFeMnNi HEA, Ni is the slowest diffusing element, while Mn is the fastest diffusing element. The order of increasing diffusion rate is Ni < Co < Fe < Cr < Mn. Because of the diversity of atoms surrounding each lattice site, an atom/vacancy can face a variable path to diffuse/migrate, and the vacancy trapping effect of low-energy sites would lead to the sluggish diffusion.

To evaluate the quantity of low-energy sites and high-energy barriers, the energetic data for the vacancy migration in the CoCrFeMnNi HEA have been quantitatively examined based on atomistic simulations [8]. Initially, a vacancy on a lattice site (numbered "0" in Fig. 1a) was introduced in a sample from the Canonical Monte Carlo (CMC) simulation. Then, a nearest neighbouring atom was moved to the vacant site. After each movement, the neighbouring atoms surrounding the vacancy were relaxed. Finally, the variation of potential energy with positions as the atoms repeatedly move is plotted in Fig. 1b. Because the migration of a vacancy to a nearest neighbouring site corresponds to the opposite movement of the neighbouring atom, the energy barrier of vacancy migration could be calculated according to the potential energy curve. The average energy barriers for the five elements are shown in Fig. 1c. These data demonstrate that the average migration energy barriers are different for the five elements, and the order is Ni > Co > Cr > Fe > Mn, which is close to the diffusivity measured in experiment (Ni < Co < Fe < Cr < Mn) [7].

Sluggish diffusion effect is very important for HEA since it provides many advantages [3]. For example, sluggish diffusion facilitates super-saturated states and fine precipitates in HEA structures. It can also enhance the creep resistance,

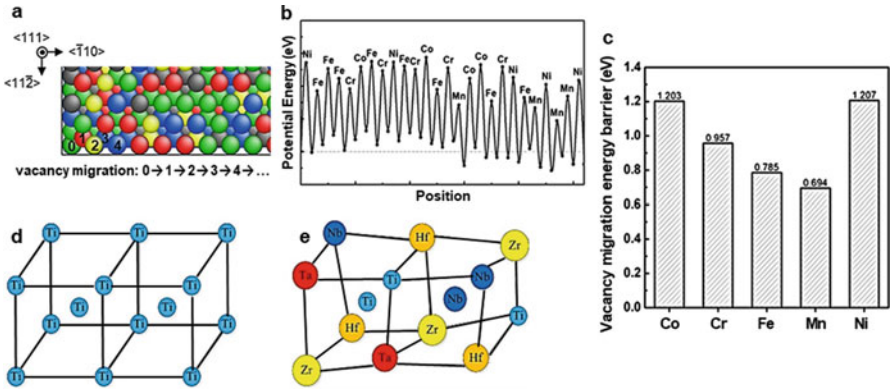

Fig. 1 (**a**) A schematic diagram of an HEA sample with a vacancy. (**b**) Variation of potential energy with vacancy position during the vacancy migration. (**c**) Average energy barrier of vacancy migration for the five elements [8]. A schematic illustration of BCC crystal structure: (**d**) perfect lattice of β-Ti metal; (**e**) severely distorted lattice of TiNbTaZrHf HEA [9]

weaken the particle coarsening, increase the recrystallization temperature, and reduce the grain growth rate, which benefit the microstructures and properties of HEAs for high-performance structural materials. Moreover, in practical applications demanding slow diffusion kinetics, such as high-temperature applications, this effect makes HEAs extremely competitive.

1.1.3 Severe Lattice Distortion Effect

A solid-solution phase is formed stably as a whole matrix in a HEA due to high-entropy effect, regardless of the fact whether its structure is body-centre-cubic (BCC), FCC, hexagonal-close-packed (HCP), B2 (ordered BCC), or $L1_2$ (ordered FCC). In the matrix, there is severe lattice distortion since every atom in the lattice site is surrounded by diverse types of atoms. As shown in Fig. 1d [9], the pure β-Ti metal has a perfect BCC crystal structure, which consists of atoms with the same size. Adding Nb, Ta, Zr, and Hf elements in the β-Ti metal for composing TiNbTaZrHf HEA, as shown in Fig. 1e, results in severe lattice distortions due to different sized atoms, where the elemental components are considered to occupy a lattice site with the same probability. Due to the severe lattice distortions, the crystal structure of HEA suffers local lattice strain and stress, making dislocation motion more difficult, as compared with the pure metals or conventional alloys.

A quantitative parameter considering the atomic size difference by Zhang et al. [5] is widely used to evaluate the lattice distortion.

$$\delta = \sqrt{\sum_{i=1}^{n} c_i (1 - r_i/\overline{r})^2} \tag{5}$$

where n is the number of elemental components in the HEA system, c_i the mole fraction of the i^{th} element, r_i the atomic radius of the i^{th} element, and $\overline{r}$ the average atomic radius $\left(= \sum_{i=1}^{n} c_i r_i \right)$.

Direct characterizations of lattice distortion are extremely challenging in experiment. The pair distribution function (PDF), which describes the distribution of distances between atomic pairs contained within a given volume, has been utilized to quantitatively estimate the distorted local structure of HEA by Tong et al. [10] under the measurement of high-energy synchrotron X-ray and neutron scattering. Based on the PDF measurement, the lattice distortion can be quantified as $\varepsilon = (a_{1\text{st}} - a_{\text{avg}})/a_{\text{avg}}$, where $a_{1\text{st}}$ is the lattice parameter obtained by fitting to the first peak of PDF curve, and a_{avg} is the lattice parameter obtained by fitting to the overall spectrum. Tong et al. [10] found that the FeCoNiCrPd HEA had a lattice distortion parameter $\varepsilon = 0.79\%$, about twice as large as that of the $Ni_{80}Pd_{20}$ alloy ($\varepsilon = 0.41\%$). Clearly, substituting Ni atoms with similar-sized Fe, Co, and Cr atoms resulted in a dramatic increase in lattice distortion. This unexpected increase cannot be simply explained by the difference in atomic size. Besides the atomic size difference, differences in crystal-structure tendencies (FCC, BCC, HCP, B2, or $L1_2$) and bonding energies among constituents can also cause severe lattice distortions. The lattice distortion effect is very broad, which not only influences the thermodynamic stability and deformation mechanisms, but can also affect a wide range of other properties. For example, the lattice distortion seems to have some effect on ductility and can substantially improve the friction stress, leading to enhanced strength and sensitivity to the grain size [11, 12].

1.1.4 Cocktail Effect

The cocktail effect is a term commonly used in the acoustic field to describe the ability to focus one's listening attention on the voice of a single speaker among a mixture of other conversations and background noises [13]. Multi-metallic cocktail effect was first put forward by Ranganathan [14] to highlight the advantages of conventional alloys, compared to which this effect becomes even more pronounced in HEAs. For HEAs, the cocktail effect refers to unexpected properties which do not exist in a single element but can be obtained by mixing diverse types of elements. This effect emphasizes the fact that the properties of HEA can be dramatically tuned by adjusting the elemental compositions and preparation method. Some examples on the excellent properties of HEAs due to the cocktail effect will be discussed in Sect. 1.3.

For an HEA, its crystal structure is a multicomponent solid solution, which can be considered as an atomic-scale composite. Therefore, its properties originate not

only from the intrinsic properties of the constituents following the mixture rules but also from the cocktail effects of mixing different elements, providing greater opportunities for alloy designers to achieve unprecedented properties. However, it is also challenging since the cocktail effect is complicated and difficult to predict based on the available theoretical frameworks. For example, the phase diagrams of most binary and ternary alloy systems are available. For HEAs, however, there is not a single integrated phase diagram to guide the researchers to design the alloys with specific target. Here, ML approach has proven useful in guiding the HEA design based on limited data. These four core effects play fundamental roles in the investigation and understanding on the microstructures and properties of HEAs. It can be expected that great efforts will be made to establish the fundamental framework of multi-principal HEAs in the coming years.

1.2 Preparation Methods of High-Entropy Alloys

The development of HEAs is closely associated with the investigation of amorphous alloys [13]. Therefore, the preparation and fabrication methods of HEAs often refer to those of amorphous alloys, which can be categorized into three major approaches [3]. The first approach is liquid-state mixing, which is also the main route, including arc melting, laser melting, inductive melting, electric-resistance melting, laser engineered net shaping, and laser cladding [15]. The second approach is solid-state mixing, containing mechanical alloying and subsequent consolidation. The third approach is gas-state mixing, and the techniques include sputter deposition, atomic layer deposition, pulse-laser deposition, molecular-beam epitaxy, and vapour-phase deposition. Through these preparation methods various morphologies of HEAs could be fabricated, including three-dimensional bulk, two-dimensional film/coating, and one-dimensional fibrous HEAs. We will choose one typical preparation method from each route for detailed introduction, i.e., arc melting, mechanical alloying, and sputter deposition.

1.2.1 Arc Melting

Arc melting is the dominant preparation method to synthesize bulk HEAs among the diverse fabrication routes. Figure 2a demonstrates a schematic diagram of the arc-melting method [16]. The temperature of torch can reach as high as 3000 °C, which is tuned by adjusting the electrical power. The arc-melting method is applicable to most of the elemental compositions, including those with high melting temperatures, by mixing them in the liquid state. However, this method may not be the best choice for those elements with a relatively low melting temperature, e.g., Mg, Mn, and Zn, since they tend to evaporate after heating. In that case, the elemental compositions of HEAs are difficult to be precisely controlled for arc melting if these elements are added. For these elements, electric-resistance melting or inductive melting may be much more suitable.

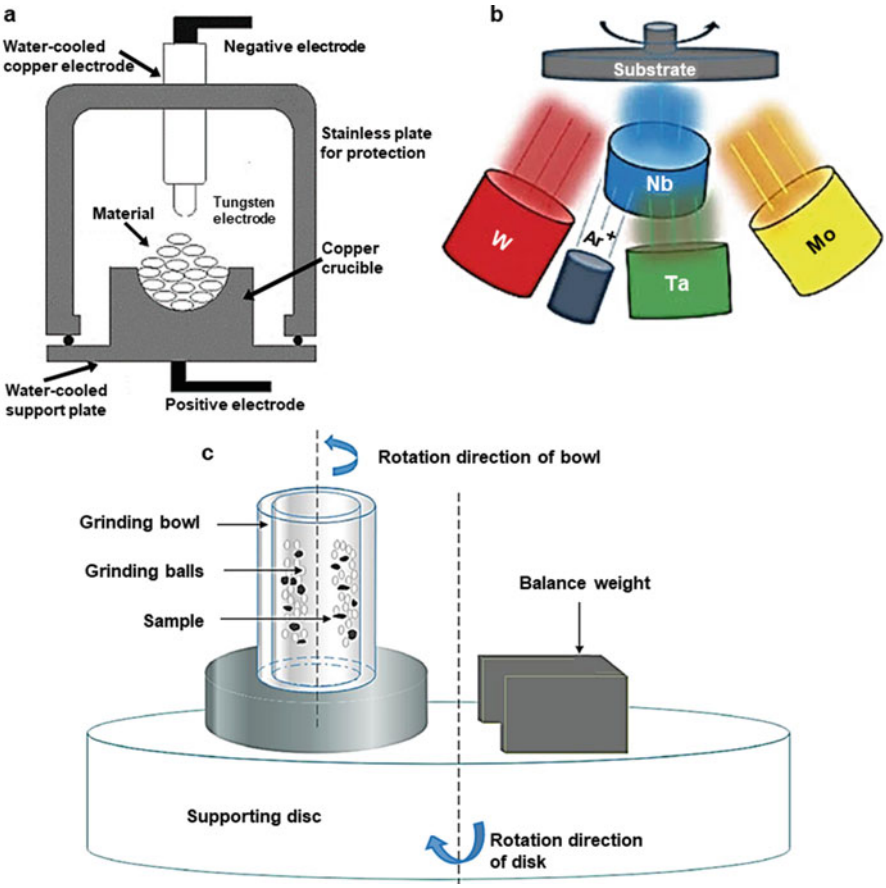

Fig. 2 A schematic diagram of HEA preparation methods: (**a**) arc melting [16]; (**b**) sputter deposition [17]; and (**c**) mechanical alloying [18]

Tsao et al. [16] synthesized an $Al_{0.3}CrFe_{1.5}MnNi_{0.5}$ HEA by the arc-melting method, as shown in Fig. 2a. The HEA sample was melted at a temperature around 1530–1580 °C for 2–3 min repeatedly and solidified with turning of the solidified ingots for five times to reach a completely alloyed state. The HEA microstructures consisted of dendrites (DR) as matrix and interdendrites (IR). IR were Ni-rich FCC phase, DR were Cr-rich BCC phase, and a small portion of cross-like Ni-rich FCC phase was also formed. The as-prepared samples were under heat treatment at 650–750 °C for 8 h and then quenched in water to further explore the effects of age treatment on the microstructure and hardness of this $Al_{0.3}CrFe_{1.5}MnNi_{0.5}$ HEA. After ageing at 650 °C, both AlNi and $Cr_5Fe_6Mn_8$ precipitations appeared within the DR, where cross-like FCC phase disappeared. During ageing at 750 °C, the AlNi precipitations in the DR were larger and formed globular shape inside the grain matrix, contributing to a hardening effect. This work demonstrates that dual-phase

(FCC + BCC) structures are formed in HEAs, and the precipitations are beneficial to the mechanical properties.

For the effect of cooling rate on the crystal structure and chemical composition of HEAs during arc melting, Singh et al. [19] performed a detailed investigation of AlCoCrCuFeNi HEA by melting the constituent elements in an induction levitation furnace and then following two different processing conditions (splat quenching and normal casting) in a copper crucible under a pure argon atmosphere. Normal casting was produced in flowing argon, which provided a normal cooling rate of 10–20 K/s. They observed similar microstructures consisting of dendrites and interdendrites in HEA samples after normal cooling as in Tsao et al.'s experiments [16]. Splat quenching was operated in vacuum (10^{-6} mbar) in an electromagnetic levitation chamber, which reached an ultrafast cooling rate of 10^6–10^7 K/s. Interestingly, a single BCC phase is obtained by ultrafast cooling. Singh et al.'s work [19] indicates that, for some HEAs, a solid-solution phase can only be formed at a relatively fast cooling rate, which is a metastable state. A relatively slow cooling rate causes the formation of multiple phases, leading to a remarkable reduction in the mixing entropy because of the elemental segregation among these phases [13].

1.2.2 Mechanical Alloying

Mechanical alloying is a processing technique of solid-state powder involving repeated cold welding, fracturing, and re-welding of powder particles in a high-energy ball mill [20]. A schematic diagram of mechanical-alloying method is shown in Fig. 2c [18]. Originally developed to produce oxide-dispersion strengthened Fe- and Ni-base superalloys for aerospace applications, mechanical alloying has been shown capable of synthesizing a wide variety of equilibrium and non-equilibrium alloys ranging from blended elemental to pre-alloyed powders. Mechanical alloying of HEAs normally follows a three-step procedure. First, the elemental constituents are mixed and milled into fine powders in a ball mill. Then, a hot-isostatic-pressing process is performed to impact and sinter these fine powders simultaneously. Last, a heat-treatment process is applied to remove internal stresses induced by cold compaction.

The greatest advantage of mechanical alloying is to synthesize novel HEAs that are impossible to prepare by other techniques, such as alloying of normally immiscible elements or directly coating HEA on a substrate. The reason is that the limitations imposed by phase diagrams are not applicable to mechanical alloying for its completely solid-state processing. The CrMnFeCoNi HEA is one of the most notable and promising HEAs that has been studied and widely termed as Cantor alloy. However, there are only a few published papers on CrMnFeCoNi HEA coating. Tian et al. [18] synthesized CrMnFeCoNi HEA coating on a Q235 steel substrate by mechanical-alloying method. First, HEA powders were prepared. Then, the Q235 substrate was put into the prepared powders. Last, a milling process was performed for 10 h, after that the HEA coating was successfully prepared. Both the as-prepared powders and the final coating presented single FCC solid solutions.

The coating thickness was 180 μm, exhibiting a good bonding strength with the substrate. The constituents were homogeneously distributed in the coating without component segregation. The corrosion results show that the HEA coated Q235 has better corrosion resistance than the pure Q235 in 3.5 wt% NaCl solution.

High-pressure torsion is a popular technique that achieves not only grain refinement up to the nanometre scale but also diverse phase transformations. Kilmametov et al. [21] applied the high-pressure torsion technique to a multicomponent powder for the first time to produce a bulk nanostructured CoCrFeMnNi HEA by high-pressure-torsion induced mechanical alloying. Micrometre sized elemental powders were blended in equimolar concentrations, consolidated and deformed at 5 GPa using imposed shear strain equivalent up to 100 rotations, leading to a fully dense bulk CoCrFeMnNi HEA. Single-phase nanocrystalline HEA (grain size of 50 nm) with smaller chromium oxide precipitates (particle size of 7–10 nm) exhibited an amazing hardness of 6.7 GPa, which is one of the highest reported values for bulk CoCrFeMnNi HEAs.

1.2.3 Sputter Deposition

Among gas-state preparation methods, sputter deposition, as shown in Fig. 2b [17], is the most widely used one to synthesize HEA films. To date, bulk HEAs have been extensively investigated, but small-dimensional HEAs have drawn less attentions, such as HEA films/coatings and small-sized pillars. With incremental demands for micro-/nanoscale devices for practical applications in high-temperature and harsh environments, the fabrication and investigation of small-dimensional HEAs become increasingly important, where magnetron-sputtering deposition exhibits great potentials. In the sputter deposition of HEAs, the sputtered atoms are ejected from the sputtering target by ion or atom bombardment from the sputtering gas, and then randomly deposited on the substrate to form HEA. The microstructures of the HEA are mainly determined by the processing parameters, including the form of source material, atmosphere pressure, work piece temperature, and substrate bias voltage.

Using magnetron co-sputtering technique, Zou et al. [17] deposited NbMoTaW HEA films and small-sized pillars on silicon and sapphire substrates at room temperature. Ion beam-assisted deposition (IBAD) method [22] was employed to reduce deposition rate and grain size. During mechanical testing under a nanoindenter, the HEA pillars exhibited extraordinarily high yield strengths of ~10 GPa, which were among the highest reported values for the compressions of micro- and nano-pillars. The strength of such HEA pillar was one order of magnitude higher than that of its bulk form, along with significantly enhanced ductility (compressive plastic strains > 30%). The HEA films demonstrated substantially enhanced stability under long-duration high-temperature conditions (at 1100 °C for 3 days). Such excellent properties of small-dimensional HEAs have potential applications in high-temperature and high-stress conditions.

1.3 Excellent Properties of High-Entropy Alloys

Since they were proposed in 2004, HEAs with extraordinary mechanical, physical, and chemical properties have been reported in succession, such as high hardness, enhanced strength–ductility synergy, excellent thermal stability, superior wear/corrosion/irradiation resistance, and high-performance catalytic properties [23–25]. Alloying-element compositions, crystal-phase structures, grain sizes, preparation techniques, and annealing treatments play important roles in the microstructural evolutions and associated properties of HEAs. Here we mainly discuss the hardness, strength–ductility synergy, and high-temperature properties of HEAs.

1.3.1 Hardness

Hardness is one of the most popular approaches to examining the mechanical properties of HEAs since Vickers hardness measurement can be performed efficiently and effectively with less requirement for the size and shape of the sample. For some thin films of HEAs, their yield stresses are difficult to measure directly, but micro-hardness tests can be easily performed with high precision. The hardness values of HEAs change widely in each alloy system. In the Al_xCoCrCuFeNi HEAs, the hardness varies from 133 to 655 HV when the x value increases from 0.0 to 3.0, along with a phase transformation from FCC to BCC structures [1]. With the substitution of Co or Cu with Mo or Ti, the hardness value generally increases. For example, $AlCo_{0.5}CrFeMo_{0.5}Ni$ and $Al_{0.2}Co_{1.5}CrFeNi_{1.5}Ti$ HEAs exhibit a high hardness value of 788 HV [26] and 717 HV [27], respectively. Thus, the selection of the HEA system and adjustment of the elemental concentrations are critical in determining the hardness of HEA.

To systematically investigate the compositional dependence of HEA hardness, Zhu et al. [28] tuned the atomic ratio of the constituent elements in three typical equimolar CoCrFeNiMn, CoCrFeNiAl, and CoCrFeNiCu HEAs to form 78 alloys, whose phase structures and hardness values are shown in Fig. 3. Single phase (FCC or BCC), duplex FCC phases, and duplex BCC phases, formed within a wide compositional space in 68 out of the 78 HEAs, were not limited to the equimolar compositions with the maximum mixing entropy. With the precipitation of hard sigma phases, the hardness of the FeNiCrMn alloy is 528 ± 82 HV (Fig. 3a). With Ni addition, the hardness decreases to 145–166 HV when x reaches 10% for $(CoCrFeMn)_{(100-x)}Ni_x$ HEAs due to the decreased volume fraction of sigma phase. $(CrFeNiMn)_{(100-x)}Co_x$ HEAs exhibit almost the same value of hardness, which may be attributed to the small volume fraction of sigma phase.

Differed from the $(CoCrFeMn)_{(100-x)}Ni_x$ and $(CrFeNiMn)_{(100-x)}Co_x$ HEAs with a single FCC phase, CoCrFeNiAl HEAs have BCC structures, exhibiting relatively high hardness as shown in Fig. 3b. The hardness of $(CoCrFeAl)_{(100-x)}Ni_x$

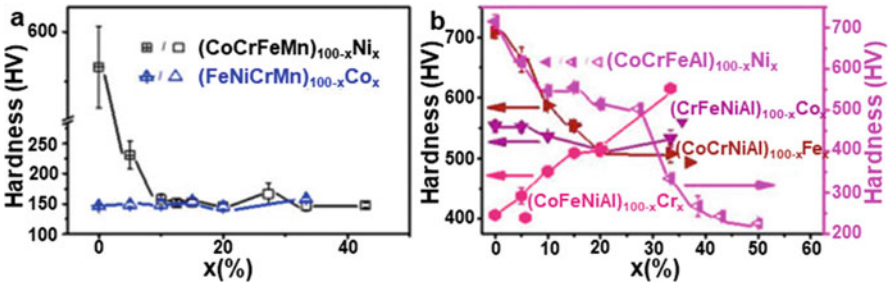

Fig. 3 Hardness of the as-cast (**a**) $(CoCrFeMn)_{(100-x)}Ni_x$ and $(CrFeNiMn)_{(100-x)}Co_x$ HEAs, and (**b**) $(CoCrFeAl)_{(100-x)}Ni_x$, $(CrFeNiAl)_{(100-x)}Co_x$, $(CoCrNiAl)_{(100-x)}Fe_x$, and $(CoFeNiAl)_{(100-x)}Cr_x$ HEAs. The legend "+" centred symbols denote multiple phases, fully open symbols represent either single or duplex FCC phases, fully closed symbols denote duplex BCC phases, and left-half open symbols represent FCC and duplex disordered plus ordered BCC phases [28]

HEAs decreases since phase transformation from BCC to FCC structures occurs with increasing Ni concentration. Even though the $(CoCrNiAl)_{(100-x)}Fe_x$, $(CoFeNiAl)_{(100-x)}Cr_x$ and $(CrFeNiAl)_{(100-x)}Co_x$ HEAs have similar BCC structures, their variation trends of hardness are different. With the increase of x value, the hardness value of $(CrFeNiAl)_{(100-x)}Co_x$ and $(CoCrNiAl)_{(100-x)}Fe_x$ HEAs decreases, while that of $(CoFeNiAl)_{(100-x)}Cr_x$ increases. As mentioned by Zhu et al. [28], the different variation trends of hardness among different HEAs may be due to the different bond energies, which need further investigation. Therefore, an optimal design of HEAs with desired hardness is a complicated task, which can be especially challenging for trial-and-error experimental developments. This is where an ML approach could provide some valuable insights.

1.3.2 Strength and Ductility Synergy

Metallic materials have been widely used as structural materials, where the strength and ductility are two baseline mechanical properties. The goal is to achieve high strength and high ductility in such materials as much as we can, which is challenging since these two properties often exhibit a trade-off, i.e., a gain in strength usually induces a sacrifice in ductility. Heterogeneities have been intentionally introduced into conventional metals/alloys, such as a grain/twin size gradient, lamellae thickness gradient, and phase structure gradient [29], to promote strain hardening and hence uniform tensile ductility, achieving considerably improved strength–ductility synergy. Motivated by the role of heterogeneities in conventional metals/alloys, researcher also tailored heterogeneities in HEAs to promote strength–ductility synergy.

Ma et al. [12] categorized the heterogeneities in HEAs into multiple levels. The first level arises from the multiple principal elements at the atomic level, i.e., the compositional and packing arrangements of various elemental atoms (short−/medium-range ordering in the neighbour shells). For example, Ding et al. [30] synthesized a CrFeCoNiPd HEA, where all five elements formed atomic aggregation with a wavelength of 1–3 nm. This heterogeneity exhibited considerable resistance to dislocation glide, leading to higher yield strength without compromising ductility. The next level of heterogeneity refers to the nanoscaled clusters, complexes, or precipitates. For example, Lei et al. [31] doped a TiZrHfNb HEA with 2.0 atomic percent oxygen, leading to a strength–ductility synergy with tensile strength improved by 48.5 ± 1.8% and ductility enhanced by 95.2 ± 8.1%. The underlying mechanism is that oxygen tends to form ordered interstitial complexes, changing the dislocation shear mode from planar slip to wavy slip, promoting double cross-slip and dislocation multiplication during deformation.

The third level of heterogeneity comes from multi-phase structures that evolve from a single-phase solid solution, including transforming to dual phase, eutectic lamellae structure, martensites, etc. For example, Shi et al. [32] synthesized a $AlCoCrFeNi_{2.1}$ eutectic HEA (EHEA) with a dual-phase heterogeneous lamella (DPHL) structure. Mechanical properties of the DPHL HEAs and various reported superior metallic materials are compared in Fig. 4. Both Shi et al.'s DPHL HEAs [32] and other reported HEAs [33–39] are separated from the general trend of conventional metallic materials for the tensile strength-elongation map (Fig. 4a), suggesting a promoted strength–ductility synergy in HEAs. However, in the yield strength-elongation map (Fig. 4b), only Shi et al.'s HEAs [32] stand out from the trend, with yield strength of ~1.5 GPa and elongation of ~16%. Due to phase decomposition, there are substantial hard intergranular ordered BCC phases in the soft FCC lamella matrix to impart an additional rigid deformation constraint to FCC grains, thereby strengthening the HEAs. Moreover, the as-prepared EHEAs can activate microcrack-arresting mechanisms to further extend their strain-hardening ability for improved ductility.

The fourth level originates from the defects in the crystal structures and the grain-size distribution with a length scale from nanometre to micrometre. For example, Wu et al. [40] designed an $Al_{0.1}CoCrFeNi$ HEA by combining non-recrystallized and recrystallized grains in heterogeneous structures, which exhibits enhanced strength-ductility synergy from both the underlying plastic accommodation and hardening processes (dislocation hardening, back-stress hardening and twinning). The above multiple levels of heterogeneities in HEAs, leading to lattice friction and back stress hardening, can be utilized as efficient strategies to enhance the strength–ductility synergy of HEAs. The high strength and good ductility provide great potentials for HEAs to outperform conventional metals/alloys in numerous fields, such as civilian infrastructure, transportation, and aerospace.

1.3.3 High-Temperature Properties

To develop novel HEAs with desired properties for high-temperature applications has been one of the major interests of the HEA research community. Among the various HEAs, those consisting of refractory elements, i.e., refractory HEAs, have been of particular interest due to their high strength at elevated temperatures. For example, Senkov et al. [41] produced single BCC phase NbMoTaW and VNbMoTaW refractory HEAs, with yield strengths as high as 400–500 MPa at 1600 °C. Strength retention at elevated temperatures has drawn a large amount of attention. However, the densities of refractory HEAs are usually very high, such as 13.8 g/cm^3 for NbMoTaW HEA, and 12.4 g/cm^3 for VNbMoTaW HEA, and refractory HEAs often exhibit an inferior elongation to fracture at room temperature.

To reduce density and enhance ductility at room temperature, the high-density constituents can be substituted by some lower density ones. For example, HfNbTaTiZr HEA (with density of 9.94 g/cm^3) exhibits a high compression yield strength of 929 MPa and a superior room temperature ductility greater than 50% [42]. To further increase the high-temperature strength and decrease the density of HfNbTaTiZr HEA, different strategies could be adopted, e.g., by adding low-density elements like Mo, Cr, and Al [43, 44] or alternatively by adding Si so that a low-density secondary phase could be formed [45]. For example, Juan et al. [46] enhanced the yield strength from 100 to 550 MPa at 1200 °C by adding Mo in HfNbTaTiZr HEA, while maintaining a reasonable room temperature ductility of 12%. To date, the refractory HEA family mainly consists of eleven elements: Hf, Nb, Ta, Ti, Zr, V, W, Mo, Cr, Al, and Si. Other refractory elements, such as Ir, Os, Re, Rh, and Ru, have not yet been utilized in refractory HEAs.

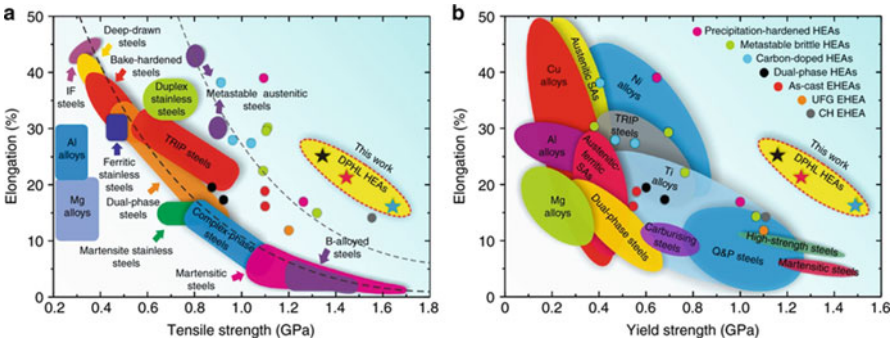

Fig. 4 (**a**, **b**) Mechanical properties of dual-phase heterogeneous lamella (DPHL) HEAs [32] in comparison with conventional metallic materials and other HEAs, including precipitation-hardened HEAs [33], metastable brittle HEAs [34], carbon-doped HEAs [35], dual-phase HEAs [36], as-cast eutectic HEA (EHEA) [37], ultrafine-grained (UFG) EHEA [38], complex and hierarchical (CH) EHEA [39]

2 Computational Modelling and Machine Learning Approaches for High-Entropy Alloys

The huge elemental and compositional space of HEAs provides great opportunities to discover new HEAs with desired properties. Meanwhile, the large unexplored material search space is also challenging for the conventional experimental/simulation techniques in the field. Data-driven ML approaches provide an accurate, computationally inexpensive, interpretable, and transferable way to rapidly screen a given search space to identify the most promising material candidates. In the past few decades, substantial advancement of ML algorithms has expanded the application of data-driven approach throughout science, commerce, and industry. One of the challenges in utilization of ML approaches for material discovery is the lack of large experimental datasets, especially in the space of HEA materials. This problem can be mitigated through computational methods. In this section, we will introduce some of the computational methods and ML approaches for HEA design. Computational methods for HEA design are discussed in Sect. 2.1. Some ML predictions of phase formations are introduced in Sect. 2.2, and examples of ML predictions of mechanical properties are summarized in Sect. 2.3.

2.1 Conventional Computational Methods for HEA Design

To accelerate the discovery and development of HEAs, high-throughput computations and multi-scale simulations are in demand. Computational methods can be utilized to investigate the HEAs spanning different time/length scales and to describe the structural and physical characteristics of materials qualitatively/quantitatively, assisting researchers to understand the materials from multiple aspects. High-throughput calculations can also complement the experiment to provide substantial data for ML models. Computational methods, like experimental techniques, can concentrate on different features of the material, such as different levels of structure descriptions (from atomic level to nanoscale, and to macroscale), as well as various properties (mechanical, physical, or chemical behaviour), etc. Thus, different computational methods targeting different mechanisms have been developed: density functional theory (DFT), molecular dynamics (MD), Monte Carlo (MC), discrete dislocation dynamics (DDD), phase-field method (PFM), thermodynamics model (TM), finite element method (FEM), as well as calculation of phase diagram (CALPHAD). Below we will discuss three most widely used computational methods for HEA design: DFT calculation, MD simulation, and CALPHAD modelling.

2.1.1 DFT Calculation

Generally, first-principle calculation aims to solve the Schrodinger equation with structures and atoms as the input. The Schrodinger equation, however, often has difficulties describing a complex system, and is often limited to dealing with sufficiently simple systems. To simplify the Schrodinger equation, DFT [47, 48] has emerged as one of the most popular first-principle methods. The DFT simplifies the problem of multi-electrons to that of a single electron, describes physical properties of the ground state based on the ground state electron density, and has been extensively employed to study the microstructures and properties of HEAs [49]. Plane-wave-based methods are widely utilized to solve the Kohn–Sham equation for the total energy and force of a HEA system, after which the cell structure and atomic positions are both updated towards the equilibrium state using a structural optimization algorithm. Green's function is also a powerful approach to handling the Kohn–Sham equation within a self-consistent effective medium model.

In principle, a large supercell is required to simulate a HEA, which is extremely difficult for DFT. Although DFT has already employed many simplifications in solving the Schrodinger equation, the computational cost is still quite expensive for HEA systems that consist of multiple constituents. Fortunately, the cluster expansion theory can be employed to utilize a small cell to model the large supercell. For example, one of the popular methods is the specific quasirandom structure (SQS) [50], which allows to capture the chemical disorder and to simulate the local relaxation effects via optimizing the atomic distribution by satisfying the objective functions, including pair correlation, three-body correlation and all the way to many-body correlation, etc., within the neighbouring shells of a solid solution. Moreover, Jiang et al. [51] reported a small set of ordered structures (SSOS) approach to capture the random structures of HEAs, achieving a good accuracy yet with significantly reduced computational cost. For example, an SSOS-3 $\times$ 5 containing only three 5-atom cell structures (Fig. 5a–c) can perfectly match 20 pair correlation functions of the random BCC five-element HEA for the first- and second-nearest neighbours. To achieve the same level of accuracy, it is necessary to use a much larger 125-atom structure in the SQS approach (Fig. 5d).

2.1.2 MD Simulation

Molecular dynamics is a computational method capable of simulating the movements of atoms/molecules (defined as particles). The particles interact with each other and move to energetically favourable sites, capturing a dynamic evolution of the simulated system. The forces exerted on the particles and the system energies are calculated according to the interatomic potentials. The trajectories of particles are updated by solving Newton's equations of motion for each particle numerically. MD simulations are capable of relating atomic-level structures to microscopic behaviours, which have a very extensive range of applications, such as for predicting the mechanical and thermal properties of HEAs [52–54]. Compared with DFT

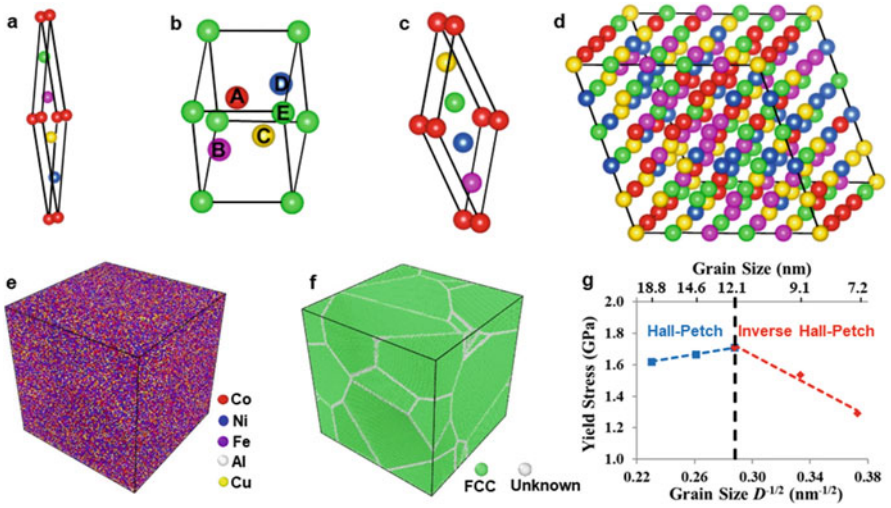

Fig. 5 Three 5-atom cell structures in SSOS-3 × 5 for DFT calculation are shown in (**a**–**c**), respectively. A 125-atom SQS structure for DFT calculation is shown in (**d**) [51]. Polycrystalline model of $CoNiFeAl_{0.3}Cu_{0.7}$ for MD simulation where colour indicates (**e**) atom type and (**f**) phase as determined from common neighbour analysis. (**g**) Variation of yield strength with average grain size for polycrystalline $CoNiFeAl_{0.3}Cu_{0.7}$ HEA under compression along the x direction by MD simulation [52]

calculations, MD simulations can handle much larger time and length scales. MD simulation can also be combined with MC simulation to further extend the simulation scales [8].

HEAs with FCC structures always possess a low yield strength in the range of 200–600 MPa [55]. To tackle this issue, Fu et al. [56] synthesized a nanocrystalline $CoNiFeAl_{0.3}Cu_{0.7}$ HEA with a single FCC phase. This HEA exhibited an amazing yield strength of 1.8 GPa, which was remarkably higher than that of other FCC structured HEAs [55]. To reveal the deformation mechanisms in Fu et al.'s experiments [56], Li et al. [57] performed MD simulations to investigate the compressive process of nanocrystalline HEA with the same composition and similar grain size, from which they concluded that the high strength were associated with a strain-induced phase transformation from FCC to BCC structures. The phase transformation in HEA occurs when the stress induced by severe lattice distortion and external loading exceeds the critical stress required for the nucleation of BCC phase in the matrix.

Chen et al. [52] systematically investigated the phase stability, mechanical properties, and deformation mechanisms of $CoFeNiAl_xCu_{1-x}$ ($x = 0.1$–0.9) HEAs. Cohesive energy data demonstrate that, when Al concentrations is low ($x < 0.4$), FCC structure is more stable. Otherwise, BCC structure is more stable. Hall-Petch and inverse Hall-Petch relations were obtained in both FCC and BCC HEAs (FCC $CoNiFeAl_{0.3}Cu_{0.7}$ HEA is shown in Fig. 5e–g). Microstructural evolutions indicate

that the dominant deformation mechanisms are dislocation slip and deformation twinning in the Hall-Petch regime of FCC HEA because of the low stacking fault energy. In contrast, the deformation mechanism of BCC structures is phase transformation. For the inverse Hall-Petch relation, the deformation mechanisms are grain rotation and grain boundary migration for both FCC and BCC HEAs.

2.1.3 CALPHAD Modelling

Different from DFT calculation and MD simulation, CALPHAD [58] is used to perform thermodynamic and kinetic calculations to obtain the phase diagrams and thermodynamic properties of HEAs according to the thermodynamic databases. Phase diagrams play a key role in understanding the HEA formation and usually refer to a graph with axes for composition and temperature of a HEA system, displaying regions where different single phases are stable and where two or more of them coexist. CALPHAD calculations also allow to investigate the phase compositions, fractions, and stabilities as a function of constituents, pressures, and temperatures. This is a powerful tool for predicting the HEA structure under different conditions, providing not only rational guidance for experimental preparation but also substantial data for ML models. Besides, CALPHAD can be used to predict the thermodynamic properties for each phase and multiple phases.

A reliable thermodynamic database is a prerequisite for CALPHAD modelling of HEAs. Gao et al. [3] stated that the top priority in establishing a reliable database of HEAs is to gather the phase-equilibrium data from the lower-order alloy systems, i.e., the corresponding binaries and ternaries. Unfortunately, such experimental data are usually not sufficient. Fortunately, DFT calculations and MD simulations often can complement experiment to fill up the thermodynamic data. To date, several commercial software with robust thermodynamic database are available, such as Thermo-Calc [59], Pandat [60], and FactSage [61]. In particular, the TCHEA database [59] developed for HEAs includes all the binary and most ternary systems associated with 26 elements, while the PanHEA database [60] contains all the binary and ternary systems related to HEAs consisting of Al, Co, Cr, Cu, Fe, Mn, and Ni, providing unprecedented possibilities for computational method assisted discovery of HEAs.

MacDonald et al. [62] employed Thermo-Calc's TCHEA database to perform systemic analysis by comparing the CALPHAD-predicted phases and the experimentally observed phases in the CoCuFeMnNi HEA. Figure 6a plots a step diagram with the equilibrium phases over a range of temperatures predicted by CALPHAD. This diagram indicates a disordered FCC phase with all the constituent elements (labelled as L12#2 in red) from the melting temperature (1157 °C) to 727 °C. A Cu-rich disordered FCC phase (labelled as L12 in green) is predicted from low temperature to 727 °C, and an Fe-Co-rich B2 phase (labelled as B2 in light blue) is predicted from low temperature to 559 °C. The step diagram agrees with the experimentally observed phases well, except for some errors in the precise temperature points at which the phases form.

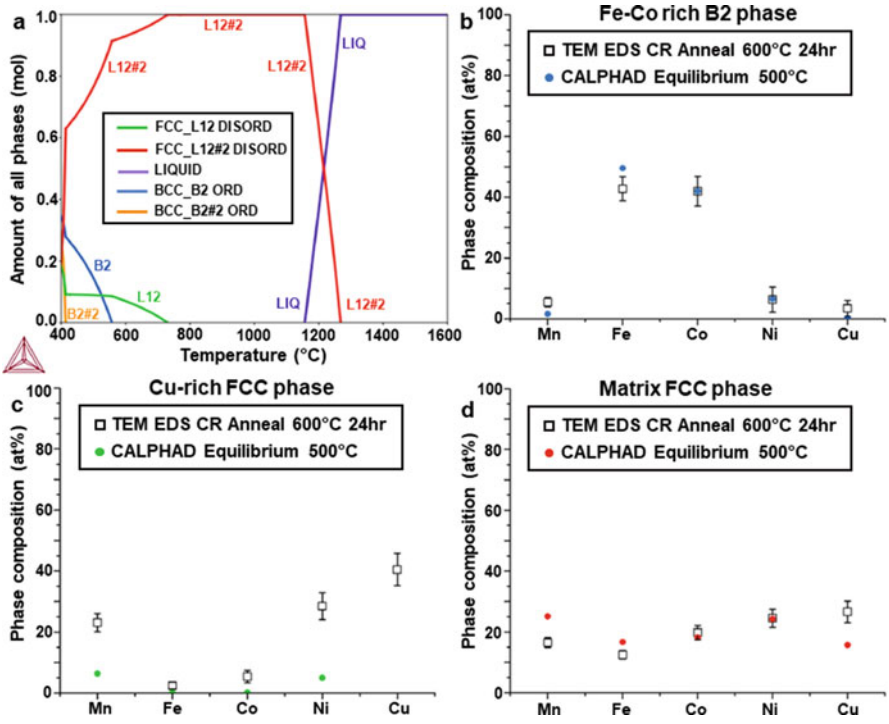

Fig. 6 (**a**) Phase diagram of the CoCuFeMnNi HEA in the temperature range of 400–1600 °C predicted by CALPHAD. Phase compositions by CALPHAD predictions and experimental measurements for the three phases: (**b**) Fe-Co-rich B2 phase, (**c**) Cu-rich FCC phase, and (**d**) matrix FCC phase [62]

The coarsening of secondary phases during post deformation annealing treatment at 600 °C for 24 h allows for quantitative energy dispersive X-ray spectrometer measurements of each phase observed. These experimental measurements are compared with the CALPHAD predicted compositions of each phase at 500 °C in Fig. 6b–d, since 500 °C is the highest temperature that CALPHAD predicts the formations of all three phases. For the compositions of the ordered Fe-Co B2 phase (Fig. 6b) and the matrix disordered FCC phase (Fig. 6d), the predicted data are in relatively good agreement with experimental data. The experimental Cu-rich phase contains dramatically higher compositions of Ni and Mn than CALPHAD predicted. This trend indicates that the modelling of a segregating element in an HEA appears to be unreliable in Thermo-Calc software with this TCHEA database [62]. ML approaches are likely to provide guidance in addressing this inconsistence.

2.2 Machine Learning Predictions of Phase Formations

The intrinsic property of an HEA highly depends on the phase structure: single solid-solution phase (FCC, BCC or HCP), intermetallic compound or amorphous phase. Therefore, accurate prediction of the resulting phase for a given elemental composition is crucial to the rational design and development of new HEAs. Computational methods, such as DFT and CALPHAD, have been employed for predicting the phase formation. However, these methods are not always efficient for a large search space of HEAs. Based on experimental data, parametric methods with various empirical thermo-physical parameters, such as entropy of mixing, enthalpy of mixing, valence electron concentration, and atomic size difference, have been used to make predictions of phase formations [1]. However, these empirical rules only provide limited representation capability and their performance is not always satisfactory. In contrast to conventional computational and parametric methods, data-based ML can improve both the accuracy and efficiency of predictions for HEAs. We will discuss some of ML predictions on single phase (FCC, BCC & HCP), intermetallic compound, and amorphous phase of HEAs below.

2.2.1 Single-/Multi-Phase Solid Solution

Yeh et al. [1] proposed that equimolar compositions maximize the configurational entropy of HEAs, stabilizing the formation of solid-solution (SS) phase. This trend indicates that the possibility for the SS formation in HEAs increases with the number of constituent elements increasing. However, it is well known that the SS formation in HEAs does not merely depend on the elemental quantities [5]. The Hume-Rothery rules [63] have been widely used to predict the SS formations of binary alloys, indicating that the misfit in the features of constituent elements strongly influences the SS formations in binary alloys. For HEAs, King et al. [64] proposed an empirical rule, correctly predicting the formation and stability of 177 single-phase structures of the 185 experimentally reported HEAs. However, the empirical rules for the prediction of SS formation proposed so far usually have very compromised predictability [65].

Motivated by this idea, Pei et al. [65] performed an ML study with a large dataset (1252 samples) and showed that the SS formations could be quite accurately predicted (93%). The dataset for ML consisted of 625 single-phase and 627 multi-phase samples from binary to quinary alloys, whose compositions, phase structures, and thermodynamic properties were obtained from CALPHAD modelling, DFT calculation, and hybrid MC/MD simulation [66]. The descriptors used for ML were elemental properties, whose pair correlations with alloy phases are shown in Fig. 7a. The correlation matrix indicates that the elemental properties, such as bulk modulus, vaporization heat, and valence, possess quite strong correlations (>0.6). Because most elemental properties exhibit strong correlations with each other (i.e., collinearity), it is impossible to employ a simple linear model to predict the phases

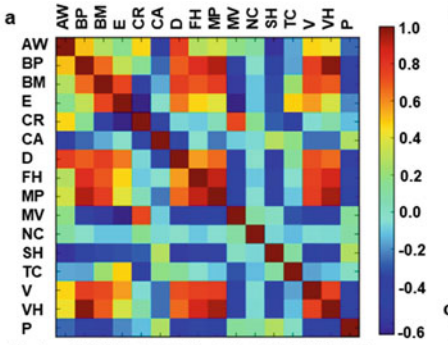

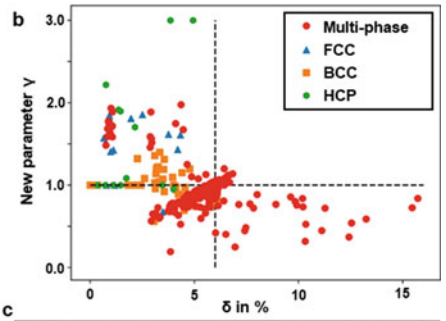

c

Structure	#Single-phase	#Total	Consistency (%)
i. The new rule ≥1 with α = 0.2			
FCC	21	24	88
BCC	27	41	66
HCP	13	14	93
Multi-phase	63	217	71
Average			73
ii. The new rule ≥1 with α = 0.2 jointly with δ ≤ 6%			
FCC	21	24	88
BCC	27	41	66
HCP	13	14	93
Multi-phase	38	217	82
Average			81

d

Group	New rule γ ≥ 1	CALPHAD	Consistency (%)
FCC	5	5	100
BCC	71	67	94
HCP	1	0	0
Summary	77	72	94

Fig. 7 (**a**) The correlation matrix of elemental properties with alloy phases. (**b**) The variation of new parameter γ with lattice misfit δ. The values of $\gamma \geq 3$ are tuned to 3 for better visualization. (**c**) The predictability of the new rule when $\gamma \geq 1$ with $\alpha = 0.2$ (*i*) only and (*ii*) hybrid with $\delta \leq 6\%$. (**d**) Validation of the new rule $\gamma \geq 1$ with $\alpha = 0.2$ rule by CALPHAD method [65]

accurately. It is obvious that simple pair correlations are not robust to map elemental properties to the phases; hence a nonlinear ML model is highly demanded.

Nonlinear Gaussian process is a powerful ML algorithm, which has led to high predictability with an accuracy of 93% [65]. For ML predictions of phase formations, Pei et al. [65] identified the most important descriptors: molar volume, bulk modulus, and melting temperature. By utilizing these descriptors, a new thermodynamics-based rule was developed to predict SS phases, with a new parameter γ calculated as the ratio of Gibbs free energy of N-component alloys to the lowest Gibbs free energy of its binaries. If $\gamma \geq 1$, a single-phase solid solution is predicted to form. The ML prediction results are shown in Fig. 7b, c, which accurately predicts 88% FCC, 66% BCC, and 93% HCP alloys with an optimized parameter $a = 0.2$. The average accuracy is 73% by the empirical rule alone. If it is hybrid with the empirical rule of atomic size misfit $\delta \leq 6\%$, the accuracy increases to 81%, giving much better predictability than by the rule alone. To test the predictability of this rule, the phase structures of new alloys were also predicted and compared with CALPHAD modelling. The high consistency between CALPHAD and ML in Fig. 7d indicates that Pei et al.'s rule [65] obtained from ML can act as a guide to discover HEAs with desired phase structures.

By coupling thermodynamic and chemical features with a random forest model, Kaufmann et al. [67] also proposed a high-throughput ML approach to predict the single- or multi-phase SS formation. The dataset contained a total of 1798 unique samples with equimolar compositions from Lederer et al.'s DFT calculations [68]. The 1798 samples consisted of 117 binaries, 441 ternaries, 1110 quaternaries, and 130 quinaries. The ML prediction accuracy for the binary, ternary, quaternary, and quinary samples were 87.2%, 63.3%, 62.2%, and 72.3%, respectively. The incorrect predictions were found to be related to the lack of training data for the ternary compositions as well as the absence of compositions that were not single-phase BCC or FCC in the quaternaries and quinaries. This model can be employed as a primary tool or integrated into existing alloy discovery workflows to explore material space in an unconstrained manner and to predict the results of new experiments.

With an experimental dataset containing 322 as-cast samples consisting of ternary to nonary multi-principal element alloys, Li et al. [69] built a support vector machine model to distinguish the FCC, BCC single phases, and the remaining phases, achieving a cross-validation accuracy over 90% after training and testing. Five elemental properties, i.e., atomic size difference, valence electron concentration, configurational entropy, mixing enthalpy, and melting temperature, were selected as descriptors to reduce the risk of overfitting. With this model, the phases of 267 BCC and 369 FCC equimolar HEAs in the composition space of 16 metallic elements were further predicted. Interestingly, dozens of refractory HEAs possessing high ratios of melting point to density have been sought out. In particular, 11 of them are well consistent with the experimental measurements [70–72]. Besides, 20 quinary refractory HEAs with highest melting points also agree well with DFT calculations. This proposed ML model complements the calculation of phase diagrams and provides useful guidance for designing new HEAs.

2.2.2 Solid-Solution, Intermetallic, and Amorphous Phases

Beside the above SS phase, diverse other phases, such as intermetallic (IM) compound or amorphous phase (AM), also appeared in HEAs. Based on ML algorithm, Zhou et al. [73] examined the commonly used design rules for HEA phases. The dataset used for ML contained 601 as-cast alloys with 131 SS alloys, 248 IM alloys, 165 AM alloys, 6 mixed IM and AM alloys, and 51 mixed SS and IM alloys. The descriptors contained 13 parameters, including mean atomic radius (a), atomic size difference (δ), electronegativity (χ), standard deviation of electronegativity ($\Delta\chi$), average valance electron concentration (VEC), standard deviation of VEC (σ_{VEC}), average mixing enthalpy (ΔH_{mix}), standard deviation of mixing enthalpy ($\sigma_{\Delta H}$), ideal mixing entropy (S_{id}), average of the melting temperatures of constituent elements (T_{m}), standard deviation of melting temperature (σ_{T}), mean bulk modulus (K), and standard deviation of bulk modulus (σ_{K}).

Figure 8 shows a comparison of sensitivity measures of the 13 descriptors for AM, IM, and SS phases, which are coloured according to the ratio of mean to standard deviation. Red colour stands for positive correlation, while blue colour for

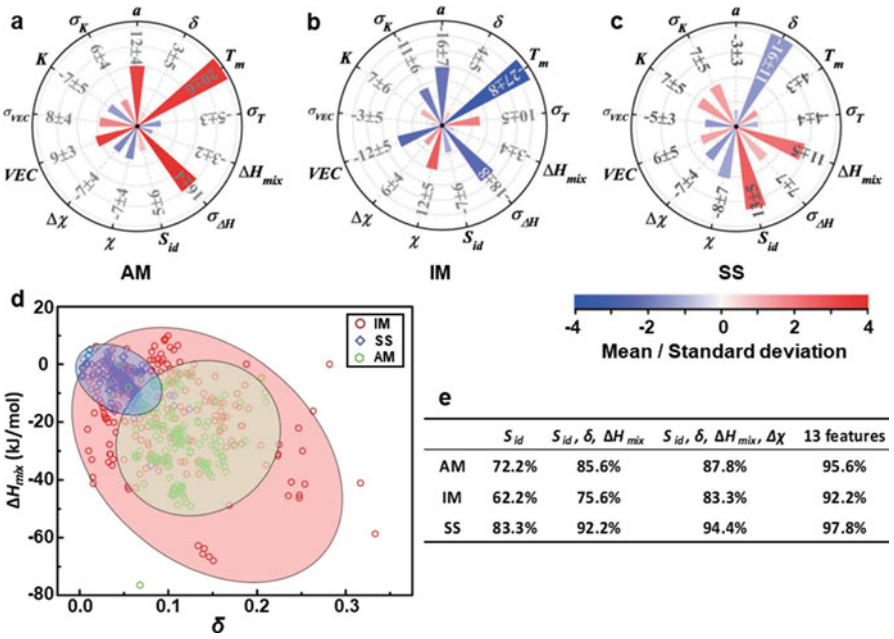

	S_{id}	S_{id}, δ, ΔH_{mix}	S_{id}, δ, ΔH_{mix}, $\Delta\chi$	13 features
AM	72.2%	85.6%	87.8%	95.6%
IM	62.2%	75.6%	83.3%	92.2%
SS	83.3%	92.2%	94.4%	97.8%

Fig. 8 The sensitivity measures of 13 design parameters for (**a**) amorphous (AM), (**b**) intermetallics (IM), and (**c**) solid-solution (SS) phases. (**d**) The plot of δ vs. ΔH_{mix} for SS, IM, and AM. (**e**) Comparison of the accuracy of 1-descriptor, 3-descriptor, 4-descriptor, and 13-descriptor model [73]

negative correlation. The sensitivity measure of S_{id} for SS is highly positive (+13 in Fig. 8c), while that for IM is quite negative (−7 in Fig. 8b). Figure 8c indicates that a higher value of S_{id} tends to form SS phase, which is consistent with the high entropy effect. In particular, the sensitivity measure of S_{id} is positive for AM (+5 in Fig. 8a), suggesting that increasing the chemical complexity does promote glass formation. Figure 8c also shows that δ has a remarkable influence on the SS formation, whereas ΔH_{mix} and S_{id} exhibit similar degrees of influence on the SS formation. The highly negative value of δ (−16 in Fig. 8c) indicates that the atomic size mismatch needs to be minimized in order to obtain SS phase.

As shown in Fig. 8d, SS has a narrower distribution of δ and ΔH_{mix} than AM and IM, indicating that SS is more related to the variation of δ or ΔH_{mix} as compared with IM and AM. It also demonstrates that increasing δ will promote AM and IM and inhibit SS, which is consistent with the negative values of δ for SS in Fig. 8c (−16). For a quantitative comparison, ML prediction accuracies with different sets of descriptors are estimated and compared in Fig. 8e. Clearly, ML model with a single parameter S_{id} exhibits the poorest accuracy, as low as ~62% for IM. Generally, the addition of other elemental properties as descriptors, such as δ, ΔH_{mix}, and $\Delta\chi$, increases the prediction accuracy for all three phases. Therefore, the ML model with all elemental properties (13 descriptors) is better than the other

models with only partial design parameters. The extremely high accuracy for the best ML model (95.6% for AM, 92.2% for IM, and 97.8% for SS) demonstrates that the ML approach is a powerful tool for designing HEAs with desired phase structures.

Using a comprehensive experimental dataset summarized in the review article of HEAs [4], including 401 different HEAs with 174 SS, 54 IM, and 173 mixed SS and IM (SS + IM) phases, Huang et al. [74] also employed ML algorithms to explore phase selection rules. Three popular ML algorithms, i.e., support vector machine (SVM), K-nearest neighbours (KNN), and artificial neural network (ANN), were adopted to screen out the most suitable ML model. Five parameters were employed as descriptors, including VEC, $\Delta\chi$, δ, S_{id}, and ΔH_{mix}. The whole dataset was divided into four nearly equal portions to execute a cross-validation to avoid overfitting. Each portion was utilized as the testing data only once. When one portion of data was used as testing data, the others were training data. Therefore, four times training and testing of the ML model were performed on different subsets of the full data to execute the cross-validation process, creating a robust model with improved accuracy. The final accuracy was calculated as the average value of these four testing results. The testing accuracy for the SVM, KNN, and ANN models are 64.3%, 68.6%, and 74.3%, respectively. Therefore, the trained ANN model outperforms others and is used for the subsequent predictions of new HEAs.

Utilizing a genetic algorithm (GA) to choose the ML model and associated descriptors efficiently, Zhang et al. [75] collected 550 as-cast HEAs with stable phase formation information from literature sources [76] to construct a dataset and performed a systematic framework. Single BCC phase, single FCC phase, and dual FCC and BCC phase were considered as the SS phase, while intermetallic compounds and amorphous phases were regarded as the non-solid-solution (NSS) phase. Nine ML models with combinations of seventy material descriptors were tested, where GA was employed to achieve an efficient search. The optimized classification model exhibited an accuracy up to 88.7% for identifying SS and NSS HEAs and further to 91.3% for distinguishing BCC, FCC, and dual-phase HEAs. With a small dataset of 118 samples, Islam et al. [77] employed neural network ML model to recognize the underlying data pattern and predict the corresponding phase of multi-principal element alloys. The trained ML model reached an accuracy of over 99% for the full dataset, while an average generalization accuracy higher than 80% were obtained for the cross-validation training and testing datasets.

2.2.3 Precipitation

For the precipitation in HEAs, Sato et al. [78] studied the strengthening of ordered $L1_2$ precipitate (γ') in the CoAlW alloy system in 2006, which has sparked the research interest in designing novel γ'-strengthened Co-base superalloys with excellent properties for aircraft applications. For example, Liu et al. [79] proposed an ML strategy to design Co-base superalloys ($Co_aAl_bW_cNi_dTi_eTa_fCr_g$) with multiple targeted properties optimized simultaneously. Among all the properties

that the γ'-strengthened superalloys possess, the γ' solvus temperature is one of the most important, since it reflects the upper limit of temperature capability. Hence, to develop superior γ'-strengthened Co-base alloys, a high γ' solvus temperature (i.e., $T_{\gamma'\text{-solvus}} > 1250$ °C) is essential. Moreover, the targeted processing window ($\Delta T_p = T_{\text{solidus}} - T_{\gamma'\text{-solvus}} \geq 40$ °C), freezing range ($\Delta T_f = T_{\text{liquidus}} - T_{\text{solidus}} \leq 60$ °C), microstructural stability, and density ($\rho \leq 8.7$ g/cm^3) were also optimized simultaneously by Liu et al. [79].

In Liu et al.'s work [79], the quantities of samples in the original dataset were 31, 68, 94, and 134 for the density, liquidus, solidus, and γ' solvus temperature, respectively. With the chemical compositions as the descriptors, six different regression models, including AdaBoost, support vector machine with a kernel of radial basis function, decision tree, k-nearest neighbours, random forest (RF), and gradient tree boosting (GTB) algorithms, were built by Liu et al. [79]. The receiver operating characteristic (ROC) curve was used to evaluate the performance of the ML model, as shown in Fig. 9a. When the ROC curve is closer to the upper left corner of the graph, the model shows better performance. The area under the ROC curve (i.e., AUC value) can also be employed to evaluate the accuracy of ML predictions. The closer the AUC value is to 1, the higher the accuracy of the ML model. The mean value of 100 AUC values for the GTB model is 0.96 and larger than that of other models. The best ML models for predicting the γ' solvus temperature, liquidus, density, and solidus were the GTB, GTB, GTB, and RF, respectively, whose performances on the testing dataset are shown in Fig. 9b–e. Therefore, the GTB model is the best among the six different regression models and chosen as the ML model for the subsequent predictions of new alloys in the potential composition space.

For the $Co_aAl_bW_cNi_dTi_eTa_fCr_g$ alloys, the potential composition space was defined by Liu et al. [79] as: $30\% \leq a \leq 100\%$, $10\% \leq b \leq 15\%$, $1\% \leq c \leq 8\%$, $20\% \leq d \leq 50\%$, $1\% \leq e \leq 8\%$, $1\% \leq f \leq 4\%$, $2\% \leq g \leq 10\%$, where the concentrations of elements were in atomic percent. Each alloy in this space was constrained by $a > d$ to satisfy the concept of Co-base alloys with $a + b + c + d + e + f + g = 100\%$. A series of new Co-base superalloys were screened out successfully and synthesized out of 210,000 candidates experimentally. As shown in Fig. 9f, three iterations were performed in experiments until the as-prepared alloy's γ' solvus temperature was >1250 °C and no longer increased significantly. The best candidate, Co-36Ni-12Al-2Ti-4Ta-1W-2Cr, exhibited the highest γ' solvus temperature (1266.5 °C), a satisfying density of 8.68 g/cm^3, a γ' volume fraction of 74.5%, and excellent high-temperature (1000 °C) oxidation resistance. Thus, ML has provided a new strategy to optimize multicomponent alloys with precipitations to obtain multi-target properties.

For more complicated precipitations in HEAs, Qi et al. [80] classified 600+ reported HEAs for ML based on their phases and precipitations: disordered FCC (A1), disordered BCC (A2), disordered HCP (A3), mixed disordered FCC + BCC (A1 + A2), ordered BCC (B2), disordered solid-solution phases + B2 precipitations (SS + B2), and IM mixed with the other phases (IM+). Single-phase HEA predictions (89–90% success rates) had higher accuracy than mixed

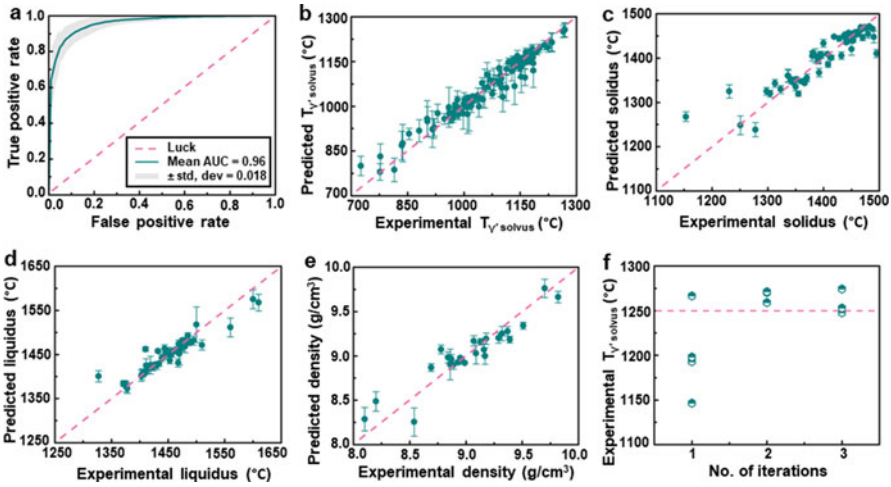

Fig. 9 (**a**) The ROC curve of ML model. The standard deviation of 100 ROC curves is marked in grey, and a random classification is plotted by the pink dashed line. The ML predictions of the best model on the testing dataset as a function of experimental measurements for the (**b**) γ' solvus temperature, (**c**) solidus, (**d**) liquidus and (**e**) density, respectively. The error bars are the standard deviation of 1000 ML predictions. The pink dotted line indicates perfect match, i.e., the ML predictions and experimental measurements are in good agreement. (**f**) The experimental γ' solvus temperature as a function of the number of iterations. The pink dashed line plots the target 1250 °C [79]

phase predictions (78–85% success rates) with 50–90% training sets. Overall, this ML model gave accurate predictions on phase formations, where both the overall predictions and single-phase predictions of HEAs were >80%. Furthermore, 42 new HEAs with randomly selected complex compositions were prepared by suction casting to validate the ML predictions, and 34 out of the 42 HEA samples were correctly predicted by ML, exhibiting an accuracy of 81%. This highly predictive ML approach can be employed to complement experiment in guiding HEA design.

2.3 Machine Learning Predictions of Mechanical Properties

As mentioned above, the huge compositional space of HEAs provides a nice opportunity to improve mechanical properties, such as hardness, yield strength, ductility, Young's modulus, and elastic constant, yet at the same time sets a great challenge in elemental selection and concentration optimization, especially if only explored through trial-and-error type of experiments. ML approach has proven to be a powerful strategy to predict phase formations of HEAs, as discussed in the above section. Here in this section, we discuss some of the ML predictions on hardness, Young's modulus, and elastic constant of HEAs.

2.3.1 Hardness

Hardness is a measure of the resistance to localized plastic deformation induced by mechanical indentation or abrasion. Wen et al. [81] formulated a materials design strategy combining a ML surrogate model with design of experiment (DOE) to search for HEAs with large hardness in AlCoCrCuFeNi HEA system. The dataset consisted of 155 samples, which included 22 quaternaries, 95 quinaries, and 38 senaries, all with measured hardness. The iterative design loops are schematically shown in Fig. 10, where iteration loop I (blue dashed line) only uses composition as descriptor and iteration loop II (red solid line) utilizes both composition and feature as descriptors. A ML surrogate model (Fig. 10c) was trained first based on the dataset with hardness (Fig. 10a) and composition and feature as descriptors (Fig. 10b*1* and b*2*). Then, the obtained ML model (Fig. 10c) was employed to predict the hardness of new HEAs in a virtual search space (Fig. 10d). A utility function was used (Fig. 10e) to select a candidate for experimental synthesis (Fig. 10f) by balancing exploitation (relatively high predicted hardness) and exploration (acceptable predicted uncertainties). The measured hardness of newly synthesized sample was added into the training set (Fig. 10a) to perform the next round of iteration to improve the surrogate model.

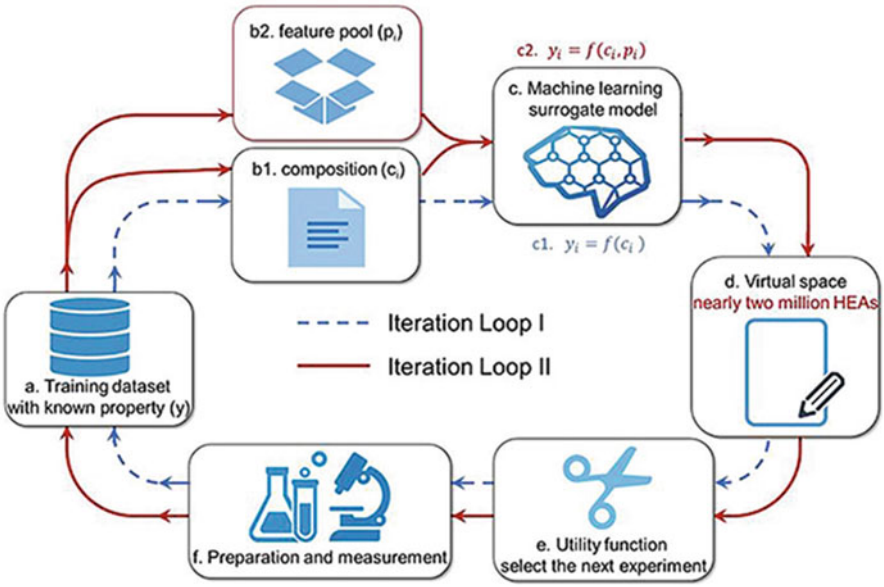

Fig. 10 A schematic of the iteration loop by ML for accelerated discovery of HEAs, including (**a**) dataset construction with hardness, (**b**) descriptor selection (b*1*: composition and b*2*: feature), (**c**) ML surrogate model training, (**d**) new predictions for a search space, (**e**) utility function to choose experimental candidates, and (**f**) experimental preparation and measurement. A feature pool is added into the descriptors of Iteration Loop II, as compared with Iteration Loop I [81]

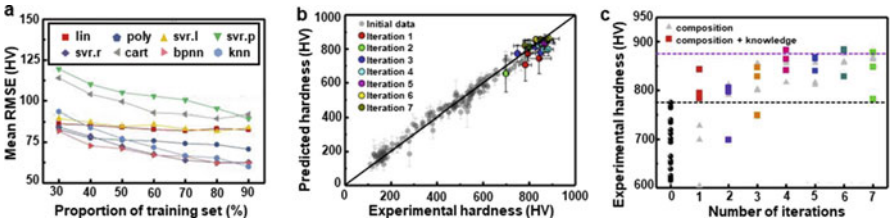

Fig. 11 (**a**) Model evaluation by calculating the mean RMSE for different regression models in Iteration Loop I. The inset enlarges the curves for the three best models of svr.r, bpnn, and knn. (**b**) The predicted hardness values versus the measured ones for samples in the datasets for Iterative Loop II, including the new experimental data during seven iterations. (**c**) The hardness values of the newly synthesized samples during iterations. The inset draws the highest predicted values during iterations. Black and purple dashed lines indicate the best values in the original training dataset and obtained using Iterative Loop I, respectively [81]

For the ML models, Wen et al. [81] used a series of regression algorithms, including linear regression (lin), polynomial regression (poly), back propagation neural network (bpnn), regression tree (cart), k-nearest neighbour (knn), and support vector regression with linear kernel (svr.l), polynomial kernel (svr.p), and radial basis function kernel (svr.r), to predict the hardness. The performance of each ML model in Iteration Loop I was evaluated by calculating the mean root mean square error (mean RMSE) on the testing set, whose results with different split ratios of training and testing sets are shown in Fig. 11a. Overall, the error of each ML model decreased with increasing the size of training set. When the size of training set was 70% and that of testing set was 30%, the svr.r model presented the minimum prediction error. Thus, the svr.r model was selected to predict the hardness of new alloys in the virtual search space for subsequent iterations.

Figure 11b shows the ML predicted hardness as a function of the experimental measurements for all samples from the original dataset and the newly synthesized ones by experiment. The closer the data is to the diagonal line, the more adequate the model is. Figure 11c shows the measured hardness of the newly synthesized samples for Iteration Loop I (labelled as composition in grey) and II (labelled as composition + knowledge in colour). Compared with Iteration Loop I, the samples predicted in the first iteration of Iteration Loop II exhibited higher hardness than all of the original samples. A sample with hardness of 843 HV was discovered for Iteration Loop II, which was 8.8% higher than the highest value in the original dataset. The hardness values obtained in Iteration Loop II were always higher than those in Iteration Loop I during the iterations. The best performer, $Al_{47}Co_{20}Cr_{18}Cu_5Fe_5Ni_5$, possessing the highest hardness, was predicted in the fourth iteration of Iteration Loop II. Its hardness value reached as high as 883 HV, which was 14% larger than the highest value in the original dataset. This strategy offers a recipe to rapidly optimize HEA systems towards desired properties.

For an AlCoCrFeMnNi HEA system by substituting Cu with Mn, Chang et al. [82] utilized an artificial neural network (ANN) model to explore promising

compositions for synthesis of high-hardness HEAs. In the dataset, 91 experimental records composed of targeted elements were collected from literature, including compounds from binary alloys to senary alloys. Simulated annealing (SA), a probabilistic algorithm for approaching the global optimum of a function, was adopted in this work to screen out the candidate with targeted hardness and risk. The ML results demonstrated that the SA algorithm could accelerate the discovery of novel alloys in the unexplored compositional space, by identifying three candidates with hardness >600 HV. In particular, one candidate showed a 20% increase compared with the highest value in the original dataset. The correlations between the predicted composition, hardness, and microstructure were further explored by experiment. Experimental measurements indicate that the evolution of the hardness is related to the phase transition from FCC to BCC + B2.

To design HEAs with high hardness and low density, Menou et al. [83] utilized a multi-objective optimization genetic algorithm combining solid solution hardening (SSH) and CALPHAD modelling with data mining. This approach screened out 3155 alloys that were Pareto-optimal or non-dominated, meaning that no other candidate would form single solid solution and have higher SSH and lower density simultaneously than any one of them. Among the 3155 samples, $Al_{35}Cr_{35}Mn_8Mo_5Ti_{17}$ was chosen for experimental validation by vacuum arc melting. This as-prepared alloy formed a single disordered solid solution, exhibiting a Vickers hardness of 658 HV and a density below 5.5 g/cm^3. This is one of the hardest metals/alloys ever reported for such a low density, demonstrating the promise of ML in discovering novel alloys with multi-objective optimization, as compared with experimental trial-and-error approaches.

2.3.2 Young's Modulus

Young's modulus is a mechanical property that measures the stiffness of a solid material. It defines the relationship between stress (force per unit area) and strain (proportional deformation) in the linear elasticity regime of a material under uniaxial deformation. In the TiMoNbZrSnTa alloy system, Yang et al. [84] formulated a ML approach to explore BCC β-Ti alloys with low Young's modulus (shown in Fig. 12). The dataset was composed of 82 reported β-Ti alloy samples with low Young's modulus from literature, including binary, ternary, quaternary, and quinary alloys in TiMoNbZrSnTa systems. ML algorithms, including random forest (RF), auxiliary gradient-boosting regression tree (XGBoost), and support vector regression (SVR), were trained based on the dataset with Young's modulus and elemental composition. In the forward design (Loop I in Fig. 12), when the alloy compositions are chosen, the Young's modulus can be predicted. Moreover, if the target Young's modulus is set, then alloy compositions can be predicted in the reverse design (Loop II in Fig. 12). To increase the accuracy of ML prediction, some features reflecting the low Young's modulus and β structural stability were implemented into the ML process as descriptors, including the Mo equivalence and the cluster-formula approach, in which the former feature represented the β structural stability, and the

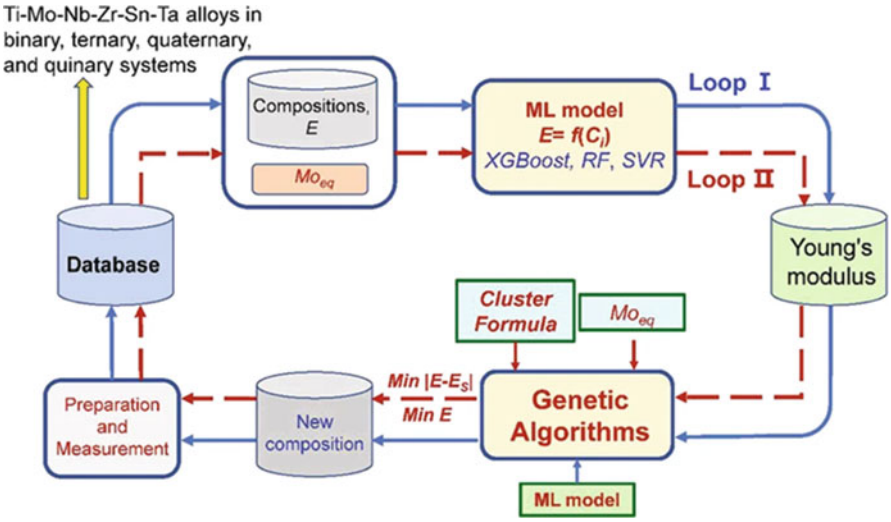

Fig. 12 A schematic diagram for the design loop of multicomponent β-Ti alloys with target Young's modulus in the TiMoNbZrSnTa system by machine learning [84]

latter reflected the interactions among elements. Besides, the genetic algorithm was utilized to handle the nonlinear optimization problem. By setting different objective functions, new alloys were screened out by ML and then validated by experimental preparations and measurements. The newly synthesized samples would be put into the original database for another round of training and prediction.

For the forward design (Loop I), both the RMSE and the coefficient of determination (R^2) were utilized as the criterion for evaluating the prediction accuracy. Since the dataset size of 82 samples was somewhat limited, the multiple hold-out method was employed to ensure accuracy. This process was performed for 500 times in these three models by randomly partitioning samples into training set (90%) and testing set (10%). Figure 13a shows that the mean RMSE values for the training (testing) set are 1.3 ± 0.6 (4.6 ± 0.7) GPa, 3.8 ± 0.3 (4.9 ± 0.9) GPa, and 3.9 ± 0.4 (5.2 ± 0.9) GPa for XGBoost, RF, and SVR methods, respectively. Moreover, Fig. 13b shows that the mean values of R^2 for the training (testing) set are 98 ± 1 (87 ± 2)%, 89 ± 1 (84 ± 4)%, and 88 ± 2 (73 ± 3)% for XGBoost, RF, and SVR, respectively. Therefore, the predicted accuracy of the XGBoost method is higher than those of the RF and SVR methods for the ML prediction of Young's modulus in this alloy system.

For the reverse design (Loop II) of new alloys with low Young's modulus, the evolution histories of the genetic algorithm with the objective function of low Young's modulus are shown in Fig. 13c, d, in which the objective function and the mean value of Young's modulus are plotted as the red and black lines, respectively. These evolution curves indicate that the predicted values are converged to objective values after about 50 iterations to obtain $[(Mo_{0.5}Sn_{0.5})-(Ti_{13}Zr_1)](Nb_{0.5}Ta_{0.5})$

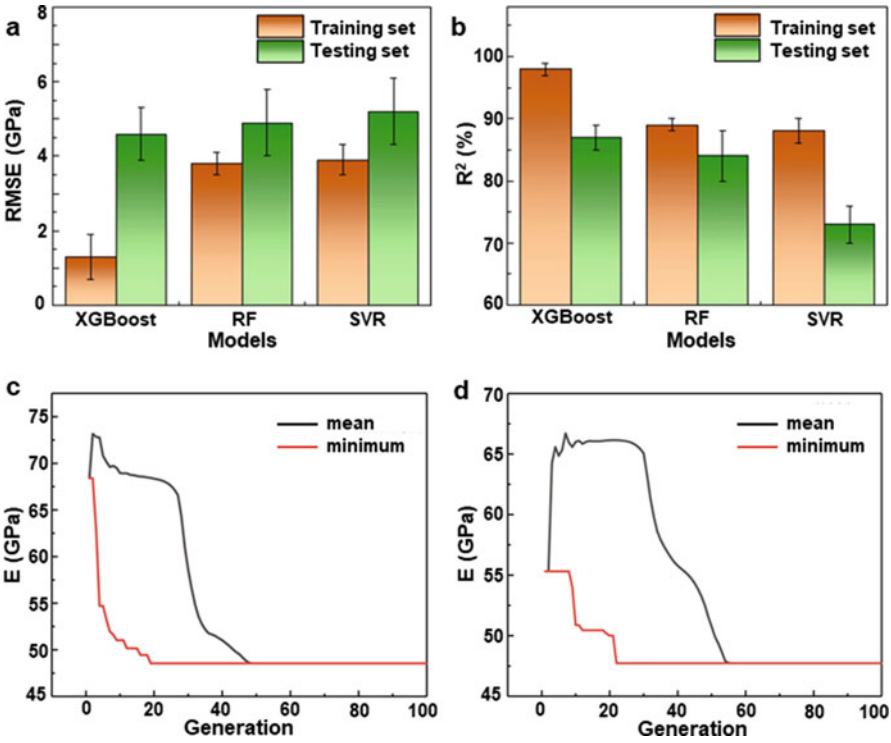

Fig. 13 (**a**) RMSE and (**b**) R^2 values of XGBoost, RF, and SVR methods with 90% training set and 10% testing set. The evolution histories of the genetic algorithm with the objective function of low Young's modulus to obtain (**c**) $[(Mo_{0.5}Sn_{0.5})-(Ti_{13}Zr_1)](Nb_{0.5}Ta_{0.5})$ and (**d**) $[(Mo_{0.3}Sn_{0.7})-(Ti_{13.5}Zr_{0.5})](Nb_{1.5}Ta_{0.5})$ alloys. The objective function and the mean value of Young's modulus are plotted as the red and black lines, respectively [84]

(Fig. 13c) and $[(Mo_{0.3}Sn_{0.7})-(Ti_{13.5}Zr_{0.5})](Nb_{1.5}Ta_{0.5})$ (Fig. 13d) alloys, respectively, indicating a high efficiency of this reverse design. Experimental measurements of Young's modulus for these two predicted new alloys (not included in the original database) indeed reached the minimum values (46–49 GPa). Therefore, this design framework seems capable of predicting high-performance alloys with desired properties including Young's modulus.

For low- (binary), medium- (ternary, quaternary), and high-entropy (quinary) alloys, Roy et al. [85] implemented gradient boost classification model to explore the crystal phase and Young's modulus of an alloy system composed of 5 refractory elements (Mo, Ta, Ti, W, and Zr). The database for phase prediction consisted of 329 samples where 159 entries were BCC phase, 111 entries were FCC phase, and 59 entries were multi-phase, while the database for Young's modulus consisted of only 87 samples because of limited experimental reports. The ML predictions with experimental validations indicate that the electronegativity difference and mean melting temperature contribute most to the phase formation of these refractory

alloys, while the enthalpy of mixing and melting temperature have dominant influences on the Young's modulus of these alloys. Moreover, it also indicates that the entropy of mixing only has negligible impacts on the phase formation and Young's modulus, reigniting the debate on its veritable role in determining the phase and property of HEAs.

2.3.3 Elastic Constants

Elastic constants (e.g., bulk and shear moduli) are parameters that linearly relate stress and strain within the elastic range of a material. As observed in many alloy systems, the elastic constants are closely related to the lattice-distortion-induced strain [86]. It is known that severe lattice distortion naturally exists in HEAs, which may be partly due to the atomic size differences of the constituent elements. For example, the single-phase FCC $Al_{0.3}CoCrFeNi$ HEA, which possesses large size differences among its five types of components, is a typical system to adopt for detailed investigation of the relationship between the elastic properties and lattice distortion. Kim et al. [86] used an integrated experimental and computational approach to explore the elasticity of FCC $Al_{0.3}CoCrFeNi$ HEA based on in situ neutron diffractions, DFT calculations, and ML predictions. It has been reported that, for studying the elastic parameters of HEAs, both Coherent Potential Approximation (CPA) and SQS are generally suitable [87]. Therefore, Kim et al. [86] utilized both CPA and SQS methods to calculate elastic constants for comparison.

The calculated values (SQS and CPA) and experimental measurements (neutron diffraction) for the elastic constants of $Al_{0.3}CoCrFeNi$ HEA are compared in Fig. 14a. Compared with the CPA results, the elastic constants obtained from the SQS method are more consistent with those from neutron-diffraction experiments. The differences between SQS calculations and experimental measurements are within 5% for all elastic constants, indicating reasonable accuracy of the SQS method. To evaluate the effects of lattice distortion on the elastic properties of HEAs, a series of DFT calculations based on a volume-only optimized SQS with atoms fixed on the lattice sites and a fully relaxed SQS structure with the lattice distortion were performed. Figure 14b indicates that the relaxed SQS structure with lattice distortion considered gives more accurate results on bulk and shear moduli, as compared with SQS method with fixed atoms and CPA method. ML was performed using two models, the gradient boosting machine local polynomial regression (GBM-Locfit) and the gradient boosting trees algorithm (GB Trees), with the database containing the results of DFT calculations. The bulk and shear moduli of GBM-Locfit and GB Trees predictions are also plotted in Fig. 14b, indicating that the GB-Trees model exhibits better predictions than the GBM-Locfit model for the bulk modulus. For the shear modulus, GBM-Locfit model overestimated the experimental measurement, while GB-Trees model underestimated the value. This work could inspire more future studies to search for novel alloy based on similar integrated approaches.

Using a similar approach with integrated experimental measurements, theoretical DFT calculations, and ML predictions, Lee et al. [88] also studied the elastic

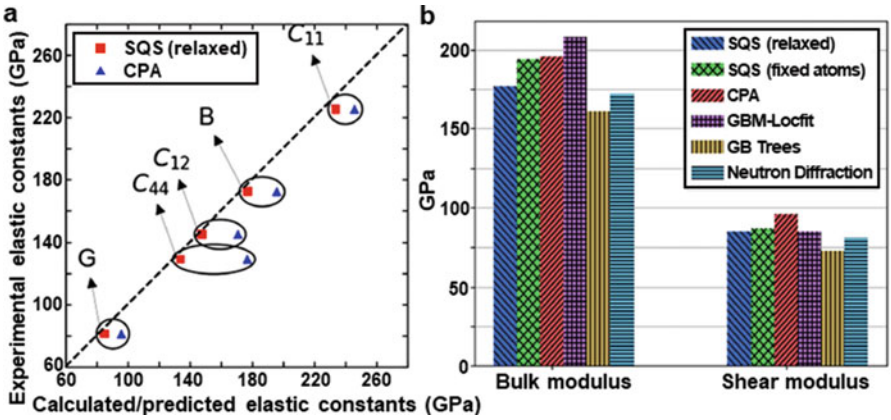

Fig. 14 (**a**) Comparison of experimentally measured and computationally calculated bulk and shear moduli of $Al_{0.3}$CoCrFeNi HEA. (**b**) Comparison of computationally calculated, experimentally measured, and ML predicted bulk and shear moduli

and plastic deformation behaviours of a single BCC NbTaTiV refractory HEA at elevated temperatures. ML models with the GB Trees algorithm were trained based on the DFT-calculated bulk and shear moduli, compound structural information, and elemental properties. A temperature-dependent elastic anisotropic deformation behaviour was revealed by in situ neutron-diffraction experiments. The single-crystal elastic moduli and macroscopic Young's, bulk, and shear moduli were measured by in situ neutron diffraction, with results exhibiting excellent agreement with those from DFT calculations, ML predictions, and resonant ultrasound spectroscopy. The ML predicted shear and bulk moduli were 36.6 GPa and 146.3 GPa with relative errors of 2.5% and 6%, respectively. This work further highlights an integrated experimental and computational approach in the discovery of new HEAs for structural materials applications.

Dai et al. [89] demonstrated that ML can also serve as a powerful tool to help study HEAs through MD simulations. In their work, a deep learning potential (DLP) for high entropy $(Zr_{0.2}Hf_{0.2}Ti_{0.2}Nb_{0.2}Ta_{0.2})C$ was fitted with prediction errors in energy and force being 9.4 meV/atom and 217 meV/Å, respectively. The robustness of the DLP was validated by accurately predicting the variation of structures and properties of mono-phase carbides TMC (TM = Ti, Zr, Hf, Nb, and Ta) with temperature. For example, they were able to predict an increase from 4.5707 to 4.6727 Å in lattice constants, an increase from 7.85×10^{-6} K^{-1} to 10.58×10^{-6} K^{-1} in thermal expansion coefficients, while a decrease from 2.02 $W{\cdot}m^{-1}{\cdot}K^{-1}$ to 0.95 $W{\cdot}m^{-1}{\cdot}K^{-1}$ in phonon thermal conductivities of high entropy $(Zr_{0.2}Hf_{0.2}Ti_{0.2}Nb_{0.2}Ta_{0.2})C$ in temperature ranging from 0 °C to 2400 °C. The predicted properties at room temperature agree well with experimental measurements, demonstrating the accuracy of the DLP. With introduction of ML potentials in MD simulations, one could address many complicated problems that are intractable by conventional computational methods.

3 Summary

This chapter is dedicated to an overview of machine learning approaches and applications for high-entropy alloys, a relatively new class of materials that have attracted considerable interest from the materials research communities in the past decade. Towards this goal, we started by reviewing some of the most fundamental features that characterize HEAs, such as high entropy, sluggish diffusion, severe lattice distortion, and cocktail effects. The high entropy effect tends to stabilize a solid-solution phase as matrix, while the sluggish diffusion effect facilitates accesses to super-saturated states and fine precipitates. The lattice distortion effect improves lattice friction and leads to strength enhancement. The cocktail effect underlines the superior properties beyond the rules of mixture in a multi-principal element alloy. Major preparation methods of HEAs include arc melting, mechanical alloying, and sputter deposition. Arc melting is a dominant preparation method to synthesize bulk HEAs, while sputter deposition is suitable for film/coating deposition. Mechanical alloying has the advantage in alloying of normally immiscible elements. Superior properties of HEAs include high hardness, excellent balance between strength and ductility, and performance under extreme conditions such as high temperature. FCC structured HEAs typically possess a low hardness. By tuning elemental types and concentrations, one can induce phase transformation or precipitate formation to increase the hardness. By tailoring heterogeneities in HEAs, such as short-range ordering, dual phase, and gradient grains, strain hardening and uniform tensile ductility can be substantially enhanced, resulting in considerably improved strength–ductility synergy. Moreover, HEAs consisting of refractory elements can achieve superior high-temperature properties.

Conventional computational methods to investigate the structures and properties of HEAs include DFT, MD, and CALPHAD. DFT calculation is suitable to obtain the energetic data and to predict the structural stability of HEAs by utilizing SQS or SOSS approaches. MD simulation is a powerful method to calculate some of the mechanical and physical properties as well as reveal deformation mechanisms in HEAs, reaching time and length scales way beyond those of DFT. CALPHAD modelling can predict not only the phase compositions, fractions, and stability as functions of composition, pressure, and temperature, but also the thermodynamic properties for each phase and multiple phases. CALPHAD is a powerful tool to relate the HEA structure to property under different conditions, providing not only useful guidance for experimental synthesis but also abundant data for ML approach.

One of the most exciting recent developments in the field is the rapid advance of ML approaches to predict the phase structures and mechanical properties of HEAs. For phase formation in HEAs, accurate predictions of the resulting phases, including solid-solution phase, intermetallic compound, and amorphous phase, can be realized. The database for ML usually comes from both experiment and CALPHAD, reaching thousands of data points. The validated high-performance ML algorithms are Gaussian process, random forest regression, support vector machine, artificial neural network, and gradient tree boosting. The mechanical properties, hardness,

Young's modulus, and elastic constant have all been studied by the ML approach, achieving good accuracy with support vector machine, artificial neural network, or gradient-boosting regression. Compared with phase predictions, the database of property prediction is mostly collected from experiment, whose size is relatively small (typically only hundreds of samples). Therefore, high-throughput experimental or computational methods are desperately needed to provide large amount of data for the ML approach. Although there are abundant studies focusing on HEAs in recent years, current exploration on the structure and property of HEAs is only at the tip of an iceberg. More aspects on microstructures (short−/medium-range ordering), deformation mechanisms (dislocation motion and twinning formation), and thermal properties (melting point and thermal conductivity) still call for ML and other approaches to provide more insights. The huge compositional space of HEAs offers unlimited opportunities for academic and industrial research and development, where ML can be integrated with experimental and simulation methods to accelerate the discovery of next generation materials with unprecedented properties.

References

1. Yeh, J. W., Chen, S. K., Lin, S. J., Gan, J. Y., Chin, T. S., Shun, T. T., Tsau, C. H., & Chang, S. Y. (2004). Nanostructured high-entropy alloys with multiple principal elements: Novel alloy design concepts and outcomes. *Advanced Engineering Materials, 6*(5), 299–303.
2. Cantor, B., Chang, I. T. H., Knight, P., & Vincent, A. J. B. (2004). Microstructural development in equiatomic multicomponent alloys. *Materials Science and Engineering A, 375*, 213–218.
3. Gao, M., Yeh, J., Liaw, P., & Zhang, Y. (2016). *High-Entropy alloys: Fundamentals and applications*. Springer International Publishing AG Switzerland: Springer Nature.
4. Miracle, D. B., & Senkov, O. N. (2017). A critical review of high entropy alloys and related concepts. *Acta Materialia, 122*, 448–511.
5. Zhang, Y., Zhou, Y. J., Lin, J. P., Chen, G. L., & Liaw, P. K. (2008). Solid-solution phase formation rules for multi-component alloys. *Advanced Engineering Materials, 10*(6), 534–538.
6. Takeuchi, A., & Inoue, A. (2001). Quantitative evaluation of critical cooling rate for metallic glasses. *Materials Science and Engineering A, 304*, 446–451.
7. Tsai, K.-Y., Tsai, M.-H., & Yeh, J.-W. (2013). Sluggish diffusion in Co–Cr–Fe–Mn–Ni high-entropy alloys. *Acta Materialia, 61*(13), 4887–4897.
8. Choi, W.-M., Jo, Y. H., Sohn, S. S., Lee, S., & Lee, B.-J. (2018). Understanding the physical metallurgy of the CoCrFeMnNi high-entropy alloy: An atomistic simulation study. *npj Computational Materials, 4*(1), 1–9.
9. Wang, Z., Fang, Q., Li, J., Liu, B., & Liu, Y. (2018). Effect of lattice distortion on solid solution strengthening of BCC high-entropy alloys. *Journal of Materials Science and Technology, 34*(2), 349–354.
10. Tong, Y., Zhao, S., Jin, K., Bei, H., Ko, J., Zhang, Y., & Zhang, F. (2018). A comparison study of local lattice distortion in Ni80Pd20 binary alloy and FeCoNiCrPd high-entropy alloy. *Scripta Materialia, 156*, 14–18.
11. Sohn, S. S., Kwiatkowski da Silva, A., Ikeda, Y., Körmann, F., Lu, W., Choi, W. S., Gault, B., Ponge, D., Neugebauer, J., & Raabe, D. (2019). Ultrastrong medium-entropy single-phase alloys designed via severe lattice distortion. *Advanced Materials, 31*(8), 1807142.
12. Ma, E., & Wu, X. (2019). Tailoring heterogeneities in high-entropy alloys to promote strength–ductility synergy. *Nature Communications, 10*(1), 1–10.

13. Zhang, Y., Zuo, T. T., Tang, Z., Gao, M. C., Dahmen, K. A., Liaw, P. K., & Lu, Z. P. (2014). Microstructures and properties of high-entropy alloys. *Progress in Materials Science, 61*, 1–93.
14. Ranganathan, S. (2003). Alloyed pleasures: Multimetallic cocktails. *Current Science, 85*(10), 1404–1406.
15. Zhang, W., Liaw, P. K., & Zhang, Y. (2018). Science and technology in high-entropy alloys. *Science China Materials, 61*(1), 2–22.
16. Tsao, L., Chen, C., & Chu, C. (2012). Age hardening reaction of the Al0. 3CrFe1. 5MnNi0. 5 high entropy alloy. *Materials & Design (1980–2015), 36*, 854–858.
17. Zou, Y., Ma, H., & Spolenak, R. (2015). Ultrastrong ductile and stable high-entropy alloys at small scales. *Nature Communications, 6*(1), 1–8.
18. Tian, Y., Lu, C., Shen, Y., & Feng, X. (2019). Microstructure and corrosion property of CrMnFeCoNi high entropy alloy coating on Q235 substrate via mechanical alloying method. *Surfaces and Interfaces, 15*, 135–140.
19. Singh, S., Wanderka, N., Murty, B., Glatzel, U., & Banhart, J. (2011). Decomposition in multi-component AlCoCrCuFeNi high-entropy alloy. *Acta Materialia, 59*(1), 182–190.
20. Suryanarayana, C. (2001). Mechanical alloying and milling. *Progress in Materials Science, 46*(1-2), 1–184.
21. Kilmametov, A., Kulagin, R., Mazilkin, A., Seils, S., Boll, T., Heilmaier, M., & Hahn, H. (2019). High-pressure torsion driven mechanical alloying of CoCrFeMnNi high entropy alloy. *Scripta Materialia, 158*, 29–33.
22. Smidt, F. (1990). Use of ion beam assisted deposition to modify the microstructure and properties of thin films. *International Materials Reviews, 35*(1), 61–128.
23. Tsai, M.-H., & Yeh, J.-W. (2014). High-entropy alloys: A critical review. *Materials Research Letters, 2*(3), 107–123.
24. Praveen, S., & Kim, H. S. (2018). High-entropy alloys: Potential candidates for high-temperature applications—an overview. *Advanced Engineering Materials, 20*(1), 1700645.
25. Li, W., Liu, P., & Liaw, P. K. (2018). Microstructures and properties of high-entropy alloy films and coatings: A review. *Materials Research Letters, 6*(4), 199–229.
26. Hsu, C. Y., Wang, W. R., Tang, W. Y., Chen, S. K., & Yeh, J. W. (2010). Microstructure and mechanical properties of new AlCoxCrFeMo0. 5Ni high-entropy alloys. *Advanced Engineering Materials, 12*(1–2), 44–49.
27. Chuang, M.-H., Tsai, M.-H., Wang, W.-R., Lin, S.-J., & Yeh, J.-W. (2011). Microstructure and wear behavior of AlxCo1. 5CrFeNi1. 5Tiy high-entropy alloys. *Acta Materialia, 59*(16), 6308–6317.
28. Zhu, Z., Ma, K., Wang, Q., & Shek, C. (2016). Compositional dependence of phase formation and mechanical properties in three CoCrFeNi-(Mn/Al/Cu) high entropy alloys. *Intermetallics, 79*, 1–11.
29. Li, X., Lu, L., Li, J., Zhang, X., & Gao, H. (2020). Mechanical properties and deformation mechanisms of gradient nanostructured metals and alloys. *Nature Reviews Materials, 5*, 706–723.
30. Ding, Q., Zhang, Y., Chen, X., Fu, X., Chen, D., Chen, S., Gu, L., Wei, F., Bei, H., & Gao, Y. (2019). Tuning element distribution, structure and properties by composition in high-entropy alloys. *Nature, 574*(7777), 223–227.
31. Lei, Z., Liu, X., Wu, Y., Wang, H., Jiang, S., Wang, S., Hui, X., Wu, Y., Gault, B., & Kontis, P. (2018). Enhanced strength and ductility in a high-entropy alloy via ordered oxygen complexes. *Nature, 563*(7732), 546–550.
32. Shi, P., Ren, W., Zheng, T., Ren, Z., Hou, X., Peng, J., Hu, P., Gao, Y., Zhong, Y., & Liaw, P. K. (2019). Enhanced strength–ductility synergy in ultrafine-grained eutectic high-entropy alloys by inheriting microstructural lamellae. *Nature Communications, 10*(1), 1–8.

33. He, J., Wang, H., Huang, H., Xu, X., Chen, M., Wu, Y., Liu, X., Nieh, T., An, K., & Lu, Z. (2016). A precipitation-hardened high-entropy alloy with outstanding tensile properties. *Acta Materialia, 102*, 187–196.
34. Huang, H., Wu, Y., He, J., Wang, H., Liu, X., An, K., Wu, W., & Lu, Z. (2017). Phase-transformation ductilization of brittle high-entropy alloys via metastability engineering. *Advanced Materials, 29*(30), 1701678.
35. Wang, Z., Baker, I., Guo, W., & Poplawsky, J. D. (2017). The effect of carbon on the microstructures, mechanical properties, and deformation mechanisms of thermo-mechanically treated Fe40. 4Ni11. 3Mn34. 8Al7. 5Cr6 high entropy alloys. *Acta Materialia, 126*, 346–360.
36. Baker, I., Meng, F., Wu, M., & Brandenberg, A. (2016). Recrystallization of a novel two-phase FeNiMnAlCr high entropy alloy. *Journal of Alloys and Compounds, 656*, 458–464.
37. Lu, Y., Gao, X., Jiang, L., Chen, Z., Wang, T., Jie, J., Kang, H., Zhang, Y., Guo, S., & Ruan, H. (2017). Directly cast bulk eutectic and near-eutectic high entropy alloys with balanced strength and ductility in a wide temperature range. *Acta Materialia, 124*, 143–150.
38. Wani, I., Bhattacharjee, T., Sheikh, S., Lu, Y., Chatterjee, S., Bhattacharjee, P. P., Guo, S., & Tsuji, N. (2016). Ultrafine-grained AlCoCrFeNi2. 1 eutectic high-entropy alloy. *Materials Research Letters, 4*(3), 174–179.
39. Bhattacharjee, T., Wani, I., Sheikh, S., Clark, I., Okawa, T., Guo, S., Bhattacharjee, P. P., & Tsuji, N. (2018). Simultaneous strength-ductility enhancement of a nano-lamellar AlCoCrFeNi 2.1 eutectic high entropy alloy by cryo-rolling and annealing. *Scientific Reports, 8*(1), 1–8.
40. Wu, S., Wang, G., Wang, Q., Jia, Y., Yi, J., Zhai, Q., Liu, J., Sun, B., Chu, H., & Shen, J. (2019). Enhancement of strength-ductility trade-off in a high-entropy alloy through a heterogeneous structure. *Acta Materialia, 165*, 444–458.
41. Senkov, O., Wilks, G., Miracle, D., Chuang, C., & Liaw, P. (2010). Refractory high-entropy alloys. *Intermetallics, 18*(9), 1758–1765.
42. Senkov, O., Scott, J., Senkova, S., Miracle, D., & Woodward, C. (2011). Microstructure and room temperature properties of a high-entropy TaNbHfZrTi alloy. *Journal of Alloys and Compounds, 509*(20), 6043–6048.
43. Senkov, O., & Woodward, C. (2011). Microstructure and properties of a NbCrMo0. 5Ta0. 5TiZr alloy refractory. *Materials Science and Engineering, 529*, 311–320.
44. Senkov, O., Senkova, S., & Woodward, C. (2014). Effect of aluminum on the microstructure and properties of two refractory high-entropy alloys. *Acta Materialia, 68*, 214–228.
45. Liu, Y., Zhang, Y., Zhang, H., Wang, N., Chen, X., Zhang, H., & Li, Y. (2017). Microstructure and mechanical properties of refractory HfMo0. 5NbTiV0. 5Six high-entropy composites. *Journal of Alloys and Compounds, 694*, 869–876.
46. Juan, C.-C., Tsai, M.-H., Tsai, C.-W., Lin, C.-M., Wang, W.-R., Yang, C.-C., Chen, S.-K., Lin, S.-J., & Yeh, J.-W. (2015). Enhanced mechanical properties of HfMoTaTiZr and HfMoNbTaTiZr refractory high-entropy alloys. *Intermetallics, 62*, 76–83.
47. Hohenberg, P., & Kohn, W. (1964). Inhomogeneous electron gas. *Physical Review, 136*(3B), B864.
48. Kohn, W., & Sham, L. J. (1965). Self-consistent equations including exchange and correlation effects. *Physical Review, 140*(4A), A1133.
49. Ge, H., & Tian, F. (2019). A review of ab initio calculation on lattice distortion in high-entropy alloys. *JOM, 71*(11), 4225–4237.
50. Zunger, A., Wei, S.-H., Ferreira, L., & Bernard, J. E. (1990). Special quasirandom structures. *Physical Review Letters, 65*(3), 353.
51. Jiang, C., & Uberuaga, B. P. (2016). Efficient ab initio modeling of random multicomponent alloys. *Physical Review Letters, 116*(10), 105501.
52. Chen, S., Aitken, Z. H., Wu, Z., Yu, Z., Banerjee, R., & Zhang, Y.-W. (2020). Hall-Petch and inverse Hall-Petch relations in high-entropy CoNiFeAlxCu1-x alloys. *Materials Science and Engineering A, 773*, 138873.

53. Choudhuri, D., Gwalani, B., Gorsse, S., Komarasamy, M., Mantri, S. A., Srinivasan, S. G., Mishra, R. S., & Banerjee, R. (2019). Enhancing strength and strain hardenability via deformation twinning in fcc-based high entropy alloys reinforced with intermetallic compounds. *Acta Materialia, 165*, 420–430.
54. Zhang, Y., Stocks, G. M., Jin, K., Lu, C., Bei, H., Sales, B. C., Wang, L., Béland, L. K., Stoller, R. E., & Samolyuk, G. D. (2015). Influence of chemical disorder on energy dissipation and defect evolution in concentrated solid solution alloys. *Nature Communications, 6*(1), 1–9.
55. Jo, Y., Jung, S., Choi, W., Sohn, S. S., Kim, H. S., Lee, B., Kim, N. J., & Lee, S. (2017). Cryogenic strength improvement by utilizing room-temperature deformation twinning in a partially recrystallized VCrMnFeCoNi high-entropy alloy. *Nature Communications, 8*(1), 1–8.
56. Fu, Z., Chen, W., Wen, H., Zhang, D., Chen, Z., Zheng, B., Zhou, Y., & Lavernia, E. J. (2016). Microstructure and strengthening mechanisms in an FCC structured single-phase nanocrystalline Co25Ni25Fe25Al7. 5Cu17. 5 high-entropy alloy. *Acta Materialia, 107*, 59–71.
57. Li, J., Fang, Q., Liu, B., & Liu, Y. (2018). Transformation induced softening and plasticity in high entropy alloys. *Acta Materialia, 147*, 35–41.
58. Kaufman, L., & Bernstein, H. (1970). *Computer calculation of phase diagrams. With special reference to refractory metals* (Refractory Materials. A Series of Monographs) (Vol. 4). New York: Academic Press Inc..
59. Andersson, J.-O., Helander, T., Höglund, L., Shi, P., & Sundman, B. (2002). Thermo-Calc & DICTRA, computational tools for materials science. *Calphad, 26*(2), 273–312.
60. Chen, S.-L., Daniel, S., Zhang, F., Chang, Y., Yan, X.-Y., Xie, F.-Y., Schmid-Fetzer, R., & Oates, W. (2002). The PANDAT software package and its applications. *Calphad, 26*(2), 175–188.
61. Bale, C. W., Chartrand, P., Degterov, S., Eriksson, G., Hack, K., Mahfoud, R. B., Melançon, J., Pelton, A., & Petersen, S. (2002). FactSage thermochemical software and databases. *Calphad, 26*(2), 189–228.
62. MacDonald, B. E., Fu, Z., Wang, X., Li, Z., Chen, W., Zhou, Y., Raabe, D., Schoenung, J., Hahn, H., & Lavernia, E. J. (2019). Influence of phase decomposition on mechanical behavior of an equiatomic CoCuFeMnNi high entropy alloy. *Acta Materialia, 181*, 25–35.
63. Hume-Rothery, W., & Powell, H. M. (1935). On the theory of super-lattice structures in alloys. *Zeitschrift für Kristallographie-Crystalline Materials, 91*(1-6), 23–47.
64. King, D., Middleburgh, S., McGregor, A., & Cortie, M. (2016). Predicting the formation and stability of single phase high-entropy alloys. *Acta Materialia, 104*, 172–179.
65. Pei, Z., Yin, J., Hawk, J. A., Alman, D. E., & Gao, M. C. (2020). Machine-learning informed prediction of high-entropy solid solution formation: Beyond the Hume-Rothery rules. *npj Computational Materials, 6*(1), 1–8.
66. Gao, M. C., Zhang, C., Gao, P., Zhang, F., Ouyang, L., Widom, M., & Hawk, J. (2017). Thermodynamics of concentrated solid solution alloys. *Current Opinion in Solid State and Materials Science, 21*(5), 238–251.
67. Kaufmann, K., & Vecchio, K. S. (2020). Searching for high entropy alloys: A machine learning approach. *Acta Materialia, 198*, 178–222.
68. Lederer, Y., Toher, C., Vecchio, K. S., & Curtarolo, S. (2018). The search for high entropy alloys: A high-throughput ab-initio approach. *Acta Materialia, 159*, 364–383.
69. Li, Y., & Guo, W. (2019). Machine-learning model for predicting phase formations of high-entropy alloys. *Physical Review Materials, 3*(9), 095005.
70. Yao, H., Qiao, J., Gao, M., Hawk, J., Ma, S., Zhou, H., & Zhang, Y. (2016). NbTaV-(Ti, W) refractory high-entropy alloys: Experiments and modeling. *Materials Science and Engineering A, 674*, 203–211.
71. Todai, M., Nagase, T., Hori, T., Matsugaki, A., Sekita, A., & Nakano, T. (2017). Novel TiNbTaZrMo high-entropy alloys for metallic biomaterials. *Scripta Materialia, 129*, 65–68.

72. Yao, H., Qiao, J., Hawk, J., Zhou, H., Chen, M., & Gao, M. (2017). Mechanical properties of refractory high-entropy alloys: Experiments and modeling. *Journal of Alloys and Compounds, 696*, 1139–1150.
73. Zhou, Z., Zhou, Y., He, Q., Ding, Z., Li, F., & Yang, Y. (2019). Machine learning guided appraisal and exploration of phase design for high entropy alloys. *npj Computational Materials, 5*(1), 1–9.
74. Huang, W., Martin, P., & Zhuang, H. L. (2019). Machine-learning phase prediction of high-entropy alloys. *Acta Materialia, 169*, 225–236.
75. Zhang, Y., Wen, C., Wang, C., Antonov, S., Xue, D., Bai, Y., & Su, Y. (2020). Phase prediction in high entropy alloys with a rational selection of materials descriptors and machine learning models. *Acta Materialia, 185*, 528–539.
76. Sheng, G., & Liu, C. T. (2011). Phase stability in high entropy alloys: Formation of solid-solution phase or amorphous phase. *Progress in Natural Science: Materials International, 21*(6), 433–446.
77. Islam, N., Huang, W., & Zhuang, H. L. (2018). Machine learning for phase selection in multi-principal element alloys. *Computational Materials Science, 150*, 230–235.
78. Sato, J., Omori, T., Oikawa, K., Ohnuma, I., Kainuma, R., & Ishida, K. (2006). Cobalt-base high-temperature alloys. *Science, 312*(5770), 90–91.
79. Liu, P., Huang, H., Antonov, S., Wen, C., Xue, D., Chen, H., Li, L., Feng, Q., Omori, T., & Su, Y. (2020). Machine learning assisted design of γ'-strengthened Co-base superalloys with multi-performance optimization. *npj Computational Materials, 6*(1), 1–9.
80. Qi, J., Cheung, A. M., & Poon, S. J. (2019). High entropy alloys mined from binary phase diagrams. *Scientific Reports, 9*(1), 1–10.
81. Wen, C., Zhang, Y., Wang, C., Xue, D., Bai, Y., Antonov, S., Dai, L., Lookman, T., & Su, Y. (2019). Machine learning assisted design of high entropy alloys with desired property. *Acta Materialia, 170*, 109–117.
82. Chang, Y.-J., Jui, C.-Y., Lee, W.-J., & Yeh, A.-C. (2019). Prediction of the composition and hardness of high-entropy alloys by machine learning. *JOM, 71*(10), 3433–3442.
83. Menou, E., Tancret, F., Toda-Caraballo, I., Ramstein, G., Castany, P., Bertrand, E., Gautier, N., & Díaz-Del, P. E. J. R. (2018). Computational design of light and strong high entropy alloys (HEA): Obtainment of an extremely high specific solid solution hardening. *Scripta Materialia, 156*, 120–123.
84. Yang, F., Li, Z., Wang, Q., Jiang, B., Yan, B., Zhang, P., Xu, W., Dong, C., & Liaw, P. K. (2020). Cluster-formula-embedded machine learning for design of multicomponent β-Ti alloys with low Young's modulus. *npj Computational Materials, 6*(1), 1–11.
85. Roy, A., Babuska, T., Krick, B., & Balasubramanian, G. (2020). Machine learned feature identification for predicting phase and Young's modulus of low-, medium-and high-entropy alloys. *Scripta Materialia, 185*, 152–158.
86. Kim, G., Diao, H., Lee, C., Samaei, A., Phan, T., de Jong, M., An, K., Ma, D., Liaw, P. K., & Chen, W. (2019). First-principles and machine learning predictions of elasticity in severely lattice-distorted high-entropy alloys with experimental validation. *Acta Materialia, 181*, 124–138.
87. Huang, S., Tian, F., & Vitos, L. (2018). Elasticity of high-entropy alloys from ab initio theory. *Journal of Materials Research, 33*(19), 2938–2953.
88. Lee, C., Kim, G., Chou, Y., Musicó, B. L., Gao, M. C., An, K., Song, G., Chou, Y.-C., Keppens, V., & Chen, W. (2020). Temperature dependence of elastic and plastic deformation behavior of a refractory high-entropy alloy. *Science Advances, 6*(37), eaaz4748.
89. Dai, F.-Z., Wen, B., Sun, Y., Xiang, H., & Zhou, Y. (2020). Theoretical prediction on thermal and mechanical properties of high entropy (Zr0. 2Hf0. 2Ti0. 2Nb0. 2Ta0. 2) C by deep learning potential. *Journal of Materials Science and Technology, 43*, 168–174.

Two-Way TrumpetNets and TubeNets for Identification of Material Parameters

S. Y. Duan, X. Han, and G. R. Liu

1 Introduction

Reliable specification of material parameters is critically important in structural evaluation, health monitoring, and default detection. It helps to ensure the reliability of the structures and the system performance during services [1, 2]. In many cases, the nominal material properties used in the design or analysis or evaluation of the structure are obtained by testing the standard samples of raw materials [2]. Such material parameters can be substantially different from the actual properties of the material in the structure manufactured through hot or code work processes to produce desired shapes and geometry. The discrepancy could be as much as 20% of the nominal data [3]. This situation is also true for the composite structures, which are often made of fibers and matrix materials through a curing process of heating cycles. Depending on the actual manufacturing process and the desired shape of the structure, the material property can also be inhomogeneous, that is varying from locations to locations [1]. Moreover, for fiber-reinforced composites, the number of material constants has increased and the properties are anisotropic in nature [4]. In order to obtain actual material parameters of composite structures, effective techniques are explored. Among these techniques, the nondestructive evaluation of composite material properties by computational inverse techniques is most preferential [5–13].

S. Y. Duan · X. Han (✉)
State Key Laboratory of Reliability and Intelligence of Electrical Equipment, Hebei University of Technology, Tianjin, China
e-mail: xhan@hebut.edu.cn

G. R. Liu
Department of Aerospace Engineering and Engineering Mechanics, University of Cincinnati, Cincinnati, OH, USA

Y. Cheng et al. (eds.), *Artificial Intelligence for Materials Science*, Springer Series in Materials Science 312, https://doi.org/10.1007/978-3-030-68310-8_3

Advanced nondestructive methods for material characterization of composites utilize complex relationships between the structure behavior (or responses) and material constants. These relationships are often represented by a mathematical and/or computational model at least in one direction, which defines the forward problem. In the revise direction, such relationship can often only be expressed in an implicit manner, and hence the problem becomes an inverse problem. If a set of reasonably accurate experimentally measured data of structure responses, or/and a sufficiently accurate predicative computer model for the structural responses is available, the inverse problem can be casted into a parameter identification problem. In such an inverse procedure, a set of parameters corresponding to the material property can be identified by minimizing error functions formulated using the measured or/and computed responses, such as in displacements, strains, and natural frequencies [14–16]. However, such an inverse procedure can often be expensive, due to the need for a large number of calls for forward model in the minimization process.

Neural network (NN) has been applied to solve inverse problems. Examples include the reconstruction of constitutive properties using depth–load responses [17], group velocities, phase velocities, and slowness measurements [18]. Estimation of contact forces was performed from impact-induced time-history of strains [19, 20]. The implementation of the NN technique has greatly assisted the research in the material science and technology [21]. In general, the forward problem is often well defined for a stable and unique solution, because it is governed explicitly by partial differential equations and obtaining the responses is an integral (and hence a smoothing) operators [14]. The inverse problem, on the other hand, is difficult to define well, and hence is often ill-posed, because the inverse solution is obtained thorough essentially a differential (and hence a harshening) operators [14]. In addition, these harshening operators are usually not possible to formulate explicitly, and theoretical analysis of solution stability becomes largely impossible, leading to difficulties to find proper remedies. Therefore, solutions can change significantly for small changes in settings in the inverse problem, in addition to the high computational costs. The NN approach offers means to simplify the setting of inverse problems in the form of a NN structure.

An NN mimics the functional process of the biological neurons, and is often configured artificially in a structure of layers of neurons. The output of a neuron in a layer is idealized as an affine mapping (with is linear) of the inputs from the previous layer of neurons, and is regulated by proper "activation" functions to introduce nonlinearity. A loss (or error) function, usually in terms of a sum of mean-squared-error, can then be built between the outputs of these neurons at the last layer (as the predicted responses for given training sample sets) and the true (measured) responses. Because these activation functions are usually chosen to be differentiable, at least in piecewise, and together with the simple affine mapping in all these previous layers, the (seemly complicated) loss function becomes differentiable. Hence, a gradient-based minimization technique can be used to "train" the NN by minimizing the loss function in the back-propagation process. The effective use of gradient-based minimization techniques allows the NN to be trained efficiently,

using essentially the steepest decent methods. Note also that the true responses can be "simulated" by a predictive computer model using true parameters with properly added noises simulating the measurement errors. In addition, computer models can also be used to generate training samples, by sampling over the entire given parameter space where the inverse solution leaves. Therefore, when a computer model is made available, NN can be trained for many types of inverse problems [13, 22, 23]. Due to the unique structure of the NN, it can offer a systematic approach to solve inverse problems, provided a proper configuration can be found. It has been demonstrated that once properly trained, an NN can become a real-time computational tool as a surrogate model in place of the expensive computer model for complex mechanics problems [14].

Recently, TrumpetNets were proposed for unified analyses of both forward and inverse problems [24]. It has a unique architecture of trumpet shape, allowing possible direct inversion over the trained net. The TrumpetNets can be trained using any physics-law-based numerical solver (typically a predicative computer model) as a trainer. Once successfully trained, the TrumpetNets can then be used for real-time computations of both forward and inverse problems. Applications of this method for mechanical problems of materials and structures can be found in Ref. [24, 25]. The major breakthrough of the TrumpetNet concept is that it reveals the physics of the underline problem explicitly in terms of numerical numbers of weights and biases of the trained nets. Moreover, using the TrumpetNet, the solution to the inverse problem for some problems can even be "analytically" derived by a chain of inversions of matrices of the weight matrices in the network layers. In these cases, the training of the inverse NN is no longer necessary. It is, to the best knowledge of the authors, the simplest procedure to solve inverse problems for an explicit form of solutions. It is thus an enabling technology for at least certain types of inverse problems. This claim has been corroborated by some problems of mechanics of materials and structures [16, 24, 25].

It is generally understood that training a forward problem is usually much more straightforward compared to training the corresponding inverse problem [26]. This is especially true for mechanics problems governed by partial differential equations, which generally have smooth forward solutions. It is also expected that the same idea of TrumpetNet maybe extended to problems governed by integral equations in a reverse manner. For integral problems, however, the training of the inverse problem may be easier, and thus can be trained first. The trained TrumpetNet for the forward problem can then be "analytically" derived. Moreover, the TrumpetNet approach enables the variable in a problem flowing in two-way in the neural networks. Thus, the effort for establishment of pair TrumpetNets (forward and inverse) can be roughly at the same level of the effort for training the single forward TrumpetNet. This enables effective processing both forward and inverse problems simultaneously to realize the idea of "total solution" to a problem [24].

For many problems, the TrumpetNet can be further simplified into a tubular shape. In such cases, TubeNet is practically a flattened TrumpetNet via special treatments for dimensionality adjustment of the training datasets. It is expected that the TubeNet is applicable for many inverse problems. It has been demonstrated to

be effective for inverse problems of mechanics for composites with as many as eight material parameters [25]. The technique for dimension reduction in the TubeNet is the principal component analysis (PCA) technique invented by Pearson [26]. PCA reduces the dimension of the training dataset to that of the input parameter dataset [25]. For some problems, the TubeNet can use the explicit inversion procedure termed as DWI approach, which is a chain of matrix inversions for the weight matrices of the network layers in the trained forward TubeNet.

In this chapter, our discussion will be focused on the latest NN techniques of the TrumpetNets and the TubeNets for inverse analysis of mechanics problems. The contents of this chapter are largely based on our published journal papers [24, 25].

2 Problem Setting and Solving Strategy

2.1 Production of Composites

Composite materials are typically made from two or more components with different properties, and hence usually microscopically heterogeneous. The property of the combined materials at macroscopical level can be obtained using methods of rule-of-mixture [27]. It derived from the micro-mechanics principle using the properties of the components by assuming some pattern of fiber arrangement within the matrix. However, the manufacturing process of composite materials will inevitably change the volume fraction, fiber arrangement, and fiber direction. Moreover, depending on the actual manufacturing process and the desired shape of the structure shown in Fig. 1, the material property can also be inhomogeneous and varying from locations to locations [3]. In this study our focus is on continuous-fiber-reinforced thermosetting-resin composites that are produced using an advanced manufacture process known as high-pressure resin transfer molding, which are used in mass production of composites. The flowchart of the high-pressure resin transfer molding is schematically shown in Fig. 1. The composite porous prepreg is placed into the mold cavity. The mold is then enclosed and hydraulic pressure is applied to compact the material to the design thickness and shape. Once the mold is enclosed, more resin and a hardener mixture are injected through high pressure into the cavity in the prepreg. The high throughput rate for the mixed resin flows allows the cavity to be filled quickly to significantly reduce the manufacturing time. The prepreg is then heated up and highly pressured, via controlled manner. In such a temperature- and pressure-controlled environment, the resin curing reaction occurs until completion, and finally the composite material product is demolded [28].

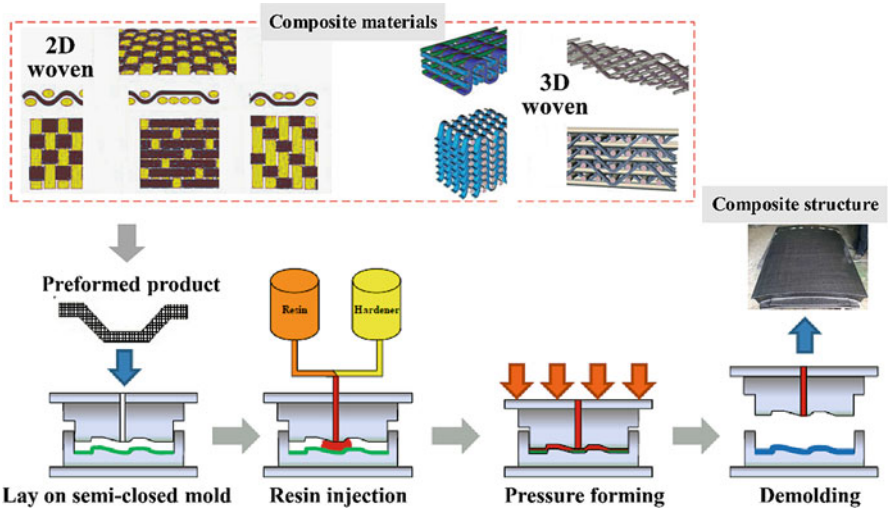

Fig. 1 Manufacturing processes to form composite materials into desired shapes

2.2 Strategy for Solving Inverse Problems

2.2.1 Measurement Strategy

A composite laminate produced using the above process is considered to demonstrate the process of identification of the material constants of each layers in the laminate, in a systematic way by performing an inverse analysis. For an effective inverse analysis, a best possible measurement strategy must be designed to set up the experiments [14]. This includes how to support the laminate, what type of loading (such as tension, compression, locations) should be applied, and what type of responses (such as displacement, strains, locations) should be measured.

2.2.2 Sensitivity Analysis

The measurement strategy mentioned above shall ensure that the parameters (material constants in our case) to be identified is sufficiently sensitive to the responses to be measured. This process is called sensitivity analysis, and critical to overcome the ill-posedness in the inverse analysis [14]. The sensitivity analysis can always be done using a predictive computer model (called forward model) created based on mechanics principle governing the behavior of the laminate. Once a forward model is created, a detailed sensitive analysis should be carried out, by perturbation techniques [29]. It shall evaluate the relative contribution of each individual parameters set to be inversely identified parameters to the structural response [30]. It computes and then ranks the contribution ratios for

each model parameter [31]. The insensitive parameters should next be removed, because it is unlikely to be identified accurately, using the current inverse analysis strategy. This would reduce the numbers of the model parameters to be identified. If these insensitive parameters must be identified, one has to change the inverse analysis strategy (such as boundary conditions, loading conditions and measurement variables and locations), so as to improve the sensitivity.

In actual inverse parameter identification, one shall use the actual measured response data. In this study, however, we use simulated measurement data for the training of TrumpetNets or TubeNets for inverse analyses: using FEM model to compute the responses and then add in proper levels of noises to mimic the measurement error. This allows us to focus our study on the methodology on network configuration and the features of the proposed TrumpetNets and TubeNets. Local sensitivity study will be conducted in this work, to ensure sufficient sensitivities in the obtaining dataset for training of the TrumpetNets or TubeNets. Parameters that are not sufficiently sensitive to the responses are removed, and only sensitive parameters are kept to be inversely identified. The final number of the neurons in the input layer for the TrumpetNets or TubeNets is finally determined.

2.2.3 Inverse Analysis Using Two-Way NN Models

The schematic flowchart is shown in Fig. 2. The procedure includes the following major steps.

1. Establish a two-way NN model architecture for both forward and inverse analyses (see Figs. 3 and 4).
2. Create a forward computer model using the FEM. The FEM model is then used to generate a training dataset for all parameters of material constants sampled form a predefined parameter space.
3. Train the forward NN model using the training dataset and the standard back-propagation algorithm, and then export and store the weights and biases of the trained forward NN when necessary.
4. Use the trained forward NN to generate a dataset for training the inverse NN. Or,
5. Using Direct-weight-inversion (DWI) method (see Sect. 3.2) to compute directly all the weights and biases for neurons in all layer in the inverse NN.
6. Once the inverse NN is trained and created, it is ready to produce the parameters (material constants), by feeding it with a set of structural responses.
7. Finally, one can assess the quality of the identified material constants, by feeding those into the forward NN (or the FEM model) to compute the structural response, and checking its discrepancy from the response data used in step 6.

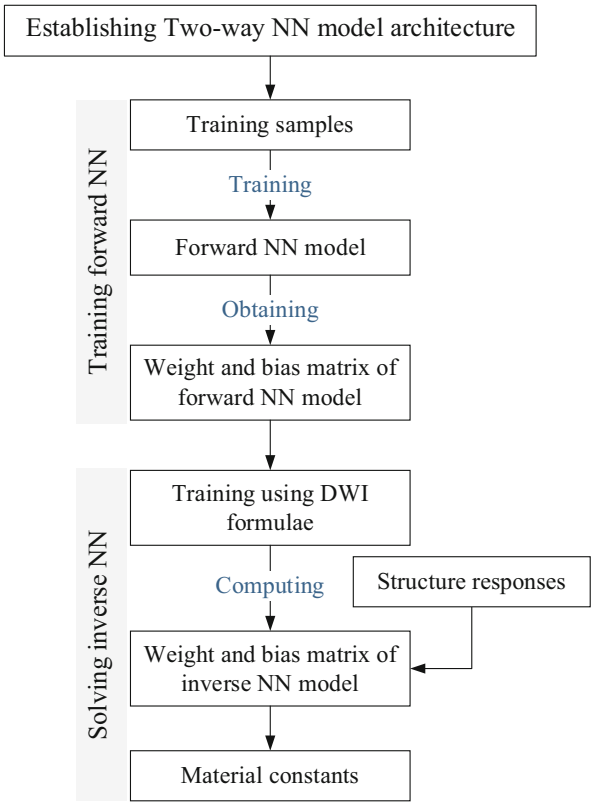

Fig. 2 Flowchart for inverse identification of material properties of composites using Two-way NN models

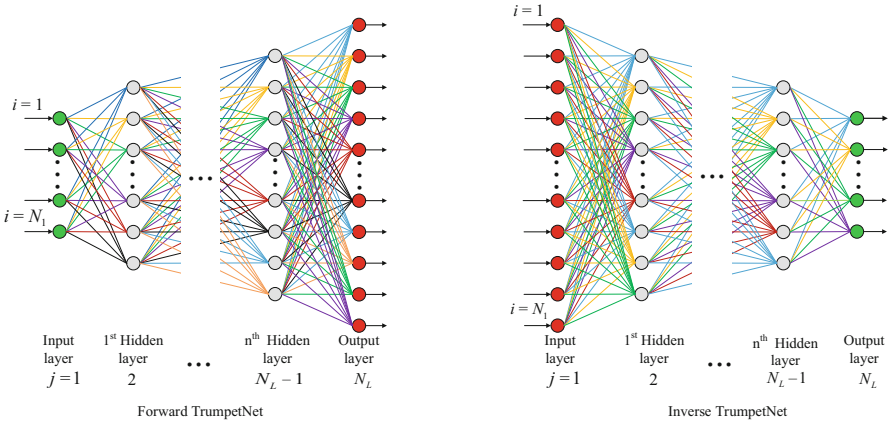

Fig. 3 Two-way TrumpetNets [24]

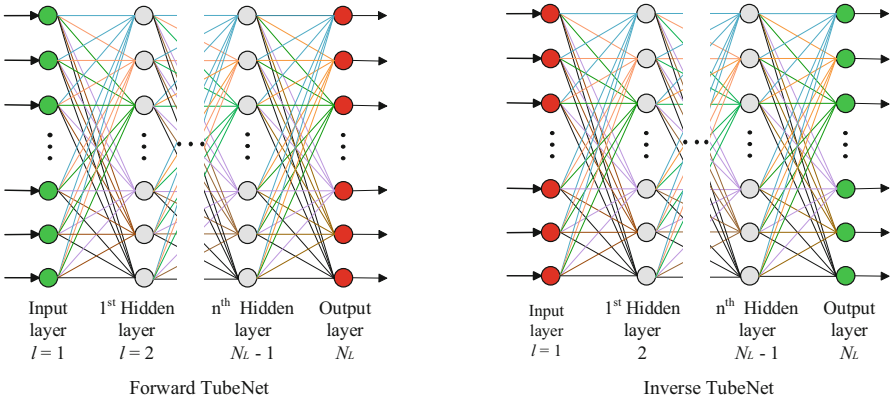

Fig. 4 Two-way TubeNets [25]

3 Two-Way TrumpetNets and TubeNets

In this study, two-way NN models of both the TrumpetNets and the TubeNets will be used. The configuration of the two-way TrumpetNets for forward and inverse problems is shown in Fig. 3 [24]. This special NN structure with trumpet shape is based on the over-posedness concept [14] that an inverse problem is usually posed with much more numbers of measurable responses compared to the numbers of parameters to be identified. This is usually necessary for parameters' intercorrelated nature of inverse problems.

The configuration of the TubeNets, a special form of TrumpetNets, is shown in Fig. 4 [25], in which the number of inputs, outputs, as well as the neuron number of the hidden layers are all the same. In this case, more measurable responses are still used, because of the requirements for solution existence in inverse problems. To reduce the number of measured responses to the same number of inputs, some dimensionality reduction methods, such as PCA technique, is used.

3.1 Setting Up Forward or Inverse Problem

As discussed earlier, an inverse problem cannot usually formulate explicitly. However, we know that it is always related to its corresponding forward problem. Inverse is simply reciprocal to forward. In this chapter, we assume the forward problem is governed by a set of given partial differential equations. Based on our definition, the forward problems can often be well posed, to which one can obtain stable solution, as long as a proper computational method can be used [32, 33]. A corresponding inverse problem usually cannot be posed well, and have some ill-posedness [14]. This is because the solution to a forward problem is obtained

essentially through an integration process, and hence it is smooth. The solution to an inverse problem, on the other hand, often can only obtained through a complicated implicit process that is essentially equivalent to a differential process to the given inputs [14].

This chapter considers inverse problems of structural mechanics. The forward problem is governed by the equilibrium equations with all the material parameters, loading, and boundary conditions given. Solving the forward problem is to find the responses (in terms of displacements and/or strains). Our inverse problem is to determine the material parameters using given (measured or simulated) responses [14]. A computer model, such as FEM model, is created for the structure, with a set of given or assumed material parameters. For the training of forward NN, a set of material parameters will be sampled from predefined parameter space (based on the existing knowledge on the problems). The sampling uses a standard orthogonal Latin hypercube sampling method that is often used for creating data point with proper coverage [34].

3.2 Direct-Weight-Inversion (DWI) Approach

3.2.1 DWI Formulae for TrumpetNets

This technique computes directly all the weights and biases for each and every layer in the inverse TrumpetNet using explicit formulae and the weights and biases of the already derived forward TrumpetNet. This is because the trained weights and biases of the forward TrumpetNet practically unearthed the "net" or "connections" between the variables in interest for the inverse problem. Training samples are thus no longer needed for the inverse TrumpetNet creation if the numerical inversion is successful. The formulations for the proposed TrumpetNet are briefed herein for quick reference.

For the trained forward TrumpetNet, it is supposed to have the weights and biases for all the layers of neurons. For the ith neuron in the lth layer, one shall have [24]

$$\overrightarrow{a}^{\,l}_{\,i} = \varphi\left(\overrightarrow{w}^{\,l}_{\,i1}\, a_1^{l-1} + \overrightarrow{w}^{\,l}_{\,i2}\, a_2^{l-1} + \cdots + \overrightarrow{w}^{\,l}_{\,iN_n^{l-1}}\, a_{N_n^{l-1}}^{l-1} + \overrightarrow{b}^{\,l}_{\,i}\right) \tag{1}$$

or

$$\overrightarrow{a}^{\,l}_{\,i} = \varphi\left(z_i^l\right) = \varphi\left(\underbrace{\sum_{j=1}^{N_n^{l-1}} \overrightarrow{w}^{\,l}_{\,ij}\, \overrightarrow{a}^{\,l-1}_{\,j} + \overrightarrow{b}^{\,l}_{\,i}}_{z_i^l}\right), i = 1, 2, \ldots, N_n^l;\ j = 1, 2, \ldots, N_n^{l-1} \tag{2}$$

where "$\rightarrow$" hat stands for the forward TubeNet; N_n^l denotes the number of neurons in the lth layer; $\overrightarrow{w}_{ij}^{l}$ specifies the weights of the ith neuron in the lth layer in connection with the jth neuron in the (l-1th) layer; and $\overrightarrow{b}_{i}^{l}$ represents the bias of the ith neuron in the lth layer; φ denotes the activation function for the ith neuron in the lth layer. Often than not the activation function is the same for neurons at the hidden layers, but it can also be different from neuron to neuron.

It is worth noting that the elements in w, b, z, and φ are all known by the end of the forward TrumpetNet training. Therefore, Eq. (2) can be rewritten as

$$\underbrace{\sum_{j=1}^{N_n^{l-1}} \overrightarrow{w}_{ij}^{l} \overrightarrow{a}_{j}^{l-1} + \overrightarrow{b}_{i}^{l}}_{z_i^l} = \varphi^{-1}\left(\overrightarrow{a}_{i}^{l}\right) \tag{3}$$

wherein φ^{-1} indicates the inverse activation function for the current neuron in the current layer. Equation (3) can be also rewritten in matrix form:

$$\left(\boldsymbol{\varphi}^{l}\right)^{-1} \overrightarrow{\boldsymbol{a}}^{l} = \overrightarrow{\boldsymbol{W}}^{l} \overrightarrow{\boldsymbol{a}}^{l-1} + \overrightarrow{\boldsymbol{b}}^{l} \tag{4}$$

where the vector $\boldsymbol{a}$ and $\boldsymbol{b}$ collect, respectively, all the values of the neurons in the layer.

The activation function matrix has the form of

$$\left(\boldsymbol{\varphi}^{l}\right)^{-1} = \begin{bmatrix} \varphi_{11}^{l} & \cdots & 0 \\ \vdots & \ddots & \vdots \\ 0 & \cdots & \varphi_{N_n^l N_n^l}^{l} \end{bmatrix}^{-1} \tag{5}$$

The weight matrix has the form of

$$\overrightarrow{\boldsymbol{W}}^{l} = \begin{bmatrix} \overrightarrow{w}_{11}^{l} & \overrightarrow{w}_{12}^{l} & \cdots & \overrightarrow{w}_{1N_n^{l-1}}^{l} \\ \overrightarrow{w}_{21}^{l} & \overrightarrow{w}_{22}^{l} & \cdots & \overrightarrow{w}_{2N_n^{l-1}}^{l} \\ \vdots & \cdots & \cdots & \vdots \\ \vdots & \cdots & \cdots & \vdots \\ \overrightarrow{w}_{N_n^l 1}^{l} & \overrightarrow{w}_{N_n^l 2}^{l} & \cdots & \overrightarrow{w}_{N_n^l N_n^{l-1}}^{l} \end{bmatrix} \tag{6}$$

which is in general a "slender" matrix for a TrumpetNet. The "flow" of the forward TrumpetNet is then inversed to create the inverse TrumpetNet as shown in Fig. 1. Solving Eq. (4) obtains

$$\overrightarrow{\boldsymbol{a}}^{l-1} \approx \left[\left(\overrightarrow{\boldsymbol{W}}^{l}\right)^{\mathrm{T}}\overrightarrow{\boldsymbol{W}}^{l} + \alpha^2 \boldsymbol{I}_{\alpha}\right]^{-1}\left(\overrightarrow{\boldsymbol{W}}^{l}\right)^{\mathrm{T}}\left\{\left(\boldsymbol{\varphi}^{l}\right)^{-1}\overrightarrow{\boldsymbol{a}}^{l} - \overrightarrow{\boldsymbol{b}}^{l}\right\} \tag{7}$$

where the standard regularized least square approach is applied; α^2 expresses the Tikhonov regularization parameter; $\boldsymbol{I}_{\alpha}$ stands for the corresponding identity matrix. The regularization parameter should be determined based on the level of noise in the measurements for outputs of measurable or the level of the added noise into the computed response. It is worth noting that the matrix $\left(\overrightarrow{\boldsymbol{W}}^{l}\right)^{\mathrm{T}}\overrightarrow{\boldsymbol{W}}^{l}$ in Eq. (7) has become a square matrix. Equation (7) can be rewritten as

$$\overrightarrow{\boldsymbol{a}}^{l-1} \approx \underbrace{\left[\left(\overrightarrow{\boldsymbol{W}}^{l}\right)^{\mathrm{T}}\overrightarrow{\boldsymbol{W}}^{l} + \alpha^2 \boldsymbol{I}_{\alpha}\right]^{-1}\left(\overrightarrow{\boldsymbol{W}}^{l}\right)^{\mathrm{T}}}_{\overleftarrow{\boldsymbol{W}}^{l}}\overrightarrow{\boldsymbol{a}}^{l}\left(\boldsymbol{\varphi}^{l}\right)^{-1} + \left\{\underbrace{-\overleftarrow{\boldsymbol{W}}^{l}\overrightarrow{\boldsymbol{b}}^{l}}_{\overleftarrow{\boldsymbol{b}}^{l}}\right\} \tag{8}$$

where the leftward arrow stands for inverse TrumpetNet.

When the Leaky ReLU activation function is used, there is

$$\varphi(z) = \text{Leaky Relu}(z) = \begin{cases} \lambda^{+} z \text{ when } z \geq 0 \\ \lambda^{-} z \text{ when } z < 0 \end{cases} \tag{9}$$

where λ^{+} and λ^{-} are given nonzero constants. In many cases, $\lambda^{+} = 1$, and $\lambda^{-} < 1$. Their values could be different for different neurons in different layers, but they should be nonzero, which is a prerequisite for TrumpetNets. The inverse of the Leaky ReLU function becomes

$$\varphi^{-1}\left(\overrightarrow{a}_{i}^{l}\right) = \begin{cases} \frac{1}{\lambda^{+}}\overrightarrow{a}_{i}^{l} \text{ when } z_i^{l} \geq 0 \\ \frac{1}{\lambda^{-}}\overrightarrow{a}_{i}^{l} \text{ when } z_i^{l} < 0 \end{cases} \tag{10}$$

It should be noted that the sign switch is determined by ${z_i}^{l}$ instead of $\overrightarrow{a}_{i}^{l}$. In the current study, we attempted to solve it by trial-and-error. Specifically, in the allowable value range of λ, different values of λ are used to train neural network before λ can be roughly determined according to the accuracy requirement of the neural network. The underlying principle is to derive a largest possible value for λ. Therefore, the condition number of the system can be small, while maintaining λ small enough for the required nonlinearity.

Tanh activation function can be expressed in general as follows,

$$\varphi(z) = y = \frac{\sinh(z)}{\cosh(z)} = \frac{\left(e^{z} - e^{-z}\right)}{\left(e^{z} + e^{-z}\right)} \tag{11}$$

Inversion of the tanh function has the form of

$$z = \varphi^{-1}(y) = \frac{1}{2}\log\left(\frac{y+1}{1-y}\right) \tag{12}$$

When the tanh activation function is used, at the lth layer, there is

$$\begin{aligned} \overrightarrow{a}_i^l &= \varphi\left(z_i^l\right) = \frac{\left(e^{z_i^l} - e^{-z_i^l}\right)}{\left(e^{z_i^l} + e^{-z_i^l}\right)} \\ z_i^l &= \varphi^{-1}\left(\overrightarrow{a}_i^l\right) = \frac{1}{2}\log\left(\frac{\overrightarrow{a}_i^l + 1}{1 - \overrightarrow{a}_i^l}\right) \end{aligned} \tag{13}$$

The values for all neurons at different layers in the inverse TrumpetNet can be calculated using the above equations and those weights and biases for the trained forward TrumpetNet. Because number of neurons in each layer of the current TrumpetNets is in an order of thousands at most in general, the computations in Eq. (8) span a time interval of seconds even on a notebook. On another positive note, because $\left(\overrightarrow{\boldsymbol{W}}^l\right)^{\mathrm{T}}\overrightarrow{\boldsymbol{W}}^l$ is a square matrix for the sensitivity conditions of inputs and outputs, it is expected to behave well and even symmetric positive definite. The regularization term $\alpha^2\boldsymbol{I}_\alpha$ offers an additive stability if needed, especially for noisy data. Therefore, the current DWI approach is expected to be efficient. Our inverse TrumpetNets is thus, in theory, capable of performing inverse analysis in real time if the inverse is successful and sufficiently accurate.

3.2.2 DWI Formulae for TubeNets

Because of the architecture of the TubeNet, as shown in Fig. 4, $\overrightarrow{\boldsymbol{W}}^l$ is a square matrix, which can be inverted directly without the use of the least-square formulation. Equation (7) thus becomes

$$\overrightarrow{\boldsymbol{a}}^{l-1} \approx \left[\overrightarrow{\boldsymbol{W}}^l + \alpha^2\boldsymbol{I}_\alpha\right]^{-1}\left\{\boldsymbol{\varphi}^{-l}\overrightarrow{\boldsymbol{a}}^l - \overrightarrow{\boldsymbol{b}}^l\right\} \tag{14}$$

where the standard regularization technique is also used. Equation (14) can be rewritten as

$$\overrightarrow{\boldsymbol{a}}^{l-1} \approx \underbrace{\left[\overrightarrow{\boldsymbol{W}}^l + \alpha^2\boldsymbol{I}_\alpha\right]^{-1}}_{\overleftarrow{\boldsymbol{W}}^l}\boldsymbol{\varphi}^{-l}\overrightarrow{\boldsymbol{a}}^l + \underbrace{\left\{-\overleftarrow{\boldsymbol{W}}^l\overrightarrow{\boldsymbol{b}}^l\right\}}_{\overleftarrow{\boldsymbol{b}}^l} \tag{15}$$

From this formulation, it is seen that the explicit computations of the weights and biases of the inverse TubeNet is even simpler than those for the TrumpetNet. It is worth noting that weight matrix $\overrightarrow{\boldsymbol{W}}^l$ is square, but not symmetric in general. Therefore, it may not necessarily be invertible. In our practice, however, it is found that $\overrightarrow{\boldsymbol{W}}^l$ is often well conditioned for many problems for successful inversion. It is believed to be attributed to adoption of PCA, which renders the training dataset orthogonal and the trained forward TubeNet to behave well. More rigorous proofs for the invertibility of the weight matrix of a TubeNet using PCA training dataset is, however, necessary. In this chapter, we simply pick the necessary number of principle components starting from largest as approximation and discard all the rest. It is understood that if too small number of components are adopted, the system may become ill-conditioned. More researches are expected to circumvent this kind of situations. We believe the best way is to change the inverse analysis strategy by increasing the sensitivity, so that more principal components can yield larger value.

Noting that in Eq. (15), the Tikhonov regularization with a positive regularization parameter α^2 is used. This ensures that Eq. (15) will always have a solution in theory because the regularized weight matrix is made positive definite invertible. However, in our study so far, we have not yet found a case to require nonzero α, and the weight matrix alone is already well behaved and invertible, at least for many of the problems we have studied, as discussed in detail in Sect. 4. The regularization term will be kept in Eq. (15) because the formulation is more theoretically rigorous. It is helpful for problems that are strongly ill-posed [14].

4 Identification of Material Parameters for Composites

An example is to identify the engineering elastic constants of a composite laminate made of anisotropic materials with many layers of different fiber orientations. Material constants include the elastic constants (as well as engineering constants) at macro scale and the fiber orientation of laminates. Examples are presented to evaluate both TrumpetNet and TubeNets using an idealized benchmark problem of a composite laminated plate. We aim to inversely identify the material elastic constants of the carbon and glass fiber reinforced plies from the displacement or strain responses on the surface of the laminate. Totally five cases are studied.

4.1 Setup of the Forward Problem

A rectangular composite laminated plate is considered, which are composed from twelve layers of hybrid fiber-reinforced materials, i.e., carbon and glass fiber reinforced plies, as shown in Fig. 5. It is symmetrically stacked in a sequence of $[C_{90}/G_{-45}/C_{+45}/G_0/C_{+45}/G_{-45}]_s$, where C stands for carbon fiber reinforced

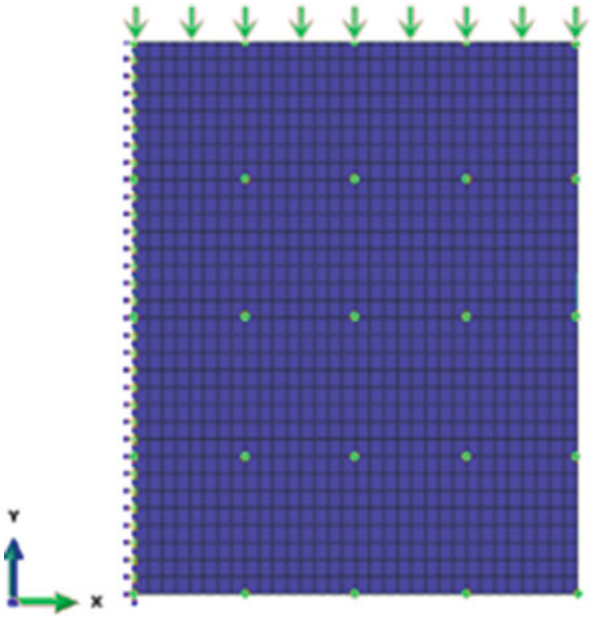

Fig. 5 Hybrid composite laminated plate subjected to load

Table 1 Material parameters of carbon fiber and glass fiber [14]

Material	E_1 (GPa)	E_2 (GPa)	μ	G_{12} (GPa)	G_{23} (GPa)
Carbon	142.20	9.26	0.33	4.80	12.43
Glass	38.48	9.38	0.29	3.14	12.44

ply, G represents glass fiber reinforced ply, and the number in the subscript of C or G denotes the lay-up angle. The length, width, and thickness of the laminate are 50 mm, 40 mm, and 2.4 mm, respectively. The nominal values of Young's modulus (E_1, E_2), Poisson's ratio (μ), and shear modulus (G_{12}, G_{23}) for the material parameters of carbon fiber and glass fiber are shown in Table 1.

The laminated plate is constrained on the left edge as shown in Fig. 5. It is subjected to vertical uniform pressure on the top edge. Firstly, a FEM model is created to compute the displacement responses for specified externally forces. A mesh sensitivity study is then conducted to eliminate mesh dependence of the solution to identify that the mesh with 1024 (32×32) elements is sufficiently fine for converged solutions as shown in Fig. 5. This mesh is used for production runs throughout the study in this chapter for generation of multiple sets of training samples for TrumpetNets and TubeNets. The computation is implemented for a set of parameters in the parameter space, which is determined based on the setting of the study case. The popular TensorFlow© is utilized to create all the neural networks throughout this study. The following settings are adopted in all the current case studies unless specified explicitly otherwise.

1. **TrumpetNets**: When training a TrumpetNet, totally 25 nodes marked with green dots in Fig. 5 are evenly selected from the 1024 (32×32) element mesh as the "measurement" points for structural displacement responses. No PCA is performed for all the TrumpetNet cases, meaning that the output layer of the TrumpetNet always has 25 neurons.
2. **TubeNets**: When training a TubeNet, all the 1089 (33×33) nodal displacements (see Fig. 5 as the "raw" measurement points for structural displacement responses) are selected as the training dataset. PCA is performed to reduce 1089 dimensions of the training dataset to a number that matches the neuron number in the layers of the corresponding TubeNet. This means that for a TubeNet with n neurons in a layer, we keep only n leading principal components to discard all the rest components.

4.2 Sensitivity Analysis

Before an inverse procedure is initiated, sensitivity analyses are carried out to investigate effects of the parameters in the input data on the output data. This is particularly important for an inverse problem to ensure the measurements are usable in the identification of parameters [35]. It is endowed by our experiences in processing inverse problems that good understanding for the corresponding forward problem is indispensable for conducting successful inverse mechanics problem. Sensitive analysis study is an effective method to establish such an understanding. The sensitivity study will thus be carried out using the forward computer model by varying the parameters in the input data in the relevant domain and computing the corresponding changes in the measurable displacements. When a displacement is found not sensitive to a parameter, the displacement will be removed from the input data. The inverse procedure is thus modified to improve effectiveness. Otherwise, when other parameters are found having strong effects on the displacements and if they are measurable, these displacements will be included in the input data.

The local sensitivity (S) of structure responses to the variety of material parameter is introduced as an index to evaluate the contribution of load condition to this correlation. Some proper steps should be followed in sensitivity analysis:

1. A simulation experiment is designed according to material mechanics and standards for material parameters testing. The appropriate structural responses, e.g., stress, displacement, or strain, are selected.
2. Making one material parameter vary around a fixed value (nominal parameter) with all the other parameters kept constant. Uniform samples of material parameters are then generated.
3. Using the samples obtained in the above step 2 and the FE solver to calculate the structural responses.
4. Calculate the sensitivity (S) using the following formulae.

Table 2 Sensitivity of strain to the material parameters

	Strain	Parameters				
		E_1	E_2	μ	G_{12}	G_{23}
Mean sensitivity for the 25 nodes	ε_{xx}	58.5	7.4	4	16.5	0.3
	ε_{xy}	25.9	13.5	4.7	23.8	0.5
	ε_{xy}	30.1	8.1	1.3	10.9	0.3

Table 3 Sensitivity of displacements to the material parameters

	Direction	Parameters				
		E_1	E_2	μ	G_{12}	G_{23}
Mean sensitivity for the 25 nodes	X	54.5	5.5	4.5	14.0	2.2
	Y	54.2	3.0	1.2	6.7	0
	Z	18	13.1	2.6	9.7	0.3

$$S = \frac{\Delta \mathrm{sr}}{\Delta \mathrm{mp}} \tag{16}$$

where Δsr denotes the gradient of the structural response; Δmp represents the gradient of the material parameters.

5. Repeat the above steps 2–4 to get the sensitivity of the structural response to each material parameter.

The abovementioned sensitivity analyses are carried out to investigate effects of the five parameters in Table 1 on the displacement or strain of the composite laminated plate. The results are shown in Tables 2 and 3. Table 2 shows the mean sensitivity of strain ε_{xx}, ε_{yy}, and ε_{xy} to the material parameters for the 25 test nodes in Fig. 5, respectively. Table 3 shows the mean sensitivity of displacements to the material parameters in x, y, and z directions for the 25 test nodes in Fig. 5. Comparing the mean sensitivity results of Tables 2 and 3, they all show that the order of sensitivity from the largest to the smallest is E_1, G_{12}, E_2, μ, and G_{23}. Only G_{23} are found not sensitive to the strain or displacement. The G_{23} needs measured through other means that uses measurements sensitive to G_{23}. Therefore, we concentrate on the inverse identification of material parameters (E_1, E_2, μ, G_{12}). From Table 2, the material parameters are more sensitive to ε_{xx} than that to ε_{yy} and ε_{xy}. Therefore, in the further study, the ε_{xx} will be selected as the structural response to each material parameter. As shown in Table 3, all the four material parameters are more sensitive to the displacement responses in x and z directions than that to the displacement responses in the y direction. While comparing with z direction displacement, the value of the displacement in x direction is tiny as shown in Fig. 6. Considering the measurement error in practical application, the z direction and y direction can be selected as the structural response.

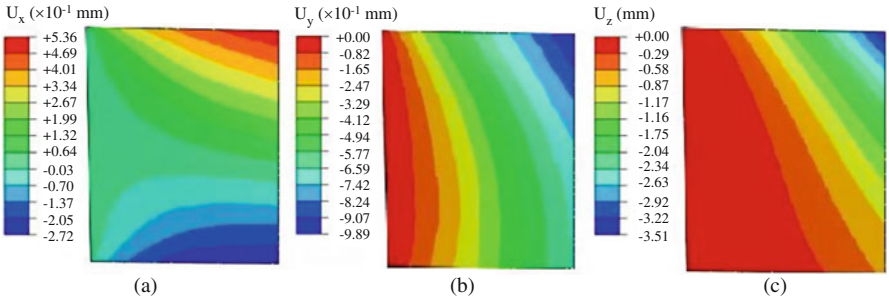

Fig. 6 Displacement distribution: (**a**) in x direction, (**b**) in y direction, and (**c**) in z direction

4.3 Case 1: Training Inverse TrumpetNet Using Datasets Generated by FEM Model

An inverse TrumpetNet is then directly trained using the sample points calculated by an FEM model as a trainer. This is a standard practice for solving inverse problems [14]. It also serves as a benchmark for other case studies. The difference in this study is that we will use a particular TrumpetNet that has a structure as shown in Fig. 1 with 25-15-4 neurons for input-hidden-output layers.

A set of forward problems is firstly solved: the displacements at the 25 nodes on the surface of the plate marked as green dots in Fig. 5 are computed for a set of different material elastic constants for the carbon fiber layers in the laminated plates. An inverse problem is then solved: inversely identify the E_1, E_2, μ, G_{12} for the carbon-fiber plies with assumptions that the material constants for the glass fiber plies and all the other parameters are given. The domain of the parameter space is confined in a hyper-polygon as follows:

$$E_1 \epsilon\, [127.98, 156.42]\ \text{GPa};\ E_2 \epsilon\, [8.334, 10.186]\ \text{GPa};$$

$$\mu \epsilon\, [0.297, 0.363]\ ;\ G_{12} \epsilon\, [4.32, 5.28]\ \text{GPa}.$$

The computed response is the displacement in y-direction for this case. Standard orthogonal Latin hypercube sampling method is used [34] to generate totally 2400 discrete sampling points in the four-dimensional parameter space. 2400 FEM models are created and run in batch on ABAQUS for all these 2400 cases, which give us a 2400 training samples. The inverse TrumpetNet using the ReLU activation function is then trained directly by these 2400 samples. The loss function value converges to 5×10^{-5} in 486 mins to complete the inverse TrumpetNet training. The trained inverse TrumpetNet is then tested using 100 test samples, which are generated independently also using the standard orthogonal Latin hypercube sampling method. The root-mean-square (RMS) of test errors for the four identified parameters are all lower than 1% as shown in Fig. 7. This proves the solvability of

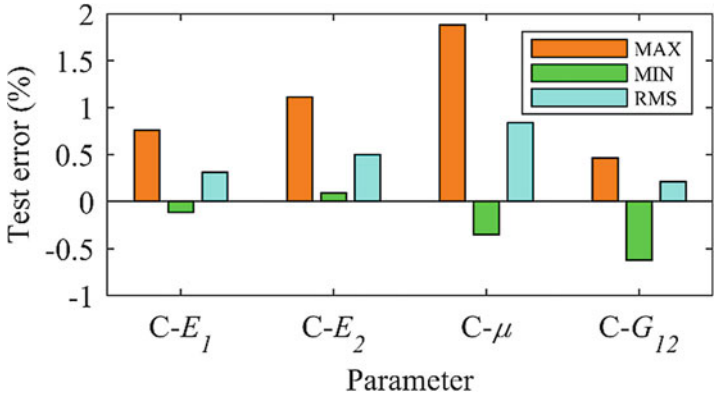

Fig. 7 Test errors of inverse TrumpetNet using the training dataset calculated by FEM model (Note: inverse TrumpetNet structure: 25-15-4; activation function: ReLU; training samples: 2400; test samples: 100; final loss: 5×10^{-5})

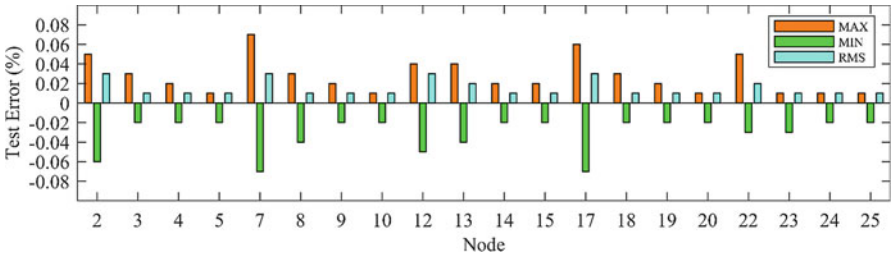

Fig. 8 Test errors of forward TrumpetNet with 4-15-25 neurons (Note: activation function: ReLU; training samples: 2400; test samples: 100; final loss: 6×10^{-5})

the inverse solution to this inverse problem using the standard approach: training the inverse TrumpetNet directly using physic-law-based models [24, 36–38].

4.4 Case 2: Training Inverse TrumpetNet Using Datasets Generated by the Trained Forward TrumpetNet

In this case study, a forward TrumpetNet is firstly trained using the 2400 training samples generated in Case 1. It has an input layer of 4 neurons, a hidden layer of 15 neurons, and an output layer of 25 neurons. The activation function is still ReLU. It takes only 50 min for the loss function to converge, which is much faster than the training of the inverse TrumpetNet directly using the FEM model as discussed in Case 1. The test errors of the forward TrumpetNet are summarized in Fig. 8.

The trained forward TrumpetNet is then adopted as a surrogate model to generate training samples for the inverse TrumpetNet. Its structure contains 25-15-4 neurons

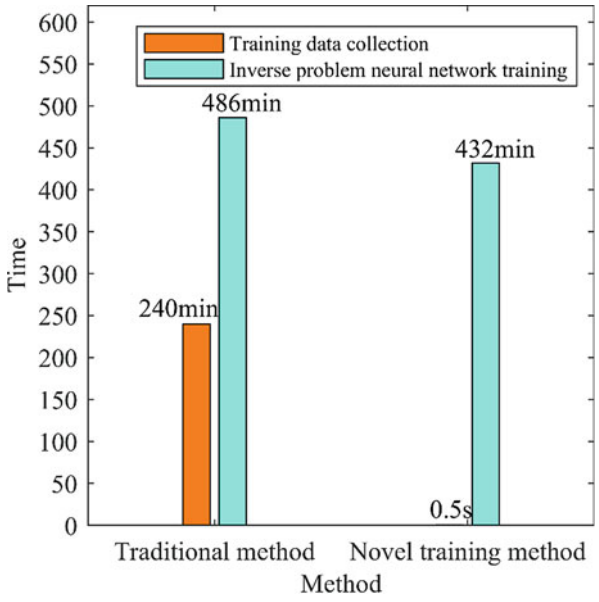

Fig. 9 Comparison of training efficiencies between traditional method and the novel method

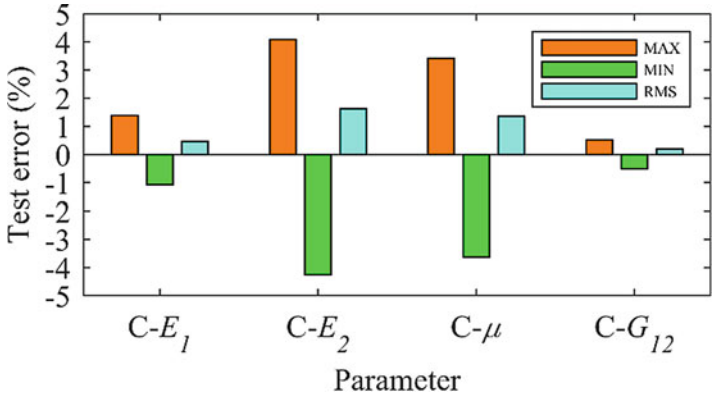

Fig. 10 Test errors of inverse TrumpetNet using the training dataset generated by forward TrumpetNet (Note: inverse TrumpetNet structure: 4-15-25; activation function: ReLU; training samples: 2400; test samples: 100; final loss: 6×10^{-5})

same as in Case 1. Another set of 2400 training sample are also generated in the four-dimensional parameter space. Because the forward TrumpetNet is used in this case, sample generation is very fast to take only 0.5 s as seen in Fig. 9. The training time for the inverse TrumpetNet, however, is 432 min, which is similar to that for Case 1. The test errors for the inverse TrumpetNet are shown in Fig. 10. The test errors of the inverse TrumpetNet trained using the training dataset calculated by the forward TrumpetNet is slightly higher than that trained directly using numerical computation samples.

The training efficiency of the novel training method is 40% higher than that of the traditional training method as shown in Fig. 9. Although roughly similar interval of time for training the inverse TrumpetNet is required, the preparation of the training samples become much faster. It should be emphasized that the total time for training both forward and inverse TrumpetNets is almost the same as that for the single inverse TrumpetNet. It is thus recommended to train both because two-way solver for real-time computations is derived simultaneously, without extra cost, for both forward and inverse problems as suggested by Liu [24].

4.5 Case 3: Inverse TrumpetNet Using DWI Approach Without Trained

Two types of TrumpetNet are constructed efficiently for both forward and inverse analyses. The first TrumpetNet is for forward analyses. It contains 4 neurons for the input layer, 15 neurons per layer for the 2 hidden layers, and 25 neurons for the output layer. The activation function in this case is Leaky ReLU. The forward TrumpetNet is trained until the error function (loss) is reduced to 1%. It takes about 250 s to complete the training on our PC. The trained forward TrumpetNet is then tested using 100 independent test samples. The maximum error for all the 100 test samples is 0.11% as shown in Fig. 11. The total time taken for running the 100 test-samples is 0.012 s, which is practically instant. This implies, for any specified set of material parameters within the trained domain, the computation with the trained forward TrumpetNet of the displacements at all the 25 nodes on the laminate surface can be registered as real-time computation. The training of the forward TrumpetNet is basically similar to that for Case 2 except for that the different activation functions and addition of one hidden layer. The reason for adding one hidden layer is to improve the accuracy of the solution.

The second TrumpetNet for inverse analyses contains 25 neurons for the input layer, 2 hidden layers with 15 neurons per layer, and 4 neurons for the output layer. In this Case 3, the DWI approach as formulated in Sect. 3.2 is used. The weight

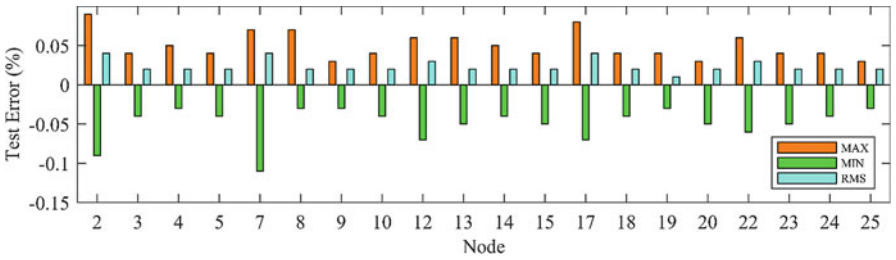

Fig. 11 Test errors for forward TrumpetNet with 4-15-15-25 neurons (Note: activation function: Leaky ReLU; training samples: 2400; test samples: 100; final loss: 5×10^{-5})

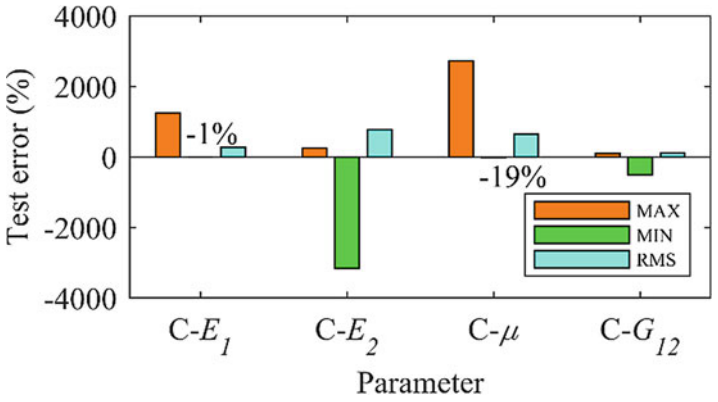

Fig. 12 Test errors of inverse TrumpetNet generated by DWI approach (Note: TrumpetNet structure: 25-15-15-4; activation function: Leaky ReLU; 100 test samples generated by FEM models)

Fig. 13 Condition number of matrix T^l in Eq. (7)

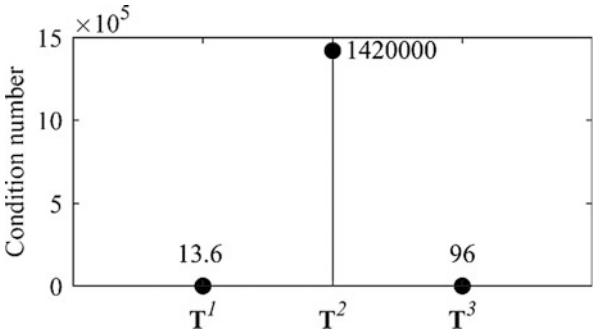

matrices and bias vectors of the inverse TrumpetNet are computed directly using the formulae and those weight matrices and bias vectors for the trained forward TrumpetNet. In this way, training of the inverse TrumpetNet is no longer necessary. The inverse TrumpetNet is also tested using 100 independent test samples created using the FEM models. The minimum RMS error from all these 100 test samples is 113% as shown in Fig. 12. This pronounced error indicator implies that the inverse TrumpetNet cannot be used to predict these 4 material constants of the carbon fiber layers for the laminated plate. The constructed inverse TrumpetNet is not valid though the total time taken for all the 100 test-samples is as short as 0.01 s.

The reason for the failure is then examined. It is found that the condition number of $\mathbf{T}^l$ in Eq. (7) is very large at the hidden layer (layer 2) as shown in Fig. 13. It suggests that $\mathbf{T}^l$ is ill-conditioned, indicating that the weight matrices of inverse TrumpetNet may not be reliable.

This may also be an indication of ill-posedness of the inverse problem. The regularization parameter α in a quite large range is thus used and further tests

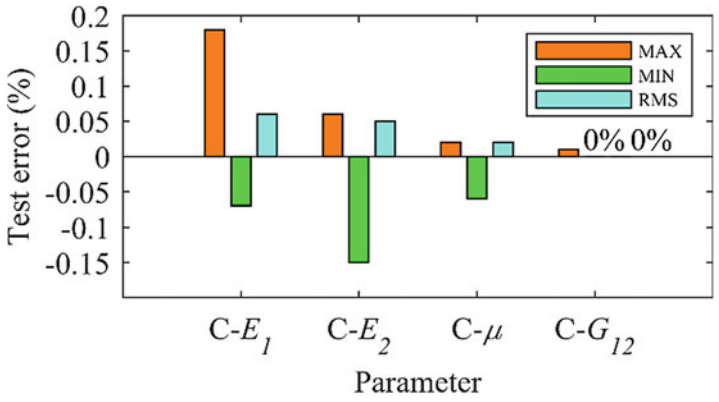

Fig. 14 Prediction errors for inverse TrumpetNet (Note: TrumpetNet structure: 25-15-15-4; activation function: Leaky ReLU; 100 test samples generated by forward TrumpetNet)

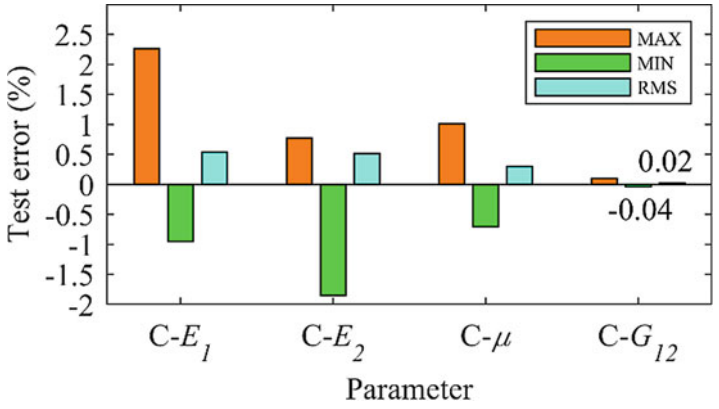

Fig. 15 Prediction errors for inverse TrumpetNet with 0.0001% noise (Note: TrumpetNet structure: 25-15-15-4; activation function: Leaky ReLU; 100 test samples generated by FEM model)

are conducted. However, the situation does not improve, suggesting that the regularization method is also not effective for our problem.

The forward TrumpetNet is then adopted to generate samples (in place of FEM model samples) for testing the inverse TrumpetNet. The test results are shown in Fig. 14. The maximum error is 0.18%. It can be stated that the inverse TrumpetNet well passes the tests. This proves that the DWI equations given in Sect. 3.2 are reliable. Note that the inverse TrumpetNet is always "overly-fitted" because of adoption of the analytical DWI approach.

To further explore the reasons, various levels of white noises to the test samples are generated by the forward TrumpetNet. The test results are listed in Figs. 15, 16,

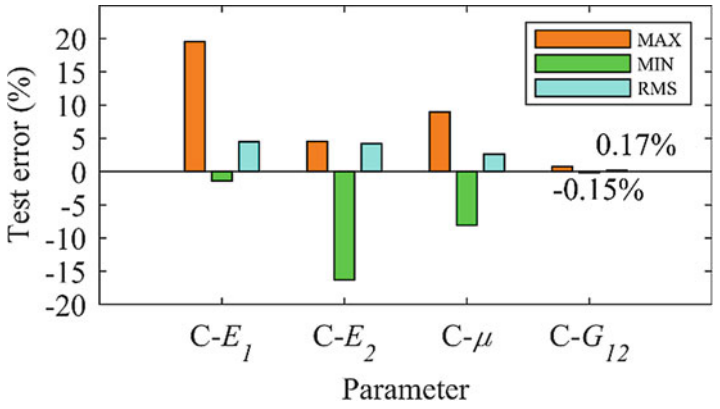

Fig. 16 Prediction errors for inverse TrumpetNet with 0.001% noise (Note: TrumpetNet structure: 25-15-15-4; activation function: Leaky ReLU; 100 test samples generated by FEM model)

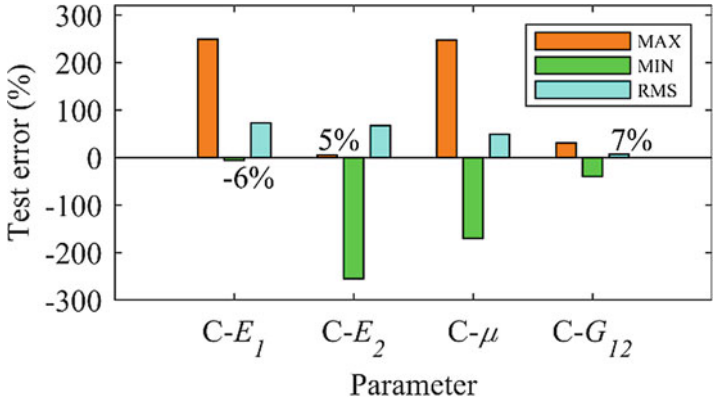

Fig. 17 Prediction errors for inverse TrumpetNet with 0.01% noise (Note: TrumpetNet structure: 25-15-15-4; activation function: Leaky ReLU; 100 test samples generated by FEM model)

and 17, respectively, for noise levels of 0.001%, 0.01%, and 0.1%. It is seen that the prediction errors increase significantly with the increasing noise level.

It can be said that the current inverse TrumpetNet is very sensitive to noise. More studies are needed to overcome this problem. For now, when TrumpetNets are used, the inverse TrumpetNet should be trained using datasets generated using the trained forward TrumpetNet. The alternative is to use TubeNet, which is discussed in the following section.

4.6 Inverse TubeNet Using DWI Approach

4.6.1 TubeNets with PCA-Treated Training Samples

The large test errors of the inverse TrumpetNet may be attributed to the least-square method in the matrix inversion process for DWI (Eq. 7), in which a 25 by 25 matrix is drastically reduced to a lower dimension matrix, such as 4 by 4 matrix or 8 by 8 matrix, in a simple averaging manner. To improve, a novel TubeNet concept is developed in this work to create a tubular network for training the forward network that has the same number of neurons for all (input, hidden, and output) layers. In these particular cases, they have 4-4-4-4 neurons and 8-8-8-8 neurons. To achieve this, the number of the outputs for the forward TubeNet should be reduced from 25 to 4 or 8 without compromising substantially the information in the displacement response data. PCA is then used for this purpose, which is a powerful method for dimension reduction by retaining only the major leading principal components. The following lists the steps for the procedure to construct the TubeNets.

1. Use the y-direction displacements of all the 1089 nodes on the plate surface as the raw output data for training the forward TubeNet.
2. Perform PCA analysis to generate principal components for all the 1089 nodal displacements for all the 2400 training samples.
3. Choose only four and eight major principal components as the final outputs to train the 4-4-4-4 and 8-8-8-8 forward TubeNet. All the weights and biases of the TubeNet after the training are then achieved.
4. Use these weights and biases of the trained forward TubeNet and DWI approach to compute directly the weights and biases for the inverse TubeNet using the Eqs. (14) and (15) given in Sect. 3.2.
5. Test the inverse TubeNet using samples independently generated using the FEM model and treated with PCA.

4.6.2 Case 4: Inverse TubeNet with 4-4-4-4 Neurons

A 4-4-4-4 inverse TubeNet following the same procedure given in Sect. 4.6.1 is then constructed. The number of parameters is now back to four: E_1, E_2, μ, G_{12} of the carbon fiber plies. In this case, the displacements in the y-direction at all the 1089 nodes on the plate surface are adopted to train the forward TubeNet. PCA is used to reduce the dimensionality from 1089 to four for all the 2400 samples generated using FEM model. The contribution rates for the first ten principal components of a typical training sample are computed as listed in Fig. 18. For the current case of 4-4-4-4 TubeNets, the first four principal components are selected as the output of the forward TubeNet. Figure 19 lists the values of the first four principal components for 10 (out of 2400) samples.

The activation function tanh is used in the training of the forward TubeNet. The time spent on the training is about 26 min. Figure 20 shows the test errors

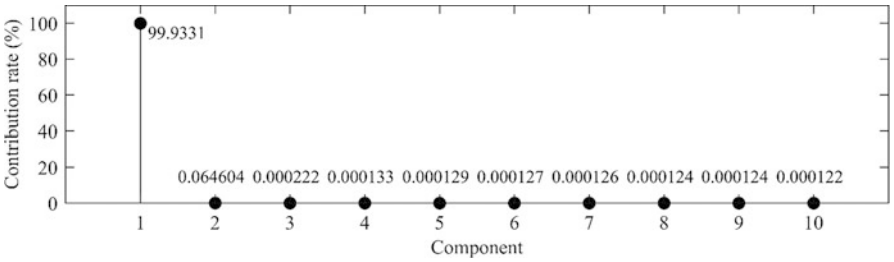

Fig. 18 Contribution rate of components

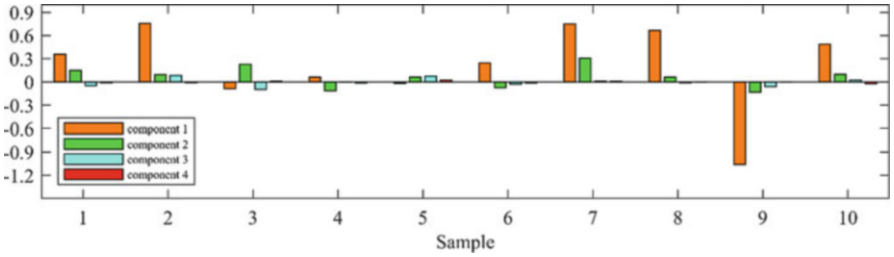

Fig. 19 Results of principal component analyses

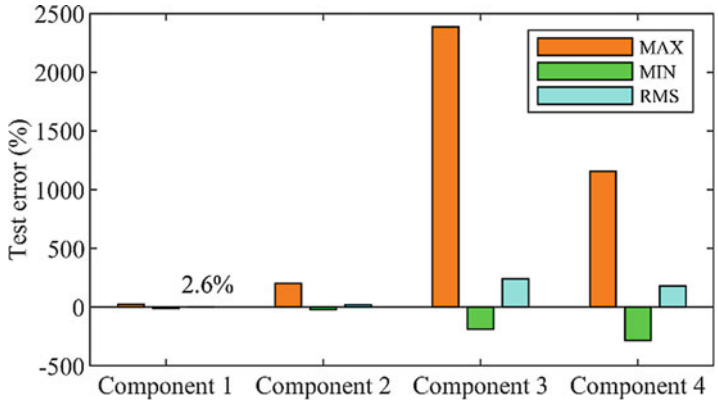

Fig. 20 Test errors of forward TubeNet trained by nodal displacements in y direction (Note: TubeNet structure: 4-4-4-4; activation function: tanh; training samples: 2400; test samples: 100; final loss: 1.4×10^{-4})

of the trained forward TubeNet when it is used to predict the first four principal components. It is seen again that the error is small for the first dominant principal component 1. Comparatively, errors for principal components 2, 3, and 4 are much higher, which is out of the concern because the objective of this study is to generate inverse TubeNet for inverse problems.

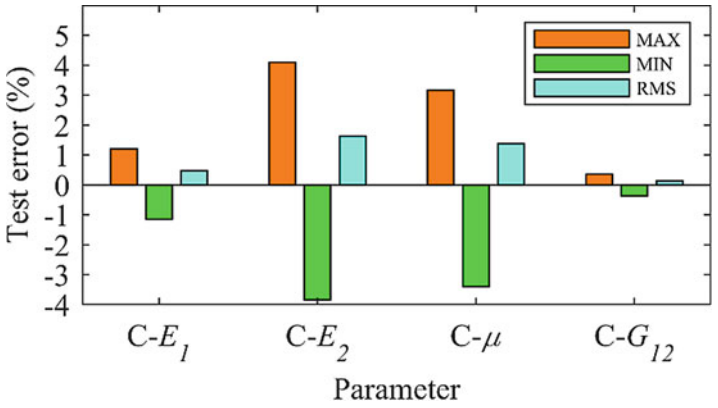

Fig. 21 Test errors of inverse TubeNet with input nodal displacements in y direction (Note: TubeNet structure: 4-4-4-4; activation function: tanh)

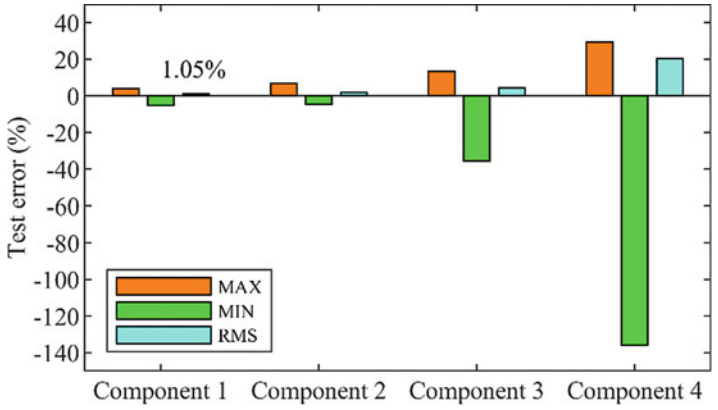

Fig. 22 Test errors of forward TubeNet trained by nodal displacements in both y and z directions (Note: TubeNet structure: 4-4-4-4; activation function: tanh)

Using the weights and biases of the trained forward TubeNet, an inverse TubeNet is generated using the DWI formulae. The inverse TubeNets are also tested using 100 test samples generated using FEM model and treated by PCA. Satisfactory accuracy of the inverse TubeNet is found as shown in Fig. 21.

Further studies using nodal displacements in both y and z directions, which leads to a totally $2 \times 1089 = 2178$ samples, are carried out to train the forward TubeNet before generating the inverse TubeNet using the DWI formulae. It is observed that the accuracy of the inverse TubeNet is further improved as shown in Fig. 22 and Fig. 23. With reference to the condition of the weight matrix of the neural network for the forward problem, it is expected to be well conditioned as shown in Fig. 24.

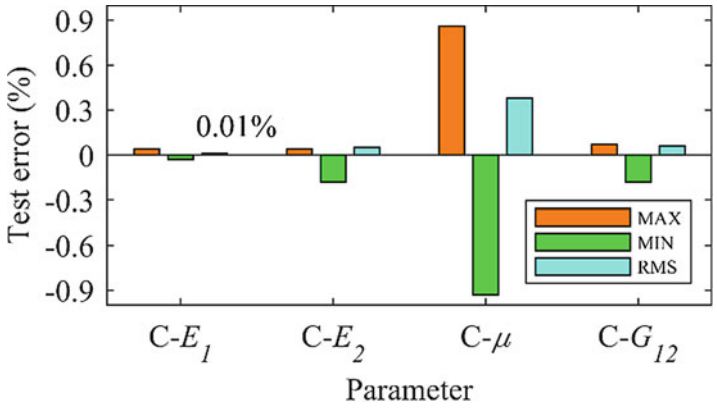

Fig. 23 Test errors of inverse TubeNet with input nodal displacements in y and z directions (Note: TubeNet structure: 4-4-4-4; activation function: tanh)

Fig. 24 Condition number of **W**

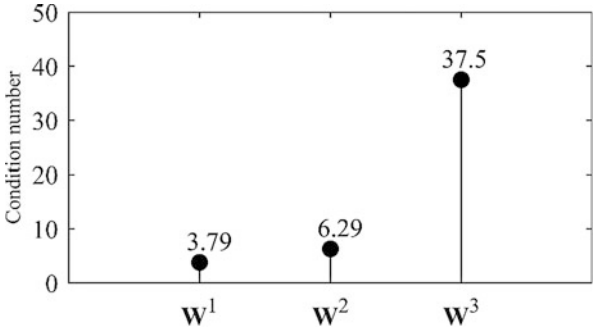

To investigate the influences of the large error of principal components 3 and 4 on the inverse TubeNet, 10% and 20% Gaussian noises are added to the components 3 and 4. The noise data are then input into the inverse TubeNet. The prediction errors are shown in Figs. 25 and 26. When the variance of Gaussian noises is 10%, the prediction results of the inverse TubeNet are barely affected. Even when the Gaussian noises become 20%, the prediction results of the inverse TubeNet still exhibit high accuracy. This is attributed to the low contribution rates of these two components. Thus, their noises have little effects on the accuracy of the inverse TubeNet.

It is worth mentioning that all the 1024 integration points in the mesh have been employed to create the TubeNets. Attempts with less number of nodal displacements, which are roughly distributed evenly on the surface of the plate, have also tried to create TubeNets. It is found that as long as the number is not too small, such as 25 nodal displacements, the creation procedure is feasible.

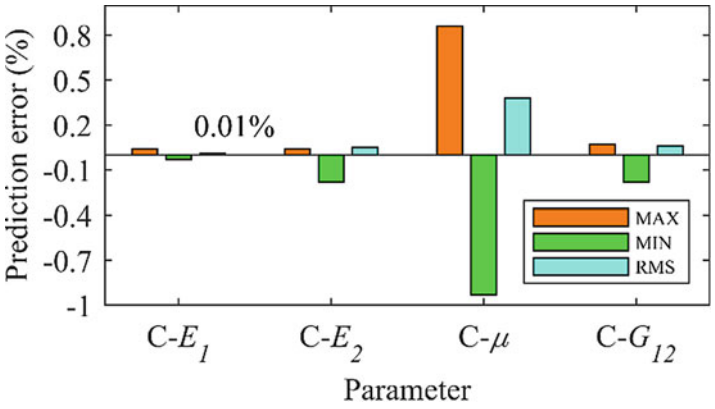

Fig. 25 Prediction errors of inverse TubeNet (10% Gaussian noise) (Note: TubeNet structure: 4-4-4-4; activation function: tanh)

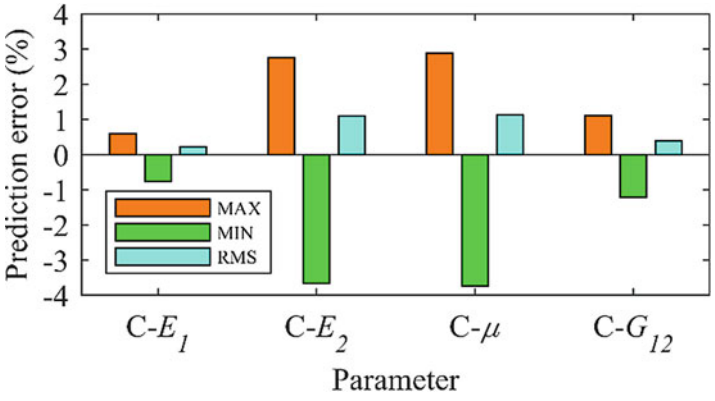

Fig. 26 Prediction errors for inverse TubeNet (20% Gaussian noise) (Note: TubeNet structure: 4-4-4-4; activation function: tanh)

4.6.3 Case 5: Inverse TubeNet with 8-8-8-8 Neurons

A 8-8-8-8 inverse TubeNet is also created following the same procedure given in Sect. 4.6.1. In this case, the number of parameters becomes eight: E_1, E_2, μ, and G_{12}, respectively, for the carbon-fiber plies and the glass-fiber plies. The parameter space now becomes eight-dimensional, which is intractable inverse problem for the standard inverse methods [11]. Herein, the nodal displacements in y-direction computed using FEM model and treated with PCA are adopted as the training samples.

An 8-8-8-8 forward TubeNet is trained using tanh activation function. Because of the high-dimensional parameter space, the samples in training dataset are increased to 12,000 to achieve reliable training results. After 23 h (1380 min) training, the loss

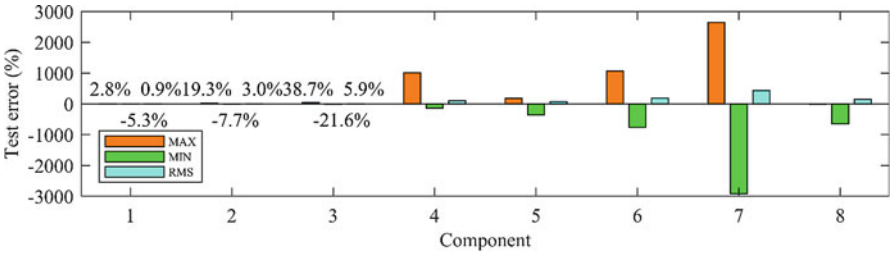

Fig. 27 Test errors of forward TubeNet trained by nodal displacement in y direction (Note: TubeNet structure: 8-8-8-8; activation function: tanh; training samples: 12,000; test samples: 100; final loss: 1.4×10^{-4})

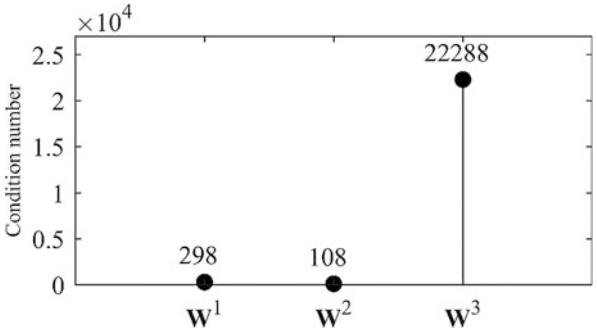

Fig. 28 Condition number of **W** of the TubeNet structure 8-8-8-8 (Note: composite structural response: nodal displacement in y direction)

function of the forward TubeNet converges to a satisfactory value of 1.4×10^{-4}. A set of 100 test samples are used to evaluate the forward TubeNet. The evaluation results are shown in Fig. 27.

The weight matrixes and bias vectors of the inverse TubeNet are subsequently computed using the DWI formulae. The inverse TubeNet is tested using 100 test samples, and complex numbers are found in the output of the inverse TubeNet. It indicates that the result is wrong and the inverse procedure fails. The condition of the weight matrix of the neural network for the forward problem is then examined, it is also found not well conditioned as shown in Fig. 28. When the number of training samples is increased, the loss value of the forward TubeNet does not drop, suggesting ineffectively low sensitivity to the displacement data.

Because strain is the derivative of displacement, the strain value may be sensitive to the changes of the parameters to be inversely identified. Thus, the strains at the Gauss points of the elements of our FEM model are tentatively adopted as the output responses of the forward problem. The forward TubeNet is then retrained. The preceding eight parameters remain the target parameters to be inversed. The strain component ε_{11} is used as the output responses of the forward problem. S4R elements are adopted in the FEM model with the default setting in ABAQUS (one Gauss point per element). There are totally 1024 integration points in the model. PCA is conducted for all the training samples. The structure of the forward TubeNet

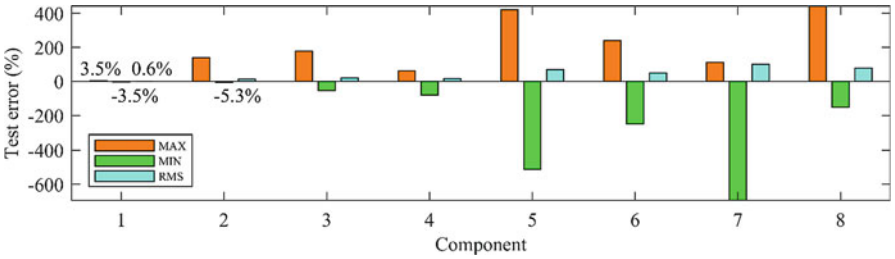

Fig. 29 Test errors of forward TubeNet trained by strain at the Gauss points (Note: TubeNet structure: 8-8-8-8; activation function: tanh; training samples: 48,000; test samples: 100; final loss: 5.2×10^{-5})

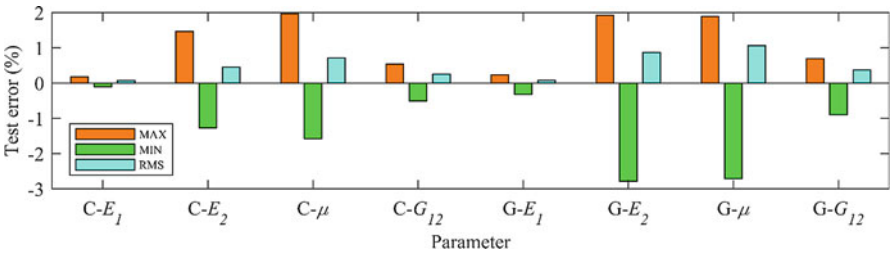

Fig. 30 Test errors for analytically derived inverse TubeNet (Note: TubeNet structure: 8-8-8-8; activation function: tanh; test samples: 100)

is 8-8-8-8; the activation functions used in the hidden layer is tanh. Due to the high dimension of the parameter space, training samples are now increased to 48,000 to avail reliable training results. After about 24 h training in our PC, the loss function of the forward TubeNet converges to a satisfactory level of 5.2×10^{-5}. A set of 100 independent test samples are used to evaluate the trained forward TubeNet, and the evaluation results are shown in Fig. 29.

Using the weight matrixes and bias vectors for the trained forward TubeNet, the weight matrixes and bias vectors for the inverse TubeNet are computed. The inverse TubeNet is also tested using 100 test samples, and the maximum RMS of test errors for all the 100 test samples is 1.06% as shown in Fig. 30. The condition of the weight matrix of the neural network for the forward problem is then checked to be well conditioned as shown in Fig. 31. It can be stated that an accurate 8-8-8-8 inverse TubeNet for inverse analyses of composite laminated plates has been successfully derived to identify eight parameters using the strain (ε_{11}) values at the Gaussian integral points.

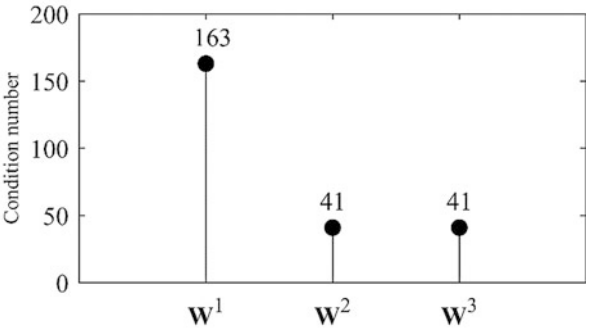

Fig. 31 Condition number of **W** of the TubeNet structure 8-8-8-8 (Note: composite structural response: strain at the Gauss points)

5 Conclusions

This chapter introduces two artificial neural networks: TrumpetNets and TubeNets. They have special configurations designed for both forward and inverse analyses. From problems of mechanics, both NNs are trained using FE models. Once properly trained, the TrumpetNets can be used for real-time analyses of both forward and inverse problems. The TubeNets is particularly effective for real-time analysis of inverse problems because of the use of explicit DWI technique developed by the authors. The idea of TrumpetNets and TubeNets serves as promising effective approach to process inverse problems. More intensive work is needed on the trainability and applicability of these types of NNs. More effective techniques on overcoming the possible ill-posedness are also needed to make the TrumpetNets and TubeNets more effective for noisy datasets.

References

1. Duan, S. Y., Han, X., & Liu, G. R. (2019). Structural optimization and reliability analysis of automotive composite bumper against low-velocity longitudinal and corner pendulum impacts. *International Journal of Computational Methods, 16*(08), 1841003.
2. Afshan, S., Zhao, O., & Gardner, L. (2019). Standardised material properties for numerical parametric studies of stainless steel structures and buckling curves for tubular columns. *Journal of Constructional Steel Research, 152*, 2–11.
3. Duan, S. Y., Yang, X. J., Tao, Y. R., Hu, Z. P., & Chen, Y. B. (2014). Hybrid reliability analysis for energy-absorbing composite structures based on evidence theory. *Journal of Reinforced Plastics and Composites, 33*(22), 2095–2105.
4. Liu, G. R., Ma, W. B., & Han, X. (2002). An inverse procedure for determination of material constants of composite laminates using elastic waves. *Computer Methods in Applied Mechanics and Engineering, 191*(33), 3543–3554.
5. Cugnoni, J., Gmür, T., & Schorderet, A. (2007). Inverse method based on modal analysis for characterizing the constitutive properties of thick composite plates. *Computers & Structures, 85*(17–18), 1310–1320.
6. Liu, G. R., & Chen, S. C. (2002). A novel technique for inverse identification of distributed stiffness factor in structures. *Journal of Sound and Vibration, 254*(5), 823–835.

7. Prou, J., Kishimoto, K., & Constantinescu, A. (2010). Identification of Young's modulus from indentation testing and inverse analysis. *Journal of Solid Mechanics and Materials Engineering, 4*(6), 781–795.
8. Ralsinghani, S. C., & Goel, A. K. (1985). Aircraft parameter identification by the Gauss-Newton method in the frequency domain. *International Journal of Systems Science, 16*(5), 509–523.
9. Klinge, S. (2012). Parameter identification for two-phase nonlinear composites. *Computers & Structures, 108*, 118–124.
10. Takatsu, T., Ohsumi, A., & Nakagawa, A. (2002). Parameter identification for a class of stochastic systems with unknown parameters via modified Gauss-Newton method. *TISCI, 15*(7), 359–367.
11. Artyukhin, E. A., & Rumyantsev, S. V. (1980). Optimal choice of descent steps in gradient methods of solution of inverse heat-conduction problems. *Journal of Engineering Physics, 39*(2), 865–869.
12. Jiping, S. (2011). Study on identified method of coal and rock interface based on image identification. *Coal Science and Technology, 39*(2), 77–79.
13. Han, X., Liu, G. R., & Li, G. Y. (2004). Computational inverse techniques: Theory, numerical analysis and application. *Computational Mechanics, Proceedings*, 363368.
14. Liu, G. R., & Han, X. (2003). *Computational inverse techniques in nondestructive evaluation*. Boca Raton: CRC Press.
15. Landweber, L. (1951). An iteration formula for Fredholm integral equations of the first kind. *American Journal of Mathematics, 73*(3), 615–624.
16. Han, X., & Liu, J. (2017). *Numerical simulation-based design*. Springer Verlag, Singapore.
17. Huber, N., & Tsakmakis, C. (1999). Determination of constitutive properties from spherical indentation data using neural networks. Part I: The case of pure kinematic hardening in plasticity laws. *Journal of the Mechanics and Physics of Solids, 47*(7), 1569–1588.
18. Sribar, R. (1994). *Solutions of inverse problems in elastic wave propagation with artificial neural networks* (Doctoral dissertation, Cornell University).
19. Chandrashekhara, K., Okafor, A. C., & Jiang, Y. P. (1998). Estimation of contact force on composite plates using impact-induced strain and neural networks. *Composites Part B: Engineering, 29*(4), 363–370.
20. Mase, H., & Kitano, T. (1999). Prediction model for occurrence of impact wave force. *Ocean Engineering, 26*(10), 949–961.
21. Sumpter, B. G., & Noid, D. W. (1996). On the design, analysis, and characterization of materials using computational neural networks. *Annual Review of Materials Science, 26*(1), 223–277.
22. Mahmoud, M. A., & Kiefa, M. A. A. (1999). Neural network solution of the inverse vibration problem. *NDT and E International, 32*(2), 91–99.
23. Liu, S. W., Huang, J. H., Sung, J. C., & Lee, C. C. (2002). Detection of cracks using neural networks and computational mechanics. *Computer Methods in Applied Mechanics and Engineering, 191*(25–26), 2831–2845.
24. Liu, G. R. (2019). FEA-AI and AI-AI: Two-way deepnets for real-time computations for both forward and inverse mechanics problems. *International Journal of Computational Methods, 16*(08), 1950045.
25. Liu, G. R., Duan, S. Y., Zhang, Z. M., & Han, X. (2021). TubeNet: A special TrumpetNet for explicit solutions to inverse problems. *International Journal of Computational Methods, 18*(01), 2050030.
26. Fairbairn, E. M. R., Ebecken, N. F. F., Paz, C. N. M., & Ulm, F. J. (2000). Determination of probabilistic parameters of concrete: Solving the inverse problem by using artificial neural networks. *Computers & Structures, 78*(1-3), 497–503.
27. Liu, G. R. (1997). A step-by-step method of rule-of-mixture of fiber-and particle-reinforced composite materials. *Composite Structures, 40*(3-4), 313–322.

28. Graf, M., Fries, E., Renkl, J., Henning, F., Chaudhari, R., & Thoma, B. (2010). High-pressure resin transfer molding-process advancements. *10th Annual Automotive Composites Conference and Exhibition*, 619–657.
29. Keller, J. B. (1976). Inverse problems. *The American Mathematical Monthly, 83*(2), 107–118.
30. Castillo, E., Conejo, A. J., Mínguez, R., & Castillo, C. (2006). A closed formula for local sensitivity analysis in mathematical programming. *Engineering Optimization, 38*(1), 93–112.
31. Liu, J., Liu, Q., Han, X., Jiang, C., & Tao, Y. (2019). A new global sensitivity measure based on derivative-integral and variance decomposition and its application in structural crashworthiness. *Structural and Multidisciplinary Optimization, 60*(6), 2249–2264.
32. Liu, G. R., & Quek, S. S. (2013). *The finite element method: A practical course*. Oxford: Butterworth-Heinemann.
33. Liu, G. R. (2009). *Meshfree methods: Moving beyond the finite element method*. Milton Park: Taylor & Francis.
34. Olsson, A., Sandberg, G., & Dahlblom, O. (2003). On Latin hypercube sampling for structural reliability analysis. *Structural Safety, 25*(1), 47–68.
35. Saltelli, A., Tarantola, S., Campolongo, F., & Ratto, M. (2004). *Sensitivity Analysis in Practice: A Guide to Assessing Scientific Models*. John Wiley & Sons, New York.
36. Liu, P., Han, X., Hu, D., & Jiang, C. (2016). Sensitivity and uncertainty analysis of SHPB tests for concrete materials. *International Journal of Applied Mechanics, 8*(08), 1650088.
37. Liu, G. R., Han, X., Xu, Y. G., & Lam, K. Y. (2001). Material characterization of functionally graded material by means of elastic waves and a progressive-learning neural network. *Composites Science and Technology, 61*(10), 1401–1411.
38. Liu, G. R., Lam, K. Y., & Han, X. (2002). Determination of elastic constants of anisotropic laminated plates using elastic waves and a progressive neural network. *Journal of Sound and Vibration, 252*(2), 239–259.

Machine Learning Interatomic Force Fields for Carbon Allotropic Materials

Xiangjun Liu, Quanjie Wang, and Jie Zhang

1 Introduction

Carbon is capable of forming many allotropes due to its valency. The well-known forms of carbon include diamond and graphene. In the past decades, many more allotropes have been further discovered and researched, such as carbon nanotube, nanotubes, and buckminsterfullerene. At the present time, around 500 hypothetical 3-periodic carbon allotropes are known; each of them exhibits significantly different properties and wide potentials of applications. Recently, due to the enhancement of high performance computing (HPC) power, and algorithmic improvements, computational materials science has gradually become an important supplement to traditional theory and experiment for the study of carbon allotropes, as well as a crucial bridge between micro and macro, theory and experiment [1–3]. On one hand, it can help us to understanding the microstructure and behavior of carbon materials in atomic level, and on the other hand, it can predict the properties and formation mechanism of carbon materials without doing experiments.

2 Traditional Force Fields

Molecular dynamic (MD) simulation is most widely used for studying atomistic systems, which can monitor the atomic-level time-evolution of physical and chemical processes and predict macroscopic properties from microscopic details. Starting with an initial atomic locations and velocities, MD simulations require the atomic

X. Liu (✉) · Q. Wang · J. Zhang
School of Mechanical Engineering, Donghua University, Shanghai, China
e-mail: xjliu@dhu.edu.cn; mezhangjie@dhu.edu.cn

Y. Cheng et al. (eds.), *Artificial Intelligence for Materials Science*, Springer Series in Materials Science 312, https://doi.org/10.1007/978-3-030-68310-8_4

forces as input to propagate the atoms locations and their velocities to the next timestep (at which point, the atomic forces are reevaluated), the cycle continues, thus allowing for an iterative time-evolution of the system. The atomic forces at each timestep may be obtained either using quantum mechanics (QM) based methods, such as density functional theory (DFT), or parameterized classical semiempirical analytical interatomic force fields, such as Stillinger-Weber potentials, Tersoff potential, and so forth [4–6]. Choosing between the two approaches depends on which side of the cost-accuracy trade-off ones wishes to be at. QM methods (also referred to as ab initio or first-principles methods) are versatile and offer the capability to accurately model a range of chemistries and chemical environments by solving for the Schrodinger equation. However, the computational complexity of QM methods is at least cubic in the number of electrons; consequently, practical applications of these methods at present are limited to studies of phenomena whose typical length and time scales are of the order of nanometers and picoseconds, respectively [1]. Parameterized classical force fields can be used to access truly large-length and long-time scales, which typically are 6–10 orders of magnitude faster than DFT, because the influence of electrons is not taken into account in the calculation of atomic force [7]. However, these approaches are also problematic, as such force fields cannot precisely reproduce QM forces and have limited transferability; for instance, they are not transferable to situations that were not originally used in the parameterization [8–10]. Facing this scenario, it is necessary to develop novel and efficient force field. The advent of big-data analytics and easy to access to HPC resources has brought powerful machine learning (ML) techniques to the forefront. Meanwhile, ML methods hold promise in resolving the disconnect between force field developers and the end-users, which is common in classical potential function development, in other words, empowering the users to develop new or tailor existing force fields to meet their needs [11].

3 Machine Learning Force Field

Since US President Barack Obama proposed the genome project in 2010, the application cases of ML in material development have been emerging. For example, rapid search for high thermal conductivity materials [12], design of low interface thermal resistance superlattice structure [13], utilizing neural network assisted drug development [14], screening of high-throughput materials [15], prediction of material structure [16], design of ultra-high hard materials [17], and so forth.

ML mainly uses a trained model (such as neural network algorithm, Bayesian optimization algorithm, and random forest) to extracting information from large historical datasets (from experiments, simulations, online database, etc.), and then accurately capture the relationship between structures and properties by data mining techniques for materials discovery and properties prediction [4]. Recently, a data-driven and ML-based atomic force field development research has attracted wide concern due to its flexibility and adaptability. In contrast to conventional interatomic

potentials and QM-based methods, the ML-based paradigm has been verified by many groups is a feasible pathway in the creation of interatomic force field that both has the accuracy and versatility of QM methods and the low computing cost of parameterized semiempirical interatomic potentials. The ML-based force field was first proposed independently by Botu [5] and Li [18]; they used vector structural descriptors as fingerprints of atomic environments, and separately learned individual force components using kernel regression and Gaussian process regression. Recently, Glielmo et al. [4] proposed a novel scheme, which predicts the forces as vector quantities using Gaussian process regression. Additionally, they added the many-body kernel to represent the dependence of force not only on interatomic distance but also bone angle. Because many more force components as a training dataset can be obtained from DFT calculation directly, the construction of the ML force field is easier than that of ML potentials. ML force field has been successfully constructed for many elemental materials, such as Al [4, 5, 19, 20], Si [21], and Cu [12], and a few multicomponent materials, such as SiO_2 [22]. Moreover, the feasibility of ML force field has been verified by several static and dynamic applications, including melting, stress-strain behavior, point defect diffusion in bulk, proper description of dislocation core regions, metal phase transition and adatom organization as surface, and so forth [4, 22].

Traditionally, the parameters in classical semiempirical interatomic potential are obtained by fitting to QM calculations or experimental data under equilibrium state, as the red dotted line region shown in Fig. 1a, therefore, overemphasis on equilibrium configurations often result in performs poorly in predicting the relative energies in transition state or far-from-equilibrium position. However, ML-based force field can overcome this issue by learning from reference datasets in the whole potential energy space, as shown in Fig. 1b.

The application of ML in molecular force field development largely falls into two broad categories: one approach is based on classical semiempirical analytical interatomic potentials, employing ML algorithms to optimize the potential parameters, namely, ML-based optimized force field. The other approach is to establish nonlinear mapping by ML models between atomic configurations and potential energies or force, which has no fixed mathematical functional form, namely,

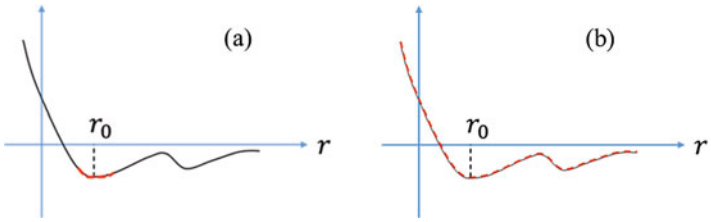

Fig. 1 The data obtained used for constructing atomic force fields: (**a**) classical semiempirical force field, (**b**) ML-based force field

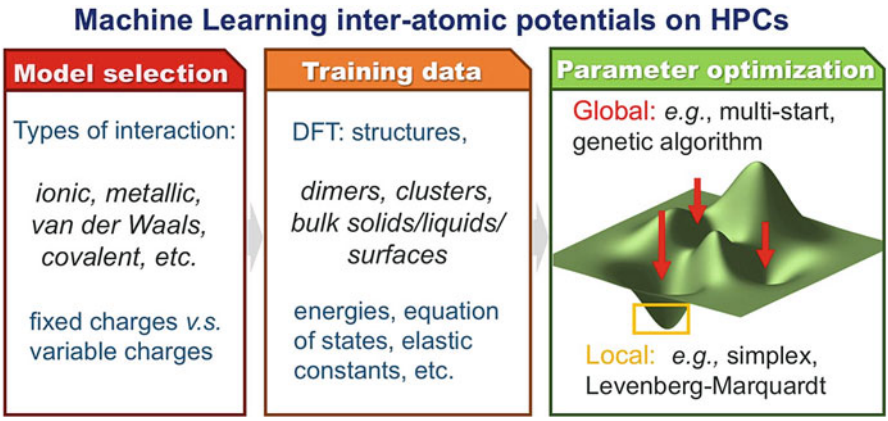

Fig. 2 An overview of ML-based potential function parameters optimization framework. (Adapted with permission from ref. [7], copyright 2019 Physical Chemistry publishing)

ML-based force field. The train datasets of these two approaches are both obtained from DFT calculation, which can ensure the accuracy of prediction [23–27].

Chan et al. [7] proposed a ML-based optimized force field to accurately simulate the dynamical process at reactive interfaces and low dimensional system, such as clusters and molecules. The procedure as shown in Fig. 2, which involves (1) defining or selecting a functional form, the functional from selection apart from the material being studied but also strongly dependent on the phenomenon being explored, (2) constructing an extensive training data set from electronic structure calculations, and the training as far as possible to encompassing all possible atomic environments and coordinates likely to be encountered in dynamic simulations, (3) optimizing force-field parameters using ML algorithms, such as genetic algorithms (GA), formulating a fitting procedure and implementing these algorithms on HPCs.

For ML-based force field, the force field is transferable and adaptive due to overcoming the limitations result from the predefined mathematical functional form. For instance, new reference configurations can be added to enhance the versatility of the force field as required [28–31]. A typical ML-based force field development workflow mainly consists of four key steps, which are: (1) generation of reference data, such as, using DFT; (2) fingerprinting or quantifying the atomic environments, in a manner that will allow the fingerprint as input in regression model; (3) choosing a subset from the reference data set, using clustering and sampling techniques to reduce the learning cost while ensuring that the dataset retain the diversity of the original reference data set; (4) learning from the training set, thus construct a nonlinear mapping between the atomic configurations and the forces, followed by testing the learned model on the remainder of the data set. The entire framework involved in the construction of force field is portrayed schematically in Fig. 3.

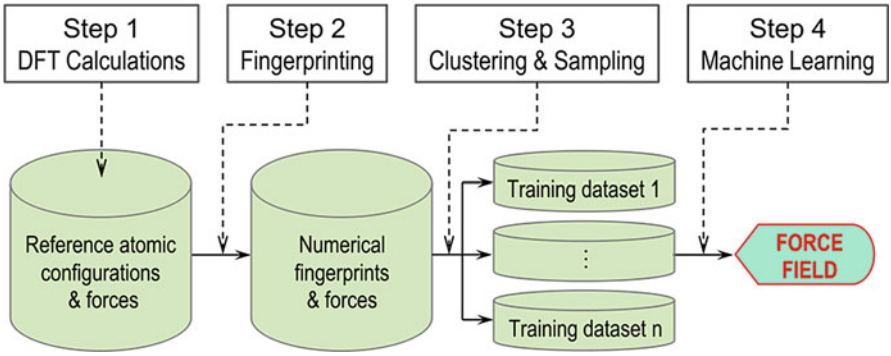

Fig. 3 Workflow for the creation of machine learning force field. (Adapted with permission from ref. [12], copyright 2017 NPJ Computational Materials publishing)

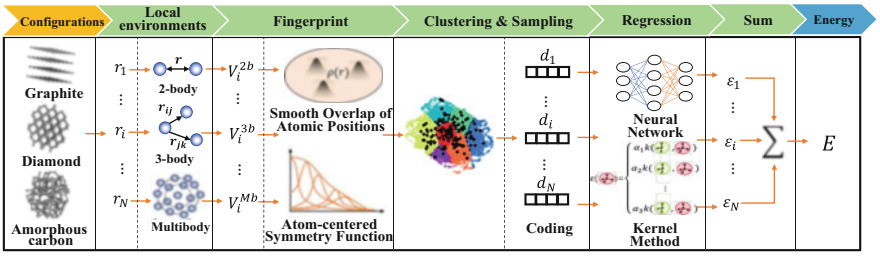

Fig. 4 ML-based force field framework for carbon allotropic

4 Procedure to Develop ML-Based Force Field

A ML-based force field framework for carbon allotropic is given in Fig. 4. First, constructing a comprehensive reference database as possible, in addition to commonly encountered crystalline phases, diamond and graphite, other relevant phase of carbon should also be taken in account, such as amorphous carbon. In order to facilitate the input of regression model, a proper fingerprint or descriptor should be selected to quantifying the local environment of an atom, the local environment of an atom typical divide into 2-body, 3-body, and many-body. Next, a cluster and sample algorithm employed to identify the redundant and noncontributing data to reduce computing costs. Finally, selecting a regression model to establish the fingerprint-force mapping, the energy E is further approximated as a sum of the atomic energies

$$E = \sum_i \varepsilon\left(d_i\right) \tag{1}$$

where d_i is the feature vector of atom i, which accounts for the chemical environment of atom i that depends on positions and chemical identities of its neighboring atoms up to a given cutoff radius. The ε represents the atomic energy as a function of descriptors. The details of each key step will be described next.

4.1 Reference Database

The reference data used for creating force field must be as accurate and comprehensive as possible, ensuring sufficiently low intrinsic errors. Generally, calculations (such as first-principles, molecular dynamics, lattice dynamics, and so forth) [32, 33], experiments [34–36] and online libraries [37, 38] have been used to collect these data. Among these approaches, first-principles is most convenient and quick approach to sample reference data for ML force field construction because abundant reference structures and corresponding quantum mechanical properties (i.e., energy and atomic force) can be directly obtained from one piece of an ab initio MD trajectory. For example, Li et al. [22] obtained abundant atomic configurations of Cu and SiO_2 by fast ab initio MD, such as face-centered cubic supercells, surface (111) supercells, surface (100) supercells, and amorphous supercells. Huan et al. further expanded the atomic configurations and corresponding force by rotating the collected atomic configurations, and providing more force components than that in the original dataset. To mimic the diverse environments an atom could exist in, Botu et al. [4] built several periodical and non-periodical equilibrium configurations, such as (a) defect free bulk, (b) surfaces, (c) point defects, vacancies and adatoms, (d) isolated clusters, (e) grain boundaries, (f) lattice expansion and compression, and (g) edge type dislocations, as shown in Fig. 5. To correctly describe the nonequilibrium behavior of an atom, initially atoms are randomly perturbed to coerce the dynamics into sampling nonequilibrium environments. The combination of ab initio MD and random perturbations resulted in a diverse set of reference atomic environments and forces.

4.2 Structural Fingerprints

Each atomic energy contribution depends only on its local environment, as shown is Fig. 6, which is represented by a feature space vector or fingerprint so as to numerically represent atomic configurations [31]. The accuracy of the ML force field will strongly depend on the selection of the fingerprint; a good fingerprint should possess the following properties: (1) it can be encoded as a fixed-length vector so as to facilitate regression, (2) it should retain basic physical symmetry invariant, such as translation, rotation, or permutation, (3) it is complete, i.e., different atomistic neighborhood configurations lead to different fingerprints and vice versa, and the "distance" between the fingerprints should be proportional

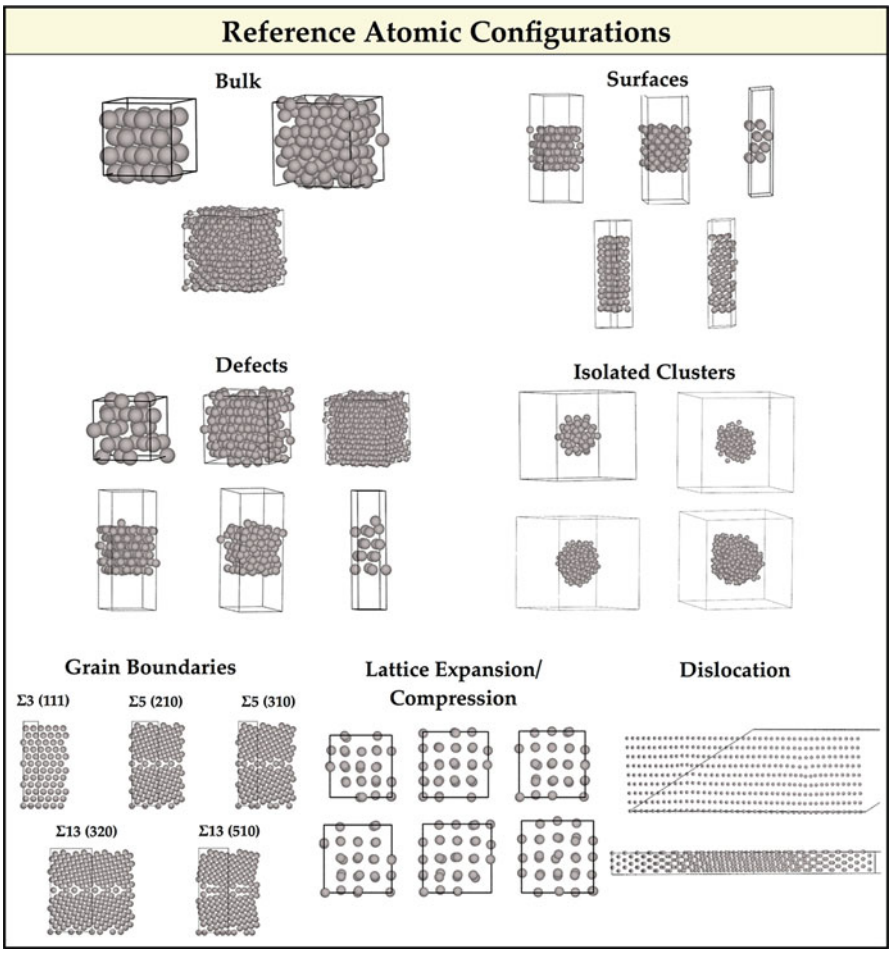

Fig. 5 Reference configurations used to sample atomic environments for training and testing of force field. (Adapted with permission from ref. [4], copyright 2017 Physical Chemistry C publishing)

to the intrinsic difference between the atomistic neighborhood configurations. A number of structural descriptors have been proposed to represent the local atomic environment, such as atom-centered symmetry functions [39], bispectrum [40], and Smooth Overlap of Atomic Positions (SOAP) kernel [41]. The most widely used descriptor is the vector atomic fingerprint function, which was proposed by Botu and Ramprasad, and has been proven to be an effective structural descriptor in the prediction of vectorial atomic properties [4]. Using the fingerprint, the atomic environment of the *i*th atom in a specific atomic configuration can be represented by

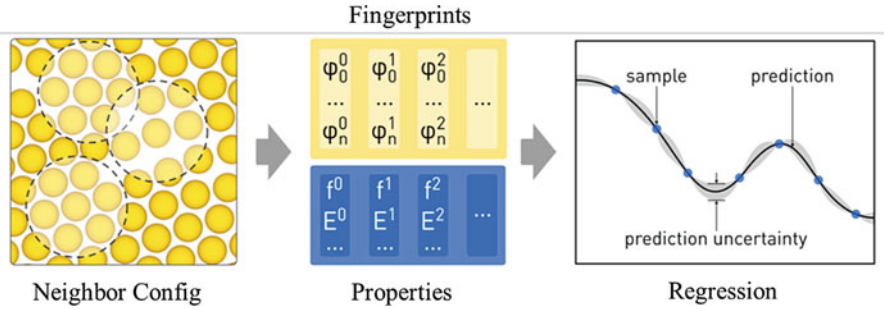

Fig. 6 Transform atomistic neighborhood configurations into feature vectors and train non-liner regression models. (Adapted with permission from ref. [1], copyright 2018 Chemical Physics publishing)

$$V_i^{\alpha} = \sum_j \frac{r_{ij}^{\alpha}}{r_{ij}} \mathrm{e}^{-\left(\frac{R_{ij}}{\eta}\right)^2} \times f_{\mathrm{c}}\left(r_{ij}\right) \tag{2}$$

where r_{ij} signifies the distance between atoms i and j, and r_{ij}^{α} is a scalar projection of this distance along the α direction ($\alpha = x$, y or z). η is a parameter that controls the decay rate, and f_{c} is the cutoff function that gradually reduces the contribution of distant atoms and truncates the interatomic interaction when r_{ij} is larger than cutoff distance R_{c}.

Although Eq. (2) has been proved to be very effective in various materials, it ignores bond angle information, which might be insufficient for complex covalent materials. For this, Li et al. [22] have modified Eq. (2) and proposed another structural fingerprint that takes the bond angle into consideration. The formulas of the two structural fingerprints are:

$$V_i^{1,\alpha} = \sum_j \frac{r_{ij}^{\alpha}}{r_{ij}} \mathrm{e}^{-\eta\left(r_{ij}-R_{\mathrm{s}}\right)^2} \times f_{\mathrm{c}}\left(r_{ij}\right) \tag{3}$$

$$V_i^{2,\alpha} = 2^{1-\zeta} \sum_j \sum_k \left(\overrightarrow{r_{ij}} + \overrightarrow{r_{ik}}\right)^{\alpha} \left(1 + \cos\left(\theta_{ijk} - \theta_{\mathrm{s}}\right)\right)^{\zeta} \times \mathrm{e}^{-\eta\left(\frac{r_{ij}+r_{ik}}{2}-R_{\mathrm{s}}\right)^2} \times f_{\mathrm{c}}\left(r_{ij}\right) \times f_{\mathrm{c}}\left(r_{ik}\right) \tag{4}$$

Equations (3) and (4) are called a radial structural fingerprint and angular structural fingerprint, respectively, where r_{ik} and r_{ij} are the interatomic distances between i and k, and i and j, respectively. θ_{ijk} is the angle between bonds ij and ik. $(r_{ij} + r_{ik})^{\alpha}$ is the scalar projection of vector $(r_{ij} + r_{ik})$ along the α direction. Two parameters of radial fingerprint $V_i^{1,\alpha}$, that is, η and R_{s}, are used to control the

width of the peak and shift the peak position. Two additional parameters, that is, ζ and θ_s, are used in angular fingerprint $V_i^{2,\alpha}$. Applying the θ_s parameter allows the probing of specific regions of the angular environment in a similar manner to that accomplished by R_s in the radial part. Finally, the ML force fields were compared with DFT and MD simulations in structural optimization, it is found that the proposed angular fingerprints can significantly improve the accuracy of ML force fields for both Cu and SiO_2.

To capture the transition state during the structural phase transformation, many-body term needs to be taken into consideration. For example, Zong et al. [42] adopt three different types of local environments related to structural phase transformations are fingerprinted, namely, the change in bond length (pairwise terms), shape change (three-body terms), as well as volume change (many-body terms). For two- and three- terms, which is similar to the above treatment, so we will not explain any more here. For the many-body contributions, which is similar to the embedding energy term of the MEAM potential. The formulas is

$$V_i^{Mb}(\mu,\sigma) = \ln\left(\rho_i^m(\mu,\sigma)\right) \tag{5}$$

where μ and σ are adjustable parameters, $\rho_i^m(\mu,\sigma)$ refers to the neighborhood density of a given atom i, define as

$$\rho_i^m(\mu,\sigma) = \sum_{j\neq i} \mathrm{e}^{-\frac{(r_{ij}-\mu)^2}{\sigma^2}} f_c\left(r_{ij}\right) \tag{6}$$

4.3 Sampling and Clustering

The next step in the construction workflow is to select a representative set of atomic environments for training purposes. To do so, it is necessary to identify the redundant and noncontributing data points from within the millions sampled. Random selection of training data from reference data is the most common approach, which typically results in the selected training configurations dominated by the high-populated domains while other domains are under-represented [5]. As shown in Fig. 7a, the training data randomly selected from the reference data contains essentially no configuration with large amplitude forces. To ensure the diversity of reference data, Huan et al. [12] proposed force-binning and clustering training data selection methods. In the force-binning method, the reference data was arranged into a number of force amplitude intervals and then the training data was selected from all the intervals, as shown in Fig. 7b. In the clustering approach, the reference data divide into a given number of clusters in fingerprint space and then the training data is selected from each cluster, as shown in Fig. 7c.

Another widely used method is dimensionality reduction techniques, such as principal component analysis (PCA) to project V_i^d onto a lower dimension space.

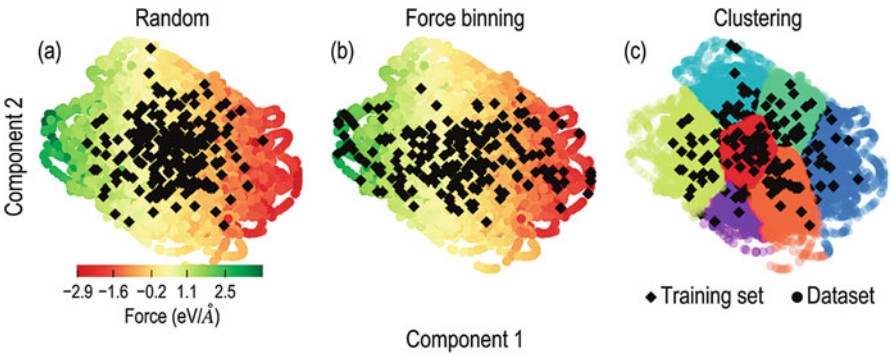

Fig. 7 An illustration of three methods for selecting a training set, including random (**a**) force amplitude sampling (**b**) and fingerprint space clustering (**c**). (Adapted with permission from ref. [12], copyright 2017 NPJ Computational Materials publishing)

In PCA the original atomic fingerprint is linearly transformed into uncorrelated and orthogonal pseudo variables. For example, Chapman et al. [43] captured more than 99% of the original fingerprint information by adopting such strategy. Moreover, some other similar dimension reduction techniques could be adopted to select representative data set, such as kernel-PCA or multidimensional scaling. Recently, using least absolute shrinkage and selection operator (LASSO) or genetic algorithm (GA) to select the important fingerprints from a large pool of candidates also have been proposed, which can have good balance between computational cost and accuracy.

4.4 Machine Learning

Once the reference data and atomic representation are in place, the final step is to carry out a learning algorithm to establish the fingerprint-force mapping. In the taxonomy of ML approaches, this is a "supervised learning" problem, because the input data (structures) are labeled (have reference energies); more specifically, it represents a regression task, because a continuous range of output values (energies) is sought. At present, various machine learning algorithms have been used in force field development, such as Kernel-based methods, linear model (LM), neural network model (NNM), and so forth. Next, we will give a brief introduction.

4.4.1 Kernel Ridge Regression

KRR is a powerful method that has widely been used in materials informatics, in which an atomic property is interpolated as a liner combination of kernel functions, as shown in Fig. 8, the latter measuring how similar a new configuration's descriptor

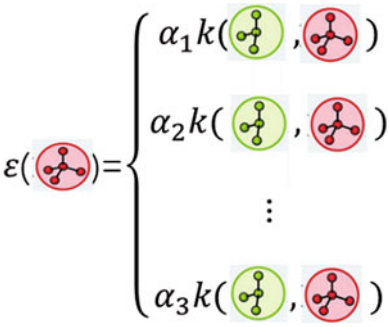

Fig. 8 Schematic of kernel methods to interpolate atomic properties by comparing an environment (red) with the reference database (green)

(red) is to those of the reference data (green). The property is typically a local energy, or a force acting on an atom, and the kernels can be understood as similarity measures (on a scale from zero to one) between the new environment and those contained in the database, both of which are represented by the descriptor. The regression coefficients that weigh each kernel basis function are computed during the fitting using simple linear algebra. Kernel ridge regression (KRR) and Gaussian Process Regression (GPR) are two currently employed techniques, differing only slightly in how these coefficients are computed.

Botu et al. [4] choose this method as the ML workhorse created a force field for six element bulk solids, including Al, Cu, Ti, W, Si, and C, and show that all of them can reach chemical accuracy. KRR predicts the atomic force F_i corresponding to the configuration i as

$$F_i = \sum_{j=1}^{N_t} a_j \exp\left[-\frac{1}{2}\left(\frac{d_{ij}}{\sigma}\right)^2\right] \tag{7}$$

where the sum runs ergodic N_t configurations in fingerprint space, d_{ij} is the "distance" between configurations i and j, here, refer to Euclidean norm. The "length" scale in this space is specified by σ.

4.4.2 Linear Model

LM is developed to describe the linear dependence between structural fingerprints and forces due to its simplicity and speed. For example, Li et al. [22] choose liner regression model to construct ML force field and compared with DFT calculation in both element (Cu) and binary (SiO_2) materials. They found that the force prediction error less than 0.1 eV/Å^{-1}. The LM takes the form

$$F_i^{\alpha} = w_1 V_i^{\alpha,(1)} + w_2 V_i^{\alpha,(2)} + \cdots + w_n V_i^{\alpha,(n)} \tag{8}$$

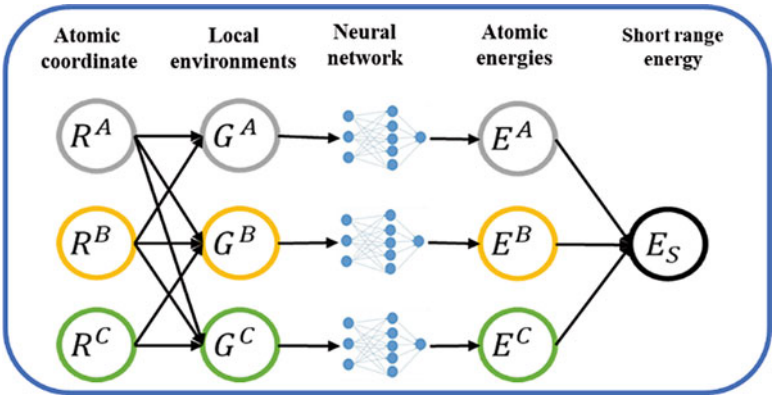

Fig. 9 High-dimensional neural network for a ternary system containing elements (**a–c**). $R^* = \left\{R_1^*, R_2^*, \cdots, R_{N_*}^*\right\}$, $G^* = \left\{G_1^*, G_2^*, \cdots, G_{N_*}^*\right\}$, $E^* = \left\{E_1^*, E_2^*, \cdots, E_{N_*}^*\right\}$, * = {A, B, C}

where w_1 is the regression coefficient, which is typically determined quickly using a standard least-squares technique. When matrix V includes the fingerprints of the reference atomic environments and F denotes the atomic forces obtained by DFT, the residual sum of squares $(\|V_w - F\|_2)^2$ is minimized in the linear regression, where $\| \bullet \|_2$ denotes the L_2 norm.

4.4.3 Neural Network Model

NNs are a set of mathematical functions that aim at resembling the functionality of neurons in brain, which was first proposed by Pro. Dr. J. Behler [3] in 2007, the structure as shown in Fig. 9, which represent a high-dimensional NN for a ternary system containing elements A, B, and C. The numbers of atoms per element are N_A, N_B, N_C, respectively. The total short-range energy E_s is the sum of all atomic energies E_i^X $(X = A, B, C)$, which are provided by individual atomic NNs. For a given element, the architecture and parameters of the atomic NNs are the same. The symmetry function vectors G_i^X provide the information about the local chemical environments of the atoms to the atomic NNs. Consequently, G_i^X depends on the Cartesian position vectors R_i^X of all the atoms within the cutoff spheres, which is represented by the black arrows. In such a method, a local atomic environment was described by generalized symmetry functions. NN potentials have been developed for many materials, such as Si, C, Cu, ZnO, TiO_2, H_2O dimers, Li_3PO_4, Cu clusters supported on Zn oxide and Au/Cu nanoparticles with water molecules. Additionally, they have been used to simulate the atom diffusion, phase transition, and search for equilibrium structures with not only MD but also the nudged elastic band (NEB) method, Monte Carlo methods and metadynamics.

5 Applications of ML Force Fields for Carbon Allotropes

5.1 ML Force Field for Graphene

Graphene has been the subject of extensive investigation since it was first isolated due to its interesting phenomena, such as the phonon-assisted diffusion of small molecules on the graphene surface, the study of thermal transport, and the incorporation of nuclear quantum effects into simulations which would benefit greatly from a highly accurate graphene model. Recently, ML-based force fields for graphene have emerged and attracted intensive attention. For example, Rowe et al. [44] constructed such an accurate interatomic potential for graphene using the GAP ML methodology. In this work, the total energy was decomposed into a sum of two-, three-, and many-body interactions, which are weighted based on their respective statistically measured contributions, the order of descriptors used in each term as follows: two atoms distance, symmetry functions, SOAP. Finally, to evaluating the accuracy of the ML model, compare the capabilities with those of empirically constructed potentials. As shown in Fig. 10, which shows the forces prediction ability of graphene GAP model and a number of other popular methods compared to the reference DFT method, black points indicate forces perpendicular to the plane of the graphene sheet (out-of-plane) while red points indicate forces oriented in the plane. The inset in the graphene GAP plot has a different scale on the *y* axis to show more clearly the distribution of force errors, it is clear that the predictions of the graphene GAP model align very closely with the reference DFT method. Additionally, the author also calculated the lattice parameters and in-plane thermal expansion of graphene using the developed GAP model and compared predictions of the finite temperature phonon spectra of graphene with experimental results.

In addition, Wen et al. [45] presented a hybrid potential that employs a neural network to describe short-range interactions and a theoretically motivated analytical term to model long-range dispersion for multilayer graphene. This potential can provide accurate energy and forces for both intralayer and interlayer interactions, correctly reproducing DFT results for structural, energetic, and elastic properties. Subsequently, Wen et al. [46] proposed another dropout uncertainty neural network potential for carbon and showed that it can be used to predict the stress and phonon dispersion in graphene.

5.2 ML Force Field for Diamond

As a significant member in carbon allotropes, diamond has been a hot spot in scientific research due to its fantastic mechanical and thermal properties. To better understand the atomistic behavior in diamond, an accuracy carbon potential is crucial. In 2017, Deringer et al. [47] reported a GAP model trained primarily on the

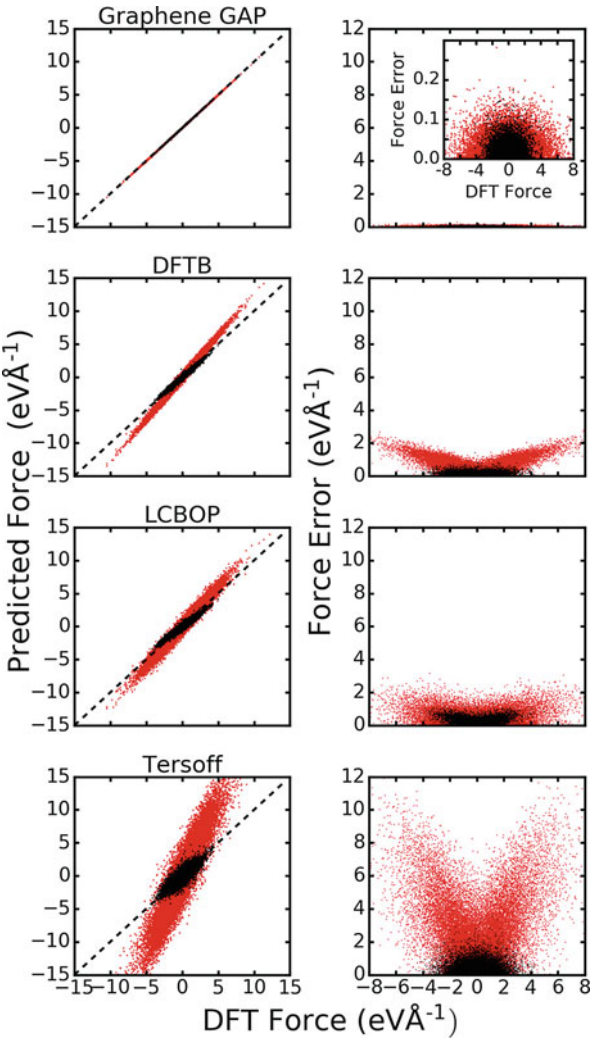

Fig. 10 The force prediction ability of graphene GAP model, DFTB, LCBOP, and Tersoff potentials compared to the reference DFT method. (Adapted with permission from ref. [44], copyright Physical Review B 2018 publishing)

amorphous and liquid phases of carbon based on DFT-local-density approximation reference data. Subsequently, Rowe and Deringer [48] proposed another improved GAP model on the basis of previous work, in which a large number of new configurations and exotic carbon allotropes are considered, such as nanotubes, cubic and hexagonal diamond and fullerene, as shown in Fig. 11a. To obtain more comprehensive database meanwhile keep the computational effort at the fitting stage tractable, they combined the farthest point sampling method with a number of mandatory configurations chosen using chemical intuition. The structural fingerprint of a configuration is quantified by SOAP descriptors. During model validation stage, they present an extensive and rigorous testing of GAP model for a wide range

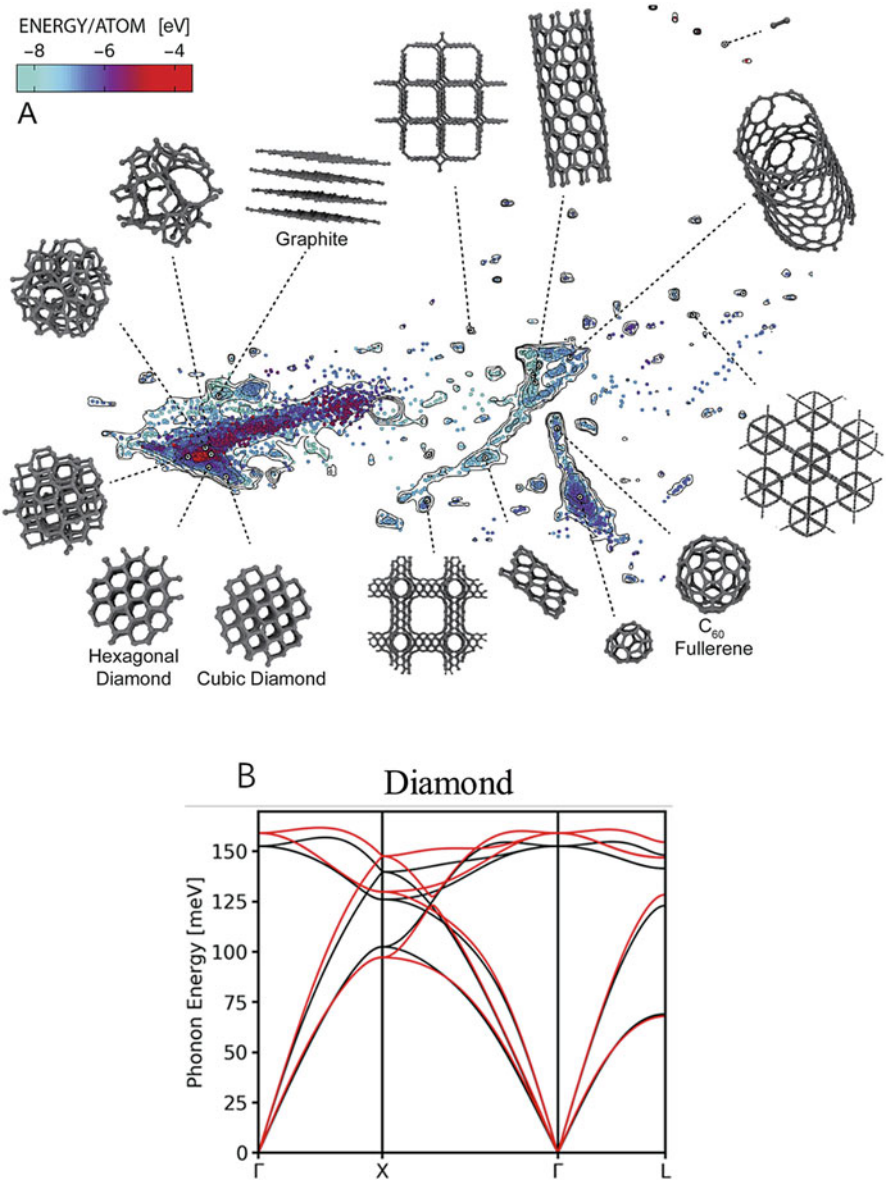

Fig. 11 (**a**) The selected configurations, as well as a representation of their position in phase space. (**b**) Phonon dispersion relation for diamond as predicted by GAP (black) with comparison to DFT reference data (red). (Adapted with permission from ref. [48], copyright 2020 Chemical Physics publishing)

of properties, as well as compare the results of GAP model to commonly used empirical potentials. As shown in Fig. 11b, the phonon dispersion of diamond is predicted successfully. In addition, the improved GAP model also correctly predicts the formation energies of diamond, graphite, fullerenes, and nanotubes, to an accuracy of a few meV, and achieves comparable accuracy for a number of crystalline and amorphous surfaces. The computed formation energies of defects are also accurate, with overall errors significantly lower than those obtained from comparable empirical models. Early, Rustam et al. [49] used an ab initio quality neural-network potential for large-scale simulations of the graphite-to-diamond transition assuming that it occurs through nucleation. The nucleation mechanism accounts for the observed phenomenology and reveals its microscopic origins. Other ML-based potentials for graphite-diamond phase study can be seen in ref. [50–52].

5.3 ML Force Field for Amorphous Carbon

The atomic structures of amorphous carbon samples depend strongly on density and are characterized by the coexistence of threefold ("sp^2") and fourfold bonded ("sp^3") carbon atoms; low- and high-density forms of amorphous carbon are loosely reminiscent of graphite and diamond, respectively. Deringer et al. [53] combined ML and DFT obtained new atomistic insight into carbonaceous energy materials. They started by modeling nanoporous carbons as used in supercapacitors. Using GAP, which has been "trained" with DFT data to fit energies and forces for amorphous and partly graphitized configurations as well as bulk graphite, they found the structural fingerprint of carbons is their atomic coordination relating to the local bonding ("sp/sp^2/sp^3"). Finally, the accuracy of GAP was tested specifically for snapshots from annealing trajectories, as shown in Fig. 12a; it achieves an energy accuracy within 2 kJ mol^{-1} of DFT data but completes the task several orders of magnitude faster. During annealing, the sp^2 count in the model systems quickly rises, as shown in Fig. 12b, which agrees well with electron energy-loss spectroscopy experiments. Comparing a calculated pair distribution function to representative experiments find that it successfully reproduces all general features, as shown in Fig. 12c. Shortly after, Deringer et al. [54] utilized this GAP fitted by a database of liquid and amorphous carbon configurations for random structure searching and readily predicted several higher- to unknown carbon allotropes. Besides, Csányi et al. [47] also introduced a similar GAP for atomistic simulations of amorphous elemental carbon and yielded accurate energetic and structural properties over a wide range of densities.

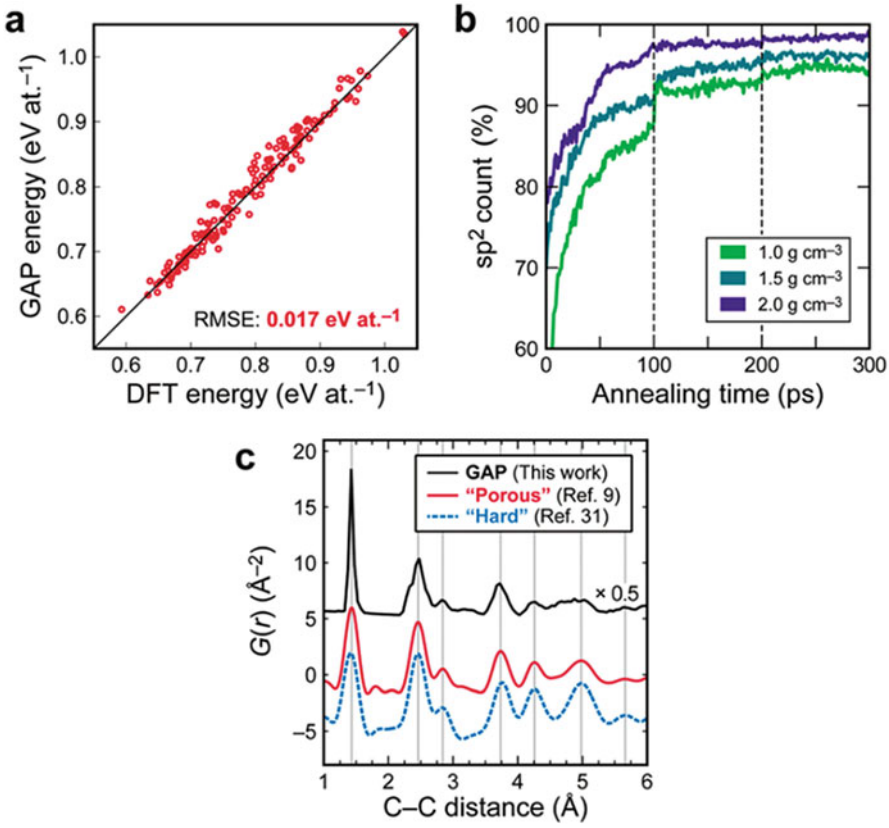

Fig. 12 (**a**) DFT versus GAP-computed energies for structures at various points of annealing trajectories. The root-mean-square error (RMSE) between these quantities is given. (**b**) Count of sp^2-bonded atoms during annealing; dashed lines indicate removal of unphysical long chains. (**c**) PDF analysis. (Adapted with permission from ref. [53], copyright 2018 Royal Society of Chemistry publishing)

6 Future Directions and Perspective

With continued increase in computing power, MD is emerging as a powerful tool for atom-level modeling as well as explore some micro mechanism without experiment. The predictive power of MD hinges strongly on the interatomic force field used to describe the atomistic interactions in the system. While the ML framework and the application cases presented above highlight the feasibility of using data-driven approaches for accurate modeling, however, there is still much room for improvement. The list below is some certain regions that would require further focused studies in the near future.

- The accuracy and speed of the ML force field depends on the choice of structural descriptors or fingerprints, so it is crucial to select the important descriptors from a large pool of candidates. For this issue, there is still controversy. Some researchers hold the view that the descriptors selected should depend on chemical or physical intuition or the basic knowledge of physic, because the essence of descriptor is physic. Some researchers proposed that blind spots exist in our intuitive judgment, for instance, the atomic force may be associated with several fingerprints combination. So ML can help us auto select descriptors.
- As materials science or chemical systems become ever increasingly complex, the configuration space for reference dataset will increase exponentially. This brings a challenge for the conventional nonlinear regression learning algorithm to handling such high dimension fitting issue, so some deep or advanced ML algorithms need to be developed.
- Most of the classical MD simulations employ predefined functional forms that can often limit the chemistry and physics that can be captured. While it appears that there can be significant improvements made by using data-driven approaches that employ extensive training data sets and advanced optimization, there will always be a ceiling limit imposed by the use of predefined functional forms. Existing force field with predefined functional form are not sufficiently flexible and cannot be transferred easily from one material class to another.
- Regardless of the application domain or area, all training data used for ML model should be carefully prepared and sufficiently diverse; for example, the reference configurations should span a wide range of energies, namely, the sampling not only includes near-equilibrium state but also consists of far-from-equilibrium configurations.
- Classical MD performs well under static or equilibrium issues while typically lacks predictive ability when it encounters dynamic and transport properties. One way to address this challenge is to include transition state configurations in the training data set. Going forward, we envisage that the temperature-dependent characteristics obtained from on-the-fly MD can also be used as part of the training program. This would allow us to directly train MD force field that can also capture dynamical and other transport properties or temperature-dependent properties of interest.
- Iterative improvement and cross-validation techniques are seldom used in the fitting of potentials. Even if with a DFT-based data set, there will always exist errors and then could be propagated to the atomistic potential model. Although higher-level theories can be introduced to generate training data and reduce errors, it is obvious that the uncertainty in prediction at various scales still needs to be quantified. Recent Strachan and his colleagues' work on quantitative methods of functional uncertainty represents an important future direction for assessing model errors. Cross-validation, sensitivity analysis, and uncertainty quantification are the key to improve the quality and prediction ability of interatomic potentials in MD.

In summary, using ML-based force field is indeed a powerful and feasible tool to accelerate atomistic simulations. Obtaining such high fidelity force prediction at a

very low cost has opened up an important way for the study of carbon materials and chemical phenomena. This can lead to revolutionary progress, enabling us to access time and length scales in carbon materials modeling that were hitherto considered to be inaccessible to MD.

References

1. Tang, Y., Zhang, D., et al. (2018). An atomistic fingerprint algorithm for learning ab initio molecular force field. *The Journal of Chemical Physics, 148*, 034101.
2. Berman, D., Sanket, A., Erdemire, A., et al. (2015). Macroscale superlubricity enabled by grapheme anoscroll formation. *Science, 14*, 126202.
3. Behler, J. (2017). First principles neural network potentials for reactive simulations of large molecular and condensed systems. *Angewandte Chemie, 56*, 12828–12840.
4. Botu, V., Batra, R., Chapman, J., et al. (2016). Machine learning force fields: construction, validation, and outlook. *The Journal of Physical Chemistry C, 121*, 511–522.
5. Botu, V., & Ramprasad, R. (2015). Adaptive machine learning framework to accelerate ab initio molecular dynamics. *International Journal of Quantum Chemistry, 115*, 1074–1083.
6. Botu, V., & Ramprasad, R. (2015). Learning scheme to predict atomic forces and accelerate materials simulations. *Physical Review B, 92*, 094306.
7. Chan, H., Narayanan, B., Cherukara, M. J., et al. (2019). Machine learning classical interatomic potentials for molecular dynamics from first-principles training data. *The Journal of Physical Chemistry C, 123*, 6941–6957.
8. Elliott, J. A. (2013). Novel approaches to multiscale modelling in materials science. *International Materials Reviews, 56*, 207–225.
9. Erdemir, A., Ramirez, G., Eryilmaz, O. L., et al. (2016). Carbon-based tribofilms from lubricating oils. *Nature, 536*, 67–71.
10. Gomez-Bombarelli, R., Aguilera-Iparraguirre, J., Hirzel, T. D., et al. (2016). Design of efficient molecular organic light-emitting diodes by a high-throughput virtual screening and experimental approach. *Nature Materials, 15*, 1120–1127.
11. Hautier, G., Jain, A., & Ong, S. P. (2012). From the computer to the laboratory: materials discovery and design using first-principles calculations. *Journal of Materials Science, 47*, 7317–7340.
12. Huan, T. D., Batra, R., Chapman, J., et al. (2017). A universal strategy for the creation of machine learning-based atomistic force fields. *npj Computational Materials, 3*, 37.
13. Isayev, O., Oses, C., Toher, C., et al. (2017). Universal fragment descriptors for predicting properties of inorganic crystals. *Nature Communications, 8*, 15679.
14. Jiang, Z., He, J., Deshmukh, S. A., et al. (2015). Subnanometre ligand-shell asymmetry leads to Janus-like nanoparticle membranes. *Nature Materials, 14*, 912–917.
15. Ju, S., Shiga, T., Feng, L., et al. (2017). Designing nanostructures for phonon transport via Bayesian optimization. *Physical Review X, 7*, 021024.
16. Neugebauer, J., & Hickel, T. (2013). Density functional theory in materials science. Wiley interdisciplinary reviews. *Computational Molecular Science, 3*, 438–448.
17. Smith, J. S., Nebgen, B. T., Zubatyuk, R., et al. (2019). Approaching coupled cluster accuracy with a general-purpose neural network potential through transfer learning. *Nature Communications, 10*, 2903.
18. Li, Z., Kermode, J. R., & De Vita, A. (2015). Molecular dynamics with on-the-fly machine learning of quantum-mechanical forces. *Physical Review Letters, 114*, 096405.
19. Botu, V., Chapman, J., & Ramprasad, R. (2017). A study of adatom ripening on an Al (1 1 1) surface with machine learning force fields. *Computational Materials Science, 129*, 332–335.

20. Kruglov, I., Sergeev, O., Yanilkin, A., et al. (2017). Energy-free machine learning force field for aluminum. *Scientific Reports, 7*, 8512.
21. Suzuki, T., Tamura, R., & Miyazaki, T. (2017). Machine learning for atomic forces in a crystalline solid: transferability to various temperatures. *International Journal of Quantum Chemistry, 117*, 33–39.
22. Li, W., & Ando, Y. (2018). Comparison of different machine learning models for the prediction of forces in copper and silicon dioxide. *Physical Chemistry Chemical Physics (PCCP), 20*, 30006–30020.
23. Artrith, N., & Behler, J. (2012). High-dimensional neural network potentials for metal surfaces: A prototype study for copper. *Physical Review B, 85*, 045439.
24. Artrith, N., & Kolpak, A. M. (2015). Grand canonical molecular dynamics simulations of Cu–Au nanoalloys in thermal equilibrium using reactive ANN potentials. *Computational Materials Science, 110*, 20–28.
25. Artrith, N., & Urban, A. (2016). An implementation of artificial neural-network potentials for atomistic materials simulations: performance for TiO_2. *Computational Materials Science, 114*, 135–150.
26. Behler, J., Martonak, R., Donadio, D., et al. (2008). Metadynamics simulations of the high-pressure phases of silicon employing a high-dimensional neural network potential. *Physical Review Letters, 100*, 185501.
27. Eshet, H., Khaliullin, R. Z., Kühne, T. D., et al. (2010). Ab initio quality neural-network potential for sodium. *Physical Review B, 81*, 184107.
28. Artrith, N., Morawietz, T., & Behler, J. (2011). High-dimensional neural-network potentials for multicomponent systems: Applications to zinc oxide. *Physical Review B, 83*, 153101.
29. Khaliullin, R. Z., Eshet, H., Kühne, T. D., et al. (2010). Graphite-diamond phase coexistence study employing a neural-network mapping of theab initiopotential energy surface. *Physical Review B, 81*, 100103.
30. Kondati Natarajan, S., Morawietz, T., & Behler, J. (2015). Representing the potential-energy surface of protonated water clusters by high-dimensional neural network potentials. *Physical Chemistry Chemical Physics (PCCP), 17*, 8356–8371.
31. Yao, K., Herr, J. E., Toth, D. W., et al. (2018). The TensorMol-0.1 model chemistry: A neural network augmented with long-range physics. *Chemical Science, 9*, 2261–2269.
32. Mi, X. Y., Yu, X., Yao, K. L., et al. (2015). Enhancing the thermoelectric figure of merit by low-dimensional electrical transport in phonon-glass crystals. *Nano Letters, 15*, 5229–5234.
33. Seko, A., Togo, A., Hayashi, H., et al. (2015). Prediction of low-thermal-conductivity compounds with first-principles anharmonic lattice-dynamics calculations and bayesian optimization. *Physical Review Letters, 115*, 205901.
34. Li, S., Yu, X., Bao, H., et al. (2018). High thermal conductivity of bulk epoxy resin by bottom-up parallel-linking and strain: A molecular dynamics study. *The Journal of Physical Chemistry C, 122*, 13140–13147.
35. Song, Q., An, M., Chen, X., et al. (2016). Adjustable thermal resistor by reversibly folding a graphene sheet. *Nanoscale, 8*, 14943–14949.
36. Yang, H., Zhang, Z., Zhang, J., et al. (2018). Machine learning and artificial neural network prediction of interfacial thermal resistance between graphene and hexagonal boron nitride. *Nanoscale, 10*, 19092–19099.
37. Ma, D., Ding, H., Wang, X., et al. (2017). The unexpected thermal conductivity from graphene disk, carbon nanocone to carbon nanotube. *International Journal of Heat and Mass Transfer, 108*, 940–944.
38. Yu, X., Li, R., Shiga, T., et al. (2019). Hybrid thermal transport characteristics of doped organic semiconductor poly(3,4-ethylenedioxythiophene): Tosylate. *The Journal of Physical Chemistry C, 123*, 26735–26741.
39. Behler, J. (2011). Atom-centered symmetry functions for constructing high-dimensional neural network potentials. *The Journal of Chemical Physics, 134*, 074106.
40. Bartók, A. P., Kondor, R., & Csányi, G. (2017). Erratum: On representing chemical environments. *Physical Review B, 96*, 019902.

41. Bartók, A. P., & Csányi, G. (2015). Gaussian approximation potentials: A brief tutorial introduction. *International Journal of Quantum Chemistry, 115*, 1051–1057.
42. Zong, H., Pilania, G., Ding, X., et al. (2018). Developing an interatomic potential for martensitic phase transformations in zirconium by machine learning. *npj Computational Materials, 4*, 48.
43. Fan, J., Sun, Q., Zhou, W.-X., et al. (2018). Principal component analysis for big data. 1–13.
44. Rowe, P., Csányi, G., Alfè, D., et al. (2018). Development of a machine learning potential for graphene. *Physical Review B, 97*, 054303.
45. Wen, M., & Tadmor, E. B. (2019). Hybrid neural network potential for multilayer graphene. *Physical Review B, 100*, 195419.
46. Wen, M., & Tadmor, E. B. (2020). Uncertainty quantification in molecular simulations with dropout neural network potentials. *npj Computational Materials, 6*, 124.
47. Deringer, V. L., & Csányi, G. (2017). Machine learning based interatomic potential for amorphous carbon. *Physical Review B, 95*, 094203.
48. Rowe, K., Deringer, V. L., & Gasprotto, P. (2020). An accurate and transferable machine learning potential for carbon. *Chemical Pysics, 153*, 034702.
49. Khaliullin, R. Z., Eshet, H., Kuhne, T. D., et al. (2011). Nucleation mechanism for the direct graphite-to-diamond phase transition. *Nature Materials, 10*, 693–697.
50. Bartok, A. P., Payne, M. C., Kondor, R., et al. (2010). Gaussian approximation potentials: The accuracy of quantum mechanics, without the electrons. *Physical Review Letters, 104*, 136403.
51. Behler, J., & Parrinello, M. (2007). Generalized neural-network representation of high-dimensional potential-energy surfaces. *Physical Review Letters, 98*, 146401.
52. Khaliullin, R. Z., Eshet, H., Kühne, T. D., et al. (2010). Graphite-diamond phase coexistence study employing a neural-network mapping of theab initiopotential energy surface. *Physical Review B, 81*, 100103(R).
53. Deringer, V. L., Merlet, C., Hu, Y., et al. (2018). Towards an atomistic understanding of disordered carbon electrode materials. *Chemical Communications, 54*, 5988–5991.
54. Deringer, V. L., Csanyi, G., & Proserpio, D. M. (2017). Extracting crystal chemistry from amorphous carbon structures. *Chemphyschem: A European Journal of Chemical Physics and Physical Chemistry, 18*, 873–877.

Genetic Algorithms

Shichang Li and Dengfeng Li

Genetic algorithms (GAs), developed by John Holland and his colleagues in 1975 [1], has been applied to many fields in search and optimization that belongs to the larger class of evolutionary algorithms (EAs). This approach is a metaheuristic inspired by the mechanisms of evolution, such as selection, crossover, and mutation. Drawing on the theory of biological evolution, the goals of their research have been solved into a biological evolution process by genetic algorithm, which generates next-generation solutions through operations such as duplication, crossover, and mutation. In this way, after n generations of evolution, it is very likely to evolve function with high fitness values. In fact, there are several methods available for solving the global optimization problems in materials science and related fields. Some of the well-known GAs include artificial bee colony, particle swarm optimization, differential evolution, etc.

1 Artificial Bee Colony Algorithms

The artificial bee colony algorithm was proposed by Karaboga (2005) [2] to simulate the intelligent behavior of a honeybee swarm. It consists of three main parts: food sources, employed foragers, and unemployed foragers. In order to better explain the basic principles of artificial bee colony algorithm, the three basic elements are introduced in detail as follows:

S. Li · D. Li (✉)
School of Science, Chongqing University of Posts and Telecommunications, Chongqing, China
e-mail: lisc@cqupt.edu.cn; lidf@cqupt.edu.cn

Y. Cheng et al. (eds.), *Artificial Intelligence for Materials Science*, Springer Series in Materials Science 312, https://doi.org/10.1007/978-3-030-68310-8_5

1. Food sources

   In the algorithm, food sources are mainly to represent different solutions, which depends on many factors such as its proximity to the nest, its richness or concentration of its energy, and the ease of extracting this energy. The "profitability" was used to evaluate the excellence of a food source.
2. Employed foragers

   Also known as a leader, it corresponds to the food source collected. The leading bee stores information about a food source (distance relative to the hive, direction, food source abundance, etc.) and shares this information with other bees with a certain probability.
3. Unemployed foragers

   The main task of unemployed foragers is to find and exploit food sources. There are two types of unemployed foragers: scouts and onlookers. Scouts begin to search for new food sources near the hive; Onlookers is waiting in the hive and to find the nectar source by sharing relevant information with the leader (employed foragers). In general, the average number of scouts is about 5–10% of the colony.

In the formation of searching the food sources, the exchange of information between bees is the most important part. The dancing area is the most important information exchange place in the hive. The dancing of the bees is called a waggle dance. The information of food source is shared with other bees in the dancing area, leading to express the profitability of food source on the dance floor. Therefore, the onlookers can observe a large number of food sources and choose more profitable sources due to some internal motivation or possible external clue. The probability of bees being recruited is proportional to the profitability of the food source.

1.1 Main Steps of the Artificial Bee Colony Algorithm

Based on the above explanation of initializing the algorithm population, employed bee phase, probabilistic selection scheme, onlooker bee phase, and scout bee phase, the pseudo-code of the artificial bee colony algorithm is given below [3]:

Algorithm 1 Artificial Bee Colony Algorithm

01: Initialize the population of solutions $x_{i,j} = 1, 2 \cdots SN, j = 1, 2 \cdots n$,
$trial_i = 0$, $trial_i = 0$ is the non-improvement number of the solution X_i, used for abandonment (food source X_i depending on its probability value p_i)
02: Evaluate the population
03: cycle = 1
04: **repeat**
{– – Produce a new food source population for employed bees – –}
06: **for** $i = 1$ to SN **do**
07: Produce a new food source V_i for the employed bee of the food source X_i using $v_{i,j} = x_{i,j} + \phi_{i,j}(x_{i,j} - x_{k,j})$ and evaluate its quality
08: Apply a greedy selection process between V_i and , select the better one.
09: If solution X_i does not improve $trial_i = trial_i + 1$, otherwise $trial_i = 0$
10: **end for**
11: Calculate the probability values p_i for the solutions using fitness values.
{– – Produce a new food source population for onlooker bees – –}
12: $t = 0, i = 1$
13: **repeat**
14: **if** $random < p_i$ **then**
15: Produce a new food source for onlooker bee
16: Apply a greedy selection process between V_i and X_i, select the better one
17: If solution X_i does not improve $trial_i = trial_i + 1$, otherwise $trial_i = 0$
18: $t = t + 1$
19: **endif**
20: **until** $(t = SN)$
{– – Determine Scout – –}
21: **if** $\max(\text{trial}_i) > \text{limit}$ **then**
22: Replace X_i with a new randomly produced solution
23: **end if**
24: Memorize the best solution achieved so far
25: cycle = cycle + 1
26: **until** (cycle=Maximum Cycle Number)

Algorithm 2 A Novel Initialization Approach

01: Set the maximum number of chaotic iteration $K \geq 300$, the population size SN, and the individual counter $i = 1, j = 1$
{– – chaotic systems – –}
03: **for** $i = 1$ to SN **do**
04: **for** $j = 1$ to n **do**
05: Randomly initialize variables $ch_{0,j} \in (0, 1)$, set iteration counter k = 0
06: **for** $k = 1$ to K **do**
07: $ch_{k+1,j} = \sin(\pi ch_{k,j})$
08: **end for**
09: $x_{ij} = x_{\min,j} + ch_{k,j}(x_{\max,j} - x_{\min,j})$
10: **end for**
11: **end for**
{– – Opposition-based learning method – –}
13: Set the individual counter $i = 1, j = 1$
14: **for** $i = 1$ to SN **do**
15: **for** $j = 1$ to n **do**
16: $ox_{i,j} = x_{\min,j} + x_{\max,j} - x_{i,j}$
17: **end for**
18: **end for**
19: Selecting SN fittest individuals from set the $\{X(SN)\} \cup OX(SN)$ as initial population
25: cycle = cycle + 1
26: **until** (cycle=Maximum Cycle Number)

1.2 Applications of the Artificial Bee Colony in Functional Materials

Interestingly, artificial bee colony has been tailored successfully, to solve a wide variety of discrete and continuous optimization problems. The distribution of published research articles on artificial bee colony with respect to applications, hybridizations, and modifications is shown in Fig. 1 [4].

The artificial bee colony also has been mostly implemented in design of many materials. For example, variables in design of multilayer radar-absorbing material with various numbers of layers are optimally determined using artificial bee colony which is one of the latest natural-inspired algorithms [5]. The multilayer radar-absorbing material in terms of electrical and geometric variables is conceptually synthesized with the aid of artificial bee colony optimization algorithm. Five truss examples with fixed-geometry and up to 200 elements were studied to verify that the ABC algorithm is an effective optimization algorithm in the creation of an optimal design for truss structures [6].

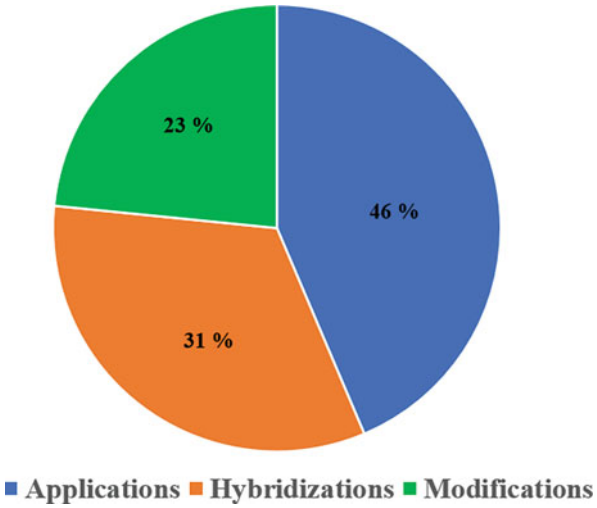

Fig. 1 The distribution of published research articles on artificial bee colony

1.3 Current Status of Research on Artificial Bee Colony Algorithms

In 2005, Karaboga proposed a more complete model of artificial bee colony algorithm and solved the function optimization problem with artificial bee colony algorithm, which achieved certain results. From the experimental results, the artificial bee colony algorithm is more excellent than the heuristic algorithm in terms of nonrestrictive numerical optimization.

More and more attempts have been made to improve the algorithm. Gao and Liu [7] introduced a new initialization approach and a novel search mechanism to improve the artificial bee colony algorithm. The results showed that the improved algorithm can outperform some conventional algorithms in accuracy, convergence speed, stability, and robustness. Zhu and Kwong [8] proposed an improved artificial bee colony algorithm, called Gbest-guided artificial bee colony algorithm. The results show that the Gbest-guided artificial bee colony algorithm possesses superior performance in most of the experiments, as compared to the conventional artificial bee colony algorithm. A modified artificial bee colony algorithm, developed by Gao and Liu [3], has been shown to be competitive to other population-based algorithms. The new optimization algorithm is based on that the bee searches only around the best solution of the previous iteration, leading to improving the exploitation.

2 Particle Swarm Optimization Algorithms

Particle swarm optimization (PSO) is a branch of evolutionary algorithms, which is inspired by the choreography of a bird flock that seems to be effective for optimizing a wide range of functions. In fact, it can be viewed as a distributed behavior algorithm that performs multidimensional search. PSO was first proposed by Kennedy and Eberhart in 1995 [9].

The principle of POS is similar to other evolutionary algorithms, and it also moves individuals in the group to a better place. Unlike other evolutionary algorithms, the particle swarm algorithm does not use any evolutionary operators, each individual member is regarded as a particle, which runs at a certain speed in space, and uses flying speed and position to adjust the entire algorithm space. Therefore, all the individuals can quickly find the global stable position and near-optimal geographical position. The PSO has been experimentally proven to be competitive and better than most of the algorithms on many optimization problems.

In the particle swarm algorithm, the position of each particle is updated using its velocity vector as depicted in Fig. 2 [10]. And the detail operation through Eq. (1) as following:

$$\begin{aligned} V_{i,j}(t+1) &= \omega V_{i,j}(t) + c_1 r_{1,j}\left[pbest_{i,j}(t) - X_{i,j}(t)\right] \\ &+ c_2 r_{2,j}\left[gbest_j(t) - X_{i,j}(t)\right] X_{i,j}(t+1) = X_{i,j}(t) + V_{i,j}(t+1) \end{aligned} \tag{1}$$

where $pbest_{i,j} = (pbest_{i1}, pbest_{i2}, \ldots, pbest_{iD})$ and $gbest_j = (pbest_1, pbest_2, \ldots, pbest_D)$ are current location and population global location, respectively. X is a set of positions of i particles in a D-dimensional space. ω is inertia weight. c_1 and c_2 are self-confidence factor and swarm confidence factor. r_1 and r_2 are two separately generated random numbers. The algorithm flowchart of PSO is presented in Fig. 3.

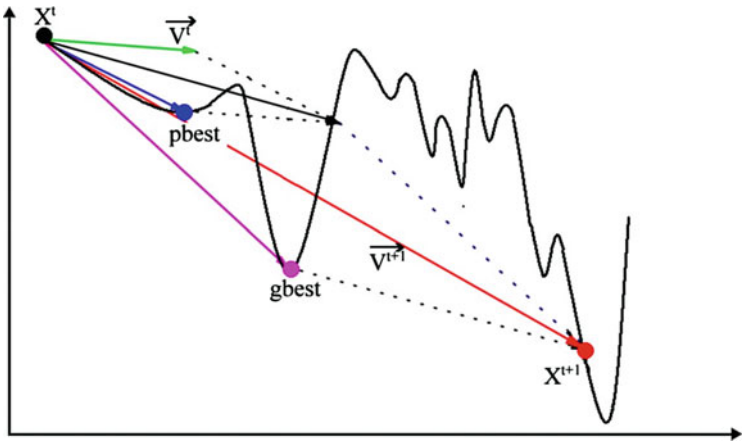

Fig. 2 Depiction of the velocity and position updates in PSO

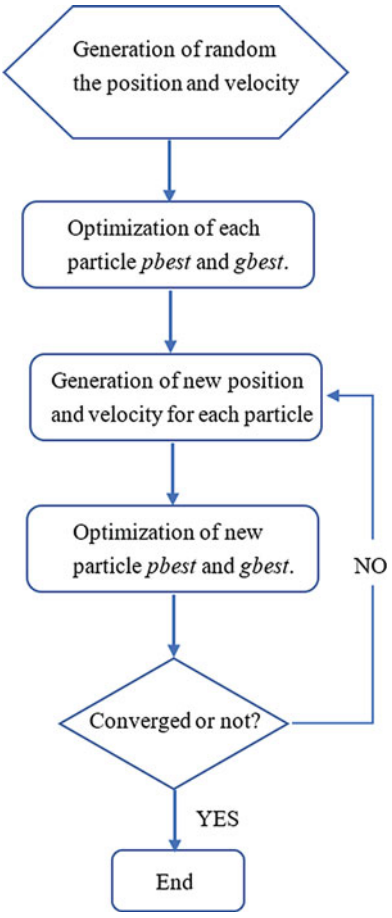

Fig. 3 The flowchart of PSO

The steps of PSO evolution are as follows:

1. Generate random the position and velocity of all particles, and optimize each particle *pbest* and *gbest*.
2. Generate new position and velocity for each particle and compare them with the previous *pbest*. If the current position is better than previous *pbest*, then replace previous *pbest*. Otherwise, keep the current value.
3. For each particle, compare its position with the previous *gbest*. If the present position is better than *gbest*, then previous *gbest* is replaced. Otherwise, keep the current value.
4. Updating of the velocity and position of each particle, using the above equation.
5. If the convergence condition is not met, return to step (2). There are several criteria for convergence, such as free energy, cell sizes, and symmetry.
6. If the convergence condition is met, the present *gbest* value is taken as the optimal solution.

2.1 Applications of the Particle Swarm Optimization in Multifunctional Materials

Recently, PSO algorithm has been employed to various optimization problems for 0D nanoparticles or clusters, 2D layers and its atom adsorption, 2D surface reconstructions, and 3D crystals. And this model has been successfully used to inversely design multifunctional materials (e.g., superhard materials, electrides, optical materials) for many ternary and ternary compounds.

For example, PSO algorithm is used to predict the structures of many ternary Np-H compounds. The searching results of the energetically most favorable structures of NpHx (x = 1–10) found by us are plotted in Fig. 4 by PSO algorithm at ambient and high pressures. The complete pressure–composition phase diagram of Np–H compounds is shown in Fig. 5, with the stable structures identified using colors and space groups. The relative formation enthalpies of the energetically most favorable structures of NpHx found by us are plotted in Fig. 6 with cell sizes of 1–6 formula units, covering the pressure range up to 200 GPa. For ternary compounds, the PSO algorithm has been successfully used to predict the ambient pressure structures of $PuGaO_3$ and $CeGaO_3$, as shown in Fig. 7 [11].

2.2 Current State of the Particle Swarm Optimization

Since the PSO was proposed in 1995, the mathematical model of PSO is relatively simple and its application is surprisingly considerable, which has prompted a lot of researchers to study it. There have been a lot of research achievements in theoretical research of algorithm, the modification of model, and the fusion arithmetic.

1. Theoretical research

   Ozcan and Mohan [12] have analyzed the theory of particle swarm algorithm in 1999, the formula of the algorithm has been updated for the first time. Then Clerc and Kennedy analyzed the operation of particle swarm algorithm in multidimensional space [13]. Trelea have investigated the convergence of particle swarm algorithm by using discrete dynamic system and proposed some methods of parameter selection that are helpful for the overall stability and convergence of the algorithm. It has been well confirmed in the experimental data [14].
2. The modification of model

   In 1998, Shi and Eberhart published a paper about modified PSO algorithms at the International Conference on Swarm Intelligence. Inertia weight was introduced for the first time by this algorithm, with such improvements widely used in the academic community, gradually converted to the standard particle swarm optimization algorithm which is widely used at present. In order to improve this algorithm, Eberhart and Shi proposed to adjust with fuzzy system

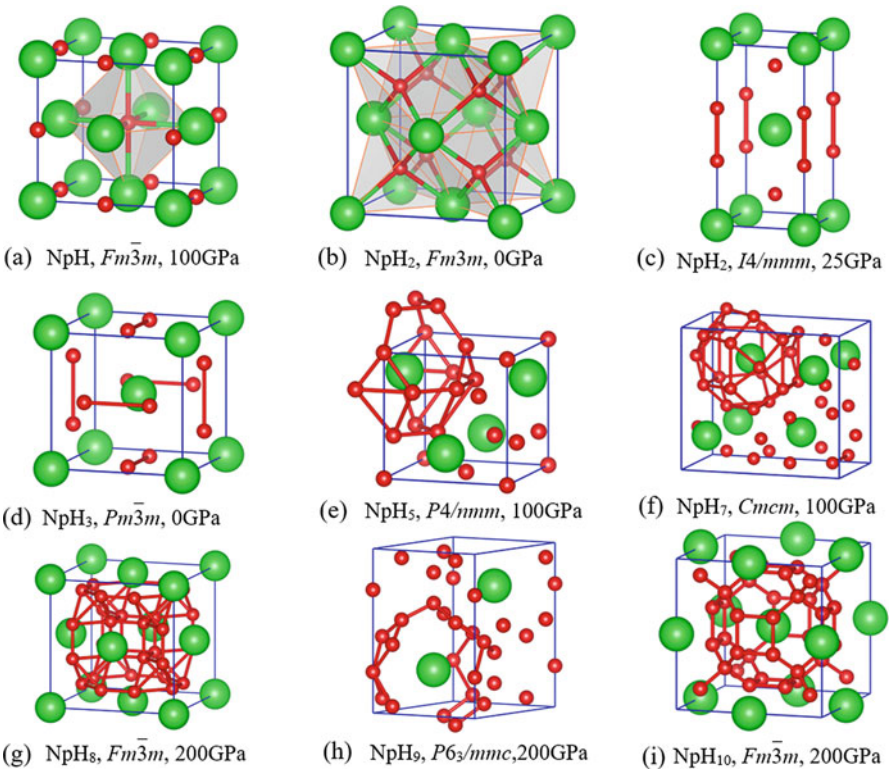

Fig. 4 Crystal structures of the predicted stable neptunium hydrides compounds: (**a**) $Fm\bar{3}m$ structure of NpH at 100 GPa, (**b**) $Fm\bar{3}m$ structure of NpH_2 at ambient pressure, (**c**) $P6_3/mmc$ structure of NpH_2 at 25 GPa, (**d**) $P6/mmm$ structure of NpH_2 at 150 GPa, (**e**) $P6_3cm$ structure of NpH_3 at ambient pressure, (**f**) $Pnma$ structure of NpH_3 at 50 GPa, (**g**) $R\bar{3}m$ structure of NpH_3 at 100 GPa, (**h**) $Cmcm$ structure of NpH_3 at 160 GPa, (**i**) $I4/mmm$ structure of NpH_4 at 200 GPa. The large and small spheres denote neptunium and hydrogen atoms, respectively

[15]. Subsequently, Clerc confirmed that the effectiveness of the proposed algorithm was convergent [13].

3. The fusion arithmetic

   Angeline has introduced the selection operation in evolutionary computation and proposed a hybrid particle swarm optimization algorithm model [16, 17].

Because the PSO algorithms have some of significant advantages, such as simple model, easy to implement, and non-gradient and less variables, it shows excellent results in the continuous discontinuous optimization, combinatorial optimization, and dynamic optimization. Recently, PSO algorithm has been employed to various optimization problems for 0D nanoparticles or clusters, 2D layers and its atom adsorption, 2D surface reconstructions, and 3D crystals. The application of PSO in structure prediction has been proved to be a popular technique. The POS algorithms

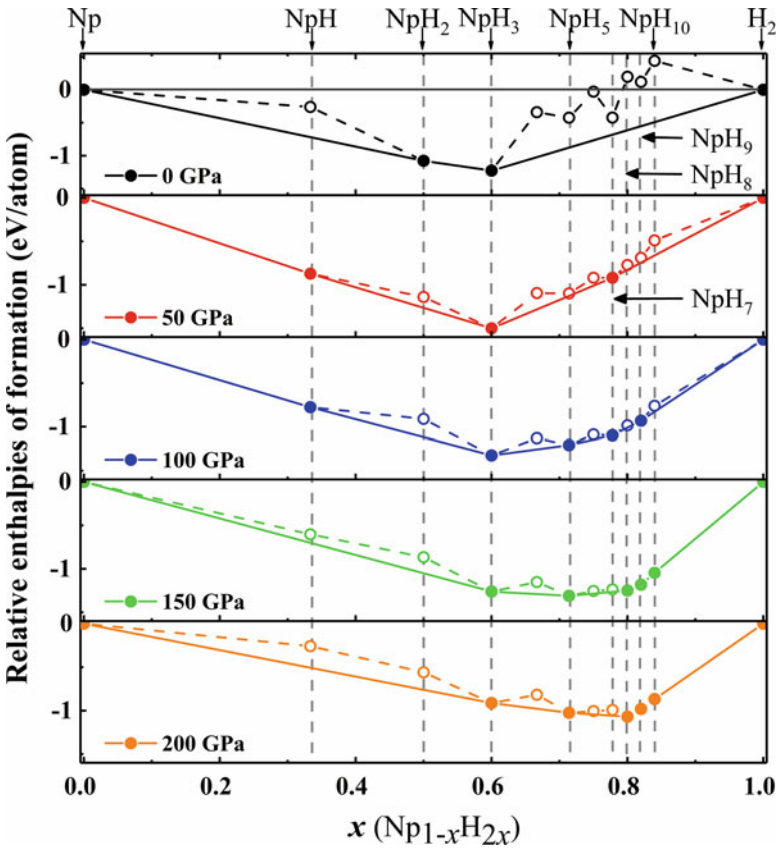

Fig. 5 Convex hulls of the Np–H system at selected pressures. Solid points connected by the solid line denote thermodynamic stable phases, while empty points connected by the dotted line represent unstable/metastable phases

have been interface to some mature structure prediction codes, such as CALYPSO [18] and USPEX [19], which have been successfully applied to investigate a great variety of materials at high pressures.

3 Differential Evolution Algorithms

3.1 Brief Introduction of the Differential Evolution Algorithm

Differential Evolution (DE) is a parallel direct search method which optimizes a problem by iteratively trying to improve a candidate solution for the multidimensional optimization problem. DE is a particular method to create new vector (also

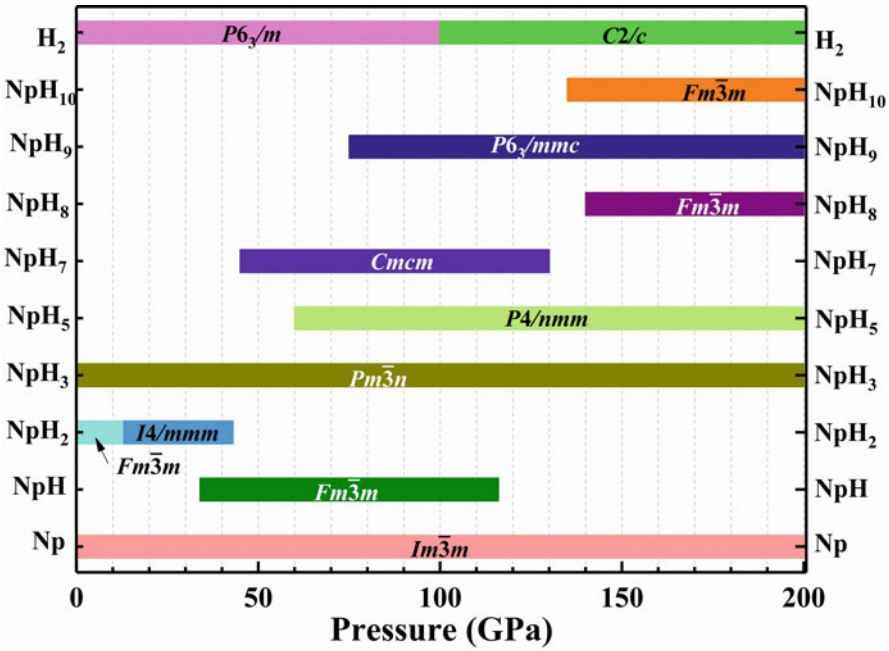

Fig. 6 Predicted pressure–composition phase diagram of the Np–H crystal phases

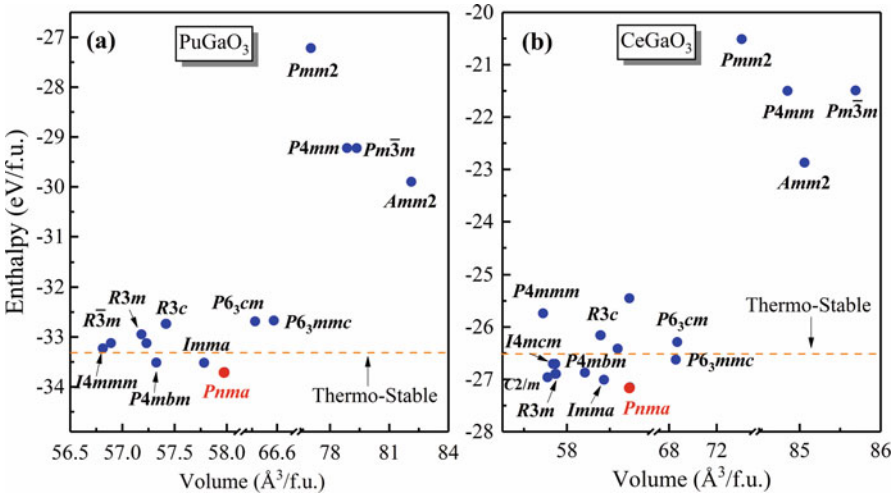

Fig. 7 Calculated enthalpy (for per formula unit) of predicted phases versus volume for (**a**) $PuGaO_3$ and (**b**) $CeGaO_3$ compounds with the PBEsol + U approach. Thermo-Stable level is the sum of the enthalpy of the decomposition products (PuO_2/CeO_2, Ga_2O_3, and α-Ga)

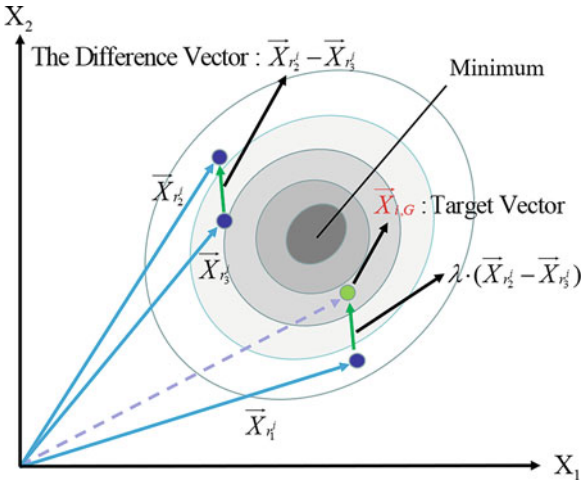

Fig. 8 DE mutation scheme for three random vectors

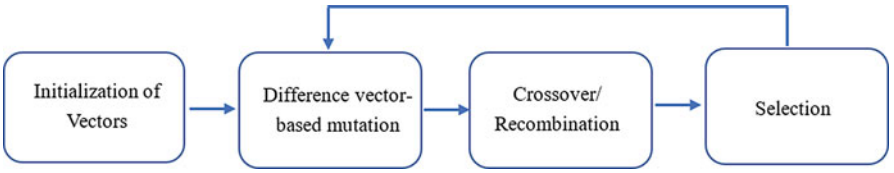

Fig. 9 The flowchart of the DE algorithm

known as genome/chromosome) for the population. While iterating over generations to evolve to an optimal state, existing chromosomes is used to create new offspring as potential candidates to make it to the subsequent generation. Diagram of the DE is depicted in Fig. 8. The main steps in DE are as follows [20]:

1. For each genome in the current population, we select three random vectors.
2. If a uniformly distributed random number ($rand_{i,j}[0,1]$) is less than the defined crossover rate, create a new offspring vector. Otherwise use the same genome as the parent.
3. Subtract two of these genome vectors.
4. Scale the difference of any two of these three vectors by a user-defined scale parameter λ.
5. Add the scaled difference vector to the third genome.

The D-dimension vector can be used to represent a set of D-dimensional parameters, called a single parameter [21]. A population consists of NP D-dimensional parameter vectors $x_{i,G}$, $i = 1, 2, \ldots,$ NP for each generation G [22]. The flowchart of the DE algorithm is shown in Fig. 9. Mutation, crossover, and selection are described below. For a more detailed description, please refer to [22].

3.1.1 Mutation

Mutation vectors are generated according to $v_{i,\,G+1} = x_{r1,\,G} + F \cdot (x_{r2,\,G} - x_{r3,\,G})$ with randomly selected indexes, corresponding to each target vector $x_{i,\,G}$. It is important to note that the indexes must be different from each other and different from the running index i. Consequently, the number of parameter vectors in a population must be at least four. F is an actual and constant factor $\in[0, 2]$ that controls the amplification of the difference vector $(x_{r2,\,G} - x_{r3,\,G})$.

It is necessary to note that the more subtle the differences between parameters of parent r_2 and r_3, the smaller the difference vector and therefore the perturbation. This means that if the population is close to the optimal value, the step size will decrease accordingly. This is similar to automatic step control in standard evolutionary strategies.

3.1.2 Crossover

The trial vector generated by the target vector is mixed with the mutated vector using the following scheme

$$u_{ji,G+1} = \begin{cases} vji, G+1 & \text{if } (r(j) \le \text{CR}) \text{ or } j = rn(i) \\ xji, G & \text{if } (r(j) > \text{CR}) \text{ and } j \ne rn(i) \end{cases}$$

where $j = 1, 2, \ldots, D$, $r(j) \in [0, 1]$ is the jth evaluation of a uniform random number generator. CR is the crossover constant $\in[0, 1]$. CR $= 0$ means that no crossover operator was used in the DE algorithm. rn$(i) \in (1, 2, \ldots, D)$ is a randomly chosen index which ensures that $u_{i,\,G+1}$ gets at least one element from . Otherwise, no new parent vector would be produced and the population would not alter.

3.1.3 Selection

If and only if the test vector produces a better cost function value than the parameter vector , it is accepted as the new parent vector of the next generation $G + 1$. This is a "greedy" option. If not, the target vector is retained again as the parent vector of generation $G + 1$. There are three strategy parameters altogether: NP: Number of members in a population, F: Amplification factor of the difference vector, CR: Crossover constant.

3.1.4 Other Variants of DE

There are numerous variants of DE which can be classified as DE/x/y/z, where x specifies the vector to be mutated, y is the number of difference vectors used, and z denotes the crossover scheme.

Table 1 Applications of differential evolution in medicine and pharmacology

Year	Researchers	Application
2004	Magoulas, Plagianakos, and Vrahatis	Colonoscopic diagnosis
2006	Koutsojannis and Hatzilygeroudis	Intelligent diagnosis and treatment of acid-base disturbances based on blood gas analysis data
2004–2005	Saastamoinen, Ketola, and Turunen	Sport medicine
2015	Konstantin Kozlov et al.	Geospatial immune
2017	T. Vivekanandan, N. ChSriman Narayana Iyengar	Heart disease

Table 2 Applications of differential evolution in optics community

Year	Researchers	Application
2004	Al-Kuzee, Matsuura, and Goodyear	Optimize plasma etch processes
2004	Zhang and Zhong	Calibrate camera
2005	Chan, Toader, and John	PBG design
2006	Akdagli and Yuksel	Laser diode nonlinearity
2006	Bluszcz and Adamiec	Optical stimulated luminescence decay
2006	Ling, Wu, Yang, and Wan	Design holographic grating
2007	Pan and Xie	Deformation measurement
2016	Fernando Lezama	Optical networks
2016	Soham Sarkar	Reflective optics system
2017	Md. Ghulam Saber	Optical material

x is note "rand" (randomly chosen population vector) or "best" (the best vector from the current population). Since we use only one difference vector, y is one in the described scheme. The current variant for z is "bin" (independent binomial experiments) which means crossover. With this notation, the conventional DE model can be written as . Another possibility is the method DE/best/2/bin, the mutant vector $v_{i,\,G+1} = x_{\text{best},\,G} + F \cdot (x_{r1,\,G} - x_{r2,\,G} + X_{r3,\,G} - x_{r4,\,G})$ can be obtained.

3.2 Applications of the Differential Evolution Algorithm

Recently, differential evolution algorithm has been intensively implemented in medical applications (focus on the diagnosis, classification, and treatment of cancer, Table 1), optics community (Table 2), the early accurate prediction of earthquakes (Table 3), and thermal engineering (Table 4) [23]. And most of the applications of differential evolution in physics focus on stellarator design and plasma. Other reported applications include chaos control [24], and optimization of the structure of atomic and molecular clusters [25].

Since the DE algorithm [26] was proposed by Storn and Price in 1995, the algorithm has been favored by more and more researchers. The research on the algorithm

Table 3 Applications of differential evolution in seismology

Year	Researchers	Application
1998, 2000	Bartal et al.	Optimize the seismic networks in Israel
2007	Ruzek et al.	Find seismic velocity models yielding travel times consistent with observed experimental data
2018	Thomas Meehan	The roots of this algorithm and main developments are examined to offer a better understanding of its essential features

Table 4 Applications of differential evolution in thermal engineering

Year	Researchers	Application
2006	Coelho	Modeling of a thermal system
2007	Babu and Munawar	Design of heat exchangers
2016	G. Balaji	Thermal generator maintenance scheduling
2017	Emerson Hochsteiner deVasconcelos Segundo	Economic optimization design for shell-and-tube heat exchangers
2019	Feng Tan	Thermal analysis of spindle
2020	Mohammad H. Nadimi-Shahraki	Introducing a multi trial vector approach to combine various search strategies

and its application has shown a rapid growth during past few years. The DE was used to solve Chebyshev polynomials at the early stages. By comparing with a variety of metaheuristic algorithms, it was found that the algorithm showed increasing effectiveness. The algorithm is currently used in many fields, including neural networks, industrial engineering, mechanical engineering, electronic engineering, electrical engineering, control engineering, civil engineering, software engineering, image processing, and other fields.

4 Conclusions

In summary, evolutionary algorithms model is a very simple but very powerful stochastic global optimizer, which is widely used in many scientific and engineering fields for function optimization. Evolutionary algorithms make it possible to use computers to extract useful knowledge from massive amounts of the acquired knowledge. It should be pointed out that there is no absolute good or bad between different evolutionary algorithms. We should select the appropriate evolutionary algorithms with different data structures in different situations.

References

1. Holland, J. (1975). *Adaptation in natural and artificial systems* (p. 100). Ann Arbor: University of Michigan Press.
2. Karaboga, D. (2005). *An idea based on honey bee swarm for numerical optimization*. Technical report-tr06, Erciyes university, engineering faculty, computer engineering department, (Vol. 200, pp. 1–10).
3. Gao, W.-F., & Liu, S.-Y. (2012). A modified artificial bee colony algorithm. *Computers & Operations Research, 39*, 687–697.
4. Khader, A. T., Al-betar, M. A., & Mohammed, A. A. (2013). Artificial bee colony algorithm, its variants and applications: A survey. *Journal of Theoretical & Applied Information Technology, 47*(2).
5. Toktas, A., Ustun, D., Yigit, E., Sabanci, K., & Tekbas, M. (2018). Optimally synthesizing multilayer radar absorbing material (Ram) using artificial bee colony algorithm. In *2018 XXIIIrd International Seminar/Workshop on Direct and Inverse Problems of Electromagnetic and Acoustic Wave Theory (DIPED), 24–27 Sept 2018* (pp. 237–241).
6. Sonmez, M. (2011). Artificial bee colony algorithm for optimization of truss structures. *Applied Soft Computing, 11*, 2406–2418.
7. Gao, W., & Liu, S. (2011). Improved artificial bee colony algorithm for global optimization. *Information Processing Letters, 111*, 871–882.
8. Zhu, G., & Kwong, S. (2010). Gbest-guided artificial bee colony algorithm for numerical function optimization. *Applied Mathematics and Computation, 217*, 3166–3173.
9. Kennedy, J., & Eberhart, R. (1995). Particle swarm optimization. In *Proceedings of ICNN'95—International Conference on Neural Networks, 27 Nov–1 Dec 1995* (Vol. 4, pp. 1942–1948).
10. Wang, Y., Lv, J., Zhu, L., & Ma, Y. (2010). Crystal structure prediction via particle-swarm optimization. *Physical Review B, 82*, 094116.
11. Li, S., Ye, X., Liu, T., Gao, T., Ma, S., & Ao, B. (2018). New insight into the structure of Pugao3 from ab initio particle-swarm optimization methodology. *Journal of Materials Chemistry A, 6*, 22798–22808.
12. Ozcan, E., & Mohan, C. K. (1999). Particle swarm optimization: Surfing the waves. In *Proceedings of the 1999 Congress on Evolutionary Computation-CEC99 (Cat. No. 99TH8406), 6–9 July 1999* (Vol. 3, pp. 1939–1944).
13. Clerc, M., & Kennedy, J. (2002). The particle swarm—Explosion, stability, and convergence in a multidimensional complex space. *IEEE Transactions on Evolutionary Computation, 6*, 58–73.
14. Trelea, I. C. (2003). The particle swarm optimization algorithm: Convergence analysis and parameter selection. *Information Processing Letters, 85*, 317–325.
15. Eberhart, R. C., & Shi, Y. (2000). Comparing inertia weights and constriction factors in particle swarm optimization. In *Proceedings of the 2000 Congress on Evolutionary Computation. CEC00 (Cat. No. 00TH8512), 16–19 July 2000* (Vol. 1, pp. 84–88).
16. Angeline, P. J. (1998). Using selection to improve particle swarm optimization. In *1998 IEEE International Conference on Evolutionary Computation Proceedings. IEEE World Congress on Computational Intelligence (Cat. No. 98TH8360)* (pp. 84–89). New York: IEEE.
17. Løvbjerg, M., Rasmussen, T. K., & Krink, T. (2001). Hybrid particle swarm optimiser with breeding and subpopulations. In Proceedings of the genetic and evolutionary computation conference (Vol. 2001, pp. 469–476). San Francisco, USA.
18. Wang, Y., Lv, J., Zhu, L., & Ma, Y. (2012). Calypso: A method for crystal structure prediction. *Computer Physics Communications, 183*, 2063–2070.
19. Glass, C. W., Oganov, A. R., & Hansen, N. (2006). Uspex—Evolutionary crystal structure prediction. *Computer Physics Communications, 175*, 713–720.
20. Das, S., & Suganthan, P. (2011). Differential evolution: A survey of the state-of-the-art. *IEEE Transactions on Evolutionary Computation, 15*, 4–31.

21. Gämperle, R., Müller, S. D., & Koumoutsakos, P. (2002). A parameter study for differential evolution. *Advances in Intelligent Systems, Fuzzy Systems, Evolutionary Computation, 10*, 293–298.
22. Storn, R., & Price, K. (1997). Differential evolution—A simple and efficient heuristic for global optimization over continuous spaces. *Journal of Global Optimization, 11*, 341–359.
23. Qing, A. (2009). Chapter 2. Fundamentals of differential evolution. In *Differential evolution: Fundamentals and applications in electrical engineering* (pp. 41–60). Hoboken, NJ: Wiley. https://doi.org/10.1002/9780470823941.
24. Zelinka, I. (2005). Investigation on evolutionary deterministic chaos control–extended study. *Heuristica, 1000*, 30.
25. Ali, M. M., Smith, R., & Hobday, S. (2006). The structure of atomic and molecular clusters, optimised using classical potentials. *Computer Physics Communications, 175*, 451–464.
26. Storn, R., & Price, K. (1995). *Differential evolution—A simple and efficient adaptive scheme for global optimization over continuous spaces*. Technical Report Tr-95-012. International Computer Science, Berkeley, CA.

Accelerated Discovery of Thermoelectric Materials Using Machine Learning

Rinkle Juneja and Abhishek K. Singh

1 Introduction

Thermoelectric materials convert heat to electricity and hence could be major contributors in addressing the global energy crisis [1–7]. The energy conversion performance of a thermoelectric material is assessed by a dimensionless figure of merit, ZT, given by $ZT = \frac{S^2\sigma}{\kappa_e+\kappa_l}T$, where S, σ, κ_e, κ_l, and T are Seebeck coefficient, electrical conductivity, electronic thermal conductivity, lattice thermal conductivity, and absolute temperature, respectively. A material exhibiting simultaneously favorable electronic and thermal transport properties will have high figure of merit and hence would be useful for designing efficient thermoelectric device. However, obtaining high figure of merit in materials is a challenging task. This is due to inherent interdependence of transport properties (S, σ, κ_e) as well as difficulty in finding materials with low κ_l, thereby limiting the use of thermoelectrics for large-scale commercial applications. To realize the full potential of thermoelectric technology, strategies to overcome these fundamental challenges are required.

Over the years, significant efforts have been made by the thermoelectric community, which has led to emergence of several novel concepts and methodologies for obtaining highly efficient thermoelectric materials. The key focus of these efforts includes addressing the interdependence of transport properties for obtaining high power factor ($S^2\sigma$) and phonon engineering to achieve ultralow lattice thermal conductivity. Some of the effective strategies employed for favorable electronic transport are carrier pocket engineering, composite engineering, quantum

The authors declare no competing financial interests.

R. Juneja · A. K. Singh (✉)
Materials Research Centre, Indian Institute of Science, Bangalore, India
e-mail: rinklejuneja@iisc.ac.in; abhishek@iisc.ac.in

Y. Cheng et al. (eds.), *Artificial Intelligence for Materials Science*, Springer Series in Materials Science 312, https://doi.org/10.1007/978-3-030-68310-8_6

confinement, and modulation doping [8–11]. For achieving ultralow lattice thermal conductivity, some of the techniques proven to be successful are introduction of rattler atoms in complex polyhedral systems, simpler materials with bonding anisotropy to host rattler atoms, introduction of atomic-scale point defects, nanostructuring, grain boundaries, and strain modulation [12–19].

Employing these conventional approaches for exploration of highly efficient thermoelectrics among the pool of large materials space is very time-consuming as well as challenging. With the advent of Materials Genome Initiative, data-assisted methods have been providing an alternative cost-effective route for accelerated discovery of materials with desired functionalities [20–24]. Based on high-throughput screening or machine learning based prediction models, reliable estimate of various resource extensive properties for a large class of materials has been successful [25–31]. The set of descriptors, which enters as an input to the machine learning models, often unravels the qualitative description of target properties in the form of simple physical properties.

In recent years, the high-throughput and machine learning methods have been used extensively for designing thermoelectrics. Since these methods rely on the quantity as well as quality of data, this requirement has spur an extensive effort to develop various databases focusing on thermoelectric properties of materials [32–37]. By specifying various screening criteria, these databases are utilized for high-throughput screening of materials with desired electronic and thermal transport properties. The very first effort in this direction was made by Madsen et al. [38], wherein an automated band structure based high-throughput screening was employed on Sb-containing compounds in Inorganic Crystal Structure Database and LiZnSb was suggested as one of the potential thermoelectric compounds. Since then, there is surge in high-throughput screening of efficient thermoelectric materials [39–48]. However, high-throughput screening requires the estimate of target property for all the compounds in the database and hence still relies on availability of extensive computational resources to compute the target property. To accelerate this process, these databases have been utilized to develop machine learning based prediction models for electronic as well as thermal transport properties [47–51].

From the perspective of thermoelectric screening, simultaneous assessment of electronic as well as thermal transport properties is required. However, the data-assisted approaches have been utilized to develop independent prediction models for these properties. The proposed material with favorable electronic transport may lack in exhibiting low thermal conductivity and vice versa, thereby may not be a potential candidate for thermoelectric. This implies that a connection, if any, between these two transport properties would be very significant for making the thermoelectric screening efficient. Recently, using machine learning, a connection between these transport properties is unraveled by identifying the common descriptors affecting both [48]. Bonding characteristics are shown to control both the transport properties and hence correlate the otherwise independent transport properties. This work demonstrated the power of machine learning in identifying hidden connections between unrelated quantities.

Although the data-assisted methods represent significant advancement in accelerated screening of materials with desired functionalities, one of the bottlenecks to be addressed is the transferability of developed models across different class of materials. Most of the machine learning models developed on one class of materials show poor transferability when tested on another class. This emphasizes the need to develop a generalized universal model for a given target property of interest. Recently, an algorithm 'guided patchwork kriging' is proposed for building a generalized model for lattice thermal conductivity [52].

In this chapter, we will discuss major milestones achieved using the high-throughput and machine learning approaches for accelerated screening of thermoelectrics. The chapter is arranged as follows: In Sect. 2, the generic computational tools required for assessing the thermoelectric properties will be discussed. It will also include a brief introduction to data-assisted algorithms for development of prediction models. Section 3 will include a brief overview of available databases and the descriptors employed for developing prediction models. Section 4 will discuss the efforts to address the electronic as well as thermal transport properties using high-throughput and machine learning methods. Section 5 will introduce the potential of machine learning in establishing a connection between electronic and thermal transport properties. Section 6 will focus on algorithmic developments for highly transferable prediction models. The final Sect. 7 will conclude the chapter along with future perspectives in the direction of accelerated thermoelectric materials discovery.

2 Methodology

Building computational databases for high-throughput and machine learning methods requires the inputs from density functional theory (DFT)-based approaches. The theoretical estimation of various properties within DFT framework can be obtained with the help of outputs from the solution of Kohn-Sham equations [53, 54]. There are different possible choices to take into consideration for solving the Kohn-Sham equations such as type of basis sets, exchange and correlation functional, and representation of ion-electron interactions. Typical calculations use plane-wave basis set in conjugation with local density approximation (LDA) or generalized gradient approximation (GGA) for exchange and correlation [55–57] by representing core and valence electron interactions via projector augmented wave (PAW) potentials [58, 59]. Due to inability of local and semi-local functionals (LDA and GGA) in accurately describing exchange and correlation, one often has to use resource-extensive approximations such as GW [60]. The choice of approximations depends on the trade-off between the required accuracy and computational efficiency. There are various widely used DFT codes available to perform these calculations such as Vienna Ab initio Simulation Package (VASP) and WIEN2k code [55, 56, 61]. These electronic structure methods have been proven successful in estimating

various microscopic properties of materials and in providing deeper insights into fundamental physical and chemical properties.

By taking the input eigenvalues from electronic structure calculations, the electronic transport properties can be obtained by solving the semi-classical Boltzmann transport equation (BTE) under constant scattering time approximation [62]. Under this approximation, it is assumed that relaxation time has very less dependence on temperature as well as carrier concentration. The electronic structure calculations coupled with solution of BTE can provide Seebeck coefficient S and scaled electrical conductivity $\frac{\sigma}{\tau}$. The numerical implementation for solving BTE for electronic transport properties is available in the software package BoltzTraP [63]. The relaxation time τ can be approximated either by using deformation potential theory [64] or by fitting scaled electrical conductivity data to experiments. For obtaining the thermal properties, BTE is coupled with harmonic and anharmonic interatomic force constants (IFCs). DFT can provide IFCs by calculating the forces using Hellmann-Feynman theorem [65]. Harmonic IFCs describing the vibrational spectrum can be obtained by various methods such as using frozen phonon method and density functional perturbation theory [66]. The software tool such as Phonopy can diagonalize the dynamical matrix and hence can provide the phonon eigenvalues [67]. The numerical implementation to obtain lattice thermal conductivity using harmonic and anharmonic IFCs is also available in various software packages such as ShengBTE [68] and Phono3py [69, 70].

For developing the machine learning based prediction models, the relationship between the input descriptors and target output is established using various statistical techniques [23, 71]. Depending upon the type of database, there are various methods, which can be employed for development of prediction models such as linear regression, polynomial regression, ridge regression, Gaussian process regression, logistic regression, Bayesian optimization, decision trees, and neural networks. The details about these methods can be found in the review article by Wang et al. [37] and references therein. The performance of developed models is often assessed by defining the metric root mean square error (RMSE) and coefficient of determination (R^2). Low RMSE along with high R^2 is considered as a quality regression metric for the developed models.

3 Ingredients for Statistical Methods

One of the most important requirements for the statistical methods is the availability of databases of properties for a large class of materials. Besides the experimentally available data, advancement in computational resources has led to development of various high-quality computational databases containing information of various physical properties of enormously large number of materials [37, 72]. Most of such databases are publicly available to the community, such as Materials Project [73], Open Quantum Materials Database [74], AFLOW for Materials [75], Novel Materials Discovery [76], Polymer Genome [77], aNANt [30], and NIST JARVIS

[78]. The efforts to generate data specific to thermoelectric properties are growing recently either by collecting the properties from the literature [40] or by explicit theoretical calculations [33, 47, 48, 50, 52]. These databases could be utilized in high-throughput screening and development of machine learning based prediction models.

For machine learning based prediction models, the choice of descriptors is another crucial ingredient besides the high-quality data for property of interest. Since the purpose of machine learning methods is to develop prediction models for resource-extensive properties, it is always preferred to have the set of descriptors, which are easily available. These descriptors may include (**a**) the information of elemental properties such as melting point, boiling point, electronegativity, and atomic mass; (**b**) information of structural properties such as number of elements, number of atoms, bond distances, and coordination number; (**c**) information from computationally inexpensive DFT calculation outputs; and (**d**) properties quantified from the emerging trends from the data or the correlations with target output. Given the enormous choice of availability of such descriptors and their dependence on the type of data as well as the property of interest, the selection process of descriptors is challenging [79]. There are several algorithms to select the optimized set of descriptors such as least absolute selection and shrinkage operator (LASSO) [80], SISSO [81], and principal component analysis (PCA) [82]. By selecting an appropriate set of descriptors, machine learning methods can be employed for accelerated prediction of target properties of interest. The schematic illustrating the data-assisted materials discovery is shown in Fig. 1.

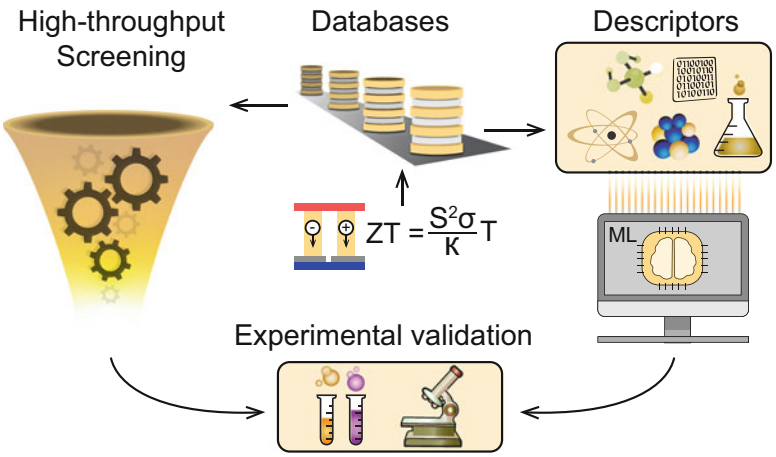

Fig. 1 Schematic illustrating the data-assisted high-throughput and machine learning based discovery of thermoelectric materials

4 High-Throughput Screening and Machine Learning Prediction Models for Thermoelectrics

For thermoelectrics, the properties need to be addressed are electronic transport properties, namely, Seebeck coefficient, electrical conductivity, and thermal transport properties, namely, lattice thermal conductivity. For the electronic transport part, the very first effort of employing high-throughput screening was on Sb-containing compounds available in the Inorganic Crystal Structure Database [38]. For the initial screening, compounds with disorders, partial occupancies, containing lanthanide atoms, or highly electronegative elements were dropped. Among the remaining 570 compounds, this study proposed the narrow band gap LiZnSb system as a potential thermoelectric material among ZnSb systems. For addressing the electronic transport properties in nanograined systems, which are considered to be efficient thermoelectrics than their corresponding bulk counterparts, high-throughput scheme by introducing constant mean free path approximation was proposed [39]. In this approximation, the mean free path was correlated with the grain size. The power factor for more than 2500 compounds from the AFLOW repository was computed in the nanograin limit, and its correlation with carrier mass and electronic band structure was presented. This work outlined the guiding rules for screening high power factor nanograined materials. The nanograined approximation to calculate the transport coefficients was further employed on half-Heusler compounds [41]. By applying electronic and thermodynamic filtering criterion for 79,057 half-Heusler compounds from AFLOW repository, the transport properties of 75 thermodynamically stable compounds were characterized in the nanograin limit. This study identifies that nanograined half-Heuslers have higher figure of merit as compared to potential thermoelectric materials belonging to Group IV and III–V. For class-independent high-throughput screening of electronic transport properties, a highly diverse database of 2838 compounds covering wide elemental, structural, and chemical space was generated [48]. Several compounds with simultaneously high Seebeck coefficient S and scaled electrical conductivity $\frac{\sigma}{\tau}$ were proposed, resulting in identification of ultrahigh power factor materials. High throughput has also been utilized to draw conclusions about the transport properties based on the trends in the certain properties. For example, high-throughput screening of data from the Materials Project was carried out to study the Fermi surface complexity [46]. It was found that the complexity factor is highly correlated with inertial effective mass, which has significant effect on power factor. Hence, this study proposed inertial effective mass as an effective descriptor affecting the power factor of materials.

Besides high-throughput screening, there are machine learning based prediction models developed for electronic transport properties. Starting from a database of 2838 compounds, the prediction models for Seebeck coefficient S and scaled electrical conductivity $\frac{\sigma}{\tau}$ were developed [48]. The descriptors used for developing the prediction models consisted of elemental and structural properties of compounds. The elemental descriptors comprised of mean and standard deviation of easily

available properties such as boiling point ($B.P.$), melting point ($M.P.$), specific heat (c_p^g), molar specific heat (c_p), molar volume (V_m), heat of fusion (H_f), heat of vaporization (H_v), Pauling electronegativity (χ_p), first ionization energy ($I.E._1$), group and period in the periodic table, elemental thermal conductivity (κ_{ele}), atomic number (Z), atomic mass (M), covalent radius (r_{cov}), van der Waals radius (r_{vdw}), and density (ρ). The structural information included average bond distance ($B.D.$), average bond strength ($B.S.$), volume per atom (V_{atom}), volume of cell (V_{cell}), and coordination number ($C.N.$). The target property was chosen to be log-scaled mean of S and $\frac{\sigma}{\tau}$ in the carrier concentration range 10^{19} to $10^{22}\,\mathrm{cm}^{-3}$. The choice of log scale was to take care of the large variation of transport properties. The chosen carrier concentration range is optimal for achieving high power factor thermoelectric materials. The mean of transport properties was chosen because the inverse coupled relationship between S and $\frac{\sigma}{\tau}$ would make the mean to correspond to the regime, where maximum of power factor occurs. For development of the models, Gaussian process regression was used, and the relevant set of descriptors employed for prediction was selected by least absolute shrinkage and selection operator (LASSO) [23, 71]. It selects the descriptors by the L_1 regularization. For n-type and p-type log-scaled mean of S, the developed model gives train/test RMSE of 0.10/0.10, R^2 of 0.98/0.98, and RMSE of 0.12/0.12, R^2 of 0.97/0.97, respectively. For the scaled electrical conductivity, the developed model for n-type and p-type log-scaled mean of $\frac{\sigma}{\tau}$ gives train/test RMSE of 0.08/0.08, R^2 of 0.99/0.99 and RMSE of 0.10/0.10, R^2 of 0.99/0.99, respectively. The unprecedented accuracies of the developed models for electronic transport properties ensure scanning a large search space of materials with favorable electronic transport properties in a very less time without the need of explicit DFT calculations. For evaluating the figure of merit, one needs to calculate σ by estimating the relaxation time τ either from experiments or approximation such as deformation potential theory [64]. Recently, a prediction model for room temperature electrical conductivity is developed on an experimental database of 124 compounds using gradient boost regression [49]. The developed model gives high accuracy with train/test RMSE of 0.21/0.22 and R^2 of 0.98/0.98. Using the predicted electrical conductivity and the calculated scaled electrical conductivity, the temperature dependence of electronic relaxation time is determined, which outperforms the dependence obtained from deformation potential approach.

Since thermal transport estimation is more resource extensive than electronic transport, extensive efforts have been devoted in employing data-assisted methods for thermal transport property κ_l. A combined high-throughput and machine learning based approach was proposed by Carrete et al. to identify low and high κ_l half-Heusler compounds [42]. Starting from a set of 79,057 half-Heusler compounds from AFLOW repository, high-throughput screening conditions such as negative formation energy, mechanical stability, and thermodynamic stability were imposed, which resulted in 75 compounds. Using the random forest regression technique and suitable descriptors, this study developed a classification model to identify high and low κ_l half-Heuslers, which resulted in accelerated screening of desired thermoelectrics among the half-Heusler compounds. In an effort to develop computationally inexpensive approach for high-throughput-based estimation of

κ_l, Automatic-Gibbs-Library (AGL) have been implemented within AFLOW and Materials Project databases, which calculates the thermal properties based on quasi-harmonic Debye approximation [34]. The AGL estimated and experimental κ_l for 75 compounds of different symmetry showed high Pearson correlation. This study provided accelerated screening of desired thermoelectrics based on the ordinal ranking of κ_l through AGL. Besides AGL, there are development of several semiempirical models, which take few inexpensive DFT parameters and structural attributes as input and hence can be utilized for high-throughput pre-screening [83, 84]. Further, to cover the large exploration space for searching low κ_l materials, Bayesian optimization-based virtual screening of materials was carried out [50]. First-principles anharmonic calculations were used to calculate κ_l of 101 compounds containing rocksalt, zincblende, and wurtzite structures. The model constructed using this dataset was used for virtual screening of 54,779 compounds through Bayesian optimization. Based on the high ranking, 221 compounds were proposed as potential candidates with low κ_l. Hence, the virtual screening can be very useful for exploring a diverse database without prior estimate of κ_l for all the compounds.

For most of the machine learning based prediction models of lattice thermal conductivity, the set of descriptors is either very large or consisted of complex physical properties. Additionally, the relevant descriptors are often screened by compressed sensing methods. Recently, by generating a high-throughput property map, a set of four descriptors, directly related to the physics of lattice thermal conductivity, has been proposed [47]. Starting from a dataset of 2162 binary, ternary, and quaternary compounds belonging to different crystal systems, the screening criterion such as non-metallic behavior and dynamical stability was employed. The screening resulted in identification of 12 ultralow and 11 ultrahigh κ_l compounds. For the selection of descriptors, an extensive property map of harmonic and quasi-harmonic properties was analyzed, as illustrated in Fig. 2. These properties exhibited the trends for broadly categorizing the compounds falling under ultralow and ultrahigh lattice thermal conductivity. For example, the span of phonon frequencies for ultralow κ_l compounds was found to be lower compared to ultrahigh κ_l compounds. Therefore, maximum phonon frequency (ω_{max}) was chosen to be one of the descriptors to capture qualitative trends in the variation of κ_l. Among the

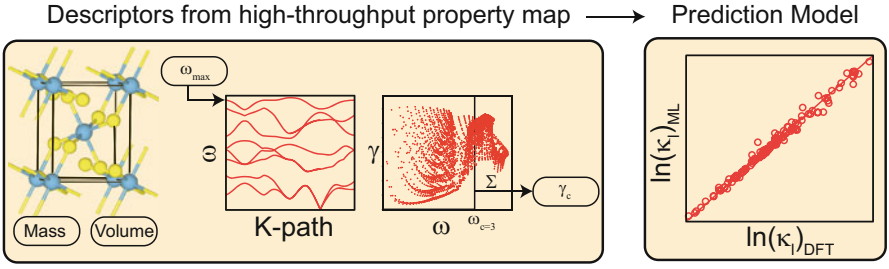

Fig. 2 Selection of descriptors from high-throughput generated property map

quasi-harmonic properties, the Grüneisen parameter is often correlated to the extent of anharmonicity in a material, wherein high Grüneisen parameter corresponding to high anharmonicity leads to low κ_l and vice versa. However, this dependence alone was not sufficient to explain the observed trends in κ_l in the database. Instead, it was found that the spread of Grüneisen parameter with respect to frequency was representative of low and high κ_l. For instance, materials with ultralow κ_l had larger spread in the low-frequency regime as compared to materials with ultrahigh κ_l, thereby confirming the fact that low-lying modes dominate the anharmonicity. Hence, the spread of Grüneisen parameter was quantified in the low-frequency regime to define another descriptor for κ_l. The cut-off to define the low-frequency regime was decided by analyzing the Pearson correlation coefficient of integrated Grüneisen parameter for different values of low frequencies with κ_l. The spread integrated upto 3 THz was found to have maximum correlation with κ_l. Hence, the second proposed descriptor was integrated Grüneisen parameter up to 3 THz ($\gamma_{c=3}$). Among the structural properties, the average mass of constituent elements (M) and the volume of the system (V) were found to be roughly correlated inversely with κ_l. Hence, the proposed four descriptors ω_{max}, $\gamma_{c=3}$, M, and V were able to broadly capture the variation in κ_l across different class of systems, without explicit evaluation of higher-order anharmonic force constants.

The property map-guided descriptors were used in development of prediction model for κ_l, as illustrated in Fig. 2. Gaussian process regression was employed in developing the model, and the best model gave train/test RMSE of 0.20/0.21 and R^2 of 0.99/0.99 for log-scaled κ_l. The proposed descriptors have close relation with widely used Slack model, where κ_l is defined as

$$\kappa_l = A\frac{M\theta_D^3 V^{\frac{1}{3}}}{\gamma^2 T n^{\frac{2}{3}}}$$

Here θ_D is Debye temperature, n is number of atoms in the unit cell, and γ is the average Grüneisen parameter. The constant A is defined as

$$A = \frac{2.43 \times 10^{-8}}{1 - \frac{0.514}{\gamma} + \frac{0.228}{\gamma^2}}.$$

By estimating θ_D from the phonon density of states in the frequency range 0 to 0.25 of maximum phonon frequency, κ_l using Slack model was estimated for all the compounds in the database. On comparison with κ_l calculated using first-principles anharmonic calculations, it was found that Slack model κ_l was overestimated for majority of compounds. To have a comparison with the machine learning prediction model, another prediction model for κ_l was developed using properties entering in Slack model as descriptors, namely, θ_D, γ, M, V, and n. The developed model using Slack descriptors gave train/test RMSE of 0.29/0.30, which was higher than the developed model using property map guided descriptors. Hence, the simpler harmonic and quasi-harmonic-based descriptors could be utilized for accelerated prediction of κ_l. These high-throughput and machine learning based methods

for both the electronic and thermal transport properties illustrate the process of accelerated identification of materials. If the search space of all these studies is combined, it covers huge diversity among the materials. Estimating the transport properties for these many compounds would have taken unrealistically long time by conventional methods, whereas the data-assisted methods are able to give the reliable estimate in fraction of time, accelerating the process by several orders of magnitude.

5 Connection Between Electronic and Thermal Transport

The data-assisted methods, described above, address the electronic and thermal transport properties independently. However, for the screening of efficient thermoelectrics, the materials need to have simultaneously favorable electronic as well as thermal transport properties. Moreover, there is no discussion of a convincing connection between these transport properties by conventional methods, despite these properties have overlapping origin lying in various forms of electron-phonon interactions. Recently, a connection between electronic and thermal transport properties has been established with the help of machine learning methods [48]. The rationale behind recognizing the connection between these otherwise independent transport properties was to identify common parameters, which control both of these properties, simultaneously. By closely analyzing the above-discussed prediction models for electronic and thermal transport properties, it is found that a set of elemental and structural descriptors predict both of these transport properties with unprecedented accuracies. This implies that these descriptors may provide a possible bridge to relate both of these properties. This has been illustrated schematically in Fig. 3.

Among elemental and structural descriptors, only a minimal set of those descriptors was chosen, which had well-defined underlying physics in controlling both the transport properties. One such descriptor was electronegativity. The difference in electronegativity of constituent elements in a compound is a deciding factor

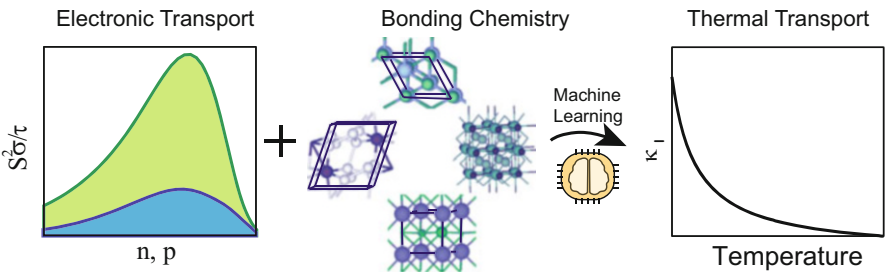

Fig. 3 Machine learning unraveling the connection between electronic and thermal transport via bonding information of materials

of covalent or ionic bonding, which eventually affects dispersion of bands [85–87]. Less or highly dispersive bands have been shown to have profound effect on electronic transport properties S and σ [9, 10, 14]. Electronegativity has also been directly related to ionicity having inverse correlation with thermal transport property, κ_l [88–90]. Hence, electronegativity could be one of the possible bridging descriptors. The other descriptors of such type included the structural attributes such as volume, coordination number, bond distances, and bond strength. These attributes have been shown to affect significantly the electronic dispersion features [91–95] and hence the electronic transport properties. These descriptors are also shown to control thermal transport properties [16, 95]. Volume of system has been shown to have inverse correlation with κ_l [47]. Coordination number has been one of the descriptors assessing anharmonicity and hence κ_l in a system [83]. Nature of chemical bonding controls the phonon group velocities. Soft lattices with weaker bonding strength and large bond distances will have low phonon group velocities and hence will have low κ_l. Hence, the descriptor set consisting of electronegativity, volume, coordination number, and bonding attributes controls both the transport properties.

These descriptors clearly indicated a possibility of connection between these transport properties. To unravel this connection, a prediction model for thermal transport property κ_l was developed by giving input to the model as electronic transport properties along with these bridging descriptors. The descriptors corresponding to electronic transport properties were mean and standard deviation of S and $\frac{\sigma}{\tau}$ for both n- and p-type carriers, wherein mean would correspond to power factor peak and standard deviation would capture the variation of these properties with respect to carrier concentration. Using these descriptors, Gaussian process regression-based prediction model for log-scaled κ_l gave train/test RMSE of 0.19/0.19 and R^2 of 0.99/0.99. The high accuracy of the developed model signified the connection between two transport properties via few bridging descriptors. To get further physical insights about the connection, simple mathematical operations were employed to generate millions of non-linear combinations of the desecrators used for the development of prediction model. By analyzing the Pearson correlation of these descriptors with κ_l, the formula showing highest correlation of 0.70 was of the form:

$$exp\left(\frac{\sigma}{\tau}_{n}^{mean} + B.S.\right)\frac{1}{exp(B.D.)}$$

This includes scaled electrical conductivity $\frac{\sigma}{\tau}$, bond distances $B.D.$, and bond strength $B.S.$ The bond strength was estimated by integrating the bonding and antibonding contributions in crystal orbital Hamilton population (COHP) [96, 97]. This analysis further substantiated the importance of bonding chemistry in unraveling the connection between the two transport properties. This connection could be utilized for efficient screening of desired thermoelectrics with simultaneous control over electronic as well as thermal transport properties of a system. The work also shows a pathway to connect oftentimes unconnected physical properties. This may open up a new and very unconventional paradigm for physical sciences.

6 Towards Universal Models: Algorithm Development

Various data-assisted efforts outlined above highlight tremendous contribution by the scientific community in accelerated discovery of materials with desired properties. However, for a single target property of interest, there is availability of various developed prediction models. These models differ broadly with respect to the set of descriptors and type of class of materials involved for training the model. Since the predictability quality of any machine learning model depends profoundly on the type of data being fed to the model for training, this poses a serious concern towards transferability of available models, when tested on different classes not included in the training database. The transferability issue has been addressed by proposing a new algorithm to develop generalized model for lattice thermal conductivity [52]. To have the generalizability in the model, the input data has to be highly diverse with respect to elemental, chemical, and structural space. As shown in Fig. 4, such a dataset was compiled, which includes materials belonging to all seven crystal systems, constituent elements belonging to any group of the periodic table representing diversity in elemental physical properties, and the target output κ_l having four orders of magnitude variation. The Gaussian process regression-based prediction model for this comprehensive dataset gave train/test RMSE of 0.24/25 for log-scaled κ_l. The accuracy of developed model was very less compared with state-of-the-art models for κ_l discussed above. Hence, increasing variability in data affects the prediction accuracy. One of the major reasons for inferior prediction accuracy for versatile database could be the inability of a single model to capture every possible local detail in the database. Hence, localized regression-based methods could be the solution to develop generalized models without compromising the prediction accuracy.

There are various successful localized regression-based approximations [98–106], wherein the input database is divided into smaller subsets and highly accurate local prediction models corresponding to each subset are developed. However, two different local developed models may not give the same prediction output at the common boundary separating the corresponding local regimes. Hence, care must be taken to smoothen out the discontinuity at the shared boundaries while using these regression techniques. Among several algorithms, which address the discontinuity issue, patchwork kriging is one of the highly numerically stable algorithms [107, 108]. In patchwork kriging, the created local regions are patched together at the common boundary. The patched region contains few data points belonging to both the local regions, with the constraint that models developed on both local regions should predict similar target output for all the data points in the patch.

For employing this approximation for prediction of κ_l, one of the crucial steps was to identify the properties with respect to which the local regimes in the database would be created. Proper subdivisions of the data are one of the detrimental factors for assessing the prediction quality of the developed local models. Hence, the database was subdivided with respect to various easily accessible properties. The

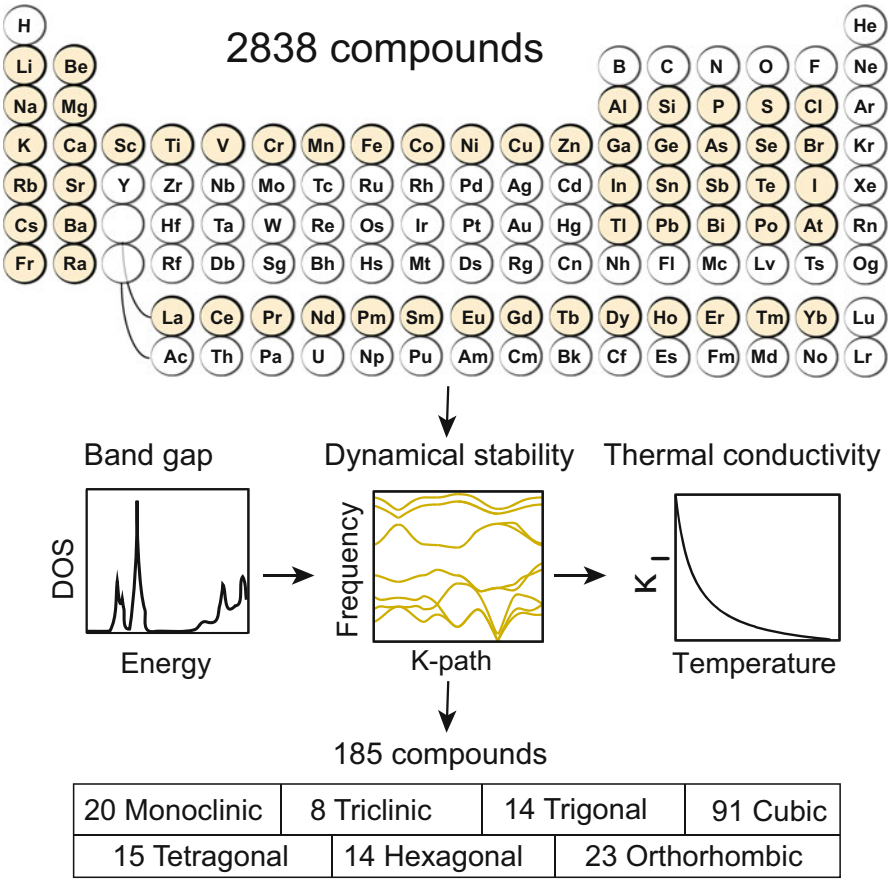

Fig. 4 Generation of extensive database consisting of compounds with all seven crystal symmetries for building transferable model

subdivisions with respect to κ_l were also considered. In each of these trials of dividing the data, only two local regions were created. This was because the size of database was not too large and increasing the local regimes would have resulted into overfitted local models due to less data points in each local region. The two partitions were created with respect to the ascending order of magnitude of different properties. The range of magnitude of a property in particular local region was decided such that there are fairly similar numbers of data points in each partition.

For each local dataset belonging to partitioning with respect to different properties, Gaussian process regression-based models were developed using elemental and structural descriptors. The prediction accuracies belonging to local regimes with respect to different properties were very different, further emphasizing the fact that localized regression-based methods depends significantly on the type of data in the created local regimes. In most of such created partitions, the model

gave high accuracy of prediction only in one partition. However, the models obtained by partitioning the data with respect to κ_l gave similar performance quality in both the partitions. It also resulted in models with highest accuracy, wherein train/test RMSE of 0.13/0.13 and 0.11/0.12 was obtained for the first and second partition, respectively. There was a significant improvement in accuracy compared to the single model developed above on this database. Additionally, the localized regression-based accuracies achieved here were higher/comparable to models developed on particular class of materials [51, 109].

Although the above approach gave excellent accuracy using patchwork kriging, the partitioning with respect to κ_l makes it challenging to deploy this approach for compounds with no available information of their κ_l magnitude. In order to decide the particular local partition for unknown κ_l compounds, the use of model developed over the entire database was proposed. This model, termed as global model, would predict at least the correct order of magnitude of κ_l for unknown compounds and hence can further guide them towards a particular partition to have accurate estimate of κ_l using the local model of that partition. This two-step prediction algorithm was termed as guided patchwork kriging, wherein the global model will guide the compounds in deciding the particular local partition model for accurate prediction. The proposed approach can spur more efforts by the scientific community in the direction of development of universal models for desired target property of interests.

7 Conclusions and Future Perspective

In conclusion, we have described the high-throughput and machine learning based approaches to screen the large search space of materials for thermoelectric applications. Given the computational complexity involved and the interdependence of transport properties, data-assisted methods have contributed significant advancement in exploring the potential materials for thermoelectrics. Based on various forms of regression analysis, many compounds in different categories have been proposed with favorable electronic and thermal transport properties, which can be confirmed experimentally. The machine learning methods have also been successful in unraveling a connection between otherwise independent electronic and thermal transport properties. This could pave way for more effective screening of thermoelectrics by addressing the inversely coupled properties simultaneously. The current efforts of the community are in the direction of developing unique universal models for a single target property of interest. The universal models will be highly transferable across different possible classes of materials.

Despite the considerable progress, there are several challenges as well as areas to focus upon to further take the accelerated thermoelectric search to newer heights. The very first challenge could be towards development of universal models. Although guided patchwork kriging approach has been proposed to provide transferable models, the database employed contains up to quaternary compounds due to involved computational complexity, with increase in system size. Hence,

universal models, which include extensively larger database of materials, are required. The compilation of such database could be possible if every database employed for high throughput and machine learning is made available to the community. Another approach to address transferability could be achieved by developing materials using adaptive design. The virtual database for adaptive design does not require the information of target output beforehand and hence could be utilized to search newer possible compositions as potential thermoelectrics. Another challenge is experimental realization of proposed thermoelectric materials by data-assisted methods. Even if a material has the highest figure of merit, there are several factors involved in utilizing it as thermoelectric device such as assembling process and finding suitable contact interface. Hence, if experimental inputs and theoretical outputs are combined, major breakthroughs could be achieved, and promises of thermoelectric towards a more greener and sustainable future could be fulfilled.

Acknowledgments The authors thank the Materials Research Centre, Thematic Unit of Excellence, and Supercomputer Education and Research Centre, Indian Institute of Science, for providing computing facilities. The authors acknowledge the support from Institute of Eminence (IoE) MHRD grant.

References

1. Wood, C. (1988). Materials for thermoelectric energy conversion. *Reports on Progress in Physics, 51*, 459.
2. Mahan, G., & Sofo, J. (1996). The best thermoelectric. *Proceedings of the National Academy of Sciences of the United States of America, 93*, 7436–7439.
3. Mahan, G. (1997). Good thermoelectrics. *Solid State Physics, 51*, 81–157.
4. DiSalvo, F. J. (1999). Thermoelectric cooling and power generation. *Science, 285*, 703–706.
5. Tritt, T. M., & Subramanian, M. (2006). Thermoelectric materials, phenomena, and applications: A bird's eye view. *MRS Bulletin, 31*, 188–198.
6. Bell, L. E. (2008). Cooling, heating, generating power, and recovering waste heat with thermoelectric systems. *Science, 321*, 1457–1461.
7. Snyder, G. J., & Toberer, E. S. (2008). Complex thermoelectric materials. *Nature Materials, 7*, 105–114.
8. Dehkordi, A. M., Zebarjadi, M., He, J., & Tritt, T. M. (2015). Thermoelectric power factor: Enhancement mechanisms and strategies for higher performance thermoelectric materials. *Materials Science and Engineering R: Reports, 97*, 1–22.
9. Juneja, R., Pandey, T., & Singh, A. K. (2017). High thermoelectric performance in n-doped siliconbased chalcogenide Si_2Te_3. *Chemistry of Materials, 29*, 3723–3730.
10. Xing, G., Sun, J., Li, Y., Fan, X., Zheng, W., & Singh, D. J. (2017). Electronic fitness function for screening semiconductors as thermoelectric materials. *Physical Review Materials, 1*, 065405.
11. Mukherjee, M., Yumnam, G., & Singh, A. K. (2018). High thermoelectric figure of merit via tunable valley convergence coupled low thermal conductivity in $A^{II}B^{IV}$ C_2^V chalcopyrites. *The Journal of Physical Chemistry C, 122*, 29150–29157.
12. Christensen, M., Abrahamsen, A. B., Christensen, N. B., Juranyi, F., Andersen, N. H., Lefmann, K., Andreasson, J., Bahl, C. R., & Iversen, B. B. (2008). Avoided crossing of rattler modes in thermoelectric materials. *Nature Materials, 7*, 811–815.

13. Nolas, G., Cohn, J., & Slack, G. (1998). Effect of partial void filling on the lattice thermal conductivity of skutterudites. *Physical Review B, 58*, 164.
14. Juneja, R., & Singh, A. K. (2019). Rattling-induced ultralow thermal conductivity leading to exceptional thermoelectric performance in $AgIn_5S_8$. *ACS Applied Materials & Interfaces, 11*, 33894–33900.
15. Meng, et al. (2019). Thermal conductivity enhancement in MoS_2 under extreme strain. *Physical Review Letters, 122*, 155901.
16. Lee, S., Esfarjani, K., Luo, T., Zhou, J., Tian, Z., & Chen, G. (2014). Resonant bonding leads to low lattice thermal conductivity. *Nature Communications, 5*, 3525.
17. Chen, Z., Ge, B., Li, W., Lin, S., Shen, J., Chang, Y., Hanus, R., Snyder, G. J., & Pei, Y. (2017). Vacancy-induced dislocations within grains for high-performance PbSe thermoelectrics. *Nature Communications, 8*, 1–8.
18. Biswas, K., He, J., Blum, I. D., Wu, C.-I., Hogan, T. P., Seidman, D. N., Dravid, V. P., & Kanatzidis, M. G. (2012). High-performance bulk thermoelectrics with all-scale hierarchical architectures. *Nature, 489*, 414–418.
19. Wei, et al. (2020). Thermodynamic routes to ultralow thermal conductivity and high thermoelectric performance. *Advanced Materials, 32*, 1906457.
20. LeSar, R. (2009). Materials informatics: An emerging technology for materials development. *Statistical Analysis and Data Mining, 1*, 372–374.
21. Curtarolo, S., Hart, G. L., Nardelli, M. B., Mingo, N., Sanvito, S., & Levy, O. (2013). The high-throughput highway to computational materials design. *Nature Materials, 12*, 191.
22. Mueller, T., Kusne, A. G., & Ramprasad, R. (2016). Machine learning in materials science: Recent progress and emerging applications. *Reviews in Computational Chemistry, 29*, 186–273.
23. Murphy, K. P. (2012). *Machine learning: A probabilistic perspective.* Cambridge, MA: Massachusetts Institute of Technology Press.
24. Pilania, G., Wang, C., Jiang, X., Rajasekaran, S., & Ramprasad, R. (2013). Accelerating materials property predictions using machine learning. *Scientific Reports, 3*, 2810.
25. Seko, A., Maekawa, T., Tsuda, K., & Tanaka, I. (2014). Machine learning with systematic density-functional theory calculations: Application to melting temperatures of single- and binary-component solids. *Physical Review B, 89*, 054303.
26. Seko, A., Takahashi, A., & Tanaka, I. (2014). Sparse representation for a potential energy surface. *Physical Review B, 90*, 024101.
27. Xue, D., Balachandran, P. V., Hogden, J., Theiler, J., Xue, D., & Lookman, T. (2016). Accelerated search for materials with targeted properties by adaptive design. *Nature Communications, 7*, 11241.
28. Kim, C., Pilania, G., & Ramprasad, R. (2016). From organized high-throughput data to phenomenological theory using machine learning: The example of dielectric breakdown. *Chemistry of Materials, 28*, 1304–1311.
29. Pilania, G., Mannodi-Kanakkithodi, A., Uberuaga, B., Ramprasad, R., Gubernatis, J., & Lookman, T. (2016). Machine learning bandgaps of double perovskites. *Scientific Reports, 6*, 19375.
30. Rajan, A. C., Mishra, A., Satsangi, S., Vaish, R., Mizuseki, H., Lee, K.-R., & Singh, A. K. (2018). Machine-learning-assisted accurate band gap predictions of functionalized MXene. *Chemistry of Materials, 30*, 4031–4038.
31. Mishra, A., Satsangi, S., Rajan, A. C., Mizuseki, H., Lee, K.-R., & Singh, A. K. (2019). Accelerated data-driven accurate positioning of the band edges of MXenes. *The Journal of Physical Chemistry Letters, 10*, 780–785.
32. Gaultois, M. W., Oliynyk, A. O., Mar, A., Sparks, T. D., Mulholland, G. J., & Meredig, B. (2016). Perspective: Web-based machine learning models for real-time screening of thermoelectric materials properties. *APL Materials, 4*, 053213.
33. Gorai, P., Gao, D., Ortiz, B., Miller, S., Barnett, S. A., Mason, T., Lv, Q., Stevanović, V., & Toberer, E. S. (2016). TE design lab: A virtual laboratory for thermoelectric material design. *Computational Materials Science, 112*, 368–376.

34. Toher, C., Plata, J. J., Levy, O., De Jong, M., Asta, M., Nardelli, M. B., & Curtarolo, S. (2014). High-throughput computational screening of thermal conductivity, debye temperature, and Grüneisen parameter using a quasiharmonic debye model. *Physical Review B, 90*, 174107.
35. Toher, et al. (2017). Combining the AFLOW GIBBS and elastic libraries to efficiently and robustly screen thermomechanical properties of solids. *Physical Review Materials, 1*, 015401.
36. Urban, J. J., Menon, A. K., Tian, Z., Jain, A., & Hippalgaonkar, K. (2019). New horizons in thermo-24 electric materials: Correlated electrons, organic transport, machine learning, and more. *Journal of Applied Physics, 125*, 180902.
37. Wang, T., Zhang, C., Snoussi, H., & Zhang, G. (2020). Machine learning approaches for thermoelectric materials research. *Advanced Functional Materials, 30*, 1906041.
38. Madsen, G. K. (2006). Automated search for new thermoelectric materials: The case of LiZnSb. *Journal of the American Chemical Society, 128*, 12140–12146.
39. Wang, S., Wang, Z., Setyawan, W., Mingo, N., & Curtarolo, S. (2011). Assessing the thermoelectric properties of sintered compounds via high-throughput ab-initio calculations. *Physical Review X, 1*, 021012.
40. Gaultois, M. W., Sparks, T. D., Borg, C. K., Seshadri, R., Bonificio, W. D., & Clarke, D. R. (2013). Data-driven review of thermoelectric materials: Performance and resource considerations. *Chemistry of Materials, 25*, 2911–2920.
41. Carrete, J., Mingo, N., Wang, S., & Curtarolo, S. (2014). Nanograined half-heusler semiconductors as advanced thermoelectrics: An ab initio high-throughput statistical study. *Advanced Functional Materials, 24*, 7427–7432.
42. Carrete, J., Li, W., Mingo, N., Wang, S., & Curtarolo, S. (2014). Finding unprecedentedly low-thermal-conductivity half-heusler semiconductors via high-throughput materials modeling. *Physical Review X, 4*, 011019.
43. Chen, et al. (2016). Understanding thermoelectric properties from high-throughput calculations: Trends, insights, and comparisons with experiment. *Journal of Materials Chemistry C, 4*, 4414–4426.
44. Tabib, M. V., Løvvik, O. M., Johannessen, K., Rasheed, A., Sagvolden, E., & Rustad, A. M. (2018). Discovering thermoelectric materials using machine learning: Insights and challenges. In *International Conference on Artificial Neural Networks* (pp. 392–401).
45. Iwasaki, et al. (2019). Machine-learning guided discovery of a new thermoelectric material. *Scientific Reports, 9*, 2751.
46. Suwardi, A., Bash, D., Ng, H. K., Gomez, J. R., Repaka, D. M., Kumar, P., & Hippalgaonkar, K. (2019). Inertial effective mass as an effective descriptor for thermoelectrics via datadriven evaluation. *Journal of Materials Chemistry A, 7*, 23762–23769.
47. Juneja, R., Yumnam, G., Satsangi, S., & Singh, A. K. (2019). Coupling high-throughput property map to machine learning for predicting lattice thermal conductivity. *Chemistry of Materials, 31*, 5145–5151.
48. Juneja, R., & Singh, A. K. (2020). Unraveling the role of bonding chemistry in connecting electronic and thermal transport by machine learning. *Journal of Materials Chemistry A, 8*, 8716–8721.
49. Mukherjee, M., Satsangi, S., & Singh, A. K. (2020). A statistical approach for the rapid prediction of electron relaxation time using elemental representatives. *Chemistry of Materials, 32*, 6507–6514.
50. Seko, A., Togo, A., Hayashi, H., Tsuda, K., Chaput, L., & Tanaka, I. (2015). Prediction of low-thermal-conductivity compounds with first-principles anharmonic lattice-dynamics calculations and Bayesian optimization. *Physical Review Letters, 115*, 205901.
51. Seko, A., Hayashi, H., Nakayama, K., Takahashi, A., & Tanaka, I. (2017). Representation of compounds for machine-learning prediction of physical properties. *Physical Review B, 95*, 144110.
52. Juneja, R., & Singh, A. K. (2020). Guided patchwork kriging to develop highly transferable thermal conductivity prediction models. *Journal of Physics: Materials, 3*, 024006.
53. Kohn, W., & Sham, L. J. (1965). Self-consistent equations including exchange and correlation effects. *Physical Review, 140*, A1133.

54. Sham, L., & Schlüter, M. (1983). Density-functional theory of the energy gap. *Physical Review Letters, 51*, 1888.
55. Kresse, G., & Furthmüller, J. (1996). Efficient iterative schemes for ab initio total-energy calculations using a plane-wave basis set. *Physical Review B, 54*, 11169.
56. Kresse, G., & Furthmüller, J. (1996). Efficiency of ab-initio total energy calculations for metals and semiconductors using a plane-wave basis set. *Computational Materials Science, 6*, 15–50.
57. Perdew, J. P., Burke, K., & Ernzerhof, M. (1996). Generalized gradient approximation made simple. *Physical Review Letters, 77*, 3865.
58. Blöchl, P. E. (1994). Projector augmented-wave method. *Physical Review B, 50*, 17953.
59. Kresse, G., & Joubert, D. (1999). From ultrasoft pseudopotentials to the projector augmented-wave method. *Physical Review B, 59*, 1758.
60. Hedin, L. (1965). New method for calculating the one-particle green's function with application to the electron-gas problem. *Physical Review, 139*, A796.
61. Blaha, P., Schwarz, K., Madsen, G. K., Kvasnicka, D., Luitz, J., Laskowsji, R., Tran, F., & Marks, L. (2001). An augmented plane wave plus local orbitals program for calculating crystal properties, Techn. Universitat Wien, Austria.
62. Ziman, J. M. (1972). *Principles of the theory of solids*. Cambridge: Cambridge University Press.
63. Madsen, G. K., & Singh, D. J. (2006). BoltzTraP. A code for calculating band-structure dependent quantities. *Computer Physics Communications, 175*, 67–71.
64. Bardeen, J., & Shockley, W. (1950). Deformation potentials and mobilities in non-polar crystals. *Physical Review, 80*, 72.
65. Feynman, R. P. (1939). Forces in molecules. *Physical Review, 56*, 340.
66. Baroni, S., De Gironcoli, S., Dal Corso, A., & Giannozzi, P. (2001). Phonons and related crystal properties from density-functional perturbation theory. *Reviews of Modern Physics, 73*, 515.
67. Togo, A., & Tanaka, I. (2015). First principles phonon calculations in materials science. *Scripta Materialia, 108*, 1–5.
68. Li, W., Carrete, J., Katcho, N. A., & Mingo, N. (2014). ShengBTE: A solver of the Boltzmann transport equation for phonons. *Computer Physics Communications, 185*, 1747–1758.
69. Chaput, L., Togo, A., Tanaka, I., & Hug, G. (2013). Direct solution to the linearized phonon Boltzmann equation. *Physical Review Letters, 110*, 265506.
70. Togo, A., Chaput, L., & Tanaka, I. (2015). Distributions of phonon lifetimes in Brillouin zones. *Physical Review B, 91*, 094306.
71. Friedman, J., Hastie, T., & Tibshirani, R. (2001). *The elements of statistical learning* (Springer series in statistics, Vol. 1). New York: Springer.
72. Himanen, L., Geurts, A., Foster, A. S., & Rinke, P. (2019). Data-driven materials science: Status, challenges, and perspectives. *Advanced Science, 6*, 1900808.
73. Jain, A., Ong, S. P., Hautier, G., Chen, W., Richards, W. D., Dacek, S., Cholia, S., Gunter, D., Skinner, D., Ceder, G., & Persson, K. A. (2013). The materials project: A materials genome approach to accelerating materials innovation. *APL Materials, 1*, 011002.
74. Kirklin, S., Saal, J. E., Meredig, B., Thompson, A., Doak, J. W., Aykol, M., Rühl, S., & Wolverton, C. (2015). The open quantum materials database (OQMD): Assessing the accuracy of DFT formation energies. *Npj Computational Materials, 1*, 15010.
75. Curtarolo, et al. (2012). AFLOWLIB.ORG: A distributed materials properties repository from high-throughput ab initio Calculations. *Computational Materials Science, 58*, 227–235.
76. Draxl, C., & Scheffler, M. (2018). NOMAD: The FAIR concept for big data-driven materials science. *MRS Bulletin, 43*, 676–682.
77. Huan, T. D., Mannodi-Kanakkithodi, A., Kim, C., Sharma, V., Pilania, G., & Ramprasad, R. (2016). A polymer dataset for accelerated property prediction and design. *Scientific Data, 3*, 160012.

78. Choudhary, K., Kalish, I., Beams, R., & Tavazza, F. (2017). High-throughput identification and characterization of two-dimensional materials using density functional theory. *Scientific Reports, 7*, 5179.
79. Ghiringhelli, L. M., Vybiral, J., Levchenko, S. V., Draxl, C., & Scheffler, M. (2015). Big data of materials science: Critical role of the descriptor. *Physical Review Letters, 114*, 105503.
80. Tibshirani, R. (1996). Regression shrinkage and selection via the lasso. *Journal of the Royal Statistical Society: Series B, 58*, 267–288.
81. Ouyang, R., Curtarolo, S., Ahmetcik, E., Scheffler, M., & Ghiringhelli, L. M. (2018). SISSO: A compressed-sensing method for identifying the best low-dimensional descriptor in an immensity of offered candidates. *Physical Review Materials, 2*, 083802.
82. Jolliffe, I. T. (1986). *Principal component analysis* (pp. 129–155). New York: Springer.
83. Miller, et al. (2017). Capturing anharmonicity in a lattice thermal conductivity model for high-throughput predictions. *Chemistry of Materials, 29*, 2494–2501.
84. Yan, J., Gorai, P., Ortiz, B., Miller, S., Barnett, S. A., Mason, T., Stevanovic, V., & Toberer, E. S. (2015). Material descriptors for predicting thermoelectric performance. *Energy & Environmental Science, 8*, 983–994.
85. Hoffmann, R. (1987). How chemistry and physics meet in the solid state. *Angewandte Chemie International, 26*, 846–878.
86. Rohrer, G. S. (2001). *Structure and bonding in crystalline materials.* Cambridge: Cambridge University Press.
87. Cox, P. A. (1987). *The electronic structure and chemistry of solids* (Vol. 231). Oxford: Oxford University Press.
88. Pauling, L. (1960). *The nature of the chemical bond* (Vol. 260). Ithaca: Cornell University Press.
89. Suchet, J. (1977). Electronegativity, ionicity, and effective atomic charges. *Journal of the Electrochemical Society, 124*, 30C–35C.
90. Spitzer, D. (1970). Lattice thermal conductivity of semiconductors: A chemical bond approach. *Journal of Physics and Chemistry of Solids, 31*, 19–40.
91. Mishra, S., & Ganguli, B. (2013). Effect of p-d hybridization, structural distortion and cation electronegativity on electronic properties of $ZnSnX_2$ (X = P, As, Sb) chalcopyrite semiconductors. *Journal of Solid State Chemistry, 200*, 279–286.
92. Yoodee, K., Woolley, J. C., & Sa-Yakanit, V. (1984). Effects of p-d hybridization on the valence band of I-III-VI_2 chalcopyrite semiconductors. *Physical Review B, 30*, 5904.
93. Miglio, A., Heinrich, C. P., Tremel, W., Hautier, G., & Zeier, W. G. (2017). Local bonding influence on the band edge and band gap formation in quaternary chalcopyrites. *Advanced Science, 4*, 1700080.
94. Juneja, R., Shinde, R., & Singh, A. K. (2018). Pressure-induced topological phase transitions in CdGeSb2 and $CdSnSb_2$. *The Journal of Physical Chemistry Letters, 9*, 2202–2207.
95. Zeier, W. G., Zevalkink, A., Gibbs, Z. M., Hautier, G., Kanatzidis, M. G., & Snyder, G. J. (2016). Thinking like a chemist: Intuition in thermoelectric materials. *Angewandte Chemie, 55*, 6826–6841.
96. Dronskowski, R., & Blöchl, P. E. (1993). Crystal orbital Hamilton populations (COHP): Energy-resolved visualization of chemical bonding in solids based on density-functional calculations. *The Journal of Physical Chemistry, 97*, 8617–8624.
97. Deringer, V. L., Tchougréeff, A. L., & Dronskowski, R. (2011). Crystal orbital Hamilton population (COHP) analysis as projected from plane-wave basis sets. *The Journal of Physical Chemistry A, 115*, 5461–5466.
98. Csató, L., & Opper, M. (2002). Sparse online Gaussian processes. *Neural Computation, 14*, 641–668.
99. Quiñonero-Candela, J., & Rasmussen, C. E. (2005). A unifying view of sparse approximate Gaussian process regression. *Journal of Machine Learning Research, 6*, 1939–1959.
100. Snelson, E., & Ghahramani, Z. (2006). Sparse Gaussian processes using pseudo-inputs. In *Advances in neural information processing systems* (pp. 1257–1264). Cambridge, MA: MIT Press.

101. Tresp, V. (2001). Mixtures of Gaussian processes. In *Advances in neural information processing systems* (pp. 654–660). Cambridge, MA: MIT Press.
102. Rasmussen, C. E., & Ghahramani, Z. (2002). Infinite mixtures of Gaussian process experts. In *Advances in neural information processing systems* (pp. 881–888). Cambridge, MA: MIT Press.
103. Snelson, E., & Ghahramani, Z. (2007). Local and global sparse Gaussian process approximations. In *Proceedings of the Eleventh International Conference on Artificial Intelligence and Statistics* (Vol. 2, pp. 524–531). San Juan, Puerto Rico: PMLR. http://proceedings.mlr.press/v2/snelson07a.html.
104. Gramacy, R. B., & Lee, H. K. H. (2008). Bayesian treed Gaussian process models with an application to computer modeling. *Journal of the American Statistical Association, 103*, 1119–1130.
105. Tresp, V. (2000). A Bayesian committee machine. *Neural Computation, 12*, 2719–2741.
106. Das, K., & Srivastava, A. N. (2010). Block-GP: Scalable Gaussian process regression for multimodal data. In *2010 IEEE International Conference on Data Mining* (pp. 791–796).
107. Park, C., & Huang, J. Z. (2016). Efficient computation of Gaussian process regression for large spatial data sets by patching local Gaussian processes. *Journal of Machine Learning Research, 17*, 1–29.
108. Park, C., & Apley, D. (2018). Patchwork kriging for large-scale Gaussian process regression. *Journal of Machine Learning Research, 19*, 269–311.
109. Zhang, Y., & Ling, C. (2018). A strategy to apply machine learning to small datasets in materials science. *Npj Computational Materials, 4*, 25.

Thermal Nanostructure Design by Materials Informatics

Run Hu and Junichiro Shiomi

1 Introduction

There has always been a demand for materials with desired thermal properties, because they are fundamentally important in various applications. For instance, materials with high thermal conductivity are in high demand for thermal management of electronic devices, especially with the increasing 5G telecommunication and cloud computing. Meanwhile, materials with low thermal conductivity are used in thermoelectrics and thermal insulation. Although the synthesis and manufacturing processes of the materials have advanced in recent years through the use of advanced micro/nano-fabrication techniques and 3D printing, material design is an important precedent step. Material design techniques have sequentially undergone several paradigms, such as empirical, model-based, computational, and big-data-driven paradigms. The accumulated data from material design experiments and simulations have contributed to the fourth paradigm, which unifies the theories, experiments, and simulations from the previous three paradigms. This has led to the emergence of a new field of material informatics (MI) [1–5]. However, there are still two obstacles that limit the efficiency of material design—material selection and structural configuration. Choosing the appropriate materials is the first challenge during the material design process. Currently, material selection can be performed on the basis of several databases that contain tens of thousands of crystal compounds, such as Material Project [6], AFLOW [7], ICSD [8], OQMD

R. Hu
School of Energy and Power Engineering, Huazhong University of Science and Technology, Wuhan, China
e-mail: hurun@hust.edu.cn

J. Shiomi (✉)
Department of Mechanical Engineering, University of Tokyo, Tokyo, Japan
e-mail: shiomi@photon.t.u-tokyo.ac.jp

Y. Cheng et al. (eds.), *Artificial Intelligence for Materials Science*, Springer Series in Materials Science 312, https://doi.org/10.1007/978-3-030-68310-8_7

[9], and AtomWork [10]. However, development of materials with specific thermal properties is challenging because of the tremendous number of available starting materials. Structural configuration is another challenge because all materials are composed of atoms that can be configured in various ways, which may surpass the computation power of most existing computers. For example, carbon exists as diamond, graphite, graphene, and amorphous carbon with varying atomic configurations. The defects [11], roughness [12, 13], nanoinclusions [14], and interfacial adhesion or bonding [15] differ in many ways. Consequently, it is challenging to quickly develop an optimal nanostructure with desired thermal properties from many starting candidates.

The rise of MI has enabled the integration of material-property calculations or measurement methods with informatics; hence, the search for an optimal structure with the desired properties has been greatly accelerated [16–18]. MI has been successfully applied in various material design fields, such as drugs, polymers, catalysis, and cathode materials for lithium-ion batteries [19–22]. The application of MI to thermal properties has also been gradually developed. In this chapter, we provide an overview of the recent progress of MI application in the field of heat transfer, mainly focusing on thermal conduction and thermal emission. In the first part of the chapter, typical MI algorithms are briefly introduced, and the emerging nanostructure designing/optimizing strategies based on MI-enabled thermal conduction and thermal emission modulation are summarized in the second part. A summary and discussion on the opportunities and challenges in this field and perspectives on the possible future direction of the field are outlined in the final part.

2 MI Algorithm

2.1 Bayesian Optimization

Bayesian optimization (BO) is a machine learning algorithm based on experimental design. As shown in Fig. 1, the optimized process can be divided into two parts: initial training set and prediction model modification. First, the black-box function is set up from a training set, whose thermal properties would have been obtained by calculation and then a new set is chosen for calculation. Then, the prediction model is built using the Bayesian linear regression model coupled with a random feature map based on the initial training set:

$$y = w^{\mathrm{T}}\varphi(x) + \varepsilon \tag{1}$$

where w denotes a D-dimensional weight vector of the same size as the available data, φ represents the feature map, x is a d-dimensional descriptor vector of the candidate, and ε is the noise term, which follows the normal distribution with mean 0 and variance ζ. The inner product corresponding to the Gaussian kernel can be

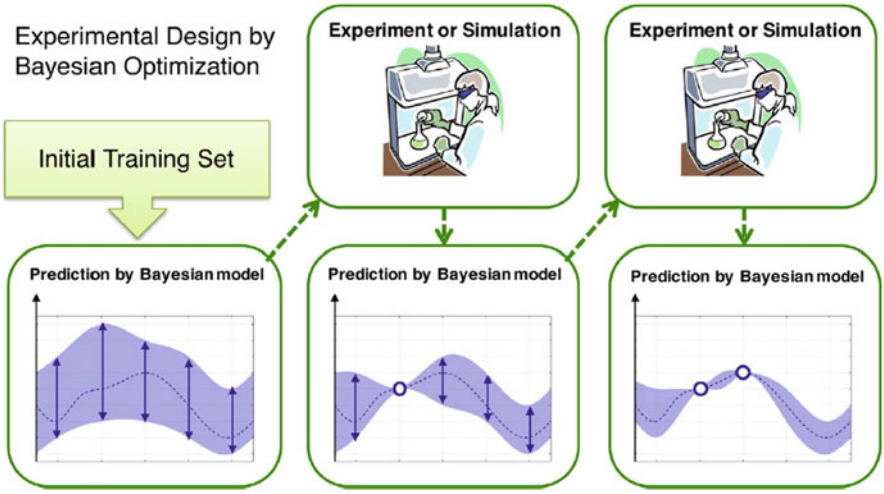

Fig. 1 BO process [24]

obtained by selecting a random feature map [23]. After developing the prediction model, the thermal property distribution of the remaining candidates is provided. The best candidate is selected based on the preset optimized criteria. Then, the accurate thermal property of the selected candidate is calculated and added to the training examples. The calculation of the thermal property is arranged optimally and search for the optimal candidate can be greatly accelerated by performing this procedure repeatedly. The open-source Python library COMBO was constructed using the BO principle to run the optimization process automatically [24].

2.2 Monte Carlo Tree Search

For candidates in the range of hundreds of thousands, BO can efficiently and accurately be used for the optimization task. However, as the quantity increases, the optimized efficiency of the BO is considerably reduced. Consequently, another effective algorithm named Monte Carlo tree search (MCTS) is used [25, 26]. MCTS couples the precise tree search with the generality of random simulation, which is suitable for selection of a candidate from a large quantity.

As shown in Fig. 2, the MCTS is based on a search tree that is constructed node by node, with each node selected based on the evaluation of the simulated case. Each node provides two important pieces of information: the times the node has been visited and estimated value based on the simulation results. The MCTS algorithm process mainly consists of four parts: selection, expansion, simulation, and backpropagation. In the first step of selection, the algorithm starts at the initial

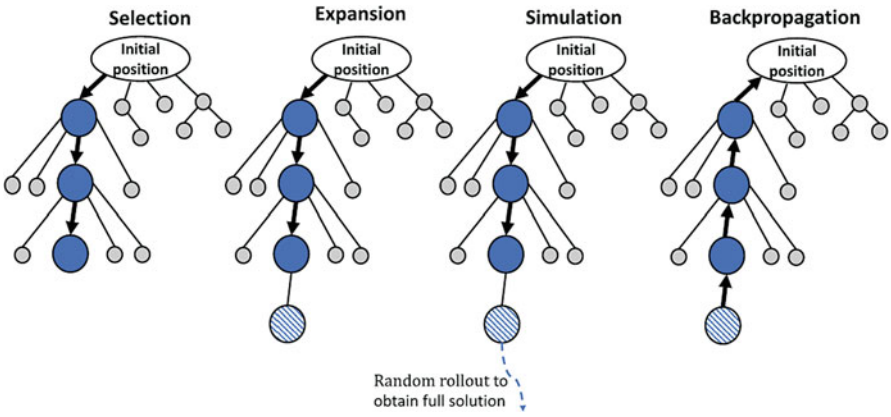

Fig. 2 MCTS process, which consists of four parts: selection, expansion, simulation, and backpropagation [25]

position (root node), then the optimal child nodes are recursively selected based on the upper confidence bound (UCB) until the leaf node is reached. The UCB score is defined as

$$u_i = \frac{V_i}{n_i} \pm b\sqrt{\frac{2\ln N_{\text{parent}}}{n_i}} \tag{2}$$

where V_i is the cumulative simulation values of all structures derived from this node, b is a tunable bias parameter for balancing the tree exploitation and exploration, n_i is the number of times this node has been visited, N_{parent} is the number of times its parent has been visited, and the operative symbols $+$ and $-$ correspond to the maximum and minimum thermal property optimization cases, respectively. In the second expansion step, one child node is added to the branch if the leaf node is not a terminal node. Then, in the simulation step, one playout is randomly selected from the terminal node and the thermal property is calculated. Finally, in the backpropagation step, the key parameters n_i, N_{parent}, and V_i are updated on the path back from the terminal node to the root node according to the calculated thermal property. Although using MCTS does not guarantee finding the global optimal structure, it can efficiently provide a suboptimal structure close to the optimal structure.

2.3 Shotgun Transfer Learning

Machine learning algorithms have become powerful research tools in MI; however, since the volume and diversity of the available data are insufficient, the potential

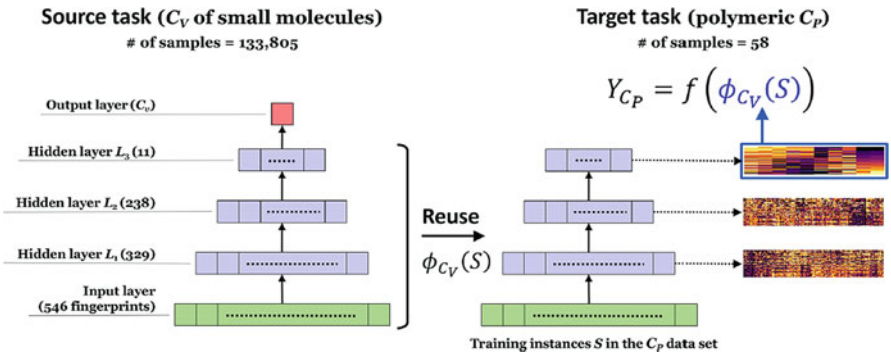

Fig. 3 Neural transfer learning using frozen featurizers [27]

of most algorithms has not been fully explored. The shotgun transfer learning algorithm has potential to overcome the limitations imposed by limited data [27].

Shotgun transfer learning is based on neural networks, which can be defined as $Y_t = f_t(S)$. The aim is to predict the corresponding thermal property Y_t for a specific material S using a small data set of size n_t:

$$D_t = \left\{Y_{t,i}, S_{t,i} | i = 1, \ldots, n_t\right\} \tag{3}$$

where $\{Y_{t,i}, S_{t,i}\}$ represents the ith training case. There are several approaches to overcome the limitations imposed by limited data, where the models trained on a different property Y_s based on an abundant data set D_s are recused and transferred to the model in the task. There are typically two processes for neural transfer learning: frozen featurizers and fine-tuning techniques. As shown in Fig. 3, an L layer pretrained neural network $Y_s = f_s(S)$ can be obtained by solving a source task on a proxy property to the target when using the frozen featurizer approach. The Lth-order composite function arranges the input, g_1, to the output layer, g_L, in which the shallow layers are responsible for creating the material description basis using general features, while only the last one or two layers gather the specific features to predict a source property. The shallow layers are frozen as a feature extractor, $\phi(S) = (g_K{}^{\circ}\ g_{K-1} \ldots {}^{\circ} g_1)(S)$ with $K < L$, while $\phi(S)$ is repurposed for supervised learning of a different property. During fine-tuning, a pretrained model is used as a starting point and fine-tuned to a target task based on available instances. First, the weights on the last few layers of the pretrained model are randomly initialized, and the learned parameters in the remaining layers are used as initial values. Then, all these parameters are retrained at a small learning rate, which controls the weight updating on each gradient descent iteration while preserving the domain-invariant knowledge.

3 MI-Enabled Thermal Conduction Modulation

3.1 Optimal Nanostructure Design

The thermal conductivity of materials plays an important role in thermal management applications, and thus the design of materials with desired thermal properties is important. However, the thermal conductivity requirements vary between each case. Ju et al. [28] developed a framework by combining the atomistic Green's function (AGF) [13] with BO methods [24], and determined the efficiency of finding the maximal and minimal thermal conductivity for Si/Ge interface nanostructures. Figure 4a shows the MI procedure. The designed structure is an interfacial region that is sandwiched between two kinds of materials, namely A (Si) and B (Si or Ge). In the transverse direction, periodic boundary conditions are set for an infinite cross-section simulation. The interface structure consists of either Si or Ge, aiming to find the optimized distribution for Si or Ge with the largest or smallest thermal conductivity based on the optimization. During optimization, the thermal conductivity of each candidate structure is calculated via the AGF method. Then, as shown in Fig. 4b, the optimal interface structures with maximal and minimal thermal conductivity were found by conducting BO training and optimizing the process repeatedly, as described in Chap. 2. For maximal thermal conductivity structures, the optimal interface structure with Si–Si lead is understandable, and the continuum Si bridge connecting the two leads provides a channel for coherent phonons. The optimal structure with Si-Ge lead can be regarded as a kind of rough interface, resulting in phonon transmission enhancement at the interface [13]. As for the minimal thermal conductivity cases, the optimal structures are all aperiodic superlattices (SLs), which are different from the periodic SLs.

To explore the structural features of the low thermal conductivity aperiodic SLs, the optimized structure of the machine learning system is reset, which is shown in Fig. 5a, with the binary codes used as the descriptors to denote each unit layer ("1" indicates Ge and "0" indicates Si) whose thickness is set as 5.43 Å. The optimized SL with different unit lengths and atomic fractions was obtained. Meanwhile, the optimal structure with the lowest thermal conductivity was aperiodic. For further analysis of the physical mechanism, the effect of the layer thickness and number of interfaces on the thermal conductivity was investigated. The results are shown in Fig. 5b, c. The dependence on the number of interfaces was apparent as the phonon scattering increased with the number of interfaces. Figure 4d shows that the thermal conductance decreased with increasing layer thickness owing to the Fabry–Pérot oscillations [29, 30]. For a given SL structure, the interface number and layer thickness are two competing parameters. On optimizing the balance between these two parameters, the aperiodic SLs gain more freedom for structural arrangement compared to their corresponding periodic SLs, resulting in their superior reduction in thermal conductivity. To further emphasize the competitive relationship between the two parameters, the thermal conductance of all candidates was calculated for the 14-unit cell (UL) SL with equal Si/Ge fraction and 10-UL SL with variable Si/Ge

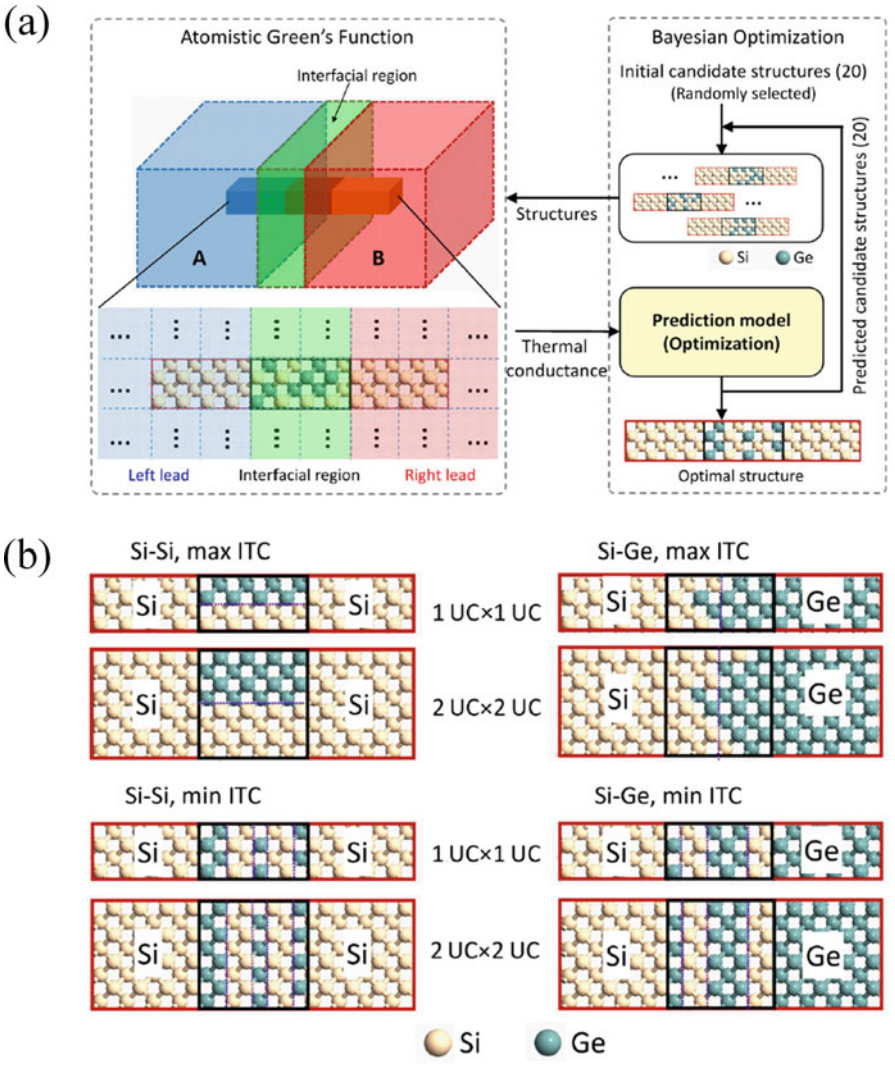

Fig. 4 (**a**) Optimization procedure for the Si/Ge interface nanostructures. (**b**) Optimal structures with the maximum and minimum interfacial thermal conductance [28]

fraction, as shown in Fig. 5d. In both cases, there was a minimum for each number of interfaces, which also proves the competitive case. In addition, for structures with the same number of interfaces, the thermal conductivity greatly varied because of the different thicknesses of each layer. Since the thermal conductance spreading range was comparable to their magnitude, the Fabry–Pérot resonance had the same effect on thermal transport as phonon scattering. This is because the phonon scattering remains unchanged in the structure with the same interface number.

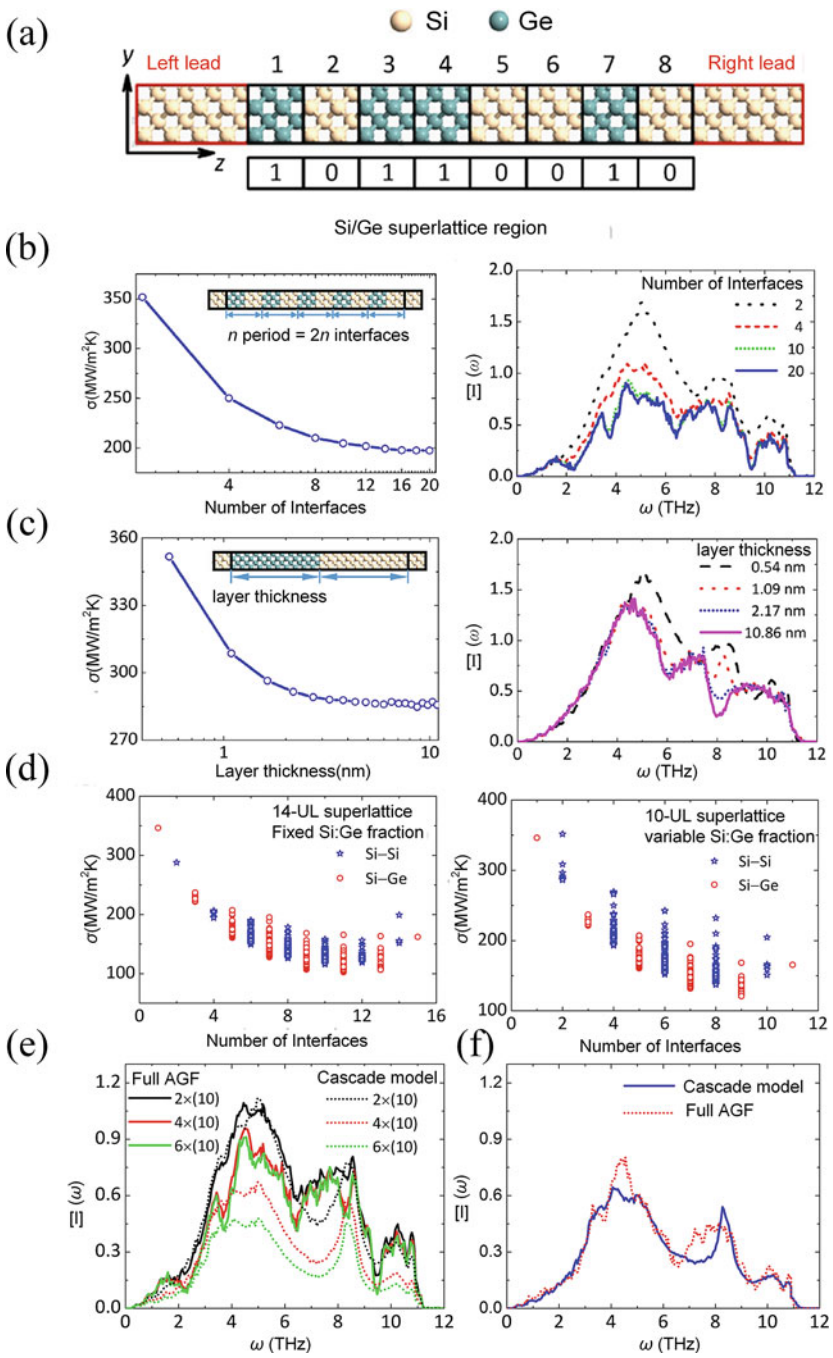

Fig. 5 (**a**) Schematic representation of the 8-UL SL with equal fraction of Si and Ge atoms at the Si–Si interface to illustrate the descriptor. (**b**) Thermal conductance and phonon transmission

To further explore the physical mechanism of the phonon properties of the optimized structure, coherent phonon effects are analyzed in terms of constructive interferences and destructive interferences. For this purpose, the phonon transmission is separated into two parts, which are coherent effects and incoherent effects by comparing the phonon transmission via the full AGF calculation and cascade transmission model. The phonon reflection at an interface leads to thermal resistance enhancement, and additional thermal resistance can be enhanced by further interference of phonons. In this process, the former reflection can be regarded as an incoherent effect because there is little effect on whether the phonon is coherent or not, while the latter interference should be regarded as coherent effect for interference requires phonons to be coherent. In the cascade model, the phonon transmission can be calculated as $\frac{1}{\Xi_{\text{cascade}}} = \sum_i \frac{1}{\Xi_i} - \frac{N-1}{\Xi_{\text{Si}}}$, where N represents the number of interfaces, Ξ_i denotes the transmission coefficients of the ith interface, and Ξ_{Si} represents the phonon transmission of a perfect silicon crystal. Figure 5e compares the transmission calculated by the cascade model and full AGF model for periodic SLs with different numbers of periods (2, 4, and 6). As the superlattice periods increase, the transmission of the cascade model decreases quickly, whereas the transmission of the full AGF calculation decreases first and then converges. This is understandable because in the cascade model, only the incoherent phonon transport can be reflected, while in the full AGF calculation, coherent phonon transport is captured when crossing multiple layers. In the full AGF calculation, the convergence phenomenon suggests that constructive and destructive interferences cancelled each other in the periodic superlattice, demonstrating that the thermal conductance of the structure can be further inhibited by adjusting the construction and destructive interferences. Taking the optimal aperiodic 10-UL superlattice as an example. The phonon transmission via the cascade model and full AGF calculation are shown in Fig. 5f. The transmission obtained by the cascade model had approximately the same trend and magnitude, which suggests that the aperiodic structure effectively suppresses the constructive phonon to destructive interference, leading to minimal thermal conductance.

Fig. 5 (continued) versus layer thickness. (**c**) Thermal conductance and phonon transmission versus the number of interfaces. (**d**) Thermal conductance versus number of interfaces for 14-UL SL with equal Si/Ge fraction and 10-UL with variable Si/Ge fraction. Comparison between the phonon transmission obtained from the cascade model and full AGF calculation, (**e**) periodic superlattices with different number of periods, where one period consists of a Si UL and Ge UL denoted as "10." (**f**) Optimal aperiodic superlattice structure with total thickness of 10 UL [28]

3.2 Experimental Realization of Optimal Nanostructure

The above study is theoretical and the interatomic force constant (IFC) is empirical; however, experimental verification remains an open question. Hu et al. [31] also employed MI design coupled with first-principle-based AGF calculations to optimize the GaAs/AlAs interface nanostructures. They succeeded in predicting the optimal GaAs/AlAs interface nanostructure with minimal thermal conductivity based on coupling BO optimization and first-principles AGF, which was then verified by experiments. The optimization of the SL is shown in Fig. 6a. All the candidate structures were prepared by denoting the GaAs unit layer as 0 and AlAs unit layer as 1. The SL structure was sandwiched between the two semi-infinite GaAs leads. First-principles were used to calculate the corresponding IFCs. Then, by combining the mass matrices and IFCs, the dynamical matrix was obtained, which was used as input in the AGF to calculate the thermal conductivity. The optimal structure with the lowest thermal conductivity was quickly found with only 2.7% calculation of the total candidate by combining the assorted calculation method with BO optimization. Then, the optimal structure was fabricated by molecular beam epitaxy and measured by the time-domain thermoreflectance (TDTR) method, which is shown in Fig. 6b, for experimental verification. Figure 6c illustrates the distribution of the theoretical and practical values of the thermal conductivity of the optimized structure at different temperatures. The simulation results agree well with the experiments, considering the SL interface roughness, demonstrating that the thermal conductance can effectively be controlled by the design of the SL structure.

Further, the physical mechanism is investigated, and the phonon properties of the optimal structure and the corresponding periodic structure are calculated. Figure 7a illustrates the inverse participation ratio (IPR) of the optimal aperiodic and periodic SLs, in which the yellow dashed lines denote the IPR of a pure GaAs crystal. Compared with the periodic structure, there is a stronger phonon localization in the optimal structure, which reaches the maximum above the optical phonon frequency of 6.37 THz. A similar trend can also be observed in the acoustic phonon, which is shown in Fig. 7b. The impact on conductivity of the number of modes should be considered since the IPR can only quantify the magnitude of phonon localization per mode. Therefore, the weighted IPR is calculated, as shown in Fig. 7d. More and stronger peaks appear in the weighted IPR of the optimal aperiodic structure, which suggests that the phonon localization effect within the acoustic phonon range is more significant. The weighted IPR curve of the optimal structure is similar to the difference between the spectral thermal conductivities of the optimal aperiodic and periodic structures shown in Fig. 7e. This indicates that the reduced thermal conductivity of the optimal structure originates from the enhanced phonon localization within the acoustic phonon range because of its constructive aperiodicity. To explore the physical mechanism underlying the localized mode, the standard deviation of the local density of states (LDOS) was calculated, as shown in Fig. 7f. Similar to the weighted IPR, the LDOS has a strong correlation with the spectral thermal conductivity difference. The projection of the x-direction-accumulated LDOS within the acoustic phonon frequency in the y–z

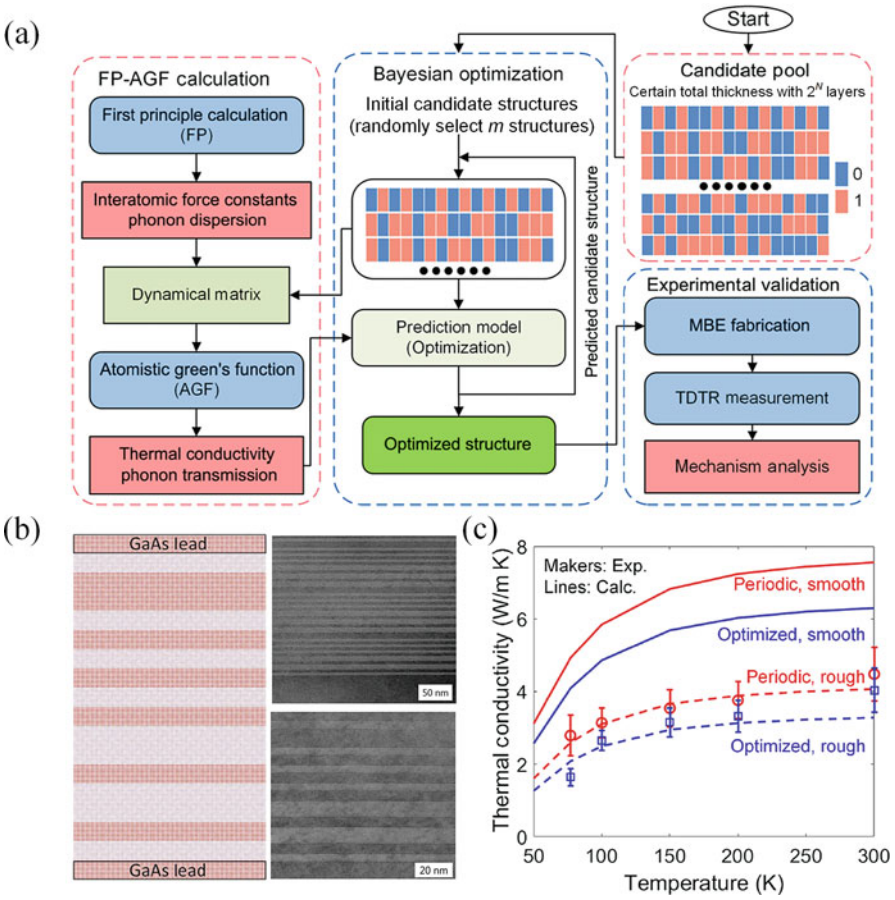

Fig. 6 (**a**) Flowchart of the optimal control of the thermal conduction of the GaAs/AlAs interface SL nanostructure. (**b**) Schematics of the optimal GaAs/AlAs SL structure obtained by materials informatics (MI) and its experimental TEM images. (**c**) Experimental and calculated thermal conductivities of the optimized aperiodic and periodic SL nanostructures [31]

plane of the periodic and optimal aperiodic structures is shown in Fig. 7g. It can be clearly observed that the phonons are mostly localized in the As atoms in the AlAs layers, whereas the phonons are uniformly distributed in the GaAs layers. This is possible because the atomic masses of As and Ga are almost the same, while that of the Al atom is smaller. This inhibits the kinetic energy transfer between Al and As atoms. Figure 7h shows the LDOS projection at three typical peak frequencies in Fig. 7d. The distribution of the localized phonons varies significantly at each frequency, while the phonon localization does not occur in periodic structures.

The above analysis indicates that some local structures in the optimized structure can effectively enhance the phonon interference. To identify the specific local structures, phonon pattern analysis was performed. These local structures are

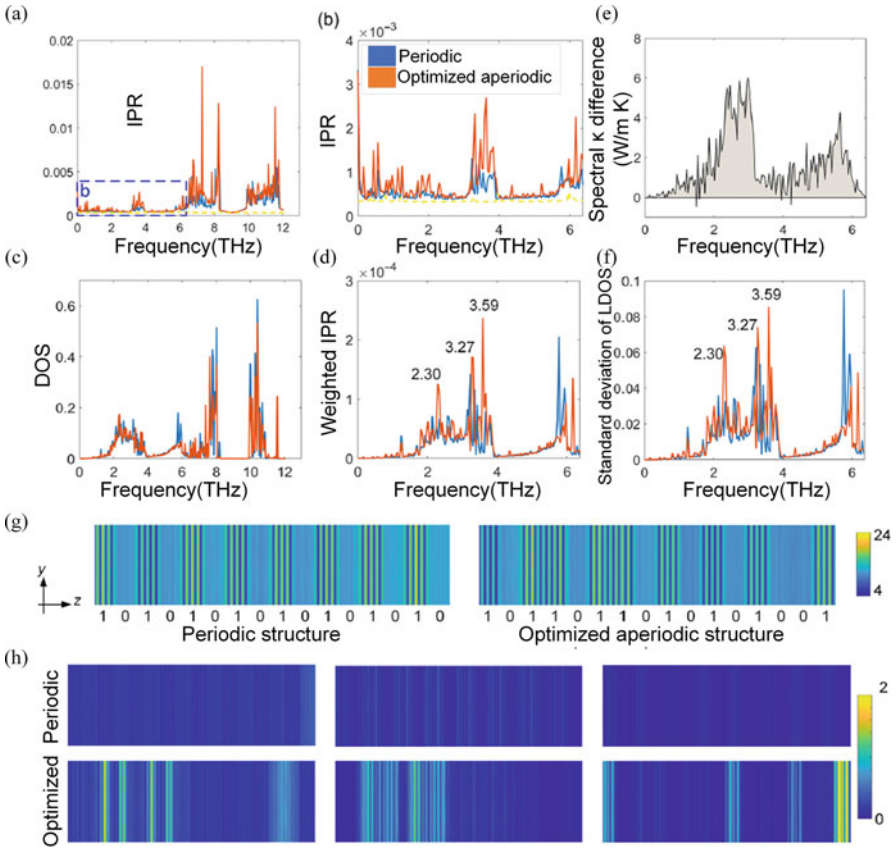

Fig. 7 Comparison of the frequency-dependent IPR $I(\omega)$ of the two structures in the (**a**) full and (**b**) acoustic phonon frequency ranges. Blue-dashed square in (**a**) denotes the acoustic phonon range and is magnified in (**b**). Yellow dashed lines denote the small and uniform IPR for pure GaAs crystals. (**c**) Spectral DOS of the two structures in the full phonon frequency range. (**d**) Spectral weighted IPR in the acoustic phonon frequency range. (**e**) Spectral thermal conductivity difference between that of the periodic structure and that of the optimized aperiodic structure. (**f**) Spectral standard deviation of the LDOS for the two structures in the acoustic phonon frequency range. (**g**) Projected LDOS distribution on the *y*–*z* plane with only the acoustic phonons in the periodic and optimized aperiodic structures. (**h**) Projected LDOS in the *y*–*z* plane of the two structures at 2.30, 3.27, and 3.59 THz [31]

important for reducing phonon transmission in four different frequency ranges from low to high frequency (−0 to 2.25 THz, 2.25 to 3.3 THz, 3.3 to 5.4 THz, and 5.4 to 6.5 THz). The pattern analysis results show that the local structures that appear most frequently in optimized structures with low thermal conductivity are 101010, 110101, 101010, and 101001 in each frequency range, respectively. Furthermore, 101101 appears as the top local structure in all frequency ranges; thus, the top four local structures are defined as 101010, 110101, 101001, and 101101.

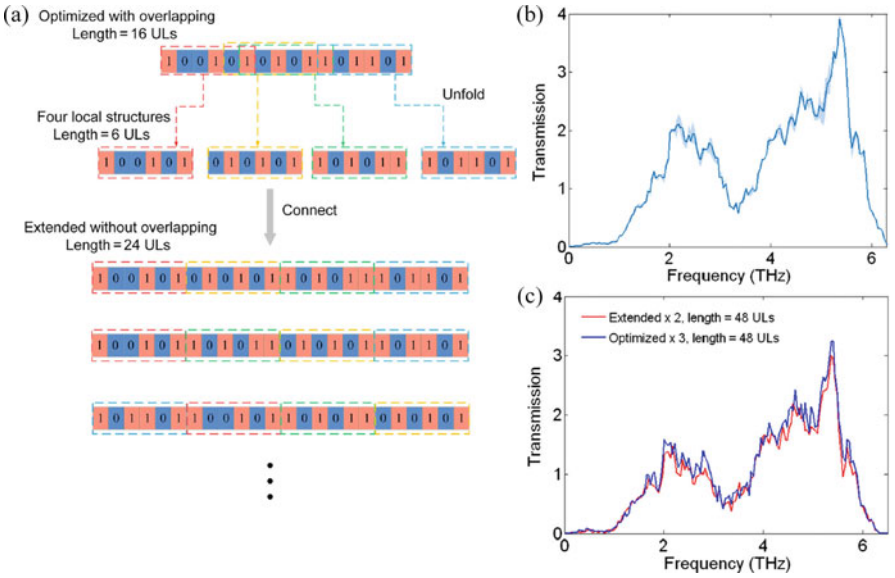

Fig. 8 (**a**) Local structure independence and correlation examination. (**a**) Schematic of the optimized SL (16-ULs) and extended SL (24-ULs). (**b**) Averaged phonon transmission of the 24 extended SLs, i.e., all possible sequences when serially connecting the four key local structures 101010, 110101, 101001, and 101101. The shadowed region denotes the standard deviation. (**c**) Comparison of the phonon transmissions of the optimized SL and extended SL (averaged) made to the same lengths (48 ULs) by repeating three times and twice, respectively [31]

The local structure can maximize the inhibition of phonon transmission within the corresponding frequency range, leading to the lowest thermal conductivity. Therefore, more local structures in an SL result in a lower thermal conductivity. The optimal SL possesses all the local structures, and hence has the lowest thermal conductivity. To further explore the function of the local structures, the optimal SL was unfolded to 101010, 110101, 101001, and 101101 and then connected in series as shown in Fig. 8a. This was done to determine whether the function of the local structures to suppress the thermal conductivity can be separated. First, the influence of the four local structures on the phonon transmission was investigated to assess whether the local structures are weakly correlated. As shown in Fig. 8b, the blue curve and shadow region represent the average phonon transmissions of all ${}_4P_4 = 24$ possibilities (Fig. 8a) and its standard deviation, respectively. The small standard deviation indicates a weak correlation among the local structures. To compare the extended SL and optimized SL, both structures were simply repeated to construct a 48-UL SL since their lengths are different. As shown in Fig. 8c, the difference in phonon transmission between the structures is small. In conclusion, the local structures were weakly correlated to inhibit the phonon transport, and the optimal aperiodic structure introduced interference over a broad range of phonon frequencies by connecting various local structures.

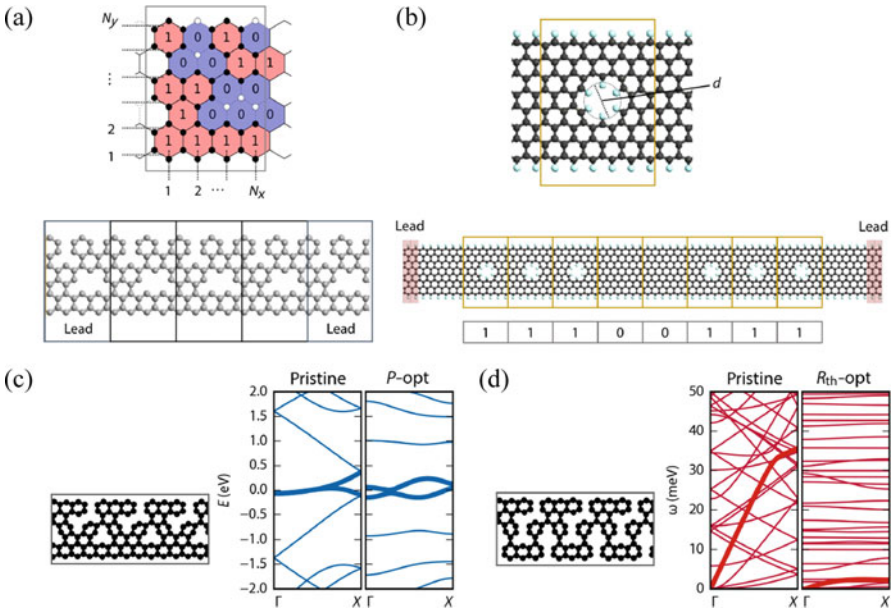

Fig. 9 (**a**) Periodically nanostructured GNR. (**b**) Antidot GNR. (**c**, **d**) Optimal structure for P/R_{th} and its electron/phonon band compared with the pristine GNR with 4 and 7 atom defects, respectively [32]

3.3 Thermoelectric Nanostructures Design

MI algorithms have shown excellent performance for single-target optimization (low thermal conductivity). However, in practice the optimized targets are numerous and usually coupled together, which is a great challenge for MI algorithms. To demonstrate the feasibility of using the MI algorithm for multi-goal optimization, Yamawaki et al. [32] successfully predicted the optimal thermoelectric structure of graphene nanoribbons (GNR) using the BO algorithm. The thermoelectric properties of a material are quantified using the expression $ZT = R_{\text{th}}S^2T/R_{\text{el}}$, where R_{th} and R_{el} denote the thermal resistance and electronic resistance, respectively, S is the Seebeck coefficient, and T is the temperature. As shown in Fig. 9a, first, to clarify the structural optimization direction, the short-period nanostructured GNRs were analyzed. The hexagonal lattices with removed carbon atoms and complete hexagonal lattices were denoted as 0 and 1, respectively. The binary sequences were then used as descriptors for MI training and prediction. Since thermoelectric properties vary with the chemical potentials (μ), the value of the peak chemical potential (μ_{peak}), which provides the maximum ZT value for the realistic chemical potential from -1 to 1 eV, should be selected for evaluating thermoelectric properties. Figure 9c, d shows the GNR structures with 4 and 10 atom defects that have the highest power factor $P(=S^2/R_{\text{el}})$ and R_{th}, respectively.

In the *P*-optimized structure, vacancies spread throughout the entire GNR area, except for the hexagonal lattices along the edge. The optimized structure resulted in the strong flattening of the electronic bands around the energy levels of the edge state, resulting in bandgap generation. Moreover, the zigzag structure in the middle area could lead to phonon scattering without affecting the edge state; thus, the thermoelectric performance was greatly enhanced. Meanwhile, for the other R_{th}-optimized structures, the labyrinthian shape of the GNR resulted in significant phonon localization, which greatly reduced their group velocity, resulting in the highest *ZT*. Although the labyrinthian shape greatly contributes to the high *ZT*, the GNR with edges are preferred owing to their stable thermodynamic properties and experimental feasibility [33]. Therefore, from the optimization results of the *P*-optimized structure, a new simulation model shown in Fig. 7b was built. This was composed of an antidot nanostructured region connected with semi-infinite pristine GNRs. The entire structure consists of a pristine structural (denoted as 1) sections and antidot structural (denoted as 0) sections, where the pore is located in the center of the section with a diameter of 2.9 Å.

Another round of BO optimization was performed using the new model. Figure 10 compares the different thermoelectric properties of the pristine structure, periodic antidot structure, and optimal aperiodic antidot structure. Figure 10a compares the different thermoelectric properties of the pristine structure (black),

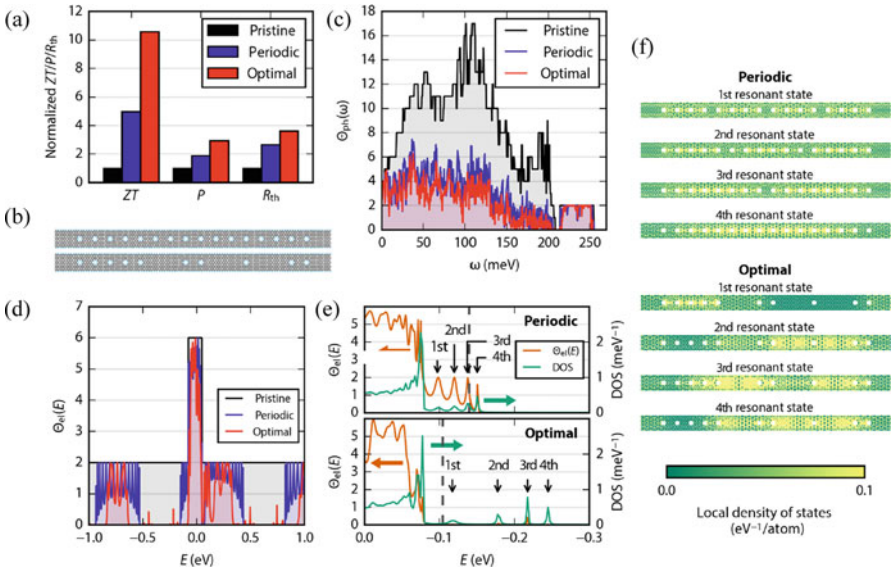

Fig. 10 (**a**) Comparison of the thermoelectric properties of the pristine, periodic, and optimal structures. (**b**) Periodic and optimal aperiodic antidot GNRs. (**c**, **d**) Phonon and electron transmission functions. (**e**) Transmission and DOS in the nanostructured region, in which the edge state is represented by the dashed line. (**f**) LDOS distribution of the resonant states of the periodic and optimal structures [32]

periodic antidot structure (blue), and optimal structure (red), while Fig. 10b shows the configuration of the periodic antidot structure and optimal structure. The distribution of the antidots in the optimal structure was aperiodic, which effectively increases its *ZT* 11 times. These results demonstrate that the thermal and electrical properties of the structure can be improved simultaneously via the optimization of the antidots distribution. To explore the mechanism underlying the enhanced thermoelectric properties of the GNRs, the phonon and electron transport properties were analyzed in detail. From the perspective of thermal conduction, there are mainly two competing factors affecting thermal transfer in the antidot structures; thus, the surface scattering effect resulting from the antidots and interference effect among antidots [34]. Therefore, similar to Ju's research results [28], aperiodic structures gain more structural regulatory freedom than the periodic structures, which further reduces their thermal conductivity. This intuitive physical knowledge cannot fully explain why this specific structure is optimal. Therefore, the design of the optimal structure still depends on machine learning. Meanwhile, in terms of electric transport, the electron transmission function of the representative structures is compared in Fig. 10d. In finite periodic structures, the peaks of electron transmission corresponding to resonant states appear and split as the number of antidots increases. The thermoelectric performance can be further enhanced by utilizing the edge state seen for electron transmission in the energy band ranging from −0.078 to 0.048 eV. For utilization of the edge state, inhibition of the electron transmission of resonant states with energy near that of the edge state is required. In general, in random infinite potential fields, the transmission of any electron states is inhibited because of state localization. However, the optimal distribution of the antidots can inhibit electron transmission in the target electron states, which is called resonant peaks in this case. Figure 10e shows that in both the periodic and optimal structures, the resonant states appear near the edge state, whereas the electron transmission in the optimal structure is strongly suppressed. To gain insights into the transmission of the resonant states, the LDOS at the resonant energy was colored onto each atom as shown in Fig. 10f. The indices of the resonant state in Fig. 10f correspond to those in Fig. 10e. The LDOS was distributed uniformly throughout the entire finite periodic structure, while state localization existed within limited areas in the optimal aperiodic structure. It is intuitive that the uniformly distributed states effectively enhance electron transport, while strong localization suppresses electron transport.

3.4 Disordered Structural Parameters Exploring in Aperiodic Superlattices

The works in sections above prove that random multilayer (RML) structures can effectively localize coherent phonons, thus reducing the lattice thermal conductivity (κ_L). However, there is poor definition of the degree of randomness in localized

structures, which is conducive to linking structures via physical mechanisms and further optimizing the material design process. Therefore, defining the degree of randomness of different RMLs and relationship between the degree of randomness and thermal conductivity is of great significance in optimizing the thermal conduction in RMLs.

Consequently, Chakraborty et al. [35] succeeded in quantitatively defining the disorder in the layer/periodic thickness of the RMLs by identifying two randomness parameters—the thickness-based and period-based index of randomization. They demonstrated the effectiveness of machine learning in optimizing the RML with lowest κ_L based on the randomness parameters. The three typical structures are shown in Fig. 11a, i.e., the periodic superlattice (SL), RML structure, and gradient multilayer (GML) structure, in which the cyan and golden blocks represent material A and material B, respectively. The thickness distributions of the GMLs and RMLs are the same; however, the layer thickness of the former is distributed in ascending order.

The impact of the arrangement of the layer thicknesses on the κ_L of the RMLs was investigated using the molecular dynamics (MD) method. Two GMLs (GML1 and GML2) were created as the origin structures, and the periods and average thicknesses of both structures were set as $N = 32$ and $d = 4$ unit cells (UCs), respectively. To gradually introduce disorder into the GMLs, the corresponding RMLs were constructed by swapping the *i*th and *j*th layers of the same type of atom that was randomly selected. In this way, the obtained RMLs shared the same thickness distribution but different thickness arrangements with the original GML. Therefore, the number of swaps (S) is used as an index to quantify the degree of disorder in GML. For each GML, 10 sets of RMLs with S varying from 0 to 50 were obtained via 10 independent swapping rounds. Figure 12a (GML1) and Fig. 12f (GML2) show that κ_L is inversely proportional to S. In addition, the specific exponential fitting curves were plotted to describe the qualitative relationship between these two parameters in GML1 and GML2. To quantify the disorder in the layer thicknesses, the thickness-based index of randomization R_d is defined as [36]:

$$R_d = \sqrt{\frac{\sum_{i=2}^{N}\left[\left(d_{A,i} - d_{A,i-1}\right)^2 + \left(d_{B,i} - d_{B,i-1}\right)^2\right]}{N}} \tag{4}$$

where $d_{A,i}$ and $d_{B,i}$ are the layer thickness of materials A and B in the *i*th period, respectively, and N is the number of periods in the RML. Figure 12b (GML1) and Fig. 12g (GML2) show that R_d increases as S increases. Furthermore, as shown in Fig. 12c, h, the κ_L of GML1 (GML2) decreases as R_d increases. Besides randomness in the layer thickness, period-wise randomness also appears during swapping. The period-based index of randomness R_p has been proposed to identify the period-wise randomness as

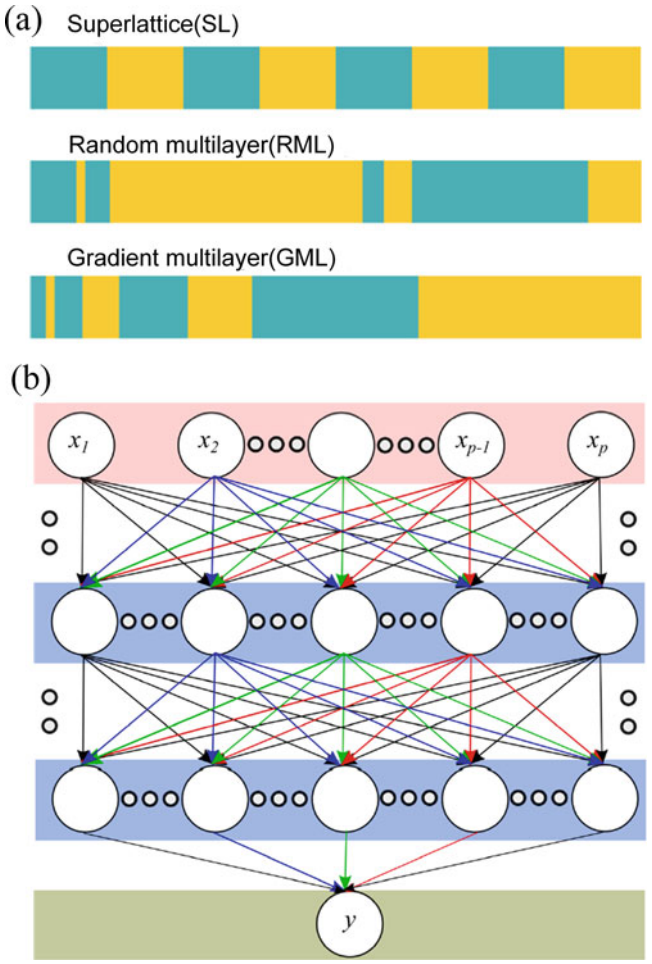

Fig. 11 (**a**) Schematic of the structures simulated in this work. Cyan and golden regions are composed of A- and B-type atoms, respectively. (**b**) Simplified schematic of a neural network (NN). The top and bottom layer are the feature vector and output layer, respectively. The middle layers are the hidden layers. $x_1, x_2, \ldots, x_p$ represent the features of the MI model, while p represents the number of features and $y = \kappa_L$ is the final output [35]

$$R_p = \sqrt{\frac{\sum_{i=2}^{N}\left[\left(\left(d_{A,i} + d_{A,i-1}\right) - \left(d_{B,i} - d_{B,i-1}\right)\right)^2\right]}{N}} \tag{5}$$

The relationship between R_p, S, and κ_L is similar to that of R_d. By comparing Fig. 12(a–e) (f–j) for GML1 (GML2), it can be concluded that R_d and R_p are the two effective structural parameters that can relate the κ_L with the randomness of

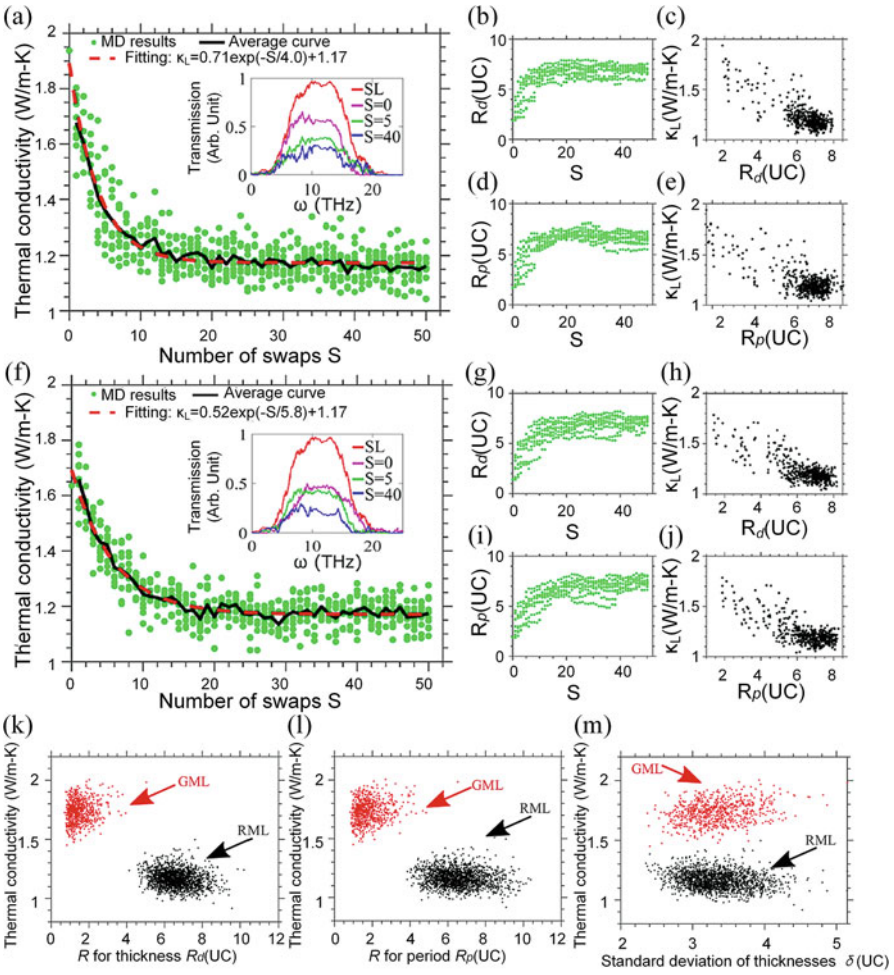

Fig. 12 (**a**) Changes in the lattice thermal conductivity as GML is introduced with randomness through the thickness position swapping method for (**a**) GML1 and (**f**) GML2. The insets of panels (**a**) and (**f**) are the normalized transmission spectra of SL, GML, RML ($S = 5$), and RML ($S = 40$), corresponding to GML1 and GML2, respectively. The changes in R_d with respect to the number of swaps are provided in (**b**) GML1 and (**g**) GML2. (**c**, **h**) Changes in κ_L with respect to R_d for GML1 (GML2). The changes in R_p with respect to the number of swaps are provided in (**d**) GML1 and (**i**) GML2. (**e**, **j**) Changes in κ_L with respect to R_p for GML1 (GML2). Changes in lattice thermal conductivity of 3400 multilayer structures with respect to the change in (**a**) R for layer thickness (R_d), (**b**) R for period (R_p), and (**c**) standard deviation of the layer thicknesses (δ) [35]

the RMLs. In addition, the swapping method is also effective in suppressing the κ_L of a structure with a specific thickness distribution. Figure 12a (GML1) and Fig. 12f (GML2) illustrate the phonon transmission of GML ($S = 0$) and two RMLs (with $S = 5$ and 40) and their corresponding periodic counterparts. When compared

with the periodic structure, broadband phonon localization appeared in the GML. In addition, the localization degree in the RMLs gradually increased as the introduction of disorder increased.

The above analysis results showed that the indexes of randomness R_d and R_P can effectively correlate the disorder with κ_L for RMLs with different thickness arrangements. However, the difference in thickness distribution is not explicitly reflected in these two parameters. Therefore, to identify the RMLs with different thickness distributions, the standard deviation (δ) is determined as

$$\delta = \sqrt{\frac{\sum_{i=1}^{N}\left[\left(d_{A,i}-d\right)^2+\left(d_{B,i}-d\right)^2\right]}{2N}} \tag{6}$$

Figure 12m shows the δ and κ_L of 3400 structures with $N = 32$ and $d = 4$ UC, half of which are randomly created RML structures while the other are corresponding GMLs. The κ_L as a function of R_d and R_p of these structures are also shown in Fig. 12k, l. The κ_L of an RML and its GML cannot be recognized only based on δ because they have the same thickness distribution. Combined with the previous research results [37], the author concludes that there is a complex nonlinear relationship between the κ_L of an RML and randomness parameters R_d, R_p, and δ.

Based on the above findings, the thickness arrangement and thickness distribution were proven to be effective structural parameters that can define the κ_L of an RML in a complex nonlinear manner. To handle this complex problem, a machine learning (ML) prediction model can be used, on the premise that the model can be adequately trained with the structural features and κ_L of the RMLs. As shown in Fig. 11b, a neural network (NN)-based ML model was developed to predict the κ_L of the RMLs. To avoid overfitting, the number of hidden layers and nodes in each hidden layer were selected based on careful experimentation. The number of layers and nodes are two main hyperparameters [38], which are responsible for the construction NN, and they rely solely on a particular data set. In this case, the authors chose to use the scaled exponential linear activation function [39] and the "Adam" [40] optimizer because it performs very well with less hyperparameter adjustments and requires a small amount of memory to compute. The training steps are as follows: first, the adjusted or assigned weights and biases are used to calculate the output y based on the feature vector x. Then, the errors between the predicted output y and actual output $\hat{y}$ are determined as $E = \hat{y} - y$. Next, the weight factor for each input at each node is tuned through the backward propagation algorithm. The above steps are repeated for adequate epochs until the desired accuracy is achieved. The biases and weights at each node are fixed when the ML model is trained for a chosen number of epochs. These fixed parameters are then used to calculate the final output based on the input feature vector.

Based on the above ML model, the prediction of κ_L for different RMLs was conducted. The input structural features for the ML model are defined as the thickness sequence, R_d, R_p, δ, Δd_max, and Δd_min, where Δd_max and Δd_min denote the maximal and minimal deviation of the monolayer thickness relative to the

average layer thickness of the RML. All the training and predicting structures were randomly constructed with the same thickness distribution. Figure 13a–d shows the comparison between the κ_L of the RMLs using the ML prediction model and actual value from the MD simulations, which are divided into four different combinations of features. The attenuation trend of the κ_L of the RMLs with increase in S was predicted by the ML model. As shown in Fig. 13a, the thickness sequence can be a sufficient feature parameter to predict the κ_L of the RMLs with the same thickness distribution. The addition of other parameters, such as R_d, δ, R_p, Δd_{max}, or Δd_{min}, did not improve the accuracy of the prediction. The disorder parameters (R_d, R_p, and δ) exhibit reasonable accuracy for ML prediction, which is certainly a more efficient approach compared with the sequence as the feature. To make the ML model more general, the training samples were changed because too many elements of the thickness sequence ($2 \times N$) slow down the training and testing process. During the training process, the ML model is trained with 3400 sets of different structures, half of which are RMLs with random thickness distribution and the remaining part is composed of the corresponding GMLs. Then, the model is used to predict the κ_L of the structures in Fig. 13a–d, whose results are shown in Fig. 13e–h. Figure 13e shows that the thickness sequence is no longer a self-sufficient feature for ML prediction with reasonable quantitative accuracy. Meanwhile, as shown in Fig. 13f, g, the randomness parameters (R_d, δ, and R_p) can improve the prediction accuracy once they are combined with the thickness sequence. Moreover, the disorder parameters can effectively distinguish the κ_L of the RMLs with a specific thickness distribution, as shown in Fig. 13h. Therefore, the sequence, R_d, R_p, and δ are significant structural features of an ML model to predict the κ_L of the RMLs with acceptable accuracy. These findings may contribute to the development of superlattices with low thermal conductivity and research on phonon localization, which is a growing field [41–44].

4 MI-Enabled Thermal Emission Modulation

4.1 Thermal Nanostructure Designs for Radiative Cooling

The radiation cooling technology, which cools by unidirectionally radiating thermal energy of objects to an atmospheric transparent window at a wavelength ranging from 8 to 13 μm, has shown great potential for application in the field of building energy conservation and thermal management [45–48]. To simultaneously increase the radiative heat flow into the atmosphere window and decrease the absorption of thermal radiation from the atmosphere, it is important for the atmospheric transparent window to have a high emissivity and near-zero emissivity in the remaining wavelength bands. Multilayered photonic crystals are often used as a platform for tailoring thermal radiative properties because of their lithography-free

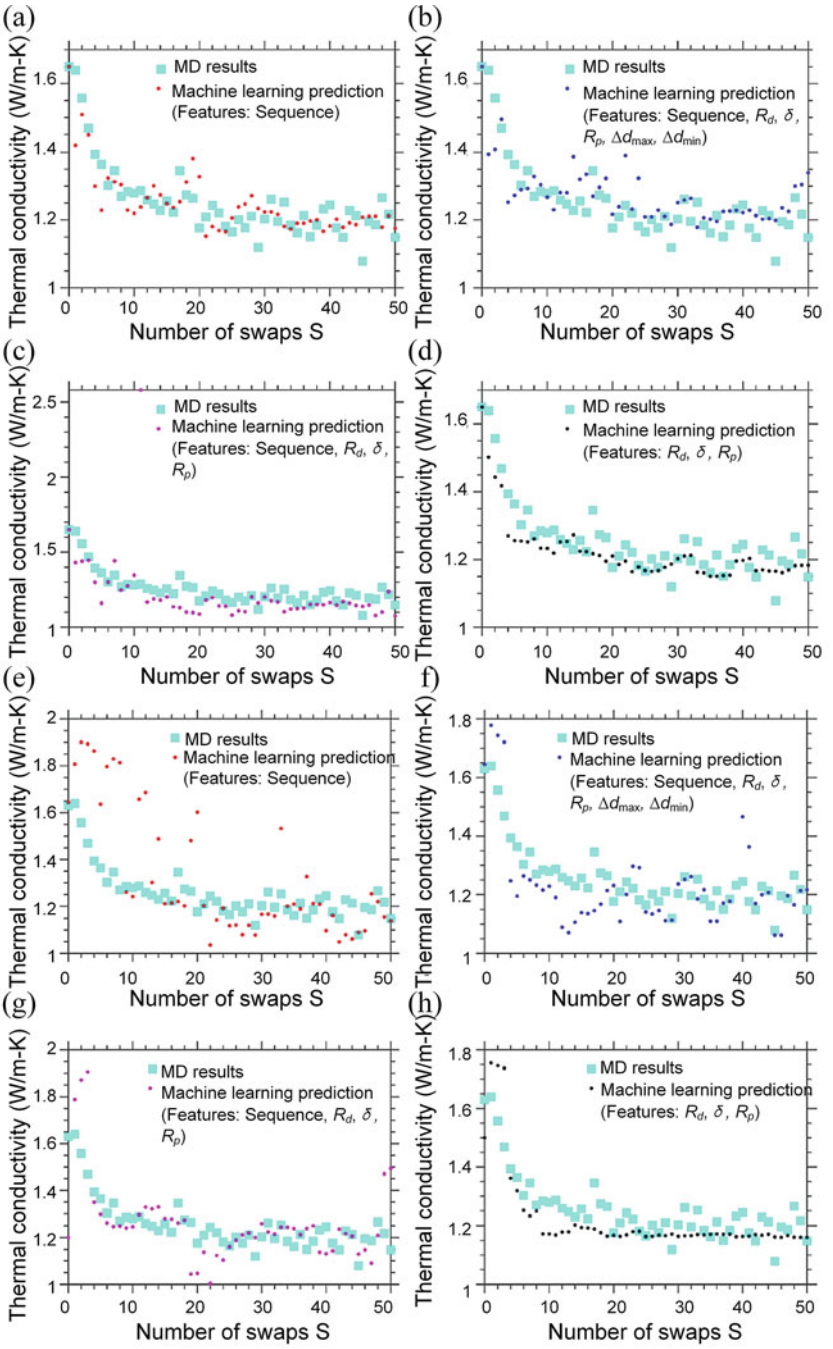

Fig. 13 Comparison between the MD-predicted thermal conductivity, that is, the true values, and ML-predicted values of a set of RMLs generated by the swapping method with S increasing from 0 (GML) to 50 based on different training data. Different combinations of parameters were used as features of the ML model. Specifically, (**a**, **e**) sequence; (**b**, **f**) sequence, R_d, δ, R_p, Δd_{max}, and Δd_{min}; (**c**, **g**) sequence, R_d, δ, and R_p; and (**d**, **h**) R_d, δ, and R_p were used to train the model [35]

fabrication and scalability. However, the structural design of the photonic crystal requires many parameters to be optimized, which makes it ideal for MI optimization.

Guo et al. [49] proposed a highly selective radiative cooling structure based on the rigorous coupled wave analysis (RCWA) method coupled with the BO algorithm. As shown in Fig. 14a, the candidate structure consists of a grating and multilayered structures that are divided into several layers, each with multiple material and thickness possibilities. The radiative properties of each structure can be determined using the RCWA method. In this work, the optimizing target, namely the figure of merit, is defined as the relative emissivity of the atmospheric transparent window minus the emissivity of the remaining wavelength bands. Therefore, the optimal structure with the best radiative cooling effect can be found by conducting the RCWA combined with the BO method. The radiative property of the optimal structure is shown in Fig. 14b. The selective emissivity peaks match the atmospheric transparent window. Figure 14c shows the *p*-polarized emissivity dispersion indicating the robustness of the high emissivity to the incident angle. This shows that the absorption enhancement originates from the excited magnetic polariton resonance [50]. The polar angle dependence of the emissivity of the optimal structure under *p*- and *s*-polarized incident waves is illustrated in Fig. 14d, e, respectively. By comparing these two images, it is apparent that the *p*-polarized incident emissivity is significantly enhanced in the range of 8–11 μm, indicating the importance of the top grating structure in phonon polariton excitation.

The normalized magnetic field shown in Fig. 14f–i for a specific wavelength at the peaks and valleys of the emissivity is used to further analyze the magnetic resonance. The strong magnetic dipoles appeared at wavelengths for the peaks of the emissivity, expand outward, and become less concentrated as the emissivity decreased. This confirms that the absorption enhancement in the optimal structure is related to the magnetic polariton resonance. In the *p*-polarized wave, the incident magnetic field can be assumed to be along the direction perpendicular to the incident plane; hence, when the high emissivity is supported by the magnetic polaritons, the incident polar angle does not affect the magnetic field. The intrinsic absorption band of SiO_2 at 12.5 and 20 μm may lead to a low emissivity in the range of 11–13 μm, which makes it harder to achieve perfect radiative properties (high emissivity in the range of 11–13 μm and low emissivity above 13 μm).

Since only one-dimensional periodic structures are considered in this work and the optimal emissivity is only applicable to *p*-polarized waves, the polarization dependency problem will appear during the practical application of this theoretical structure. To solve this problem, a two-dimensional periodic structure should be introduced during optimization. However, solving the electromagnetic field based on the RCWA entails dealing with the two-dimensional Fourier term; thus, the number of solutions would be at least a square multiple of those for the one-dimensional case, which is more time- and resource-consuming.

To solve the above challenges, Kitai et al. [51] proposed a factorization machine with a quantum annealing (FMQA) algorithm and demonstrated its effectiveness by optimizing the radiative cooling performance of a two-dimensional block stacking metamaterial. The FMQA process is illustrated in Fig. 15a, where the target property

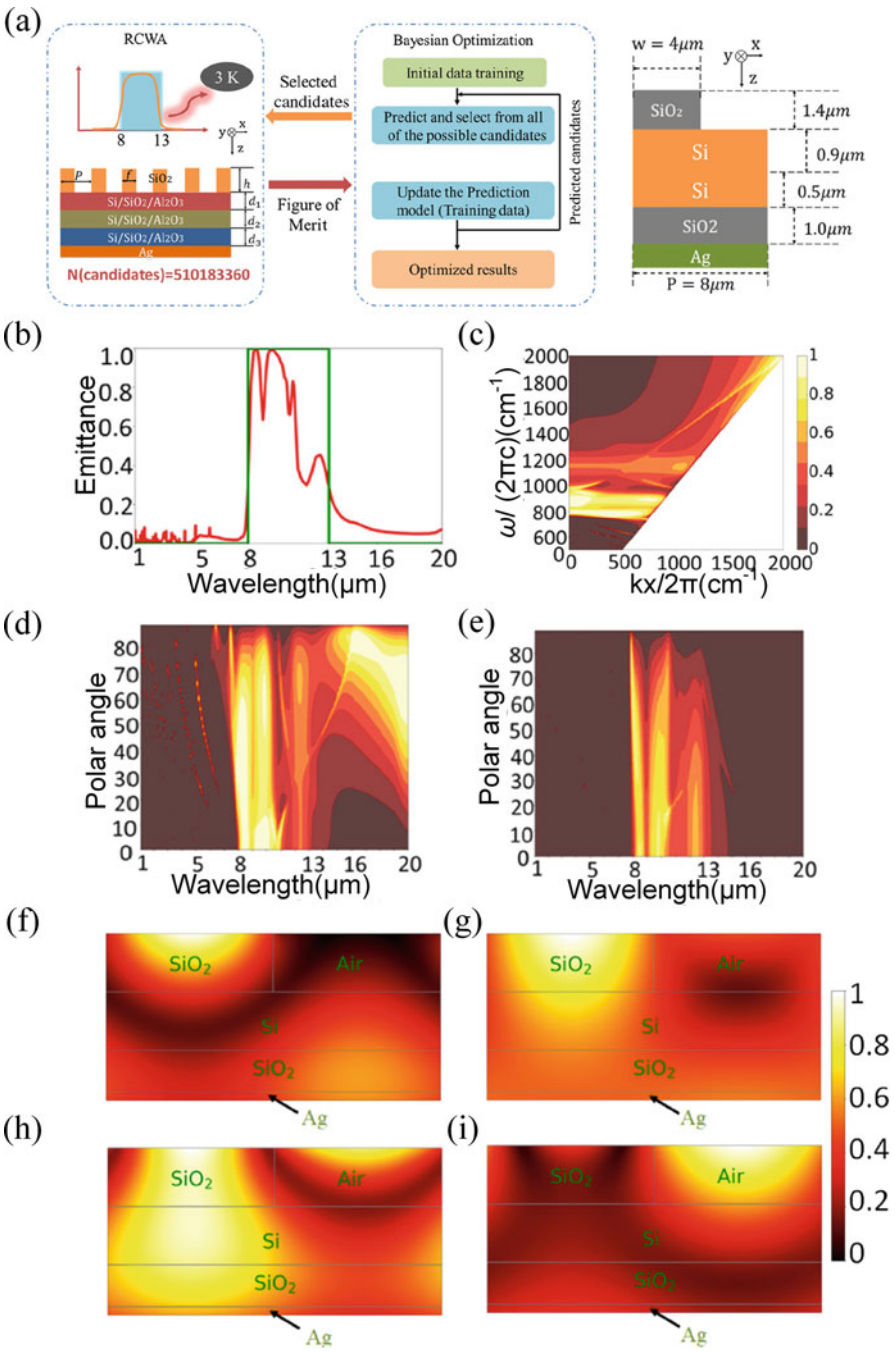

Fig. 14 (**a**) Schematic illustration of the MI method based on the RCWA coupled with the BO method. (**b**) Radiative properties of the optimal structure. (**c**) Emissivity dispersion of the optimal structure under a *p*-polarized incident wave. The polar angle dependence of the emissivity for *p*-polarized (**d**) and *s*-polarized (**e**) waves. Contour plot of the normalized magnetic field for incident wavelength of (**f**) 8.93 μm, (**g**) 9.46 μm, (**h**) 10.58 μm, (**i**) 10.82 μm, respectively [49]

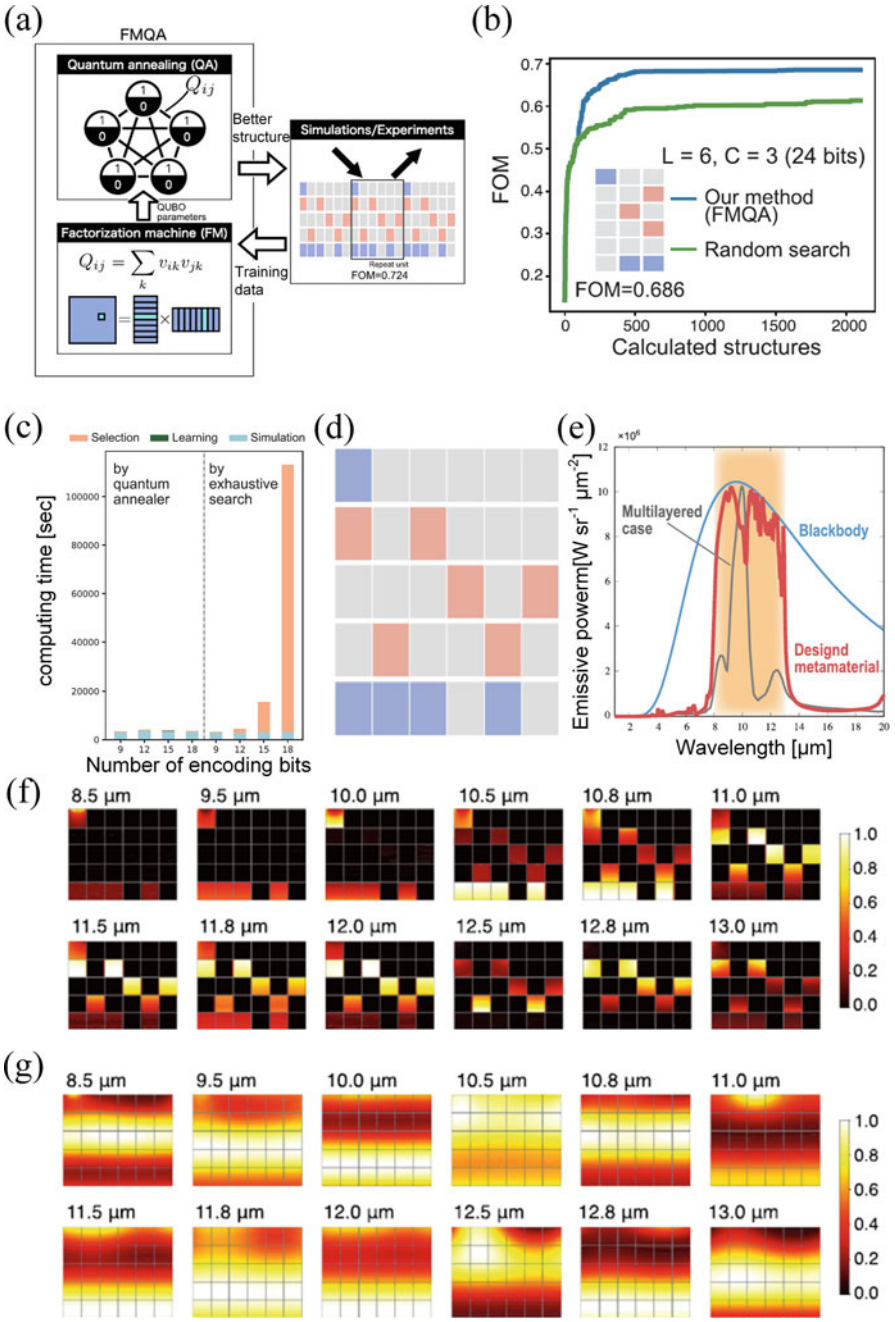

Fig. 15 (**a**) Schematics of the FMQA algorithm. (**b**) Best figure of merit as a function of the number of structures calculated (iterations) by FMQA using a quantum annealer and random search. (**c**) Comparison of the computing time required to perform 500 iterations for automated materials discovery using an exhaustive search and a quantum annealer. (**d**) Optimal metamaterial structure, in which the blue, red, and gray squares denote SiO_2, SiC, and PMMA, respectively. (**e**) Emissive power calculated by RCWA of the designed optimal structure. For comparison, the emissive power of the blackbody (blue line) and optimal structure with one column (gray line) is plotted. Contour plots of the (**f**) normalized electric power dissipation density and (**g**) normalized magnetic field for the optimal structure at selected wavelengths [51]

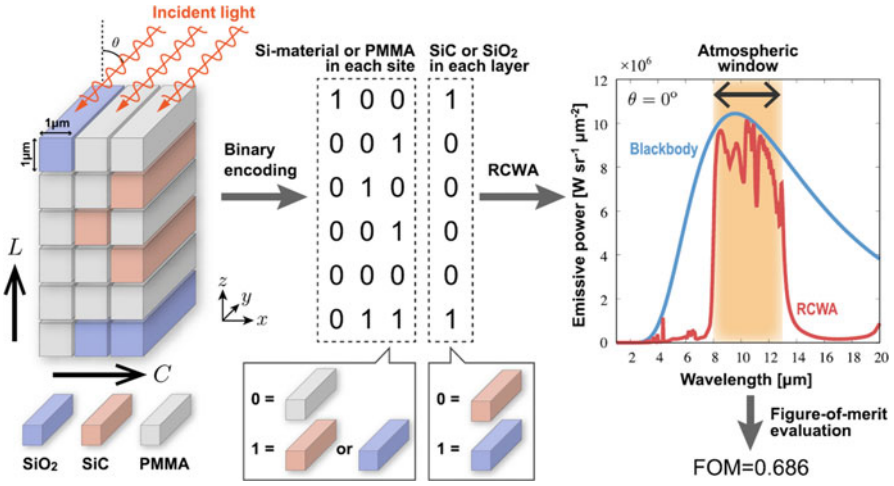

Fig. 16 Example of the target metamaterial structure for $L = 6$ and $C = 3$, binary variables expressing it, and emissive powers of the target metamaterial (red curve) and blackbody (blue curve) calculated by RCWA [51]

of the optimization task is the FOM of the radiative cooling calculated by RCWA. The target metamaterial structure was composed of SiO_2 and SiC wires placed in poly(methyl methacrylate) (PMMA). As shown in Fig. 16, each wire was deposited along the y-axis, which was set as the periodic boundary condition. The x–z plane was divided into uniform units with a side length of 1 μm, which are either SiO_2, SiC, or PMMA. The number of units in the z and x directions of the structure were denoted as L and C, respectively. The metamaterial structure was first encoded into binary sequences to utilize the quantum annealer. As shown in Fig. 16, the configuration of the wired materials (SiO_2 or SiC) and PMMA was determined by $L \times C$ bits alone with a complementary sequence, which was used to define the type of wired materials in each layer. During the ML optimization process, the factorization machine (FM) was trained first with the available data, based on which, a new candidate related to an acquisition function flows to the quadratic constrained binary optimization solved by a quantum annealer was selected. Then, the information on the property and structure of the new candidates were added to the training data for retraining the FM. To verify the superiority of the FMQA, the optimal FOM was plotted in Fig. 15b by random search and FMQA as a function of the iteration numbers, with the inset showing the optimal structure. The FMQA could find a structure with a higher figure of merit after fewer iterations, suggesting that it is a useful method for new metamaterial design. Meanwhile, many typical ML optimization algorithms controlled by an acquisition function, such as the BO algorithm, often conduct an exhaustive search in the selection part, which is time consuming. Figure 15c compares the computing time between the exhaustive search algorithm and FMQA as a function of the structure size. Both methods

could effectively determine the optimal structure within 500 iterations. However, the required time increased more than tenfold for exhaustive search compared to quantum annealers for a large 18 bits case, which indicates that the FMQA can be used to overcome the computational barrier in MI.

The FMQA is conducted over many structures with different number of layers (L) and columns (C). The structure and emissive power of the optimal candidate are shown in Fig. 15d, e, where the emittance peaks fall into the atmospheric transparent window. In addition, the emissive power of the optimal structure with one column was plotted as a gray line, which is smaller than the designed metamaterial. This means that the designed structure is essential for better performance of the radiative cooling. During the FMQA optimization process, it was found that the structures with SiO_2 located separately at the top and bottom sides and SiC occupying the middle part always exhibits a high figure of merit. To understand this phenomenon, the electric power dissipation density of the optimal structure at different wavelengths was evaluated, as shown in Fig. 15f. The SiO_2 on both ends dominate the absorption in the lower wavelength band (8–11 μm), while the middle SiC layer absorbs most of the wave energy in the higher wavelength band (11–13 μm). The physical mechanism of the high emissivity of the optimal structure was then analyzed. Since the emissivity of the p-wave dispersion relation shows incident angular independence (not shown here), it can be concluded that the resonance in the structure does not originate from the surface phonon polariton, which shows a high incident angular dependence. To further demonstrate the magnetic polariton resonance, Fig. 15g shows the normalized magnetic field at different typical wavelengths. By comparing Fig. 15f and g, it can be observed that there always exists strong magnetic field inhibition at the part with a high emissivity, where the polariton resonance is excited. In addition, the confined magnetic field becomes decentralized and flatter as the emissivity decreases, which indicates that the high emissivity of the optimal structure results from the magnetic polariton resonance.

4.2 Thermal Nanostructures Design for Ultranarrow Thermal Emission

Wavelength-selective narrow-band thermal radiation control is a key technology in the application of incandescent light sources [52], microbolometers [53], and infrared heaters [54]. In the past few decades, various state-of-the-art nanostructures have been proposed and demonstrated, such as multilayer [55, 56], photonic crystals [57], and metal-insulator-metal metamaterials [58, 59]. Among these nanostructures, multilayers have become a research hotspot because of their relatively simple processing technology and high scalability.

Sakurai et al. [60] proposed an ultranarrow-band wavelength-selective thermal radiator based on the BO method coupled with the transfer matrix method (TMM)

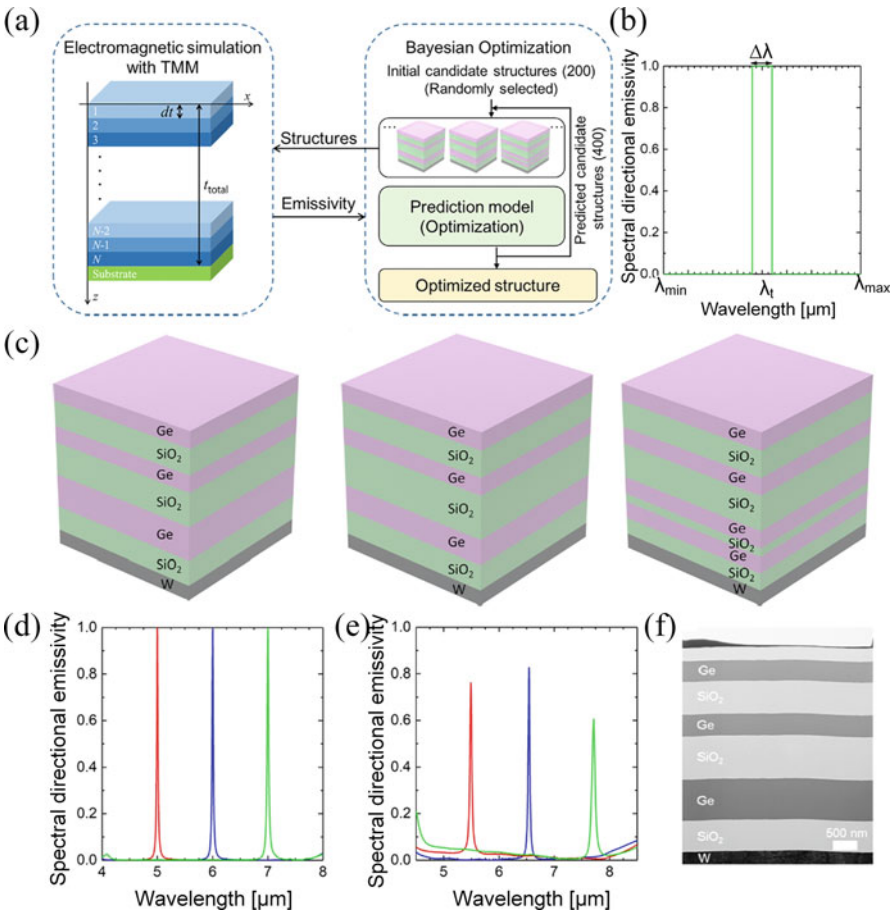

Fig. 17 (**a**) Schematic of the optimization method combining TMM and BO algorithm. (**b**) Schematic of the ideal optical property of the narrow-band thermal radiator. (**c**) Optimal structures of the narrow-band thermal radiators at target wavelength of 6.0, 5.0, and 7.0 μm, respectively. (**d**) Calculated spectral directional emissivity of the optimal structure. (**e**) Measured spectral directional emissivity of the fabricated structure. (**f**) Cross-sectional TEM images of the fabricated sample at $\lambda_t = 6.0$ μm [60]

and experimentally demonstrated the optimized radiative properties of the proposed multilayered structures. Figure 17a shows a schematic of the optimization method. The target structures consist of N unit layers, in which there are three kinds of alternative materials for each layer, i.e., Ge, Si, or SiO_2. The emissivity spectra of the candidate structure can be calculated using the TMM. The target optical property is shown in Fig. 17b. The ideal radiator exhibits a sharp and high emissivity at λ_t with a bandwidth $\Delta\lambda$, while the emissivity for the rest of the wavelengths is suppressed to prevent radiative heat loss. The optimal structures for $\lambda_t = 6.0$, 5.0, and 7.0 μm are shown in Fig. 17c and consist of a similar aperiodic multilayered

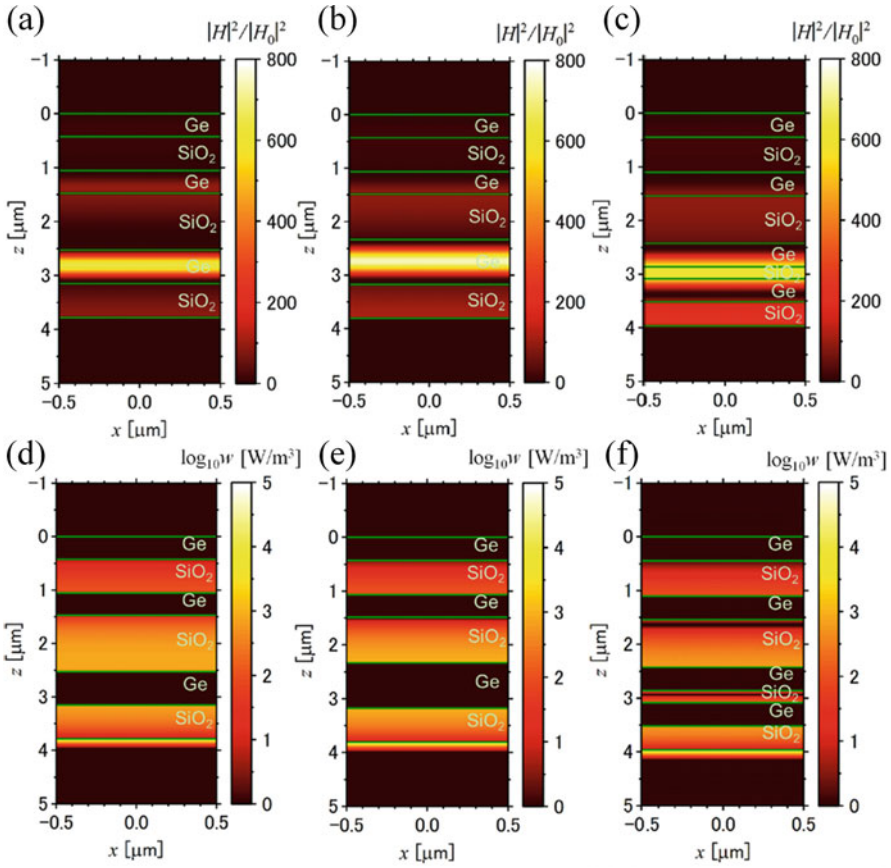

Fig. 18 Contour plots of the normalized magnetic field intensity (**a**–**c**) and power dissipation density (**d**–**f**) for target wavelengths of (**a**, **d**) 5.0 μm, (**b**, **e**) 6.0 μm, and (**c**, **f**) 7.0 μm [60]

structure. Their corresponding spectral directional emissivity is shown in Fig. 17d. The ideal sharp and high emissivity at the target wavelength is achieved based on the optimal structure, while no redundant peaks are observed within the rest of the wavelength range. To verify the optimized simulation results, the optimal structures were experimentally fabricated. As shown in Fig. 17e, the three tailored emissive peaks were observed, although the peak emissivity decreased and the peak location redshifted by approximately 0.5 μm. The discrepancy phenomenon results from the thickness deviation of the single layers in the samples from the ideal values. However, in general, the main features, thus the emissivity peak at the selective wavelength was achieved.

To further investigate the mechanism of the optimized optical properties, the magnetic field was calculated, as shown in Fig. 18. As shown in Fig. 18a–c, the electromagnetic energy is strongly confined in the Ge layer at $\lambda_t = 5$ and 6 μm,

whereas at $\lambda_t = 7\ \mu m$ the strong confinement is in the SiO_2 layer. This suggests that the enhanced emissivity in the optimized structure originates from localized modes, which is similar to the defect modes in the photonic crystals [61]. Defect modes exist inside a photonic bandgap in photonic crystals; therefore, this is a common phenomenon in periodic structures. However, it is interesting to find a similar localized mode inside the optimal aperiodic structures. In other words, the optimized defect layers, which are used to construct an emissive sharp peak, were introduced into the photonic crystals. As shown in Fig. 18c, the defect layer corresponds to a sandwich structure with two layers of Ge and one layer of SiO_2. Therefore, the optimized structure successfully inhibits the other emissive peaks because of the higher-order harmonics. To quantitatively analyze the power absorbed by the optimized structure, the power dissipation density was calculated and shown in Fig. 18d–h. The strong absorption occurs at the tungsten substrate, whereas the weak absorption occurs within the SiO_2 layer. Therefore, it can be concluded that the thermal energy dissipation mainly appears in the metallic substrate because of the large optical loss.

4.3 Thermal Nanostructure Designs for Thermophotovoltaic System

Thermophotovoltaic (TPV) systems increase the Shockley–Queisser limit of the solar photovoltaic (SPV) systems by transforming the broad input solar spectrum to tailored narrow-band thermal emission [62]. For thermal emitter structure design, the 1D-multilayer Tamm plasmon polaritons structures are superior in both tunable performance and scalable manufacturing, which is composed of a metallic mirror and distributed Bragg reflector (DBR). Hu et al. [63] constructed a TPV system by integrating a Tamm emitter with a solar cell. They optimized the Tamm emitter by taking the system efficiency and power density as coupling parameters using the MCTS algorithm. As shown in Fig. 19a, there are two typical TPV systems composed of different types of Tamm emitters, i.e., the DBR-side and metal-side emitters. The DBR consists of alternate SiO_2 and TiO_2 layers, while the metal layer is composed of W-Al_2O_3 alloy with tunable percentages of the W ingredient (f_w). Figure 20b shows the Tamm emitter optimization process using the MCTS method, in which the SiO_2 and TiO_2 layers of the DBR were encoded as 1 and 0, respectively, to form binary sequences that serve as descriptors in ML. The corresponding emissivity spectrum is then calculated by TMM and used as input to the PV cell model to determine the system efficiency and power density. The ideal emissivity of the Tamm emitter was investigated before optimization, as shown in Fig. 19c. When the bandgap wavelength λ_{bg} is fixed, the output power P increases monotonically with increase in the unity emissivity width D, whereas the system efficiency peaks at a specific width. Meanwhile, when D is maintained, even a small right shift can result in a significant drop in both system efficiency and power

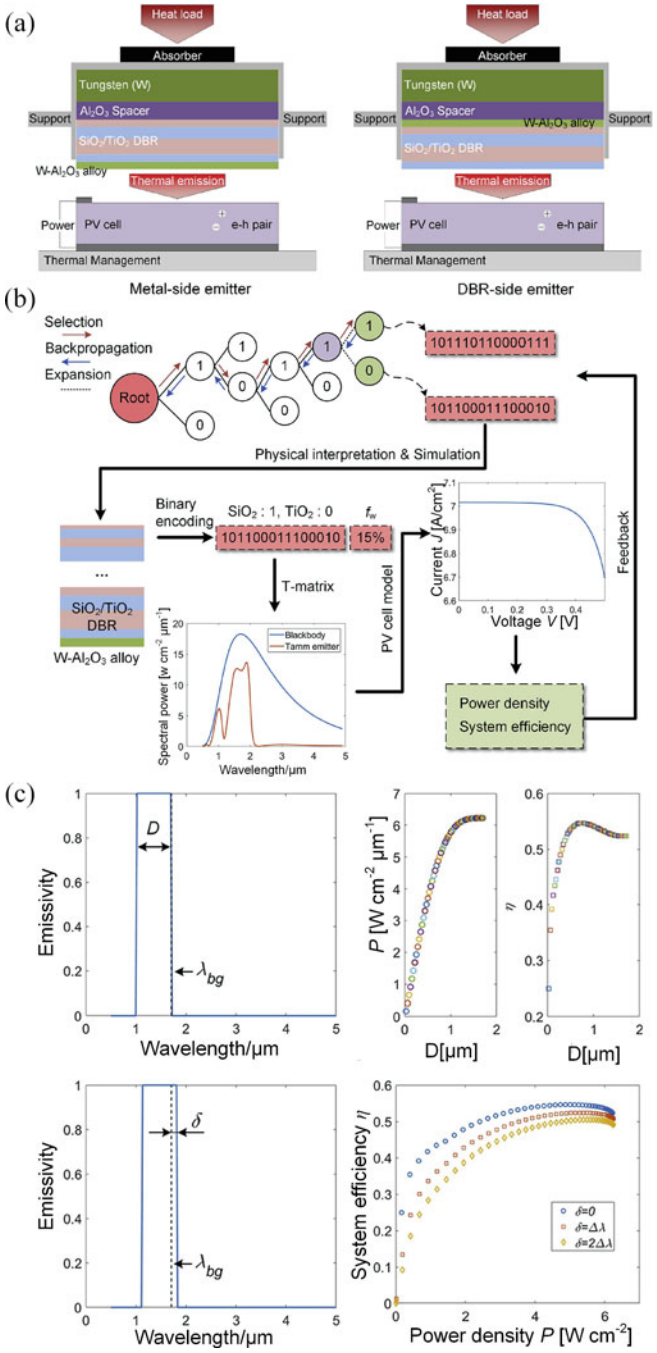

Fig. 19 (**a**) Structural diagram of the TPV system with metal-side and DBR-side emitter. (**b**) Schematic of the MCTS optimization process for a Tamm emitter, namely the sequence of the DBR layers to maximize the power density and system efficiency of the TPV. (**c**) Ideal emissivity spectrum of the TPV system [63]

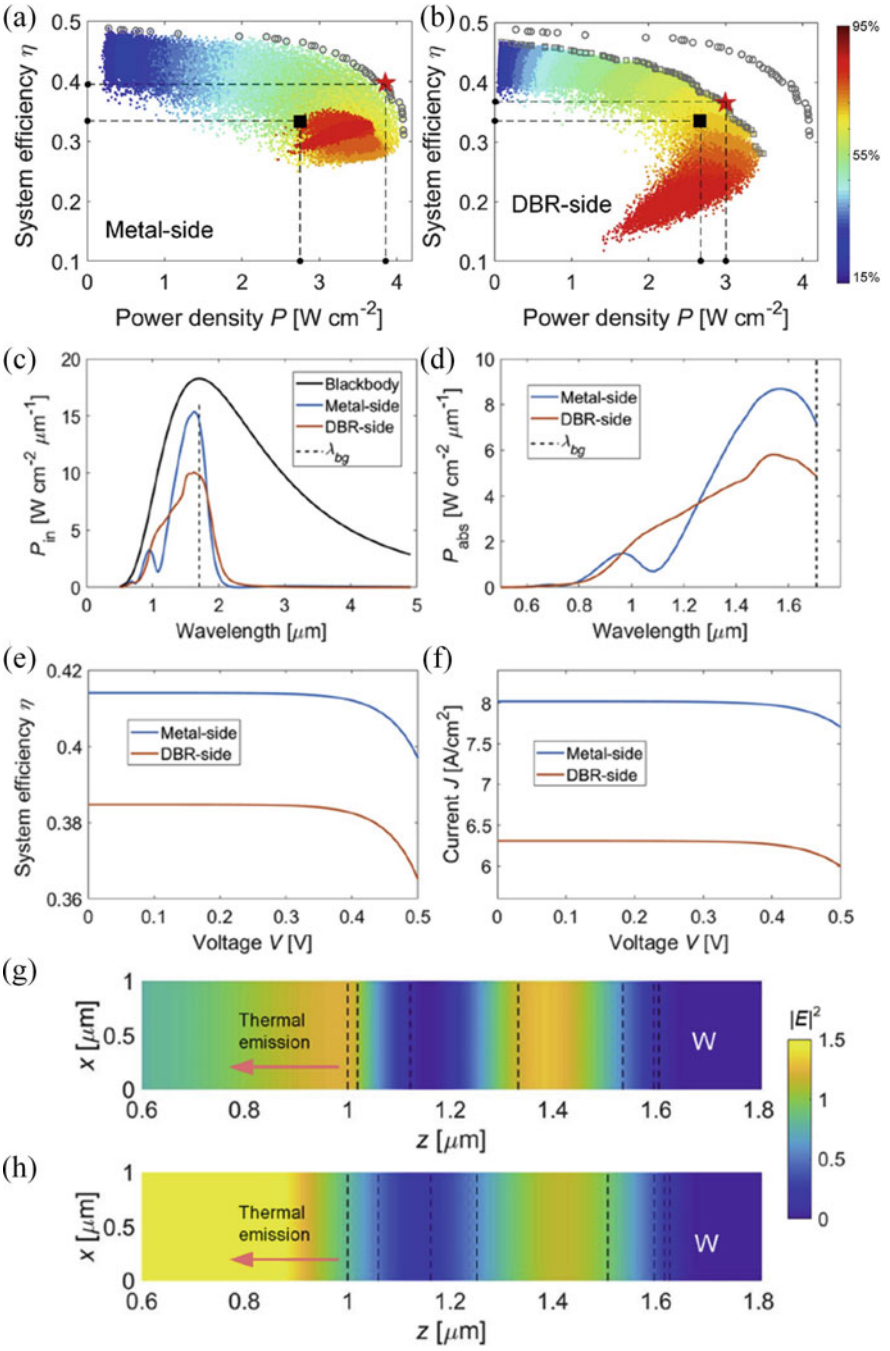

Fig. 20 Optimization results of the (**a**) metal-side and (**b**) DBR-side TPV system structures. (**c**, **d**) Incident and absorbed power spectra companions. Comparison of the (**e**) system efficiency and (**f**) photocurrent at different input voltages. Electric field of the (**g**) metal-side and (**h**) DBR-side emitter at 1.708 μm [63]

density. These findings indicate that it is difficult to achieve the ideal emissivity by manual structural design, and hence ML optimization is advantageous.

The optimized results of the Tamm emitters with different W-percentages ranging from 15% to 95% are shown in Fig. 20a, b. For the metal-side emitter, as the f_w increases, the power density P increases at first and then decreases. A similar trend is observed for the DBR-side emitter. A high system efficiency requires a low f_w, while high power demands the f_w to be as large as possible before the inflection point. The gray circles in Fig. 20a, b represent the Pareto front lines, while the global optimal results are denoted by the red star in both cases. By comparing the Pareto front lines between the two structures, the metal-side structure shows superior properties because of its higher system efficiency and power density. To further analyze the mechanism, the performance parameters of these two TPV structures were compared, as shown in Fig. 20. The power spectrum of the metal-side emitter was stronger at the bandgap wavelength than that of the DBR-side emitter, which affects the system efficiency and power density, as discussed in Fig. 19c. Figure 20d shows the power spectra absorbed by the two structures. It indicates that the PV cell can only absorb the thermal photons whose wavelength is lower than the bandgap, and the metal-side emitter is more suitable for matching the PV cell because its emissivity is closer to the ideal emissivity curve. Furthermore, the photocurrent and system efficiency of the metal-side emitter are higher than those of the DBR-side emitter at different input voltages, which is consistent with the optimization of the former. The electric field of the two optimized emitters at a specific wavelength is shown in Fig. 20g, h, both of which are typical sine functions. Meanwhile, the electric intensity of the metal-side TPV system is stronger, resulting in enhanced thermal emission. To further illustrate the superiority of the optimal aperiodic structures, the same properties in Fig. 20 of the corresponding periodic structure were simulated as shown in Fig. 21. The metal-side Tamm emitter still exhibits better performance than the DBR-side emitter, which is consistent with previous conclusions. From the above findings, it can be concluded that the Tamm emitters with aperiodic structures are better for matching the PV cells. However, such aperiodic structures cannot be designed by manual search because of the many candidate structures to select; hence ML algorithm can be applied. In addition, since there are many interfaces in the Tamm emitters, the interface quality, such as the material defects, thickness, accuracy, and roughness, have a huge influence on the radiative properties of the emitter, thus greatly affecting the performance of the TPV system. Therefore, the manufacturing precision of the fabricated samples is of great importance for experimental validation.

4.4 Thermal Nanostructure Designs for Thermal Camouflage

Thermal camouflage, another interesting thermal functionality, aims to blend the targets into the background to confront IR detection. According to the Stefan–Boltzmann law, the detected thermal energy is coupled with the target temperature

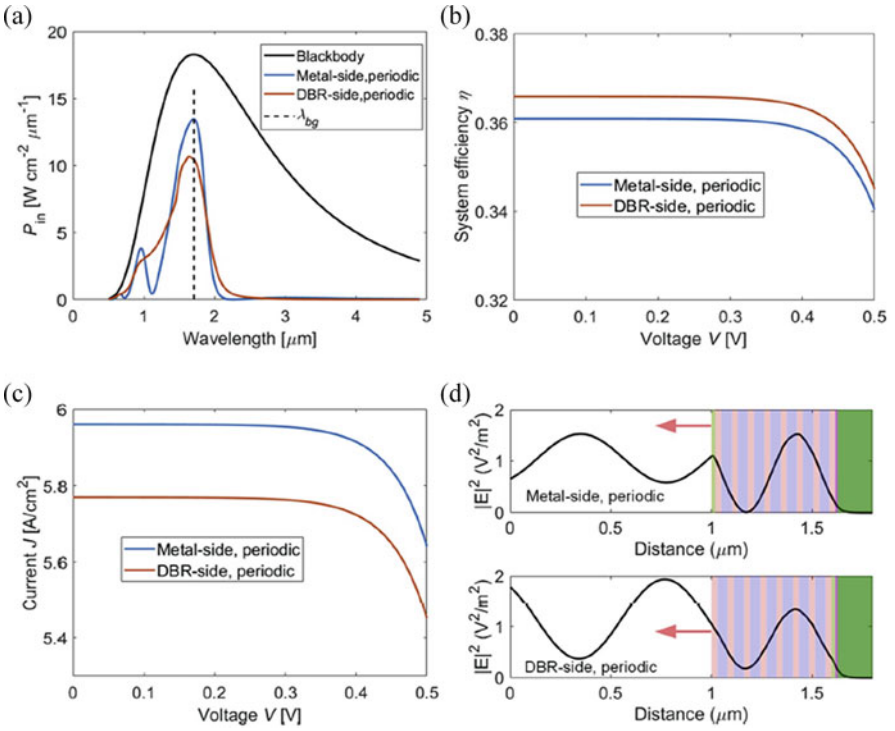

Fig. 21 Comparison of the metal-side and DBR-side TPV systems with periodic DBR. (**a**) Incident power spectral comparison. Comparison of the (**b**) system efficiency and (**c**) photocurrent different input voltages. (**d**) Electric field of the metal-side and DBR-side emitter with periodic DBR at 1.708 μm [63]

and surface emissivity. Therefore, there are two ways to achieve thermal camouflage: by maintaining temperature close to the background and changing the surface emissivity to generate an equivalent detected temperature. Conductive thermal metamaterials have been developed based on the first method [70–72]. However, the application of conductive thermal metamaterials is limited because they can only control the in-plane heat conduction. To control the out-of-plane thermal emission, radiative thermal metamaterials have been proposed. However, to date, the function of radiative thermal metamaterials have not been studied as comprehensively as their conductive counterparts. Consequently, Song et al. [73] theoretically investigated the surface emissivity of the Au/Ge/Au structure, using RCWA, and successfully achieved thermal camouflage, thermal illusion, and thermal messaging functionalities. Figure 22a illustrates the one-dimensional metal/insulator/metal (MIM) structure in a unit cell. The grating ridge is a double-layer patch consisting of Au and Ge on the top and bottom, respectively. The patches then periodically array on the Au substrate to form the metamaterial structure, in which the grating width w can be regulated to control the surface emissivity.

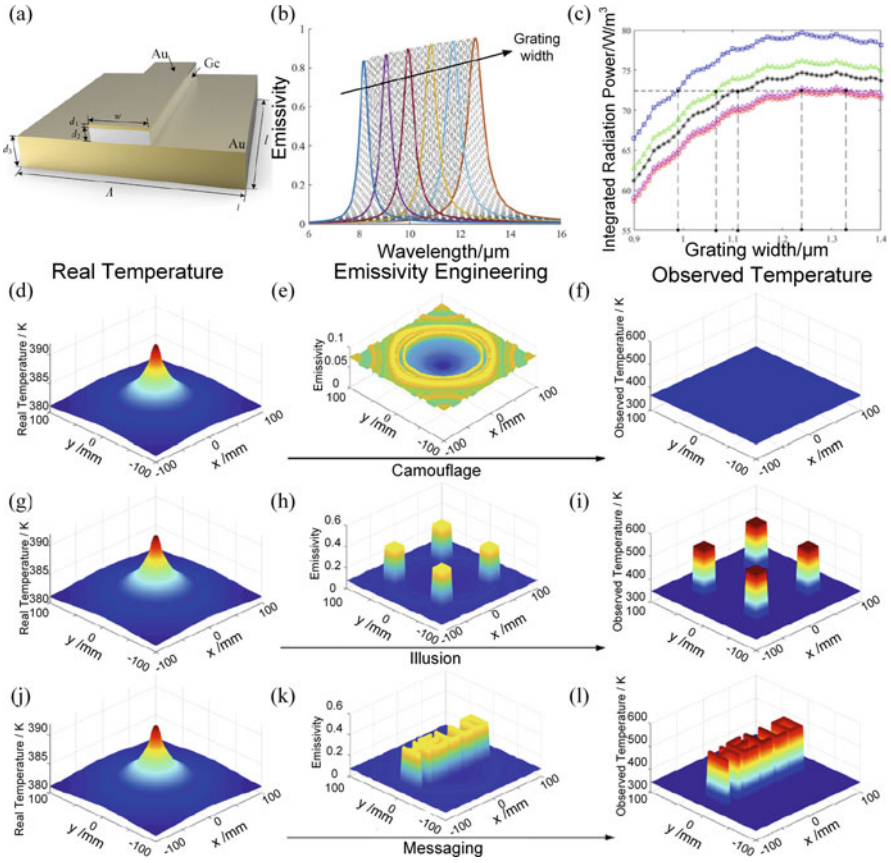

Fig. 22 (**a**) Schematic of the single Au/Ge/Au MIM structure, in which a thin-layer Ge spaces the Au grating and Au substrate. The grating width w is screened from 0.9 to 1.4 μm and the corresponding surface emissivity spectra are plotted in (**b**) where the wavelength range is 6–16 μm. (**c**) Integrated radiation power with varied grating width of five typical points in (**d**). (**d**, **g**, **j**) Original temperature field of a plate with a heat source in the center. (**e**, **h**, **k**) Surface emissivity distribution for different applications. (**f**) The hot spot is camouflaged and a uniform temperature is observed instead, demonstrating the thermal camouflage functionality. (**i**) Four separated hot spots emerge because of the uniform temperature field in (**f**), demonstrating the thermal illusion functionality. (**l**) The heat signature of "HELLO" is observed because of the uniform temperature field in (**f**), demonstrating the thermal messaging functionality [73]

Figure 22b shows the emissivity spectra as a function of the grating width. As the grating width increases, the emissivity peak of the structure continuously redshifted. These peaks result from the magnetic polaritons (MPs) in the MIM structure, which originates from the strong coupling of the magnetic resonance in the MIM structures with the external electromagnetic (EM) fields [74].

Referring to the working wavelength band of the IR camera, the authors focused on the integrated radiation power in the working wavelength range of 8–13 μm.

As shown in Fig. 22d, a real temperature field with a point heat source was generated. To achieve the thermal camouflage effect by emissivity engineering, the surface was divided into 101 × 101 UCs, and different MIM structures were deposited on each unit cell to achieve consistent surface integrated radiation power. Figure 22c shows the integrated radiation power of five UCs with different grating widths. The desired radiation power P_d is quantified when the standard deviation (STD) of the surface integrated radiation power is minimal. Then, as shown in Fig. 22c, the widths of each unit cell on the surface are selected consecutively by the dashed line. Figure 22e, f shows the distribution of the designed emissivity on the surface and its corresponding camouflage temperature field. The camouflage temperature field is evenly distributed and the real heat source vanishes in the background, demonstrating the thermal camouflage effect. Based on the same strategy, the thermal illusion and thermal messaging functionalities can be realized by engineering the local surface emissivity. The corresponding designed surface emissivity distribution and performance are shown in Fig. 22d–i.

The above work has many novel thermal functions achieved via surface emissivity regulation. However, this structure can only be applied in static scenes, once the heat source moves, the thermal functionalities fail. Nematic liquid crystals (LCs), which are typical stimuli-responsive materials, show great potential for tuning thermal radiation by external electrical stimulation because of their inherently high optical anisotropy, low energy, and adjustable LC particle orientation [75–77]. Inspired by this, Liu et al. [78] demonstrated the emissivity-engineered radiative metasurface to achieve dynamic thermal camouflage based on the metal-liquid crystal-metal (MLCM) structure. Figure 23a shows a schematic of the proposed MLCM structure. The grating ridge is a double-layer patch consisting of Au and LC on the top and bottom, respectively. The patches then are periodically distributed on the Au substrate to form the metamaterial structure; hence the transmittance can be neglected. Figure 23b shows the emissivity spectra as a function of the orientation angles from 0° to 90° in the wavelength range of 6–20 μm. As the orientation angle increases, the emissivity peak of the structure redshifted continuously from 8.7 to 11.8 μm, resulting in a significant difference between the integrated radiation power of the MLCM with different orientation angles in the working wavelength range of 8–13 μm. Therefore, the orientation angle in the MLCM structure can be utilized to control its radiative energy over a wide range to achieve a pseudo-surface temperature for dynamic thermal camouflage. Furthermore, a physical scene is established. To generate a dynamic temperature field, laser beams at the bottom of a Si plate are generated. The laser point moves at a certain velocity. Figure 23d illustrates the 3D temperature field at $t = 10$ s. To achieve thermal camouflage with emissivity engineering, the top surface of the plate is divided into $M \times N$ UCs. Then, different MLCM structures with different LC orientation angles are deposited on each unit cell. Figure 23c shows the integrated radiation power variation of five typical UCs in a plate with different orientation angles [73]. The LC orientation angle distribution on the surface at different times could be obtained using the same strategy as in the above work. To demonstrate the dynamic thermal camouflage, the laser moves from the start point to the end of the plate at a constant velocity along

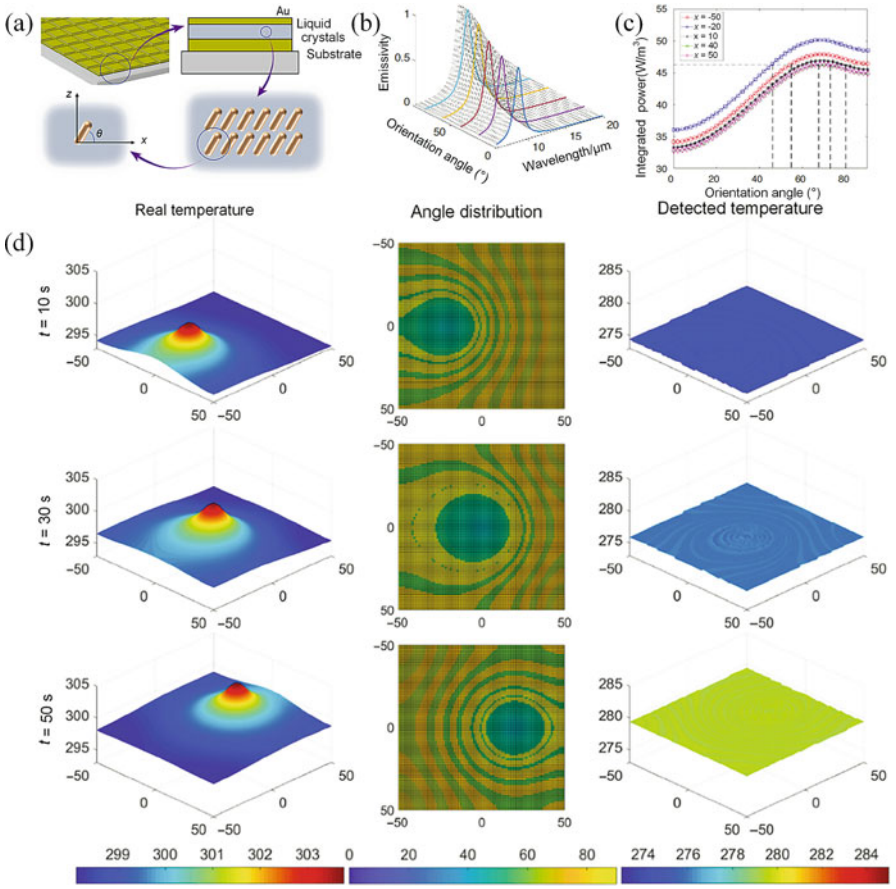

Fig. 23 (**a**) Schematic of the MLCM-based metasurface architecture. Orientation angle θ_{LC} of the crystals in liquids can be dynamically adjusted by the input voltage. (**b**) RCWA-predicted emissivity spectra in terms of wavelength and orientation angle. (**c**) Integrated radiation power with varied orientation angle of five typical unit cells along the *x*-axis. (**d**) Demonstration of the dynamic thermal camouflage via the radiative LC-based metasurfaces, including the real temperature, angle distribution, and the detected temperature at 10, 30, and 50 s [78]

the *x*-axis. Figure 23d shows the real temporal temperature fields at 10, 30, and 50 s. Following the emissivity regulation algorithm, the temporal orientation angle distributions and corresponding camouflage temperature fields at different time steps are also shown in Fig. 23d. In the real temperature field, the heat source can easily be identified; however, in the camouflage temperature field monitored by the IR camera, the heat source vanishes, demonstrating dynamic thermal camouflage.

The above work proves the superiority of the metamaterial structure in realizing different radiative thermal functionalities. However, metamaterials are usually complex with many structural parameters, especially the multilayered structures.

There are many possible combinations of materials and geometric designs for each layer. Currently, structural design is achieved by manually selecting the optimal parameters for different thermal functionalities. This consumes a lot of design time and does not lead to a better structure. Consequently, MI has great application potential in solving this complex structural design problem. Rapid ML optimization of the structure for different thermal functions reduces the design time to find the optimal material parameters and obtain better thermal functionalities.

5 Summary and Perspectives

MI has been successfully demonstrated as an effective and powerful tool for optimizing thermal materials with desired thermal properties in the last several years. For thermal conduction, MI has been applied to search for superlattices with low thermal conductance and defective GNRs with the high thermoelectric properties. For thermal radiation, MI has been applied to explore metamaterials with excellent radiative cooling effects, multilayered photonic crystals, ultranarrow-band wavelength-selective emissivity, and Tamm emitter TPV system with the highest power density and efficiency. MI assist in efficiently finding optimal structures and understanding new physics behind the optimized novel materials and structures. However, several technical challenges still need to be solved, which are described below for future exploration.

Current structure design still suffers from the limitation of small scales and systems. As the scale of the computing system increases, computing time will become a huge challenge. Moreover, the enlargement of the system is always accompanied by more complicated physics, which will further complicate the calculations. For example, for the multilayered structures discussed above, as the layer thickness increases, the phonon-phonon scattering becomes dominant. To ensure the accuracy of the calculation, the anharmonic lattice dynamics (ALD) should be introduced; however, this is more time- and resource-consuming than the harmonic AGF calculations. The increase in computing time for a single structure is greatly amplified in the subsequent MI process because the optimization process requires the calculation of thousands of structures, which makes the entire calculation expensive. Therefore, improvement in computing speed and efficiency is urgently required in MI. Another option is to find a compromise between accuracy and speed, which can be achieved in a hierarchical manner. There, a low-precision method is used for high-speed screening for the first time, followed by high-precision refining steps.

The new effective descriptor is a significant factor in the development of MI. When conducting data screening, many of the existing works only use descriptors that are related to the structural or chemical properties of the candidate, which means that descriptors do not necessarily contain the physical properties. For nanostructure design, the current descriptors are often defined as binary values denoting the element type; however, such descriptors generally contain many elements, which

will slow down the optimization process. Therefore, more effort should be put in finding better descriptors to represent the structure. For instance, as described in Sect. 3.4, the disorder structural parameters can also represent the structures. The development of new descriptors is currently underway to further improve the efficiency of the optimization.

There are also some non-technological issues that need to be addressed. For instance, although first-principles based ALD calculations have become an accepted way to calculate the thermal conductivity of materials, the results from different research groups are not systematically organized. The urgent problem is to link the difference among input and output formats of various tools used for calculations, such as VASP [64, 65], Quantum ESPRESSO [66], etc., for DFT force calculations, and ALAMODE [67], Phonon3py [68], ShengBTE [69], etc., for the ALD calculations. In addition, it is also necessary to set standards for calculating parameters, such as the cutoff length, mesh size, and pseudopotentials. There is an opportunity to expand and standardize database for collecting and sharing data from different individuals.

In any case, the application of MI to heat transfer is expected to expand across the various forms of heat transfer (conduction, convection, and radiation), from nano- to macroscale, and from simulations to experiments.

References

1. Liu, Y., Niu, C., Wang, Z., Gan, Y., Zhu, Y., Sun, S., & Shen, T. (2020). Machine learning in materials genome initiative: A review. *Journal of Materials Science & Technology, 57*, 113–122.
2. Ju, S., & Shiomi, J. (2019). Materials informatics for heat transfer: Recent progresses and perspectives. *Nanoscale and Microscale Thermophysical Engineering, 23*(2), 157–172.
3. Kim, H., Han, J., & Han, T. Y. (2020). Machine vision-driven automatic recognition of particle size and morphology in SEM images. *Nanoscale, 12*, 19461.
4. Chen, Y., Tian, Y., Zhou, Y., Fang, D., Ding, X., Sun, J., & Xue, D. (2020). Machine learning assisted multi-objective optimization for materials processing parameters: A case study in Mg alloy. *Journal of Alloys and Compounds, 844*, 156159.
5. Yamashita, T., Sato, N., Kino, H., Miyake, T., Tsuda, K., & Oguchi, T. (2018). Crystal structure prediction accelerated by Bayesian optimization. *Physical Review Materials, 2*, 013803.
6. Jain, A., Ong, S. P., Hautier, G., Chen, W., Richards, W. D., Dacek, S., Cholia, S., Gunter, D., Skinner, D., Ceder, G., & Persson, K. A. (2013). Commentary: The materials project: A materials genome approach to accelerating materials innovation. *APL Materials, 1*, 011002.
7. Curtarolo, S., Setyawan, W., Wang, S., Xue, J., Yang, K., Taylor, R. H., Nelson, L. J., Hart, G. L. W., Sanvito, S., Buongiorno-Nardelli, M., Mingo, N., & Levy, O. (2012). Aflowlib.Org: A distributed materials properties repository from high-throughput ab initio calculations. *Computational Materials Science, 58*, 227–235.
8. Belsky, A., Hellenbrandt, M., Karen, V. L., & Luksch, P. (2002). New developments in the Inorganic Crystal Structure Database (ICSD): Accessibility in support of materials research and design. *Acta Crystallographica Section B, 58*, 364.
9. Saal, J. E., Kirklin, S., Aykol, M., Meredig, B., & Wolverton, C. (2013). Materials design and discovery with high-throughput density functional theory: The open quantum materials database (oqmd). *JOM, 65*(11), 1501–1509.

10. Xu, Y., Yamazaki, M., & Villars, P. (2011). Inorganic materials database for exploring the nature of material. *Japanese Journal of Applied Physics, 50*(11), 11RH02.
11. Liu, Y., Hu, C., Huang, J., Sumpter, B. G., & Qiao, R. (2015). Tuning interfacial thermal conductance of graphene embedded in soft materials by vacancy defects. *The Journal of Chemical Physics, 142*, 244703.
12. Merabia, S., & Termentzidis, K. (2014). Thermal boundary conductance across rough interfaces probed by molecular dynamics. *Physical Review B, 89*(5), 054309.
13. Tian, Z., Esfarjani, K., & Chen, G. (2012). Enhancing phonon transmission across a Si/Ge interface by atomic roughness: First-principles study with the Green's function method. *Physical Review B, 86*(23), 235304.
14. Sakata, M., Hori, T., Oyake, T., Maire, J., Nomura, M., & Shiomi, J. (2015). Tuning thermal conductance across sintered silicon interface by local nanostructures. *Nano Energy, 13*, 601–608.
15. Sakata, M., Oyake, T., Maire, J., Nomura, M., Higurashi, E., & Shiom, J. (2015). Thermal conductance of silicon interfaces directly bonded by room-temperature surface activation. *Applied Physics Letters, 106*, 081603.
16. Agrawala, A., & Choudhary, A. (2016). Perspective: Materials informatics and big data: Realization of the "fourth paradigm"of science in materials science. *APL Materials, 4*, 053208.
17. Rajan, K. (2012). Materials informatics. *Materials Today, 15*(11), 470.
18. Rajan, K. (2015). Materials informatics: The materials "gene" and big data. *Annual Review of Materials Research, 45*(1), 153–169.
19. Mueller, T., Hautier, G., Jain, A., & Ceder, G. (2011). Evaluation of tavorite-structured cathode materials for lithium-ion batteries using high-throughput computing. *Chemistry of Materials, 23*(17), 3854–3862.
20. Greeley, J., Jaramillo, T. F., Bonde, J., Chorkendorff, I. B., & Norskov, J. K. (2006). Computational high-throughput screening of electrocatalytic materials for hydrogen evolution. *Nature Materials, 5*(11), 909–913.
21. Blundell, T. L., Sibanda, B. L., Montalvao, R. W., Brewerton, S., Chelliah, V., Worth, C. L., Harmer, N. J., Davies, O., & Burke, D. (2006). Structural biology and bioinformatics in drug design: Opportunities and challenges for target identification and lead discovery. *Philosophical Transactions of Royal Society: Biological Sciences, 361*(1467), 413–423.
22. Wu, Y., Lazic, P., Hautier, G., Persson, K., & Ceder, G. (2013). First principles high throughput screening of oxynitrides for water-splitting photocatalysts. *Energy & Environmental Science, 6*(1), 157–168.
23. Rahimi, A., & Recht, B. (2007). *Advances in neural information processing systems 20* (p. 1177). Vancouver, BC: NIPS.
24. Ueno, T., Rhone, T. D., Hou, Z., Mizoguchi, T., & Tsuda, K. (2016). Combo: An efficient Bayesian optimization library for materials science. *Materials Discovery, 4*, 18–21.
25. Dieb, T. M., Ju, S., Yoshizoe, K., Hou, Z., Shiomi, J., & Tsuda, K. (2017). MDTS: Automatic complex materials design using Monte Carlo tree search. *Science and Technology of Advanced Materials, 18*(1), 498–503.
26. Dieb, T. M., Ju, S., Shiomi, J., & Tsuda, K. (2019). Monte Carlo tree search for materials design and discovery. *MRS Communications, 9*(02), 532–536.
27. Yamada, H., Liu, C., Wu, S., Koyama, Y., Ju, S., Shiomi, J., Morikawa, J., & Yoshida, R. (2019). Predicting materials properties with little data using shotgun transfer learning. *ACS Central Science, 5*(10), 1717–1730.
28. Ju, S., Shiga, T., Feng, L., Hou, Z., Tsuda, K., & Shiomi, J. (2017). Designing nanostructures for phonon transport via Bayesian optimization. *Physical Review X, 7*(2), 021024.
29. Hopkins, P. E., Norris, P. M., Tsegaye, M. S., & Ghosh, A. W. (2009). Extracting phonon thermal conductance across atomic junctions: Nonequilibrium Green's function approach compared to semiclassical methods. *Journal of Applied Physics, 106*, 063503.
30. Hyldgaard, P. (2004). Resonant thermal transport in semiconductor barrier structures. *Physical Review B, 69*(19), 193305.

31. Hu, R., Iwamoto, S., Feng, L., Ju, S., Hu, S., Ohnishi, M., Nagai, N., Hirakawa, K., & Shiomi, J. (2020). Machine-learning-optimized aperiodic superlattice minimizes coherent phonon heat conduction. *Physical Review X, 10*(2), 021050.
32. Yamawaki, M., Ohnishi, M., Ju, S., & Shiomi, J. (2018). Multifunctional structural design of graphene thermoelectrics by Bayesian optimization. *Science Advances, 4*, eaar4192.
33. Kalhor, N., Boden, S. A., & Mizuta, H. (2014). Sub-10nm patterning by focused He-ion beam milling for fabrication of downscaled graphene nano devices. *Microelectronic Engineering, 114*, 70–77.
34. Ito, M., Koizumi, T., Kojima, H., Saito, T., & Nakamura, M. (2017). From materials to device design of a thermoelectric fabric for wearable energy harvesters. *Journal of Materials Chemistry A, 5*(24), 12068–12072.
35. Chakraborty, P., Liu, Y., Ma, T., Guo, X., Cao, L., Hu, R., & Wang, Y. (2020). Quenching thermal transport in aperiodic superlattices: A molecular dynamics and machine learning study. *ACS Applied Materials & Interfaces, 12*(7), 8795–8804.
36. Shih, Y. C. A., Sadra, K., & Streetman, B. (1994). Random-period superlattice quantum wells. *Journal of Vacuum Science & Technology B Microelectronics & Nanometer Structures, 12*, 1082–1085.
37. Juntunen, T., Vänskä, O., & Tittonen, I. (2019). Anderson localization quenches thermal transport in aperiodic superlattices. *Physical Review Letters, 122*, 105901.
38. Haykin, S. (1994). *Neural networks: A comprehensive foundation* (1st ed.). Upper Saddle River, NJ: Prentice Hall PTR.
39. Klambauer, G., Unterthiner, T., Mayr, A., & Hochreiter, S. (2017). In I. Guyon, U. V. Luxburg, S. Bengio, H. Wallach, R. Fergus, S. Vishwanathan, & R. Garnett (Eds.), *Advances in neural information processing systems 30* (pp. 971–980). Montreal: Curran Associates.
40. Kingma, D. P., & Ba, J. (2014). Adam: A method for stochastic optimization. arXiv preprint arXiv:1412.6980.
41. Wang, Y., Vallabhaneni, A., Hu, J., Qiu, B., Chen, Y. P., & Ruan, X. (2014). Phonon lateral confinement enables thermal rectification in asymmetric single-material nanostructures. *Nano Letters, 14*, 592–596.
42. Luckyanova, M. N., Mendoza, J., Lu, H., Song, B., Huang, S., Zhou, J., Li, M., Dong, Y., Zhou, H., Garlow, J., Wu, L., Kirby, B. J., Grutter, A. J., Puretzky, A. A., Zhu, Y., Dresselhaus, M. S., Gossard, A., & Chen, G. (2018). Phonon localization in heat conduction. *Science Advances, 4*, eaat9460.
43. Mendoza, J., & Chen, G. (2016). Anderson localization of thermal phonons leads to a thermal conductivity maximum. *Nano Letters, 16*, 7616–7620.
44. Tian, Z. (2019). Anderson localization for better thermoelectrics? *ACS Nano, 13*, 3750–3753.
45. Zhu, L., Raman, A., Wang, K. X., Anoma, M. A., & Fan, S. (2014). Radiative cooling of solar cells. *Optica, 1*(1), 32.
46. Lu, Y., Chen, Z., Ai, L., Zhang, X., Zhang, J., Li, J., Wang, W., Tan, R., Dai, N., & Song, W. (2017). A universal route to realize radiative cooling and light management in photovoltaic modules. *Solar RRL, 1*(10), 1700084.
47. Mandal, J., Fu, Y., Overvig, A. C., Jia, M., Sun, K., Shi, N. N., Zhou, H., Xiao, X., Yu, N., & Yang, Y. (2018). Hierarchically porous polymer coatings for highly efficient passive daytime radiative cooling. *Science, 362*, 315.
48. Raman, A. P., Anoma, M. A., Zhu, L., Rephaeli, E., & Fan, S. (2014). Passive radiative cooling below ambient air temperature under direct sunlight. *Nature, 515*(7528), 540–544.
49. Guo, J., Ju, S., & Shiomi, J. (2020). Design of a highly selective radiative cooling structure accelerated by materials informatics. *Optics Letters, 45*(2), 343.
50. Wang, L. P., & Zhang, Z. M. (2011). Phonon-mediated magnetic polaritons in the infrared region. *Optics Express, 19*, A126.
51. Kitai, K., Guo, J., Ju, S., Tanaka, S., Tsuda, K., Shiomi, J., & Tamura, R. (2020). Designing metamaterials with quantum annealing and factorization machines. *Physical Review Research, 2*(1), 013319.

52. Ilic, O., Bermel, P., Chen, G., Joannopoulos, J. D., Celanovic, I., & Soljacic, M. (2016). Tailoring high-temperature radiation and the resurrection of the incandescent source. *Nature Nanotechnology, 11*(4), 320–324.
53. Liu, X. L., Wang, L. P., & Zhang, Z. M. (2013). Wideband tunable omnidirectional infrared absorbers based on doped-silicon nanowire arrays. *Journal of Heat Transfer, 135*(6), 061602.
54. Landy, N. I., Bingham, C. M., Tyler, T., Jokerst, N., Smith, D. R., & Padilla, W. J. (2009). Design, theory, and measurement of a polarization-insensitive absorber for terahertz imaging. *Physical Review B, 79*(12), 125104.
55. Bermel, P., Ghebrebrhan, M., Chan, W., Yeng, Y. X., Araghchini, M., Hamam, R., Marton, C. H., Jensen, K. F., Soljacic, M., Joannopoulos, J. D., Johnson, S. G., & Celanovic, I. (2010). Design and global optimization of high-efficiency thermophotovoltaic systems. *Optics Express, 18*, A314.
56. Wang, H., Alshehri, H., Su, H., & Wang, L. (2018). Design, fabrication and optical characterizations of large-area lithography-free ultrathin multilayer selective solar coatings with excellent thermal stability in air. *Solar Energy Materials and Solar Cells, 174*, 445–452.
57. Yeng, Y. X., Chou, J. B., Rinnerbauer, V., Shen, Y., Kim, S. G., Joannopoulos, J. D., Soljacic, M., & Celanovic, I. (2014). Global optimization of omnidirectional wavelength selective emitters/absorbers based on dielectric-filled anti-reflection coated two-dimensional metallic photonic crystals. *Optics Express, 22*(18), 21711–21718.
58. Aydin, K., Ferry, V. E., Briggs, R. M., & Atwater, H. A. (2011). Broadband polarization-independent resonant light absorption using ultrathin plasmonic super absorbers. *Nature Communications, 2*, 517.
59. Landy, N. I., Sajuyigbe, S., Mock, J. J., Smith, D. R., & Padilla, W. J. (2008). Perfect metamaterial absorber. *Physical Review Letters, 100*(20), 207402.
60. Sakurai, A., Yada, K., Simomura, T., Ju, S., Kashiwagi, M., Okada, H., Nagao, T., Tsuda, K., & Shiomi, J. (2019). Ultranarrow-band wavelength-selective thermal emission with aperiodic multilayered metamaterials designed by Bayesian optimization. *ACS Central Science, 5*(2), 319–326.
61. Joannopoulos, J. D., Villeneuve, P. R., & Fan, S. (1997). Photonic crystals: Putting a new twist on light. *Nature, 386*, 143.
62. Datas, A., & Algora, C. (2013). Global optimization of solar thermophotovoltaic systems. *Progress in Photovoltaics Research & Applications, 21*, 1040–1055.
63. Hu, R., Song, J., Liu, Y., Xi, W., Zhao, Y., Yu, X., Cheng, Q., Tao, G., & Luo, X. (2020). Machine learning-optimized Tamm emitter for high-performance thermophotovoltaic system with detailed balance analysis. *Nano Energy, 72*, 104687.
64. Kresse, G., & Furthmuller, J. (1996). Efficiency of ab-initio total energy calculations for metals and semiconductors using a plane-wave basis set. *Computational Materials Science, 6*, 15.
65. Kresse, G., & Furthmuller, J. (1996). Efficient iterative schemes for ab initio total-energy calculations using a plane-wave basis set. *Physical Review B, 54*, 11169.
66. Giannozzi, P., Baroni, S., Bonini, N., Calandra, M., Car, R., Cavazzoni, C., Ceresoli, D., Chiarotti, G. L., Cococcioni, M., Dabo, I., Dal Corso, A., De Gironcoli, S., Fabris, S., Fratesi, G., Gebauer, R., Gerstmann, U., Gougoussis, C., Kokalj, A., Lazzeri, M., Martin-Samos, L., Marzari, N., Mauri, F., Mazzarello, R., Paolini, S., Pasquarello, A., Paulatto, L., Sbraccia, C., Scandolo, S., Sclauzero, G., Seitsonen, A. P., Smogunov, A., Umari, P., & Wentzcovitch, R. M. (2009). Quantum espresso: A modular and open-source software project for quantum simulations of materials. *Journal of Physics: Condensed Matter, 21*(39), 395502.
67. Tadano, T., Gohda, Y., & Tsuneyuki, S. (2014). Anharmonic force constants extracted from first-principles molecular dynamics: Applications to heat transfer simulations. *Journal of Physics: Condensed Matter, 26*(22), 225402.
68. Togo, A., Chaput, L., & Tanaka, I. (2015). Distributions of phonon lifetimes in Brillouin zones. *Physical Review B, 91*(9), 094306.
69. Li, W., Carrete, J., Katcho, A. N., & Mingo, N. (2014). Shengbte: A solver of the Boltzmann transport equation for phonons. *Computer Physics Communications, 185*(6), 1747–1758.

70. Han, T. C., Bai, X., Thong, J. T. L., Li, B. W., & Qiu, C. W. (2014). Full control and manipulation of heat signatures: Cloaking, camouflage and thermal metamaterial. *Advanced Materials, 26*(11), 1731–1734.
71. Narayana, S., & Sato, Y. (2012). Heat flux manipulation with engineered thermal materials. *Physical Review Letters, 108*(21), 214303.
72. Hu, R., Huang, S., Wang, M., Luo, X. B., Shiomi, J., & Qiu, C. W. (2019). Encrypted thermal printing with regionalization transformation. *Advanced Materials, 31*(25), 1807849.
73. Song, J., Huang, S., Ma, Y., Cheng, Q., Hu, R., & Luo, X. (2020). Radiative metasurface for thermal camouflage, illusion and messaging. *Optics Express, 28*(2), 875–885.
74. Zhang, Z. M. (2007). *Nano/microscale heat transfer*. New York: McGraw-Hill.
75. Shen, Z., Zhou, S., & Ge, S. (2019). Liquid crystal enabled dynamic cloaking of terahertz Fano resonators. *Applied Physics Letters, 114*, 041106.
76. Khoo, I. (2009). Nonlinear optics of liquid crystalline materials. *Physics Reports, 471*, 221–267.
77. Chen, P., Ma, L., & Hu, W. (2019). Chirality invertible superstructure mediated active planar optics. *Nature Communications, 10*, 2518.
78. Liu, Y., Song, J., Zhao, W., Ren, X., Cheng, Q., Luo, X., Fang, N. X., & Hu, R. (2020). Dynamic thermal camouflage via a liquid-crystal-based radiative metasurface. *Nanophotonics, 9*(4), 855–863.

Machine Learning Accelerated Insights of Perovskite Materials

Shuaihua Lu, Yilei Wu, Ming-Gang Ju, and Jinlan Wang

1 Introduction

Conventionally, perovskite as mineral name is applied to the class of materials possessing the same type of crystal structure as $CaTiO_3$, which initially was discovered in 1839 by the Prussian mineralogist Gustav Rose in the Ural Mountains and was named after the Russian mineralogist Count Lev Aleksevich von Perovski. Perovskites have a general formula with or derived from composition ABX_3, which exhibit many fantastic chemical and physical properties and is one of the most intensely studied material in material field. Generally, perovskites are composed with a large cation at A site and an octahedral BX_6. A corner-shared network is formed with the BX_6 octahedras and the cation A is filled in the caves between the octahedras. Nonideal ionic size ratios and electronic instabilities are compensated by tilting and distorting of BX_6 octahedras. Except these general perovskite structures, many perovskite variants also attract widespread attention, such as double perovskite and layered perovskite. Furthermore, substitution of perovskite A, B, or X sites is allowed for tailoring of properties to meet particular application. Due to the structure and composition flexibility, perovskites can vary from insulating to metallicity, with a wide range of possible applications such as electronic device and sensor [1], magnetic memory components [2], and solar cell [3].

Shuaihua Lu and Yilei Wu contributed equally with all other contributors.

S. Lu · Y. Wu · M.-G. Ju (✉) · J. Wang (✉)
School of Physics, Southeast University, Nanjing, China
e-mail: shlu@seu.edu.cn; ylwu@seu.edu.cn; juming@seu.edu.cn; jlwang@seu.edu.cn

Y. Cheng et al. (eds.), *Artificial Intelligence for Materials Science*, Springer Series in Materials Science 312, https://doi.org/10.1007/978-3-030-68310-8_8

In recent decades, lead halide perovskites have made tremendous progress in photovoltaic and optoelectronic field. High visible absorption, long carrier-diffusions lengths, and fantastic defect tolerance have led to solar cells with certified efficiency of 25.5% [4]. However, chemical stability, mechanical reliability, and toxicity still are three critical obstacles in the path of eventual commercialization of the emerging perovskite solar cells. This prompts a research focus in halide perovskites to predict new perovskites with targeted properties, especially those composed of abundant, nontoxic elements and with thermal, chemical, and dynamic stability. The latter objectives have been traditionally met through performing density functional theory (DFT) calculations of electronic properties, optical absorption properties, defect properties, and performing ab initio molecular dynamics simulations for materials at various given compositions [3, 5]. Recently, with advances in the descriptor-based modeling techniques, researchers are able to perform high-throughput (HT) screening to rapidly estimate certain targeted material properties [6, 7]. Moreover, machine learning (ML), a modeling approach that has received growing attention, has been employed to accelerate the discovery of new perovskite materials [8]. In brief, the ML method can unveil hidden physical properties of materials, if given abundant data and a learning rule, thereby mapping between inputs and output data [9]. So far, most ML studies on perovskites have been focused on all-inorganic perovskites, double perovskites, and anti-perovskites, which all possess a particular type of crystal structure. Due to their simpler and particular crystal structures compared to the prevailing hybrid organic-inorganic perovskites (HOIPs), various ML methods with different choices of descriptors have been benchmark tested for predicting new and stable perovskites [10–12]. This is because of the difficulty of representing organic cations in a fixed length vector to be compatible with many ML algorithms. To match these challenges, developing flexible, transferrable, and reasonable representations becomes one of the important areas of research in ML for HOIPs. As an alternative to learning from first-principle computational data, ML techniques are also optimal for predicting targeted properties through training with numerous experimental data, mapping between the high performance of devices and the various physical and chemical origins, such as bandgap, absorption, and defect properties.

Herein, we bring a brief and in-depth review of ML-guided design and discovery of perovskite materials for photovoltaic application, a field where LHPs with superior performance and low cost are promising candidate for Next Gen PVs. Our review begins with a discussion of construction of data sets, alongside the challenges of the various collections of material data sets. The next section will provide a review of the material representations including descriptors and feature engineering. The final section reviews the ML applications in recent studies such as the ML techniques accelerate the discovery and design of new perovskites with desire stabilities and bandgaps and discovery of factors in experimental processes, which are significantly related to performance of devices.

2 Learning with Perovskite Databases

The cornerstone of ML material discovery is high-quality material data set, and enough material data will ensure the performance of ML models. For perovskite-based photovoltaic materials, abundant data have been generated through the high-throughput calculations and experiments. Besides, some databases containing the properties of perovskites also provide considerable data. We will discuss these three data sources in detail.

In recent years, due to the continuing development of computing power, HT computational material discovery strategy has become an effective and efficient way to discover new functional materials, especially perovskite materials. Among them, tens of thousands of new perovskite-based materials have been predicted for photovoltaic applications. The HT computational method uses the first-principle calculations to build a large-scale material database, which includes existing and hypothetical materials. To facilitate such large-scale computational tasks and data analysis, a number of well-developed software frameworks are developed, including AFLOW [13], pymatgen [14], the Atomic Simulation Environment [15], MatCloud [16], and so on.

The material properties directly determine the applications of materials [17]. As shown in Fig. 1, for the design of perovskite-based photovoltaic materials, evaluating the stability of perovskites is the first step, which is also one of the challenges restricting the practical application of perovskites. The stability of perovskite is mainly evaluated by three different aspects: (1) structural stability (or formability), (2) thermodynamic stability, and (3) dynamic stability. The formability of perovskite is mainly judged by simple structure descriptors, which will be described in detail in the material representation sect. 3.1. In general, the formation energy ΔH_f and the energy above convex hull E_{hull} are utilized to evaluate the thermodynamic stability of perovskites. The formation energy ΔH_f describes the energy change of a material from an elemental component to a compound, and negative values indicate stable compounds. The energy above convex hull E_{hull} describes whether a compound tends to decompose into various elemental, binary, ternary, or more complex components, while negative values indicate unstable compounds. Thermal and dynamic stability represents a more realistic evaluation of material stability in the operating environment. Computationally, phonon calculations are main methods to assess the dynamic stability of materials and ab initio molecular dynamics is adopted to estimate thermal stability. Due to the complexity and time-consuming of these calculations, it is usually performed only for selected promising candidates in HT screening processes. Secondly, the optical and electronic properties determine the applications of perovskites. In HT calculations, the bandgap is one of the most commonly physical parameters to evaluate the photovoltaic performance of a material, because it directly affects the photovoltaic performance of perovskite materials. The effective masses of electron and hole are directly related to the mobility of the material. The small and balanced effective mass is beneficial for carrier mobility in the solar cell materials [18].

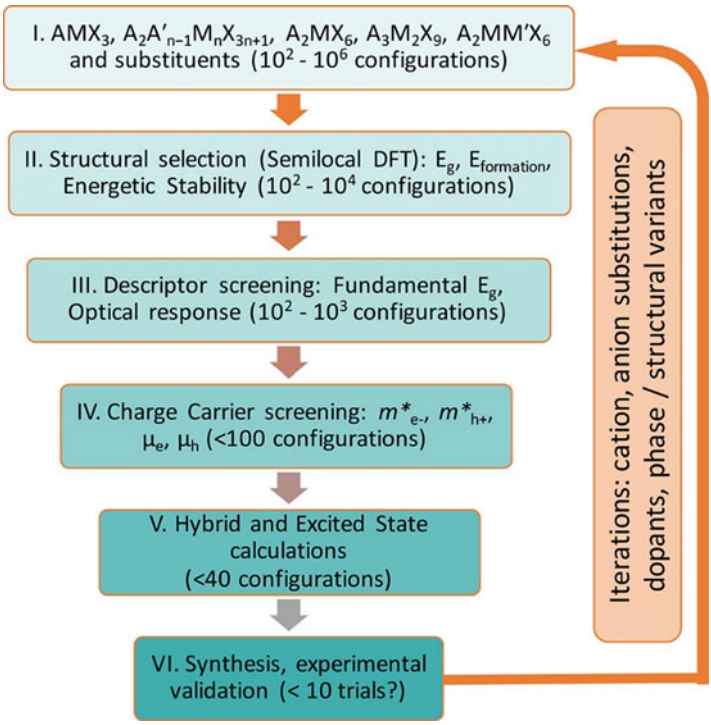

Fig. 1 Rational flowchart for perovskites discovery using HT calculations. (Reprinted with permission from Ref. 17. Copyright © 2017 American Chemical Society)

Inorganic perovskites have firstly been screened by HT first-principle calculations because of the simple crystal structures and abundant candidate materials. In 2012, Castelli et al. [23, 24] explored the bandgap of around 19,000 compounds (perovskite oxides with one or more replacements for oxygen neighbors in the periodic table) using sophisticated semi-local functional called GLLB-SC. Korbel et al. [19] extensively studied the stability and electronic properties of the possible ABX_3 perovskites, where X is a nonmetal and A and B cover a large part of the periodic table. One hundred and ninety-nine perovskites were screened out from more than 32,000 compounds after thermodynamic stability evaluation, and the selected perovskites were characterized by calculating a variety of electronic properties, such as electronic bandgap, average hole effective mass, and so on. Emery and Wolverton [20] presented an exhaustive dataset of 5329 cubic and distorted inorganic perovskites in terms of formation energies, bandgap, and some other properties, which were calculated using density functional theory (the calculation workflow is shown in Fig. 2a).

In addition to the simple inorganic perovskite materials with formula ABX_3, inorganic double perovskite materials have also received significant attention due to the phase space of possible compounds is substantially larger, which increases

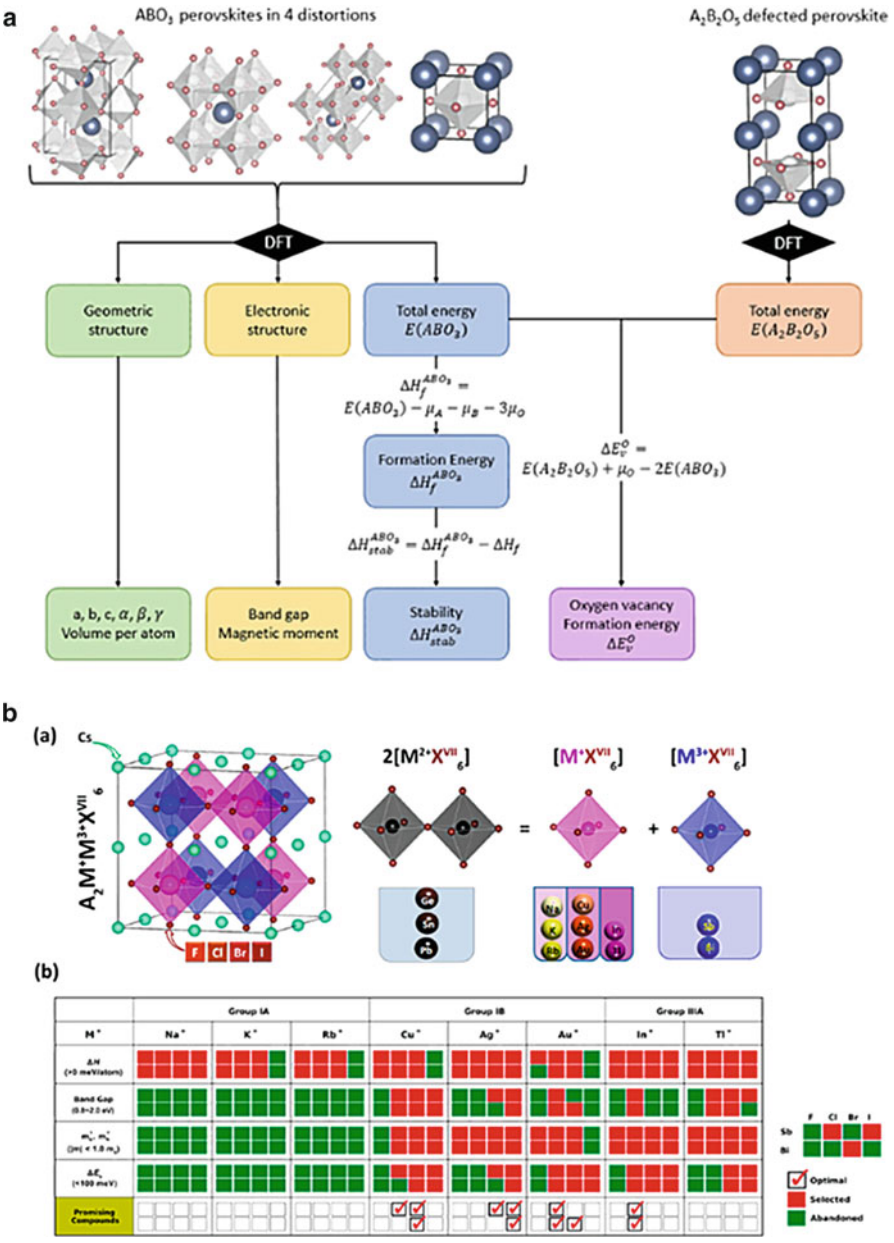

Fig. 2 (**a**) Workflow to calculate all the properties in the dataset. (Reprinted from Ref. 20). (**b**) Space of candidate perovskites for materials screening and materials screening process by considering gradually the properties relevant to photovoltaic performance. (Reprinted with permission from Ref. 21. Copyright 2017 American Chemical Society)

considerably the probability of finding promising candidates with the desired properties [21, 22, 25–27]. As shown in Fig. 2b, Zhao et al. [21] constructed a rich class of double perovskites without Pb^{2+} ions to solve the toxicity of perovskites. After gradually considering the properties relevant to photovoltaic performance, i.e., decomposition enthalpy, bandgap, carrier effective masses, and exciton binding energy, 11 optimal materials were identified as candidates in photovoltaic field. Subsequently, Cai et al. [22] computed structural, electronic, and transport properties of around 1000 double perovskite halides using high-throughput first-principles calculations to aid the discovery of photovoltaic materials (see Fig. 2d).

Compared with inorganic perovskite, hybrid organic-inorganic perovskites (HOIPs), as one of the most promising photovoltaic materials, have attracted tremendous interest recently. The most distinguished virtues of HOIPs include high power conversion efficiency (PCE), low-cost experimental synthesis, and tunable bandgaps. In order to find more stable hybrid perovskites with higher PCE, a lot of HT computing works have emerged [17, 28–33]. An HT computational screening study [28] for 11,025 compositions of HOIP compounds in ABX_3 and $A_2B'B''X_6$ forms has been reported, where A is an organic or inorganic component, B'/B'' is a metal cation, and X is a halogen anion. The computational results contain bandgap values at the scalar relativistic PBE level of all compositions. Besides, the hole and electron effective masses of 1923 candidate semiconductors with bandgaps smaller than 3.5 eV were also estimated. Another effort on computational screening of possible replacements for methylammonium or lead was shown in Fig. 3a, in which 11 different molecular organic cations and 29 different divalent cations were considered [29]. All thermodynamically stable hybrid perovskites were then further characterized by their bandgaps and effective masses. Moreover, Jacobs et al. [34] focused on finding materials that comprise nontoxic elements, stable in a humid operating environment, and have an optimal bandgap for single junction. From a set of 1845 materials, 15 materials passed all screening criteria for single junction cell applications. Notably, these efforts primarily focused on the single perovskite or double perovskite structure. Besides perovskite structures, there exist in principles other organic-inorganic hybrid ternary metal halide compounds with appropriate metal elements and the stoichiometry of component elements that are more stable and even show better optoelectronic properties than the typical perovskite structures. Li and Yang [30] carried out HT calculations on 4507 hypothetical compounds. The chemical formulas of selected candidates include A_2BX_4, $A_3B_2X_9$, and A_2BX_6, in which A = MA (CH_3NH_3), FA ($CH(NH_2)_2$), AD ($(CH_2)_2NH_2$), and X = Cl, Br, or I. As shown in Fig. 3b, the bandgap and electron/hole effective masses of all these candidates were calculated and used to screen appropriate candidates, thereby the formation enthalpy and decomposition enthalpy of those were computed to evaluate the stabilities.

HT calculations have produced considerable data on perovskite materials, especially thermodynamic stability and electronic properties, while theoretical predicted materials are often difficult to experimental synthesis. The fabrication process based on non-vacuum solution has obvious advantages, such as being suitable for scale-

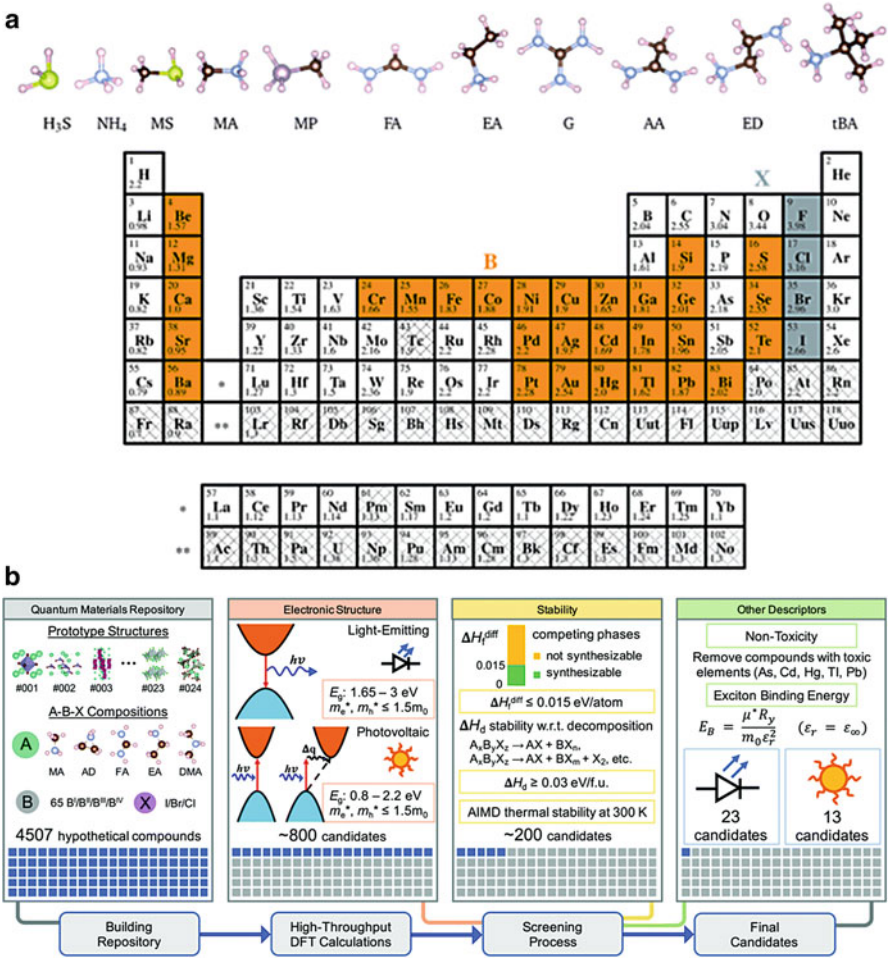

Fig. 3 (**a**) Molecular cations and periodic system of the elements considered for candidate perovskites. (Reprinted with permission from Ref. 29. Copyright 2018 The Royal Society of Chemistry). (**b**) Schematic diagram of the HT screening process for a total number of 4507 compounds, which were generated from 24 different crystal structures. (Reprinted with permission from Ref. 30. Copyright 2019 The Royal Society of Chemistry)

up production, lowering process temperature, lowering energy consumption, and lowering costs, thereby receiving increasing attention in the photovoltaic field. In addition, solvent-based methods can be implemented flexibly in automated HT experimentation, allowing rapid screening of perovskites [37–45]. Chen et al. [46] built an automatic HT experimentation platform for synthesis and characterization of HOIPs with suitable wide bandgap. This platform automatically and efficiently synthesized 95 perovskite polycrystalline samples derived from binary mixtures of five common perovskite precursors and then measured the

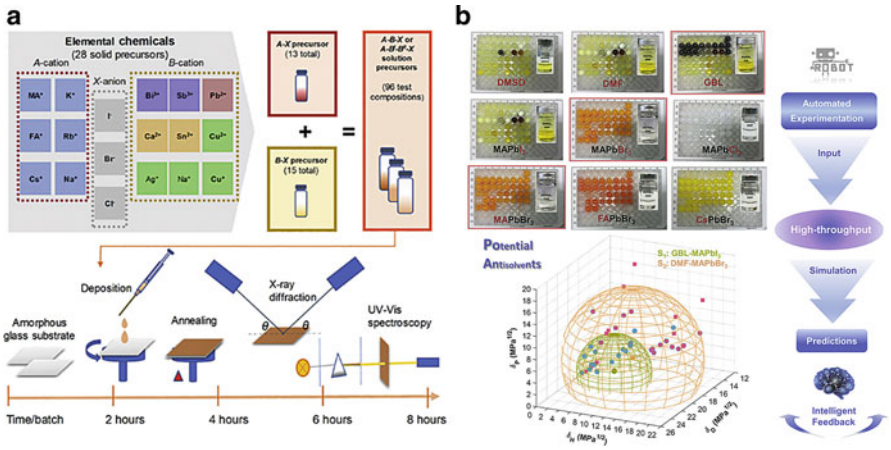

Fig. 4 (**a**) Sketch of the optimized experimental workflow. (Reprinted with permission from Ref. 35. Copyright 2019 Elsevier Inc.). (**b**) A robotic platform was adopted to conduct a comprehensive solvent engineering for making lead halide perovskites in a high-throughput manner. Deeper insights into the working mechanisms and selection criteria of antisolvents were investigated and summarized. (Reprinted with permission from Ref. 36. Copyright 2020 Elsevier Inc.)

corresponding photoluminescence and absorption, yielding six compositing perovskite sample with an optical bandgap of ≈1.75 eV. Apart from exploring stable HOIPs with wide bandgap, the discovery of new perovskite compounds has also been attempted with HT experimentations. Figure 4a illustrates the sketch of the optimized experimental workflow, which enables the realization of rapid search for new lead-free perovskites in the multi-parameter chemical space [35]. Moreover, a self-assembled semi-automated platform based on a standard pipetting robot was utilized to screen the efficient antisolvents for different solvent-perovskite systems and study the influence of interactions among the solvent molecules, cations, metal-halides, and antisolvents (Fig. 4b). In this work, 336 combinations of perovskite-solvent-antisolvent could be prepared and characterized by the platform in 2 days [36]. Although HT experimentations have made remarkable achievements on the discovery and evolution of perovskite materials, they are still in their infancy due to their higher cost and complexity with respect to HT calculations.

Besides HT computations and experimentations, some databases also provide considerable perovskite data for ML after years of development. The HybriD^3 material database [47], jointly created by Duke University and others, comprehensively collects experimental and computational material data of crystalline organic-inorganic compounds. The database contains existing, predicted, and newly synthesized materials. Researchers in the Chemical Material Solution Center of Korea Research Institute of Chemical Technology collected data on the detailed characteristics, structure, and performance of each layer of perovskite solar cells from the literatures, and established a perovskite solar cell database (Perovskite Solar Cells DB) [48]. The database collected a total of 688 documents, 2711

structures, and 17,098 properties, and readers can search independently for different properties and structures, and the database also provides corresponding links to data literatures for reference. The Computational Material Repository (CMR) [49], led by the Center for Atomic Materials Physics of the Technical University of Denmark, uses effective methods to represent and analyze the electronic structure of materials. Among them, there are a number of different CMR projects that cover different types of perovskites. The analysis shows that these perovskite projects include electronic structure, spectrum, and some other different properties. Marchenko et al. provided an open-access database of experimentally investigated hybrid organic-inorganic two-dimensional perovskite-like crystal structure, which contains various properties of 515 compounds from published literatures [50]. In addition, many comprehensive online material databases built from first-principles calculations also contain a large amount of perovskite data, including AFLOWLIB [13], Materials Project [51], Open Quantum Materials Database (OQMD) [52], and Atomly [53]. These databases not only provide a large amount of perovskite data, but also have become an important carrier of information circulation and an important link of data analysis in materials science.

3 Materials Representations

The process of converting the material system into an accurate numerical representation is the key for ML model building to achieve great performance [54–56]. In this process, the relationship between microstructure and target properties (quantitative structure property relationships (QSPR)) enables to be established by using descriptive parameters (defined as descriptors or features) [57, 58]. In general, different problems need to choose specific material descriptors, which heavily rely on the characteristics and target properties of materials. Therefore, to accurately and comprehensively describe the QSPR of materials, the construction of material descriptors usually requires the prior knowledge of the fundamental chemistry and physics [54].

The construction process of the material descriptors is actually to integrate the physical and chemical knowledge related to the target properties into the ML model, which controls the performance of a ML approach. In addition to satisfying desired accuracy of the predictions, any good material descriptor should satisfy the following conditions: (1) descriptors can uniquely describe materials and basic processes related to target properties; (2) materials with large differences (similarities) should be represented by descriptors with the same large differences (similarities); (3) the descriptors should be determined in such a way as to avoid extensive calculations to make a preliminary assessment of the material properties; and (4) the dimensions of descriptors should be kept as low as possible while ensuring model accuracy [7]. In the following content, we will give a concise summary of descriptors for perovskites in photovoltaic applications.

3.1 Descriptors for Perovskites in Photovoltaic Applications

In the past few years, numerous studies of perovskite material design based on ML techniques have emerged that target stability, bandgap, PCE, and other photovoltaic properties. Accordingly, a variety of material descriptors for perovskite have developed and provided an effective way to describe the QSPR between structures and photovoltaic properties for perovskites. These descriptors that can be obtained directly without calculations or experiments mainly fall into three categories: element properties, crystal structure, and experimental parameter. The element property descriptors are mainly used to provide the elemental information of perovskite composition, including the atomic number, Mendeleyev number, orbital radii of atoms, ionic radius of ions, electronegativity, and so on. Crystal structure descriptors contain tolerance factor, octahedral factor, Smooth Overlap of Atomic Positions (SOAP) [59], Crystal Graph Convolutional Neural Networks (CGCNN) [10], and so on. Experimental parameter descriptors, such as precursor concentration, pK_a values, and so on, are usually applied to accelerated experimental synthesis or characterization of perovskites. In addition to the three main categories mentioned above, some other descriptors are also utilized for perovskites, such as binary element descriptors (a set of binary digits representing the presence of chemical elements) [58]. After the descriptor is selected, Fig. 5 schematically illustrates the procedure to generate such descriptors for compounds.

Among these three types of descriptors, the development of crystal structure descriptors plays a significant role in perovskite design. The general chemical formula of perovskites is ABX_3, and the crystal structure of cubic perovskites is shown in Fig. 6a, respectively. To describe the formability of cubic perovskites, Goldschmidt [62] proposed an empirical formula named tolerance factor based on crystal structure in 1926, defined as $t = (r_A + r_X)/\sqrt{2}(r_B + r_X)$, in which the r_A, r_B, and r_X represent ionic radii of A-, B-, and X-site ions, respectively. According to the rigid sphere model, the length of A-X bonds and B-X bonds can be assumed as $r_A + r_X$ and $r_B + r_X$, respectively. Instead of tolerance factor, Li et al. [63]

Fig. 5 Schematic illustration of how to generate compound descriptors. In representation matrix, x_{ij} denotes the representation of feature j in compound i. Here, x_{ij} is a scalar or vector

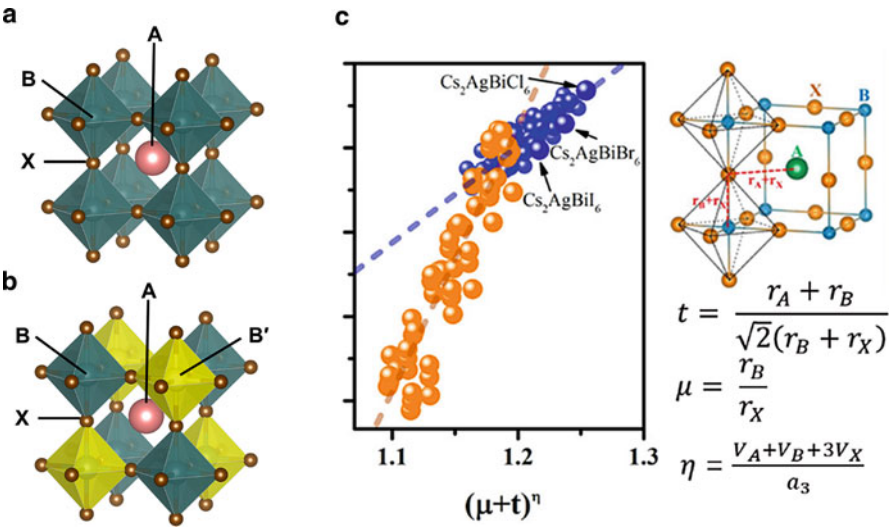

Fig. 6 Structure of (**a**) cubic perovskites ABX_3 and (**b**) double perovskites $A_2BB'X_6$. (**c**) Representation of tolerance factor (t), octahedral factor (μ), and atomic packing fraction (η) for cubic perovskites. r_A, r_B, and r_X represent the ionic radii of A-, B-, and X-site ions, respectively. According to the rigid sphere model, V_A, V_B, and V_X represent the atomic volume of A-, B-, and X-site atoms, respectively. a represents the lattice constant of the cubic cell of perovskites. (Reprinted with permission from Ref. 60. Copyright 2017 American Chemical Society)

proposed a binary descriptor (t, μ) to further clarify the formability of perovskites, which μ is the octahedral factor defined as $\mu = r_B/r_X$ [2]. Based on the analysis of existing perovskites, the stable region in (t, μ) map for halide perovskites is $0.813 < t < 1.107$ and $0.377 < \mu < 0.895$ [64]. These empirical rules successfully guide the discovery of numerous stable perovskites; however, both tolerance factor and octahedron factor are developed based on the inorganic cubic perovskite structure, resulting in the great limitation of application and low predictive accuracy for the formability of other perovskite structures, such as HOIPs and double perovskites. To improve the tolerance factor reliability for HOIPs, Kieslich et al. [65] extended the Goldschmidt tolerance factor by considering the effective radii of organic ions in HOIPs. According to the results, HOIPs were expected to form for tolerance factor between 0.8 and 1, as in the case of solid-state perovskites. To expand the application range of tolerance factor to double perovskites (structure is show in Fig. 6b), Sun and Yin [66] combined the atomic packing fraction (η) with t and μ, and developed a geometric structure descriptor $(t + \mu)^\eta$, which was linearly related to the decomposition energies of perovskites (Fig. 6c). For cubic halide and chalcogenide perovskites, the accuracy of thermodynamic stability prediction was over 86%. Filip et al. [60] developed a generalized tolerance factor $t = (r_A/r_X + 1)/[2(\overline{\mu} + 1)^2 + \Delta\mu^2]^{1/2}$ by analyzing crystal structure of double perovskites. In contrast to the traditional tolerance factor, the generalized tolerance factor was taken into account two octahedral parameters related to the B- and B′-

site cations, the average octahedral factor $\overline{\mu} = (r_B + r_{B'})/2r_X$ and the octahedral mismatch $\Delta\mu = |r_B - r_{B'}|/2r_X$. Benefitting from these careful considerations, the predictive accuracy of generalized tolerance factor for double perovskites reached 80%. These developed crystal structure descriptors have laid the foundation for subsequent ML studies of perovskite materials.

Designing descriptors based on physical and chemical intuition might introduce deviation, resulting in ignoring the best descriptor and hidden structure-property relationship. Fortunately, big-data analysis and symbolic regression technology can quickly and intelligently construct ideal descriptors for target property. One of the attractive methods is the sure independence screening and sparsifying operator (SISSO) [61]. Base on this algorithm, Bartel et al. [12] developed an improved tolerance factor $\tau = \frac{r_X}{r_B} - n_A\left(n_A - \frac{r_A/r_B}{\ln(r_A/r_B)}\right)$, where n_A represents the oxidation state of A-site ions. The new descriptor τ exposes a high prediction accuracy of perovskite stability (92%) on the dataset containing 576 experimentally existing ABX_3 compounds, while the Goldschmidt tolerance factor t only correctly classifies 74% compounds on the same dataset. In particular, the Goldschmidt tolerance factor t can correctly distinguish 49% of non-perovskites, and τ achieves 89% accuracy for non-perovskites, leading to the great improvement of predictive capability. Besides, the new descriptor τ exhibits the high accuracy for $A_2B'B''X_6$ compounds (91% accuracy), suggesting the strong generalization ability on perovskites.

3.2 *Feature Engineering*

For any ML method that targets toward a desired material property, it usually depends on certain number of features (descriptors). Although there may be many factors that affect the target property of materials, the number of features must be reasonable. The best strategy is to choose features that perfectly represent the corresponding property, and the number of features should be less than the number of materials in input dataset to avoid the curse of dimensionality and model overfitting [67]. Especially for material simulation, the amount of data available may be only about 10^3 or less. For such small-scale dataset, how to reasonably choose the material descriptor is crucial [68].

In the process of ML, we usually preliminary perform a relatively rough descriptor screening process. First of all, some features based on the prior knowledge of the physic and chemistry are chosen to build the initial feature set. Then, feature selection, basically a ranking procedure, is applied to pick out the best features by evaluating the model performance. For small-scale data sets, Lu et al. [69, 70] employed a "last-place elimination" feature selection procedure in a ML algorithm to optimize the most relevant features. One can also do feature screening through batch processing, such as principal component analysis, clustering, and so on. For large-scale data sets, because the scale of data set itself is very large, features can be

extracted automatically through a deep learning algorithm without artificial feature set construction. For example, Ziletti et al. [71] constructed a deep learning neural network model based on diffraction images for automatic classification of crystal structures.

In addition to some of the conditions mentioned above for descriptor construction, some specific conditions according to physics and chemistry should also be satisfied. Regarding the design of the descriptor, no matter which form is used, it should be invariant to certain transformations-spatial translational symmetry and rotational symmetry. Therefore, we cannot simply turn the descriptor into a pure "data problem." It should contain some physical and chemical origins.

4 Machine Learning in Perovskite-Based Material Discovery and Study

4.1 Stability

The first step in design of new perovskites is to evaluate the stability, which is usually assessed by the tolerance factor and the octahedron factor. Although these two factors provide a quantitative range for the formability of stable perovskites, their predictions are not accurate enough. The ML-based approach can describe the materials more detailed by constructing appropriate descriptors, and thereby more reliable prediction results can be obtained theoretically. To predict the formability of ABO_3 perovskite, Pilania et al. [75] trained a ML model based on 354 ABO_3 compounds, and created a high-dimensional feature space relating to perovskite structure formability. The approach achieves 95% accuracy in the prediction of perovskite formability. Subsequently, the authors utilized this ML-based approach to search new perovskite halides. In this work, a ML model based on 185 experimentally known perovskites was built to evaluate the formability of perovskite halides. After exploring a number of initial features, ionic radii, tolerance factor, and octahedron factor were determined as the three effective features affecting perovskite formability, demonstrating the great importance of geometric factor on perovskite formability. The trained model achieved an accuracy of 92% for the test set [76]. In addition to formability, some ML models made good performance in predicting the thermodynamic stability of perovskites [77, 78]. For example, ML model was applied to predict the thermodynamic stability of all possible perovskite and antiperovskite crystals that can be generated with elements from hydrogen to bismuth (excluding rare gases and lanthanides) according to the energy above the convex hull. ML algorithm gives the mean absolute error (MAE) of the energy above the convex hull (121 meV/atom) in the test set of 230,000 perovskites, after being trained in 20,000 samples (Fig. 7a) [79]. In addition to cubic perovskites, ML-based approach also makes a progress in identifications of diverse phases of perovskites. Balachandran et al. [72] developed a two-step framework to search for

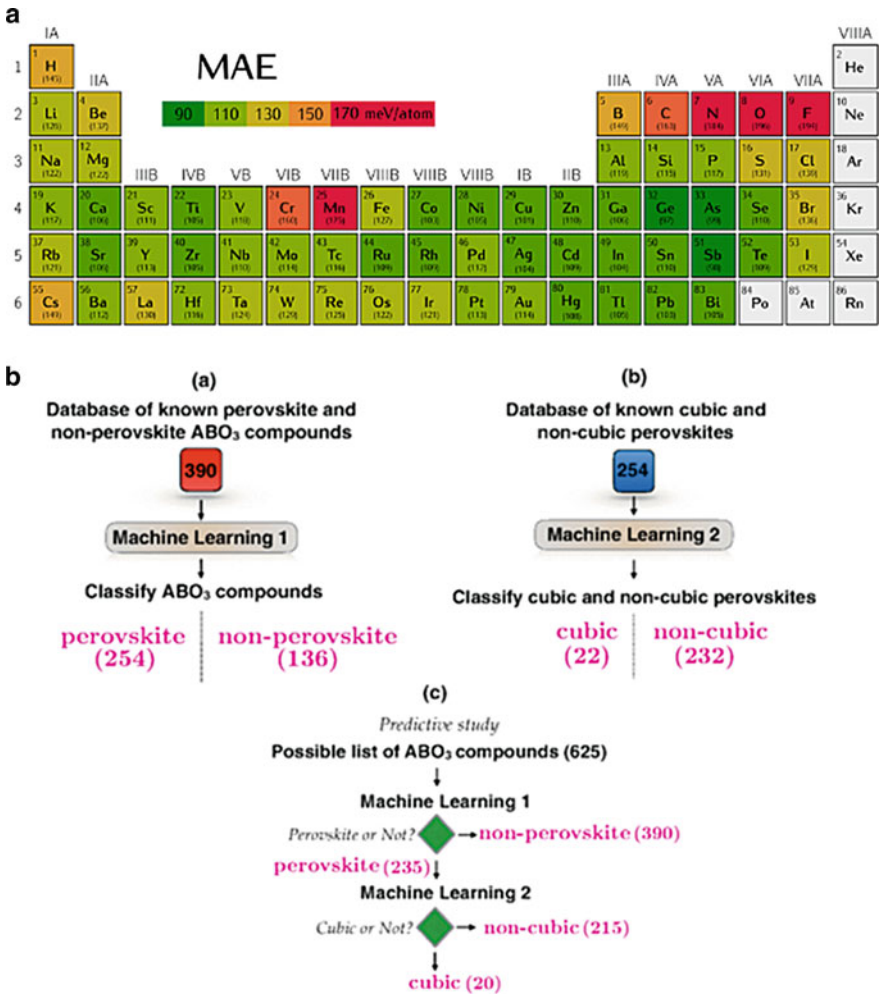

Fig. 7 (**a**) Mean absolute error (MAE, meV/atom) of the test set for AdaBoost used with extremely random tress averaged over all compounds containing each element of the periodic table. The numbers in parentheses are the actual MAE for each element. (Reprinted with permission from Ref. 72. Copyright 2017 American Chemical Society). (**b**) The ML workflow for the prediction of new ABO_3 cubic perovskites. Two independent ML models for the classification of ABO_3 into perovskites or not (machine learning 1) and cubic or noncubic perovskites (machine learning 2). (Reprinted with permission from Ref. 73. Copyright 2018 American Physical Society)

cubic perovskites in ABO_3 compounds (Fig. 7b). Firstly, a ML model was utilized for distinguishing perovskites and non-perovskites with an average cross-validation accuracy of 90%. Then, another ML model was applied for screening out cubic perovskites, and the average cross-validation accuracy was over 94%. Ye et al. [73] introduced deep neural network into predicting the formation energy of perovskite

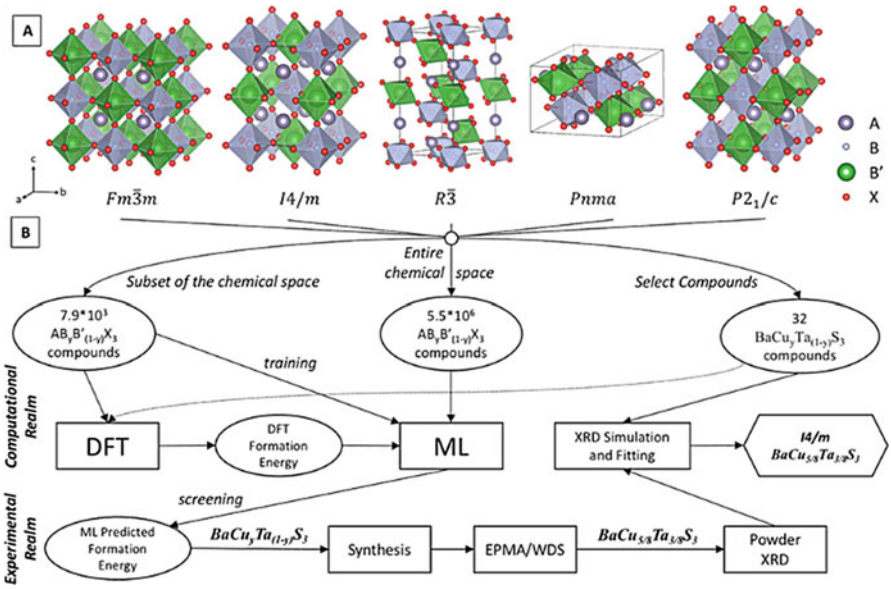

Fig. 8 (**a**) Crystal structure of $AB_yB'_{(1-y)}X_3$ perovskites in different space groups. The ML workflow for prediction of stability perovskite for experimental synthesis. (Reprinted with permission from Ref. 11. Copyright 2019 American Chemical Society)

oxides. Based on only the two descriptors of electronegativity and ionic radius, the trained ML model obtained a high accuracy and a MAE of 20–34 meV/atom. Furthermore, a new binary encoding scheme was introduced to, including the effect of cation orderings, extend ML models to mixed perovskites with low MAE (20–39 meV/atom).

The success of ML in evaluating the thermodynamic stability of single perovskites has inspired more application of ML-based approaches for other more complex perovskites, such as double perovskites, mixed perovskites, and HOIPs [11, 70, 74, 81–83]. Askerka et al. [11] proposed a learning-in-template strategy to rapidly select out double perovskites from 5×10^6 candidates. As displayed in Fig. 8, a series of possible templates corresponding to different crystal structures and stoichiometries were defined. In principle, any $A_2B'B''X_6$ compound belongs to one of these templates. The training and test sets contain formation energy data of 7.9×10^3 compounds in defined chemical space, and the accuracy of the trained ML model is up to 97%. Considering the difference of ionic radii of X-site ions in mixed X-site inorganic perovskites, Lu et al. proposed a modified Goldschmidt tolerance factor and octahedron factor using ML feature engineering. By applying the optimal feature set contained two new descriptors, the accuracy of the gradient boosting classification (GBC) model for perovskite formability is up to 89% [70]. Ali et al. [83] built a deep neural network model to study the cubic phase stability of mixed-cation perovskites. The predicted cubic phase-

stability diagram reveals that with increasing Cs proportion, perovskites possess higher cubic phase stability. This stems from that the large ionic radii of organic molecules in HOIPs bring the internal stress, and the small ionic radii of Cs might offset this internal stress. Moreover, under the guidance of ML-predicted results, $MA_{0.85}DMA_{0.15}PbI_3$ (dimethylammonium (DMA)) can be recovered to the cubic phase at room temperature by adding <10 mol% of cesium cation additives. This suggests that the established ML model can effectively guide further experimental synthesis, avoiding plenty of trial-and-error processes.

The stability of perovskite devices in the operation environment is very important for the practical application of perovskites [80, 84]. Sun et al. [35] utilized a fully connected deep neural network to classify compounds based on experimental X-ray diffraction data into 0D, 2D, and 3D structures with 90% accuracy, more than ten times faster than human analysis. Kirman et al. [85] constructed a framework by combining HT experiments and convolution neural networks to effectively guide unexplored perovskite single crystals experiments. With 7000 graphs from 96 perovskite single crystal growth experiments with different experimental parameters, the ML model was trained to recognize whether crystals could be possibly grown. In addition to distinguishing perovskite crystals, exploring the impact of experimental parameters on the crystallization of perovskite crystals can effectively guide the sequence experiments. Accordingly, a ML regression model was utilized to establish the map between experimental parameters and the probabilities of crystallization, and returned optimal experimental parameters for crystallization.

The poor environmental stability of perovskites severely hinders their practical applications. Various works have discovered that posttreatment with small molecules by dip-coating or spin-coating can effectively improve the stability of perovskites in the humid environment [80, 84]. However, the addition of some molecules (such as amines) might destroy the perovskites film structures. Therefore, it is of practical importance for improving the environmental stability of perovskites through finding suitable molecules possessing compatibility for the perovskite film. Yu et al. [86] established a ML model to study the relationship between properties of amines and their reactivity, and achieved 86% accuracy on predicting the outcomes for whether the qualities of perovskite films are maintained after posttreatment. The results show that amine compounds and pyridine derivatives with a few hydrogen bond donors, large space volume, and large number of substitutions on nitrogen atoms have high compatibility with perovskite films, which can effectively guide further experimental synthesis.

4.2 Photovoltaic Property

The most important electronic property for a solar absorber is bandgap. According to the Shockley-Queisser limit, perovskites with bandgap in the optimal range of 0.9–1.6 eV are promising for single-junction solar cells [87]. Therefore, selecting perovskites with appropriate bandgaps is a vital step in solar cell design. It is

well known that DFT calculations based on PBE functional seriously underestimates bandgaps for semiconductors and insulators. However, advanced theoretical methods (such as hybrid functional or GW) are computationally expensive and time consuming making a high-throughput search inefficient, not to mention experiments. An effective strategy is to combine HT calculation or experimentation with ML to minimize the high cost. In recent years, bandgap prediction has been attempted across a wide range of materials, especially perovskites, using different ML methods such as neural networks, support vector regression, and gradient boosting regression (GBR) [88–97]. Pilania et al. [98] applied kernel ridge regression algorithm to predict the bandgap of double perovskites at the GLLB-SC-level, in which a systematic feature-engineering approach was utilized to identify the optimal feature set from a set of more than 1.2 million candidate features. The final ML model achieved a high prediction accuracy on bandgap (about 0.947). In order to obtain more accurate bandgap values, the researchers developed a multi-fidelity framework combining first-principles calculations and ML techniques, which can estimate high-fidelity data based on low-fidelity data [99]. In this work, PBE-level bandgap values of 599 double perovskites were treated as low-fidelity data, while bandgap values at the Heyd-Scuseria-Ernzerhof (HSE06) level of the same perovskites were treated as the high-fidelity data. By utilizing the framework, high-fidelity HSE06-level bandgap values were approximated from low-fidelity PBE-level bandgap values. Besides inorganic perovskite, Lu et al. [69] developed a framework combining ML techniques and DFT calculations to rapidly predict bandgaps of HOIPs. The GBR model was trained based on PBE-level bandgap values of 212 HOIPs, and achieved high coefficient of determination (R^2) of 97% (Fig. 9c). As is shown in Fig. 9a, the feature importance reveals that, in structure features, the tolerance factor has the most significant impact on bandgap. Besides, the ionization energy, electronegativity, and electron affinity energy of B-site ions are more related to bandgap than those of A and X-site ions. Subsequently, the trained model was applied to predict the bandgap of 5158 unexplored HOIPs and the prediction result is shown in Fig. 9c. Finally, six HOIPs were picked out and validated using DFT calculations. Results in Fig. 9d show that the accuracy of ML-predicted bandgaps is comparable to that of DFT calculations. Similarly, Marchenko developed a ML model using GBR basing on the open-access database of experimentally investigated HOIPs with a 2D perovskite-like crystal structure for the prediction of a bandgap with accuracy within 0.1 eV [50]. The SOAP kernel was used to describe the local atomic environment of each atom and the trained model achieved R^2 as high as 0.9.

Rational chemical mixing is an effective approach to appropriately tune properties of perovskites. For example, mixing halogen elements can adjust the bandgap of halide perovskites, leading to higher performance as solar cells materials [101]. Choubisa et al. developed a descriptor related to the atomic arrangement for mixed perovskites, called as crystal site feature embedding (CSFE, see Fig. 10) [102]. Based on the CSFE representation, the ML model for total energies achieves an MAE of 3.5 meV/atom, and the ML model for bandgaps possesses an MAE of 0.069 eV. The trained model was applied to the predicted bandgap of triple B-site

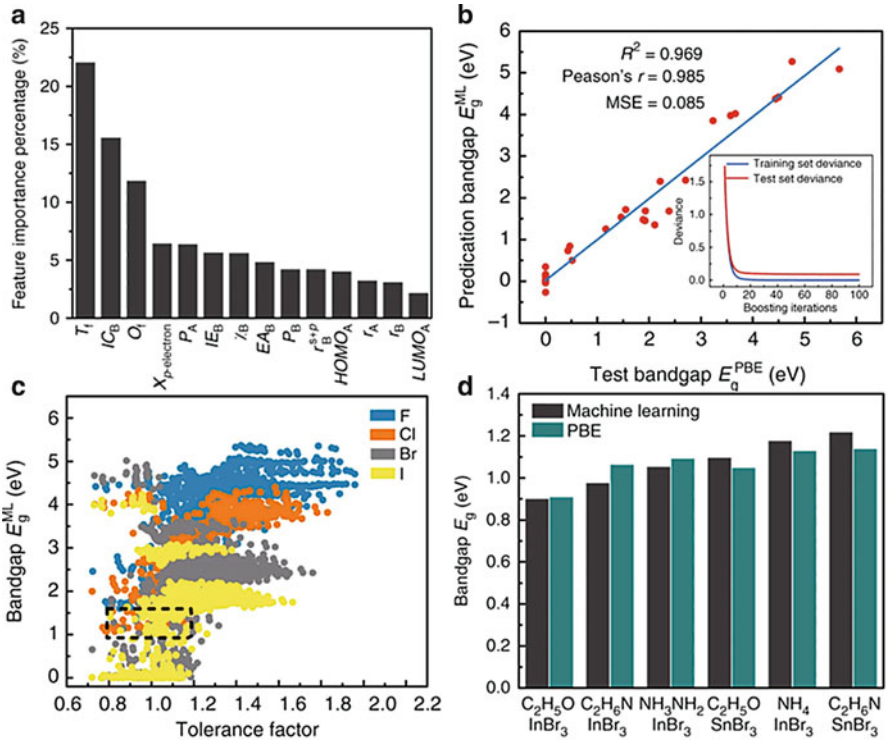

Fig. 9 (**a**) Importance of the selected features. The 14 selected features are ranked using GBR algorithm. (**b**) The fitting results of test bandgaps E_g^{PBE} and predicted bandgaps E_g^{ML}. The subplot is the convergence of model accuracy for five cross-validation split of the data. (**c**) Data visualization of predicted bandgaps for all possible HOIPs (one color represents a class of halogen perovskites) with tolerance factor. (**d**) A comparison between ML-predicted and DFT-calculated results of six selected HOIPs. (Reprinted with permission from Ref. 70)

$MAPb_xSn_yCd_zI_3$ perovskites. ML-predicted results revealed that a small proportion of Cd can tune the bandgap of perovskites to the optimal range for photovoltaic applications. Furthermore, ML models for total energies and bandgaps based on CSFE representation are also suitable for two-dimensional perovskites, with a MAE of 7 meV/atom and 0.13 eV, respectively. Moreover, a variational autoencoder was employed to realize inverse design for perovskites with target properties. Besides searching for potential solar cells materials (bandgap between 1.1 and 1.3 eV), perovskites for infrared sensors (bandgap ~1 eV) and ultraviolet lasers (bandgap ~3.2 eV) were also screened, and selected perovskites were validated by DFT calculations based on HSE06 functional.

The power conversion efficiency (PCE) is a standard parameter to assess the ability of light-electron energy conversion for photovoltaic devices, relating to the optical absorption performance of absorber materials, defect structures, energy-level mismatch, etc. [100]. Searching for high-performance PSCs generally based on the

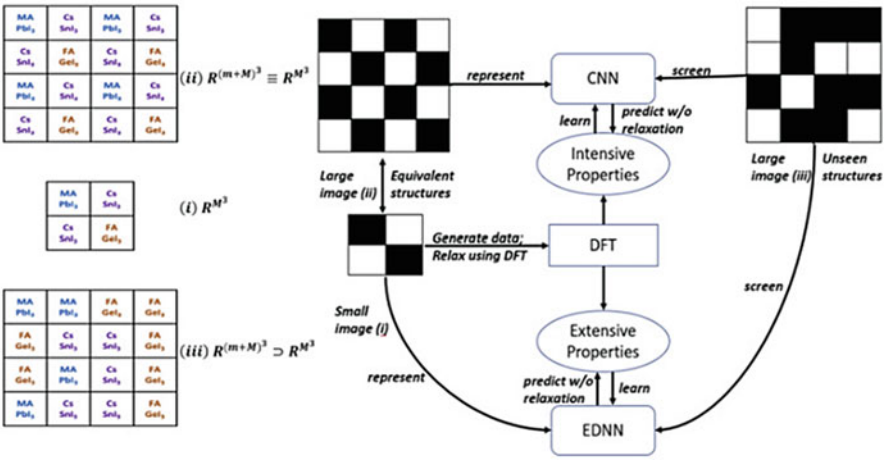

Fig. 10 Workflow for materials discovery using crystal site feature embedding. (Reprinted with permission from Ref. 100. Copyright 2020 Elsevier Inc.)

exhaustive search method, which brings expensive cost of time, materials, equipment, and man power. ML techniques could provide some guidelines and accelerate the discovery of high-performance PSCs without numerous experiments. Odabasi and Yildirim [104] systematically reviewed publications related to perovskites solar cells, and collected 1921 data from 800 publications. Constituent materials and preparation methods of perovskites solar cells were selected as the input variables of the random forest regression model, and PCE was taken as the output variable. Since the input variables of n-i-p and p-i-n perovskites based solar cells were different, two models were trained for each type of solar cells, respectively. For ML model of n-i-p solar cells, the root mean squared error (RMSE) of training set and test set is 1.70 and 3.29, respectively. The model of p-i-n solar cells achieves the RMSE of 1.51 and 2.91 for training set and test set, respectively (Fig. 11). For perovskite solar cells with PCE in the range of 18–23.3%, the association rule mining techniques results exhibit that mixing cations is an effective approach to obtain the solar cells with stabilized PCE higher than 18%. Li et al. [103] collected 333 PSC data from 2000 peer-reviewed publications, and proposed a two-step framework to study the performance of PSCs. At the first step, the experimental bandgap values of perovskites are predicted. Then an ML model to predict the PCE of PSCs was established with considering experimental bandgaps, the difference of HOMO energy level between hole transporting layers and perovskites, and the difference of LUMO energy level between electron transporting layers and perovskites. The RMSE of ML models for bandgaps and PCE is 0.06 eV and 3.23%, respectively. The optimal bandgap range corresponding to the highest PCE is from 1.15 to 1.35 eV, demonstrating high consistency with the Shockley-Queisser limit.

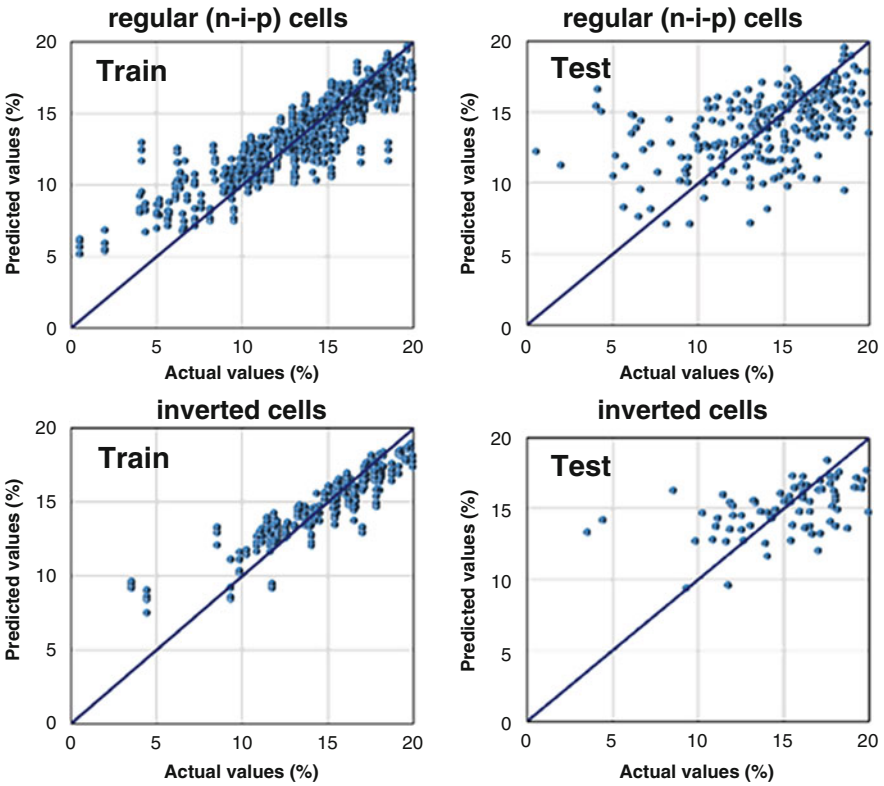

Fig. 11 Actual versus predicted performances by random forest model for training and testing for regular (n-i-p) cells; training and testing for inverted cells. (Reprinted with permission from Ref. 103. Copyright 2018 Elsevier Ltd.)

5 Conclusion and Prospects

To summarize, the rapid development of ML techniques has accelerated novel perovskite material discovery and mechanism exploration. Considering the continuous developments in experimental and computational tools, as well as the ML and data management technologies, ML-aided perovskite researches will increase dramatically. However, there are also some challenges that need to be overcome for the more effective utilization of ML in perovskite researches.

First of all, the importance of data issues in ML researches cannot be overemphasized. Perovskite data generated from the first-principle calculations are rich, especially some material properties like bandgap and formation energy. However, high-quality calculation or experimental data are still lacking due to the high cost and time consuming. Consequently, the models trained basing on low-quality datasets contain bias and are not very suitable for practical application. When high-quality datasets tend to be small, models constructed from these datasets have

limited generalization ability while they are sensitive to the outliers, noise and imbalanced data structure. The strategies to solve the above contradictions and challenges are as follows. (1) Transfer learning may be beneficial for the ML application in small-scale datasets of perovskite-based photovoltaic materials. A ML model (usually with a small data set) can be built from different (but similar) structures' data with larger-scale. In detail, the ML models are firstly utilized to analyze the large datasets created with low-cost computational methods, then the experimental or high accuracy computational data as supplements are utilized to correct the internal bias of the model. This technique can not only fix the problem of data lack, but also reduce the gap between theory and experiment. (2) Using active learning algorithm. Active learning is an iterative procedure, where the initial model is trained on a small dataset, and in each step, the model is re-trained on data expanded with new samples, which are added based on results from the previous steps in order to maximize the learning rate. (3) In fact, the overwhelming majority of scientific knowledge is published as text, so scientific literature is in fact served as data sources as well. In addition to the material data, the literatures contain valuable knowledge about the connections and relationships between the data items interpreted by the authors. Therefore, extracting data and QSPR from the literatures through techniques such as natural language processing will facilitate the development of ML in perovskite research. (4) The high-quality perovskite database should be built according to FAIR (Findable, Accessible, Interoperable, Reusable) data sharing principle [105].

There are also some issues need to be addressed for ML models. A good ML model mainly depends on two factors: first, the predictive performance of the ML model; and second, the interpretability potential of the model. On one hand, the generalization ability of the model is not always verified. A lot of work has achieved excellent performance on the training and test sets, but the prediction results of extended dataset are often not validated using first-principle calculations or experiments. On the other hand, it is often challenging to provide a physical and chemical interpretation of complex ML models, as the goal of the learning process is to find a model that maximizes prediction performance, which may require (possibly non-linear) combinations of hundreds of features. But if the model can be explained based on physical and chemical principle, it will help researchers to insight the structure-property relationship of materials more deeply. In this aspect, feature importance analysis, model visualization, and SHAP analysis [106] will help the development of interpretable models.

Acknowledgments This work is supported by the National Key Research and Development Program of China (2017YFA0204800), Natural Science Foundation of China (21525311, 21773027, 22033002), the National Natural Science Foundation of Jiangsu (BK20180353), the Fundamental Research Funds for the Central Universities of China, and Postgraduate Research & Practice Innovation Program of Jiangsu Province (KYCX20_0075) in China.

References

1. Vasala, S., & Karppinen, M. (2015). A2B′B″O6 perovskites: A review. *Progress in Solid State Chemistry, 43*, 1.
2. Kobayashi, K. I., Kimura, T., Sawada, H., Terakura, K., & Tokura, Y. (1998). Room-temperature magnetoresistance in an oxide material with an ordered double-perovskite structure. *Nature, 395*, 677.
3. Ju, M.-G., Chen, M., Zhou, Y., Dai, J., Ma, L., Padture, N. P., & Zeng, X. C. (2018). Toward eco-friendly and stable perovskite materials for photovoltaics. *Joule, 2*, 1231.
4. PCE. Retrieved from https://www.nrel.gov/pv/cell-efficiency.html.
5. Zhao, X.-G., Yang, D., Ren, J.-C., Sun, Y., Xiao, Z., & Zhang, L. (2018). Rational design of halide double perovskites for optoelectronic applications. *Joule, 2*, 1662.
6. Fuelling discovery by sharing. 2013. *Nature Materials*, *12*, 173.
7. Ghiringhelli, L. M., Vybiral, J., Levchenko, S. V., Draxl, C., & Scheffler, M. (2015). Big data of materials science: Critical role of the descriptor. *Physical Review Letters, 114*, 105503.
8. Sarmiento-Pérez, R., Cerqueira, T. F. T., Körbel, S., Botti, S., & Marques, M. A. L. (2015). Prediction of stable nitride perovskites. *Chemistry of Materials, 27*, 5957.
9. Butler, K. T., Davies, D. W., Cartwright, H., Isayev, O., & Walsh, A. (2018). Machine learning for molecular and materials science. *Nature, 559*, 547.
10. Xie, T., & Grossman, J. C. (2018). Crystal graph convolutional neural networks for an accurate and interpretable prediction of material properties. *Physical Review Letters, 120*, 145301.
11. Askerka, M., Li, Z., Lempen, M., Liu, Y., Johnston, A., Saidaminov, M. I., Zajacz, Z., & Sargent, E. H. (2019). Learning-in-templates enables accelerated discovery and synthesis of new stable double perovskites. *Journal of the American Chemical Society, 141*, 3682.
12. Bartel, C. J., Sutton, C., Goldsmith, B. R., Ouyang, R., Musgrave, C. B., Ghiringhelli, L. M., & Scheffler, M. (2019). New tolerance factor to predict the stability of perovskite oxides and halides. *Science Advances, 5*, eaav0693.
13. Curtarolo, S., Setyawan, W., Wang, S., Xue, J., Yang, K., Taylor, R. H., Nelson, L. J., Hart, G. L. W., Sanvito, S., Buongiorno-Nardelli, M., Mingo, N., & Levy, O. (2012). AFLOWLIB.ORG: A distributed materials properties repository from high-throughput ab initio calculations. *Computational Materials Science, 58*, 227.
14. Ong, S. P., Richards, W. D., Jain, A., Hautier, G., Kocher, M., Cholia, S., Gunter, D., Chevrier, V. L., Persson, K. A., & Ceder, G. (2013). Python Materials Genomics (pymatgen): A robust, open-source python library for materials analysis. *Computational Materials Science, 68*, 314.
15. Hjorth Larsen, A., Jorgen Mortensen, J., Blomqvist, J., Castelli, I. E., Christensen, R., Dulak, M., Friis, J., Groves, M. N., Hammer, B., Hargus, C., Hermes, E. D., Jennings, P. C., Bjerre Jensen, P., Kermode, J., Kitchin, J. R., Leonhard Kolsbjerg, E., Kubal, J., Kaasbjerg, K., Lysgaard, S., Bergmann Maronsson, J., Maxson, T., Olsen, T., Pastewka, L., Peterson, A., Rostgaard, C., Schiotz, J., Schutt, O., Strange, M., Thygesen, K. S., Vegge, T., Vilhelmsen, L., Walter, M., Zeng, Z., & Jacobsen, K. W. (2017). The atomic simulation environment—A Python library for working with atoms. *Journal of Physics. Condensed Matter, 29*, 273002.
16. Yang, X., Wang, Z., Zhao, X., Song, J., Zhang, M., & Liu, H. (2018). MatCloud: A high-throughput computational infrastructure for integrated management of materials simulation, data and resources. *Computational Materials Science, 146*, 319.
17. Chakraborty, S., Xie, W., Mathews, N., Sherburne, M., Ahuja, R., Asta, M., & Mhaisalkar, S. G. (2017). Rational design: A high-throughput computational screening and experimental validation methodology for lead-free and emergent hybrid perovskites. *ACS Energy Letters, 2*, 837.
18. Li, Y., & Yang, K. (2020). High-throughput computational design of halide perovskites and beyond for optoelectronics. *WIREs Computational Molecular Science*. https://doi.org/10.1002/wcms.1500.

19. Körbel, S., Marques, M. A. L., & Botti, S. (2016). Stability and electronic properties of new inorganic perovskites from high-throughput ab initio calculations. *Journal of Materials Chemistry C, 4*, 3157.
20. Emery, A. A., & Wolverton, C. (2017). High-throughput DFT calculations of formation energy, stability and oxygen vacancy formation energy of ABO3 perovskites. *Scientific Data, 4*, 170153.
21. Zhao, X. G., Yang, J. H., Fu, Y., Yang, D., Xu, Q., Yu, L., Wei, S. H., & Zhang, L. (2017). Design of lead-free inorganic halide perovskites for solar cells via cation-transmutation. *Journal of the American Chemical Society, 139*, 2630.
22. Cai, Y., Xie, W., Teng, Y. T., Harikesh, P. C., Ghosh, B., Huck, P., Persson, K. A., Mathews, N., Mhaisalkar, S. G., Sherburne, M., & Asta, M. (2019). High-throughput computational study of halide double perovskite inorganic compounds. *Chemistry of Materials, 31*, 5392.
23. Castelli, I. E., Olsen, T., Datta, S., Landis, D. D., Dahl, S., Thygesen, K. S., & Jacobsen, K. W. (2012). Computational screening of perovskite metal oxides for optimal solar light capture. *Energy & Environmental Science, 5*, 5814.
24. Castelli, I. E., Landis, D. D., Thygesen, K. S., Dahl, S., Chorkendorff, I., Jaramillo, T. F., & Jacobsen, K. W. (2012). New cubic perovskites for one- and two-photon water splitting using the computational materials repository. *Energy & Environmental Science, 5*, 9034.
25. Wang, H.-C., Pistor, P., Marques, M. A. L., & Botti, S. (2019). Double perovskites as p-type conducting transparent semiconductors: A high-throughput search. *Journal of Materials Chemistry A, 7*, 14705.
26. Jiang, X., & Yin, W.-J. (2021). High-throughput computational screening of oxide double perovskites for optoelectronic and photocatalysis applications. *Journal of Energy Chemistry, 57*, 351–358.
27. Zhang, T., Cai, Z., & Chen, S. (2020). Chemical trends in the thermodynamic stability and band gaps of 980 halide double perovskites: A high-throughput first-principles study. *ACS Applied Materials & Interfaces, 12*, 20680.
28. Nakajima, T., & Sawada, K. (2017). Discovery of Pb-free perovskite solar cells via high-throughput simulation on the K computer. *Journal of Physical Chemistry Letters, 8*, 4826.
29. Körbel, S., Marques, M. A. L., & Botti, S. (2018). Stable hybrid organic–inorganic halide perovskites for photovoltaics from ab initio high-throughput calculations. *Journal of Materials Chemistry A, 6*, 6463.
30. Li, Y., & Yang, K. (2019). High-throughput computational design of organic–inorganic hybrid halide semiconductors beyond perovskites for optoelectronics. *Energy & Environmental Science, 12*, 2233.
31. Filip, M. R., & Giustino, F. (2015). Computational screening of homovalent lead substitution in organic–inorganic halide perovskites. *The Journal of Physical Chemistry C, 120*, 166.
32. Unger, E. L., Kegelmann, L., Suchan, K., Sörell, D., Korte, L., & Albrecht, S. (2017). Roadmap and roadblocks for the band gap tunability of metal halide perovskites. *Journal of Materials Chemistry A, 5*, 11401.
33. Kim, C., Huan, T. D., Krishnan, S., & Ramprasad, R. (2017). A hybrid organic-inorganic perovskite dataset. *Scientific Data, 4*, 170057.
34. Jacobs, R., Luo, G., & Morgan, D. (2019). Materials discovery of stable and nontoxic halide perovskite materials for high-efficiency solar cells. *Advanced Functional Materials, 29*, 1804354.
35. Sun, S., Hartono, N. T. P., Ren, Z. D., Oviedo, F., Buscemi, A. M., Layurova, M., Chen, D. X., Ogunfunmi, T., Thapa, J., Ramasamy, S., Settens, C., DeCost, B. L., Kusne, A. G., Liu, Z., Tian, S. I. P., Peters, I. M., Correa-Baena, J.-P., & Buonassisi, T. (2019). Accelerated development of perovskite-inspired materials via high-throughput synthesis and machine-learning diagnosis. *Joule, 3*, 1437.
36. Gu, E., Tang, X., Langner, S., Duchstein, P., Zhao, Y., Levchuk, I., Kalancha, V., Stubhan, T., Hauch, J., Egelhaaf, H. J., Zahn, D., Osvet, A., & Brabec, C. J. (2020). Robot-based high-throughput screening of antisolvents for lead halide perovskites. *Joule, 4*, 1806.

37. Ishihara, H., Sarang, S., Chen, Y.-C., Lin, O., Phummirat, P., Thung, L., Hernandez, J., Ghosh, S., & Tung, V. (2016). Nature inspiring processing route toward high throughput production of perovskite photovoltaics. *Journal of Materials Chemistry A, 4*, 6989.
38. Baker, J., Hooper, K., Meroni, S., Pockett, A., McGettrick, J., Wei, Z., Escalante, R., Oskam, G., Carnie, M., & Watson, T. (2017). High throughput fabrication of mesoporous carbon perovskite solar cells. *Journal of Materials Chemistry A, 5*, 18643.
39. Chen, S., Zhang, L., Yan, L., Xiang, X., Zhao, X., Yang, S., & Xu, B. (2019). Accelerating the screening of perovskite compositions for photovoltaic applications through high-throughput inkjet printing. *Advanced Functional Materials, 29*, 1905487.
40. Jeong, D.-N., Lee, D.-K., Seo, S., Lim, S. Y., Zhang, Y., Shin, H., Cheong, H., & Park, N.-G. (2019). Perovskite cluster-containing solution for scalable D-Bar coating toward high-throughput perovskite solar cells. *ACS Energy Letters, 4*, 1189.
41. Li, J., Du, P., Li, S., Liu, J., Zhu, M., Tan, Z., Hu, M., Luo, J., Guo, D., Ma, L., Nie, Z., Ma, Y., Gao, L., Niu, G., & Tang, J. (2019). High-throughput combinatorial optimizations of perovskite light-emitting diodes based on all-vacuum deposition. *Advanced Functional Materials, 29*, 1903607.
42. Dahl, J. C., Wang, X., Huang, X., Chan, E. M., & Alivisatos, A. P. (2020). Elucidating the weakly reversible Cs-Pb-Br perovskite nanocrystal reaction network with high-throughput maps and transformations. *Journal of the American Chemical Society, 142*, 11915.
43. Li, Z., Najeeb, M. A., Alves, L., Sherman, A. Z., Shekar, V., Cruz Parrilla, P., Pendleton, I. M., Wang, W., Nega, P. W., Zeller, M., Schrier, J., Norquist, A. J., & Chan, E. M. (2020). Robot-accelerated perovskite investigation and discovery. *Chemistry of Materials, 13*, 5650–5663.
44. Reinhardt, E., Salaheldin, A. M., Distaso, M., Segets, D., & Peukert, W. (2020). Rapid characterization and parameter space exploration of perovskites using an automated routine. *ACS Combinatorial Science, 22*, 6.
45. Surmiak, M. A., Zhang, T., Lu, J., Rietwyk, K. J., Raga, S. R., McMeekin, D. P., & Bach, U. (2020). High-throughput characterization of perovskite solar cells for rapid combinatorial screening. *Solar RRL, 4*, 2000097.
46. Chen, S., Hou, Y., Chen, H., Tang, X., Langner, S., Li, N., Stubhan, T., Levchuk, I., Gu, E., Osvet, A., & Brabec, C. J. (2018). Exploring the stability of novel wide bandgap perovskites by a robot based high throughput approach. *Advanced Energy Materials, 8*, 1701543. https://doi.org/10.1002/aenm.201701543.
47. The HybriD^3 materials database. Retrieved from https://materials.hybrid3.duke.edu/.
48. Perovskite Solar Cells DB. Retrieved from http://www.perovskite.info/perovskite/perovSearch.
49. The Computational Material Repository. Retrieved from https://cmr.fysik.dtu.dk/#.
50. Marchenko, E. I., Fateev, S. A., Petrov, A. A., Korolev, V. V., Mitrofanov, A., Petrov, A. V., Goodilin, E. A., & Tarasov, A. B. (2020). Database of two-dimensional hybrid perovskite materials: open-access collection of crystal structures, band gaps, and atomic partial charges predicted by machine learning. *Chemistry of Materials, 32*(17), 7383–7388.
51. Jain, A., Ong, S. P., Hautier, G., Chen, W., Richards, W. D., Dacek, S., Cholia, S., Gunter, D., Skinner, D., Ceder, G., & Persson, K. A. (2013). Commentary: The Materials Project: A materials genome approach to accelerating materials innovation. *APL Materials, 1*, 011002.
52. Saal, J. E., Kirklin, S., Aykol, M., Meredig, B., & Wolverton, C. (2013). Materials design and discovery with high-throughput density functional theory: The Open Quantum Materials Database (OQMD). *JOM, 65*, 1501.
53. Atomly. Retrieved from https://atomly.net/.
54. Pilania, G., Balachandran, P. V., Gubernatis, J. E., & Lookman, T. (2020). *Data-based methods for materials design and discovery: Basic ideas and general methods* (Vol. 1, p. 1). San Rafael, CA: Morgan & Claypool Publishers.
55. Ramprasad, R., Batra, R., Pilania, G., Mannodi-Kanakkithodi, A., & Kim, C. (2017). Machine learning in materials informatics: Recent applications and prospects. *NPJ Computational Materials, 3*, 54.

56. Mueller, T., Kusne, A. G., & Ramprasad, R. (2016). Machine learning in materials science. In A. L. Parrill & K. B. Lipkowitz (Eds.), *Reviews in computational chemistry* (p. 186). Hoboken, NJ: Wiley.
57. Muratov, E. N., Bajorath, J., Sheridan, R. P., Tetko, I. V., Filimonov, D., Poroikov, V., Oprea, T. I., Baskin, I. I., Varnek, A., Roitberg, A., Isayev, O., Curtarolo, S., Fourches, D., Cohen, Y., Aspuru-Guzik, A., Winkler, D. A., Agrafiotis, D., Cherkasov, A., & Tropsha, A. (2020). QSAR without borders. *Chemical Society Reviews, 49*, 3525.
58. Seko, A., Togo, A., & Tanaka, I. (2018). Descriptors for machine learning of materials data. In *Nanoinformatics* (p. 3). Singapore: Springer.
59. Bartók, A. P., Kondor, R., & Csányi, G. (2013). On representing chemical environments. *Physical Review B, 87*, 184115.
60. Filip, M. R., & Giustino, F. (2018). The geometric blueprint of perovskites. *Proceedings of the National Academy of Sciences of the United States of America, 115*, 5397.
61. Ouyang, R., Curtarolo, S., Ahmetcik, E., Scheffler, M., & Ghiringhelli, L. M. (2018). SISSO: A compressed-sensing method for identifying the best low-dimensional descriptor in an immensity of offered candidates. *Physical Review Materials, 2*, 083802.
62. Goldschmidt, V. M. (1926). Die gesetze der krystallochemie. *Naturwissenschaften, 14*, 477.
63. Li, C., Soh, K. C. K., & Wu, P. (2004). Formability of ABO3 perovskites. *Journal of Alloys and Compounds, 372*, 40.
64. Li, C., Lu, X., Ding, W., Feng, L., Gao, Y., & Guo, Z. (2008). Formability of ABX3 (X = F, Cl, Br, I) halide perovskites. *Acta Crystallographica. Section B, 64*, 702.
65. Kieslich, G., Sun, S., & Cheetham, A. K. (2015). An extended Tolerance Factor approach for organic-inorganic perovskites. *Chemical Science, 6*, 3430.
66. Sun, Q., & Yin, W. J. (2017). Thermodynamic stability trend of cubic perovskites. *Journal of the American Chemical Society, 139*, 14905.
67. Zhou, Q., Lu, S., Wu, Y., & Wang, J. (2020). Property-oriented material design based on a data-driven machine learning technique. *Journal of Physical Chemistry Letters, 11*, 3920.
68. Balachandran, P. V., Xue, D., Theiler, J., Hogden, J., Gubernatis, J. E., & Lookman, T. (2018). Importance of feature selection in machine learning and adaptive design for materials. In *Materials discovery and design* (p. 59). Cham: Springer.
69. Lu, S. H., Zhou, Q. H., Ouyang, Y. X., Guo, Y. L., Li, Q., & Wang, J. L. (2018). Accelerated discovery of stable lead-free hybrid organic-inorganic perovskites via machine learning. *Nature Communications, 9*, 3405.
70. Lu, S., Zhou, Q., Ma, L., Guo, Y., & Wang, J. (2019). Rapid discovery of ferroelectric photovoltaic perovskites and material descriptors via machine learning. *Small Methods*. https://doi.org/10.1002/smtd.201900360.
71. Ziletti, A., Kumar, D., Scheffler, M., & Ghiringhelli, L. M. (2018). Insightful classification of crystal structures using deep learning. *Nature Communications, 9*, 2775.
72. Balachandran, P. V., Emery, A. A., Gubernatis, J. E., Lookman, T., Wolverton, C., & Zunger, A. (2018). Predictions of new ABO(3) perovskite compounds by combining machine learning and density functional theory. *Physical Review Materials, 2*, 043802.
73. Ye, W., Chen, C., Wang, Z., Chu, I.-H., & Ong, S. P. (2018). Deep neural networks for accurate predictions of crystal stability. *Nature Communications, 9*, 3800.
74. Im, J., Lee, S., Ko, T. W., Kim, H. W., Hyon, Y., & Chang, H. (2019). Identifying Pb-free perovskites for solar cells by machine learning. *NPJ Computational Materials, 5*, 37.
75. Pilania, G., Balachandran, P. V., Gubernatis, J. E., & Lookman, T. (2015). Classification of ABO3 perovskite solids: A machine learning study. *Acta Crystallographica B Structural Science, Crystal Engineering and Material, 71*, 507.
76. Pilania, G., Balachandran, P. V., Kim, C., & Lookman, T. (2016). Finding new perovskite halides via machine learning. *Frontiers in Materials, 3*, 19.
77. Li, W., Jacobs, R., & Morgan, D. (2018). Predicting the thermodynamic stability of perovskite oxides using machine learning models. *Computational Materials Science, 150*, 454.
78. Xu, Q., Li, Z., Liu, M., & Yin, W. J. (2018). Rationalizing perovskite data for machine learning and materials design. *Journal of Physical Chemistry Letters, 9*, 6948.

79. Schmidt, J., Shi, J., Borlido, P., Chen, L., Botti, S., & Marques, M. A. L. (2017). Predicting the thermodynamic stability of solids combining density functional theory and machine learning. *Chemistry of Materials, 29*, 5090.
80. Yang, S., Wang, Y., Liu, P., Cheng, Y.-B., Zhao, H. J., & Yang, H. G. (2016). Functionalization of perovskite thin films with moisture-tolerant molecules. *Nature Energy, 1*, 15016.
81. Li, Z., Xu, Q., Sun, Q., Hou, Z., & Yin, W.-J. (2019). Thermodynamic stability landscape of halide double perovskites via high-throughput computing and machine learning. *Advanced Functional Materials, 29*, 1807280.
82. Mazaheri, T., Sun, B., Scher-Zagier, J., Thind, A. S., Magee, D., Ronhovde, P., Lookman, T., Mishra, R., & Nussinov, Z. (2019). Stochastic replica voting machine prediction of stable cubic and double perovskite materials and binary alloys. *Physical Review Materials, 3*, 063802.
83. Ali, A., Park, H., Mall, R., Aissa, B., Sanvito, S., Bensmail, H., Belaidi, A., & El-Mellouhi, F. (2020). Machine learning accelerated recovery of the cubic structure in mixed-cation perovskite thin films. *Chemistry of Materials, 32*, 2998.
84. Zhang, H., Ren, X., Chen, X., Mao, J., Cheng, J., Zhao, Y., Liu, Y., Milic, J., Yin, W.-J., Grätzel, M., & Choy, W. C. H. (2018). Improving the stability and performance of perovskite solar cells via off-the-shelf post-device ligand treatment. *Energy & Environmental Science, 11*, 2253.
85. Kirman, J., Johnston, A., Kuntz, D. A., Askerka, M., Gao, Y., Todorovic, P., Ma, D., Prive, G. G., & Sargent, E. H. (2020). Machine-learning-accelerated perovskite crystallization. *Matter, 2*, 938.
86. Yu, Y., Tan, X., Ning, S., & Wu, Y. (2019). Machine learning for understanding compatibility of organic–inorganic hybrid perovskites with post-treatment amines. *ACS Energy Letters, 4*, 397.
87. Shockley, W., & Queisser, H. J. (1961). Detailed balance limit of efficiency of p-n junction solar cells. *Journal of Applied Physics, 32*, 510.
88. Zhang, L., He, M., & Shao, S. (2020). Machine learning for halide perovskite materials. *Nano Energy, 78*, 105380.
89. Yılmaz, B., & Yıldırım, R. (2021). Critical review of machine learning applications in perovskite solar research. *Nano Energy, 80*, 105546.
90. Takahashi, K., Takahashi, L., Miyazato, I., & Tanaka, Y. (2018). Searching for hidden perovskite materials for photovoltaic systems by combining data science and first principle calculations. *ACS Photonics, 5*, 771.
91. Agiorgousis, L. M., Sun, Y. Y., Choe, D. H., West, D., & Zhang, S. (2019). Machine learning augmented discovery of chalcogenide double perovskites for photovoltaics. *Advanced Theory and Simulations*. https://doi.org/10.1002/adts.201800173.
92. Wu, T., & Wang, J. (2019). Global discovery of stable and non-toxic hybrid organic-inorganic perovskites for photovoltaic systems by combining machine learning method with first principle calculations. *Nano Energy, 66*, 104070.
93. Chaube, S., Khullar, P., Srinivasan, S. G., & Rai, B. (2020). A statistical learning framework for accelerated bandgap prediction of inorganic compounds. *Journal of Electronic Materials, 49*, 752.
94. Gladkikh, V., Kim, D. Y., Hajibabaei, A., Jana, A., Myung, C. W., & Kim, K. S. (2020). Machine learning for predicting the band gaps of ABX(3) perovskites from elemental properties. *Journal of Physical Chemistry C, 124*, 8905.
95. Jao, M. H., Chan, S. H., Wu, M. C., & Lai, C. S. (2020). Element code from pseudopotential as efficient descriptors for a machine learning model to explore potential lead-free halide perovskites. *Journal of Physical Chemistry Letters, 11*, 8914.
96. Park, H., Mall, R., Ali, A., Sanvito, S., Bensmail, H., & El-Mellouhi, F. (2020). Importance of structural deformation features in the prediction of hybrid perovskite bandgaps. *Computational Materials Science, 184*, 109858.

97. Saidi, W. A., Shadid, W., & Castelli, I. E. (2020). Machine-learning structural and electronic properties of metal halide perovskites using a hierarchical convolutional neural network. *NPJ Computational Materials, 6*, 36.
98. Pilania, G., Mannodi-Kanakkithodi, A., Uberuaga, B. P., Ramprasad, R., Gubernatis, J. E., & Lookman, T. (2016). Machine learning bandgaps of double perovskites. *Scientific Reports, 6*, 19375.
99. Pilania, G., Gubernatis, J. E., & Lookman, T. (2017). Multi-fidelity machine learning models for accurate bandgap predictions of solids. *Computational Materials Science, 129*, 156.
100. Li, W., Wang, Z., Deschler, F., Gao, S., Friend, R. H., & Cheetham, A. K. (2017). Chemically diverse and multifunctional hybrid organic–inorganic perovskites. *Nature Reviews Materials, 2*, 16099.
101. Zhang, X., Li, L., Sun, Z., & Luo, J. (2019). Rational chemical doping of metal halide perovskites. *Chemical Society Reviews, 48*, 517.
102. Choubisa, H., Askerka, M., Ryczko, K., Voznyy, O., Mills, K., Tamblyn, I., & Sargent, E. H. (2020). Crystal site feature embedding enables exploration of large chemical spaces. *Matter, 3*, 433–448.
103. Li, J., Pradhan, B., Gaur, S., & Thomas, J. (2019). Predictions and strategies learned from machine learning to develop high-performing perovskite solar cells. *Advanced Energy Materials, 9*, 16099.
104. Odabasi, C., & Yildirim, R. (2019). Performance analysis of perovskite solar cells in 2013–2018 using machine-learning tools. *Nano Energy, 56*, 770.
105. Milkinson, M., Dumontier, M., Aalbersberg, I. J., Appleton, G., Axton, M., Baak, A., Blomberg, N., Boiten, J.-W., da Silva Santos, L. B., Bourne, P. E., Bouwman, J., Brookes, A. J., Clark, T., Crosas, M., Dillo, I., Dumon, O., Edmunds, S., Evelo, C. T., Finkers, R., Gonzalez-Beltran, A., Gray, A. J. G., Groth, P., Goble, C., Grethe, J. S., Heringa, J., Hoen, P. A. C., Hooft, R., Kuhn, T., Kok, R., Kok, J., Lusher, S. J., Martone, M. E., Mons, A., Packer, A. L., Persson, B., Rocca-Serra, P., Roos, M., van Schaik, R., Sansone, S.-A., Schultes, E., Sengstag, T., Slater, T., Strawn, G., Swertz, M. A., Thompson, M., van der Lei, J., van Mulligen, E., Velterop, J., Waagmeester, A., Wittenburg, P., Wolstencroft, K., Zhao, J. & Mons, B. (2016). The FAIR Guiding Principles for scientific data management and stewardship. *Sci. Data, 3*, 160018.
106. Lundberg, S. M., Chen, H., DeGrave, A., Prutkin, J. M., Nair, B., Katz, R., Himmelfarb, J., Bansal, N., & Lee, S. I. (2020). From local explanations to global understanding with explainable AI for trees. *Nat. Mach. Intell. 2*, 56–67.

Index

Y. Cheng et al. (eds.), *Artificial Intelligence for Materials Science*, Springer Series in Materials Science 312, https://doi.org/10.1007/978-3-030-68310-8